DOE/ER/10764--T2

THE UNIVERSITY OF WISCONSIN–MILWAUKEE

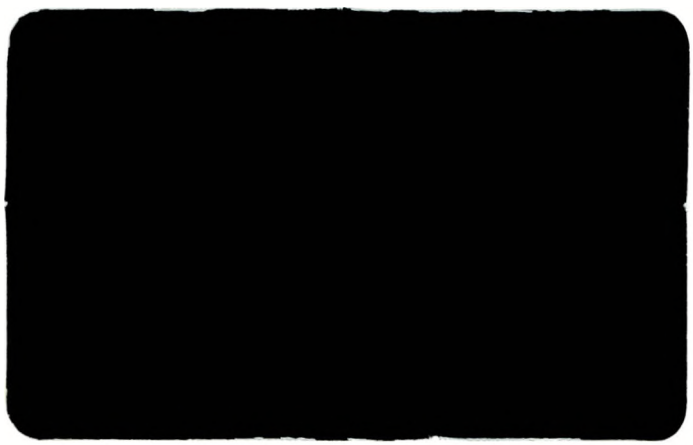

COLLEGE OF ENGINEERING AND APPLIED SCIENCE

DOE/ER/13764--T2

DE91 009803

INTERFACIAL CHARACTERISTIC MEASUREMENTS IN HORIZONTAL BUBBLY TWO-PHASE FLOW

Z. Wang, W. D. Huang,
S. Srinivasmurthy

and

G. Kocamustafaogullari

Department of Mechanical Engineering
University of Wisconsin--Milwaukee
Milwaukee, Wisconsin 53201

October 1990

Prepared for

U.S. DEPARTMENT OF ENERGY
Under Contract No. DE-FG02-87ER13764
DOE/NE/13764-4

245E/5616E/5842E

TABLE OF CONTENTS

ABSTRACT

Advances in the study of two-phase flow increasingly require detailed internal structure information upon which theoretical models can be formulated. The void fraction and interfacial area are two fundamental parameters characterizing the internal structure of two-phase flow. However, little information is currently available on these parameters, and it is mostly limited to vertical flow configurations. Particularly, there is virtually no data base for the local interfacial area concentration in spite of its necessity in multi-dimensional two-fluid model analysis.

In view of the above, the internal phase distribution of cocurrent, air-water bubbly flow in a 50.3 mm diameter transparent pipeline has been experimentally investigated by using a double-sensor resistivity probe. Liquid and gas volumetric superficial velocities ranged from 3.74 to 5.60 m/s and 0.25 to 1.59 m/s, respectively, and average void fractions ranged from 2.12 to 22.5%. The local values of void fractions, interfacial area concentration, mean bubble diameter, bubble interface velocity, bubble chord-length and bubble frequency distributions were measured.

The experimental results indicate that the void fraction, interfacial area concentration and bubble frequency have local maxima near the upper pipe wall, and the profiles tend to flatten with increasing void fraction. The observed peak void fraction can reach 0.65, the peak interfacial area can go up to 900 ~ 1000 m^2/m^3, and the bubble frequency can reach a value of 2200/s. These ranges of values have never been reported for vertical bubbly flow. It is found that either decreasing the liquid flow rate or increasing the gas flow would increase the local void fraction, the interfacial area concentration and the bubble frequency.

The axial bubble interface velocity and the Sauter mean diameter profiles show a relatively uniform distribution except near the upper pipe wall, where a sharp reduction in the velocity and mean diameter occurs. The local bubble velocity and the mean diameter generally increases with the gas flow rate.

LIST OF FIGURES

LIST OF TABLES

NOMENCLATURE

a_i	Interfacial area concentration
B_o	Factor defined in Eq. (42)
C	Concentration in liquid phase
C_A^*	Concentration of component A at gas-liquid interface
D	Fluid particle diameter
D_A	Diffusion coefficient of A in liquid phase
D_B	Diffusion coefficient of B in liquid phase
D_{sm}	Sauter mean diameter
E	Enhancement factor
f(D)	Fluid particle size distribution
g	Gravitational acceleration
h	Specific enthalpy
I	Intensity of a light beam
j	Superficial volumetric flux for two-phase mixture
j_f	Superficial volumetric flux for gaseous phase
j_g	Superficial volumetric flux for liquid phase
k_{LA}	Mass transfer coefficient in liquid phase
k_{mn}	Reaction rate constant
L	Distance between two sensor tips
l	Distance a light beam travels through fluid
$\dot{M}''_{ki}$	Interfacial momentum flux for k'th phase
$\dot{m}''_{ki}$	Interfacial mass flux for k'th phase
N	Total number of bubbles passing through a sensor in a sampling time T
N_i	Total number of interfaces passing through a sensor in a sampling time T

N_u	Total number of channels used in data processing, and total bubble size class in Eq. (52)
$\vec{n}_i$	Unit normal vector of interface
n_k	Total bubble count in k'th channel, and number of bubbles of size D_k in Eq. (52)
p	Pressure
$\dot{Q}_g$	Volumetric flow rate of gas
$\dot{q}''$	Mean conductive heat flux
$\dot{q}''^t$	Turbulent heat flux
$\dot{q}''_i$	Interfacial heat flux
R_A	Rate of absorption of gas A per unit volume of mixture
r	Radial position
S	Root mean square of fluctuating component of sensor passing velocity
S_{app}	Apparent scattering coefficient
S_n	Scattering coefficient
u_b	Axial component of bubble interface velocity
u_{bj}	Passing velocity of j'th interface measured through a sensor in the axial flow direction
$\bar{u}_b$	Area average bubble interface velocity
$\bar{u}_g$	Area average gas velocity
V	Voltage drop across a sensor
V_{max}	Maximum value of V
V_{min}	Minimum value of V
V_T	Threshold voltage
T	Sampling time
t	Time
$\vec{v}_i$	Interface velocity vector

α	Void fraction
α_k	Volumetric fraction of k'th phase
β	Attenuation coefficient
Δt_m	Most probable time delay determined by cross correlation method
Δt_{max}	Time limit corresponding to minimum bubble velocity
Δt_{min}	Time limit corresponding to maximum bubble velocity
δ	Delta function
λ	Wave length
ν_A	Stoichiometric factor
ρ	Mass density
$\underline{\underline{\tau}}$	Average viscous shear stress
$\underline{\underline{\tau}}_i$	Average interfacial shear stress
$\underline{\underline{\tau}}^t$	Average turbulent shear stress
Φ	Energy dissipation

Subscripts

f	Liquid phase, and also identifies front sensor
g	gaseous phase
i	Value at interface
j	Refers to a j'th surface
k	k'th phase (gas or liquid), and also identifies k'th channel in Eqs. (44) and (45)
r	Identifies rear sensor

1. INTRODUCTION

Two-phase flow is characterized by the existence of the interfaces between phases and discontinuities of properties associated with them. The internal structures of two-phase flow are classified by two-phase flow patterns. Advances in the study of two-phase flow increasingly require detailed internal flow structure information upon which theoretical models can be formulated. The void fraction and the interfacial area are two fundamental geometrical parameters characterizing the internal structure of two-phase flow. The void fraction represents the phase distributions and is a required parameter for hydrodynamic and thermal calculations in various industrial processes. On the other hand, the interfacial area describes available area for the interfacial transport and is of prime importance in modeling and determining the interphase transfer of mass, momentum and energy in steady and transient two-phase flows. Therefore, an accurate knowledge of these parameters is essential for any two-phase flow analysis. This fact can be further substantiated with respect to the mathematical formulation of two-phase flow.

In order to analyze the thermal-hydraulic behavior of two-phase flow, various formulations, such as the homogeneous flow model, drift-flux model [1-4], and two-fluid model [5-13], have been proposed. As suggested by Ishii and Kocamustafaogullari [14], among these models, the two-fluid formulation can be considered the most accurate model because of its detailed treatment of the two-phase interactions at the interface. As it is briefly described below, in such a model, the knowledge of the interfacial area is indispensible and must be incorporated into the model as part of the constitutive equations.

The two-fluid model is formulated by considering each phase separately in terms of two sets of conservation equations which govern the balance of mass,

momentum, and energy of each phase. These balance equations represent the macroscopic fields of each phase and are obtained from proper averaging methods. Since the macroscopic fields of each phase are not independent of the other phase, the phase interaction terms which couple the transport of mass, momentum, and energy of each phase appear in the field equations. It is expected that the two-fluid model can predict mechanical and thermal nonequilibrium between phases accurately. However, it is noted that the interfacial transfer terms should be modeled accurately for the two-fluid model to be useful.

The difficulties arise in modeling the interfacial terms since the complicated transfer mechanisms at the interfaces are coupled with the motion and geometry of the interfaces. Furthermore, the closure relations should be modeled by macroscopic variables based on proper averaging. A three-dimensional two-fluid model has been obtained by using temporal or statistical averaging, Ishii [5]. For most practical applications, the model developed by Ishii can be arranged in the following forms:

Continuity Equation

$$\frac{\partial \alpha_k \rho_k}{\partial t} + \nabla \cdot (\alpha_k \rho_k \vec{v}_k) = a_i \dot{m}''_{ki} \quad ; \quad k = f \text{ and } g \tag{1}$$

Momentum Equation

$$\frac{\partial \alpha_k \rho_k \vec{v}_k}{\partial t} + \nabla \cdot (\alpha_k \rho_k \vec{v}_k \vec{v}_k) = -\alpha_k \nabla p_k + \nabla \cdot \alpha_k (\bar{\tau}_k + \bar{\tau}^t_k)$$

$$+ \alpha_k \rho_k \vec{g} - \nabla \alpha_k \cdot \bar{\tau}_i + a_i \dot{m}''_{ki} \vec{v}_{ki} + a_i \vec{M}''_{ki} \quad ; \quad k = f \text{ and } g \tag{2}$$

Enthalpy Energy Equation

$$\frac{\partial \alpha_k \rho_k h_k}{\partial t} + \nabla \cdot (\alpha_k \rho_k h_k \vec{v}_k) = -\nabla \cdot \alpha_k \left(\dot{\dot{q}}''_k + \dot{\vec{q}}''^t_k\right) + \alpha_k \frac{D_k}{Dt} p_k$$

$$+ \Phi_k + a_i \left(\dot{m}''_{ki} h_{ki} + \dot{q}''_{ki}\right) \quad ; \quad k = f \text{ and } g \tag{3}$$

where m''_{ki}, $\vec{M}''_{ki}$, τ_i, q''_{ki}, and Φ_k are the interfacial mass flux, generalized interfacial momentum flux or generalized interfacial drag force per unit of interfacial area, interfacial shear stress, interfacial heat flux, and dissipation, respectively. The subscript k denotes the k'th phase, and i stands for the value at the interface. α_k, ρ_k, v_k, p_k and h_k denote the void fraction, density, velocity, pressure and specific enthalpy of the k'th phase, whereas τ_i, τ_k^t, $\dot{\vec{q}}''_k$, $\dot{\vec{q}}''^t_k$ and g stand for average viscous stress, turbulent stress, mean conduction heat flux, turbulent heat flux and acceleration due to gravity. h_{ki} is the enthalpy of k'th phase at the interface; thus, it may be assumed to be the saturation enthalpy for most cases. Finally, a_i denotes the interfacial area concentration. It is the interfacial area per unit mixture volume. Thus,

$$a_i = \frac{\text{Interfacial Area}}{\text{Mixture Volume}} \tag{4}$$

The above field equations indicate that several interfacial transfer terms appear on the right-hand sides of the equations. Since these interfacial transfer terms also should obey the balance laws at the interface, interfacial transfer conditions could be obtained from an average of the local interfacial conditions, [5]. They are given by

$$\sum_k \dot{m}''_{ki} = 0 \tag{5}$$

$$\sum_k \dot{\vec{M}}''_{ki} = 0 \tag{6}$$

$$\sum_k \dot{m}''_{ki} h_{ki} + \dot{q}''_{ki} = 0 \tag{7}$$

In view of the above two-fluid model formulation, it is evident that the interfacial transfer terms appearing on the right-hand side of Eqs. (1) - (3) are all expressed as the product of the interfacial area concentration and the flux terms identifying the interfacial mass, momentum and energy transports, respectively. It is essential to make a conceptual distinction between the effects of these two parameters. As demonstrated by Ishii [5] and further detailed by Ishii and Kocamustafaogullari [14] and Ishii et al. [15], the interfacial flux terms characterize the local transport mechanisms such as the turbulence molecular transport properties and can be related to the respective potentials. On the other hand, the local interfacial area concentration is related to the interfacial structure of the two-phase flow fields and should be specified by a constitutive equation, or by introducing an additional transport equation. As the above formulation indicates, the knowledge of the local interfacial area concentration is essential for a detailed analysis and prediction of the behavior of a two-phase flow system.

However, the knowledge of the interfacial area concentration is quite limited due to considerable difficulties in experimental measurements. Particularly, there is little knowledge on the local interfacial area concentration in spite of its necessity in two or three-dimensional analyses. Most of the experimental data are limited to volume averaged interfacial area concentration over a section of a flow channel. There are very few data available on local measurement of interfacial area concentration. Furthermore, according to the authors' knowledge, there has been no

experimental data available on the local distribution of interfacial area concentration in horizontal two-phase flow systems. In view of this, the local interfacial area concentration has been studied experimentally by using the double-sensor resistivity probe. The results of the double-sensor resistivity probe measurement in a horizontal air-water, bubbly, two-phase flow are presented here. In addition to the local interfacial area measurements, other characteristic interfacial parameters such as

- local void fraction profile,
- local interfacial velocity profile,
- local bubble chord-length and bubble size distribution, and
- local bubble frequency distribution

have also been studied experimentally, and the results are documented. Furthermore, the dependence of the local parameters listed above on other flow variables are demonstrated.

2. INTERFACIAL AREA MEASUREMENT METHODS

Several methods are available at present to measure interfacial area concentrations in gas-liquid and liquid-liquid two-phase flows. These are photography, light attenuation, ultrasonic, probing and chemical methods. Detailed reviews of all these methods have been given by Veteau and Morel [16], Veteau and Charlot [17,18], Veteau [19] and Ishii and Mishima [9]. In what follows, we shall briefly describe the principles of the measurement methods and discuss the advantages and limitations of each method.

2.1 Chemical Method

In this technique, integral values of interfacial areas are obtained by absorption experiments. This requires knowledge of gas solubility, dispersion characteristics of both phases, and either mass transfer coefficient in the

case of physical absorption or diffusivity and reaction rate constants in the case of chemical absorption. Many chemical systems have been proposed for determination of interfacial areas by the chemical method, including non-aqueous systems. A suitable reaction has to be chosen carefully, as the result may be specific to the system used, the properties of which can hardly be varied. The value of the interfacial area concentration obtained thus is usually referred to as "effective interfacial area" indicating that it may deviate from the geometrical interfacial area and depends strongly on the particular conditions employed.

Several factors have to be considered when choosing a chemical reaction for measuring interfacial areas if the results are to be free of excessive error. The systems useful for such measurements have been reviewed by Sharma and Danckwerts [20]. The topic has been dealt with in the literature [20-47] and will be discussed here only to the extent directly relevant to the measurement principles.

For an irreversible reaction of a gas phase component A with a liquid phase reactant B

$$\nu_A\ A + B \rightarrow \text{Products} \tag{8}$$

which is of order m, n in A and B, respectively. An approximate expression for the enhancement factor is given by Danckwerts [20] as

$$E = \frac{\sqrt{M}\ [(E_i - E)/(E_i - 1)]^{n/2}}{\tanh\ \{\sqrt{M}\ [(E_i - E)/(E_i - 1)]^{n/2}\}} \tag{9}$$

where

$$E \equiv \frac{R_A}{a_i k_{LA} C_A^*} \tag{10}$$

$$E_i \equiv 1 + \frac{\nu_A C_B D_B}{C_A^* D_A} \tag{11}$$

and

$$M \equiv \frac{1}{k_{LA}^2} \left[\left(\frac{2}{m+1}\right) k_{mn} D_A (C_A^*)^{m-1} C_B^n\right] \tag{12}$$

In these equations, ν_A is the stoichiometric factor, R_A is the rate of absorption of gas A per unit volume of the gas-liquid two-phase mixture, k_{LA} is the mass transfer coefficient of A in the liquid phase, k_{mn} is the reaction rate constant, and D_A and D_B are the diffusion coefficients of A and B, respectively. C_B is the concentration of the component B in the bulk of the liquid phase, whereas C_A^* is the concentration of A at the gas-liquid interface which is assumed to be equal to the equilibrium concentration of A in the bulk liquid phase.

A pseudo-m'th, n'th order reaction is approximated when $\sqrt{M} \ll E_i$. In this case, Eq. (9) can be approximated by

$$E = \sqrt{1 + M} \tag{13}$$

For purposes of measuring interfacial areas, only fast reactions which are characterized by

$$1 \ll \sqrt{M} \ll E_i \tag{14}$$

are relevant. In such cases, Eq. (13) can, in turn, be approximated by

$$E = \sqrt{M} \tag{15}$$

Substituting E and M from Eqs. (10) and (12), respectively, the following equation is obtained for the rate of absorption of A in an irreversible, fast m'th, n'th, order reaction:

$$R_A = a_i\left[\left(\frac{2}{m+1}\right) k_{mn} D_A (C_A^*)^{m+1} C_B^n\right]^{1/2} \qquad (16)$$

Equation (16) states that the absorption rate is independent of k_{LA}--that is of the hydrodynamic conditions. Instead, it is governed by the physiochemical parameters, reactant concentration and the area of contact surface. For the type of reaction so far discussed, the means to influence the values of M and E_i, in order to justify the inequality expressed by Eq. (14) to be valid, are rather limited.

In principle, selecting a suitable chemical reaction confirming Eq. (14) and measuring the absorption rate, R_A, the local interfacial area concentration, a_i, can be evaluated directly from Eq. (16) provided that the physiochemical parameters appearing in the right-hand side bracket are known. Thus, knowledge of reaction kinetics, solubility of gas-phase component A, the diffusion coefficient of A in the liquid-phase B, and, finally, the experimental capability of measuring the local rate of absorption are required for determining a_i from Eq. (16). While the chemical systems confirming Eq. (14) for such measurements have been reviewed by Sharma and Danckwerts [21], in principal it is extremely difficult, if not impossible, to measure the local rate of absorption. Therefore, instead of the local interfacial area measurements, in practice an averaged interfacial area concentration is obtained in terms of measurable quantities by incorporating Eq. (16) into a molar balance on the liquid phase over the total volume of the test section used in the experiment. Since the average of a product differs from the product of the averages, the interfacial area concentration obtained from the integral of Eq. (16) would be considered as an "effective interfacial area concentration" instead of the actual volume-averaged interfacial area concentration. If the fast reaction condition expressed by Eq. (14) is not

fulfilled and the absorption takes place at the transition from slow to fast reaction regime, absorption measurements at different reaction rates must be carried out. In this case, the interfacial area concentration is obtained from the so-called Danckwerts plot [21].

Based on the above principle, many chemical systems have been proposed for determination of effective interfacial areas by using the chemical method [20-47]. The relevant literature have been recently reviewed by DeJesus and Kawaji [48]. It has been observed by Schumpe and Deckwer [34,35] that in the pseudo-homogeneous flow regimes, the values of the interfacial area determined by the photographic method were greater than those obtained by the chemical method by about 35%. However, in the heterogeneous flow regime the values obtained by the photographic method were twice as high as those obtained by the chemical method. They have also observed that two different chemical methods yielded largely different values, even under similar conditions. This may be due to the fact that the effective area is evaluated on the basis of simplified reactor models which do not account for the mixing phenomena of the gas phase. Bubble shrinkage due to absorption is also neglected. They have, however, also shown that this discrepancy can be reduced greatly by accounting for bubble shrinkage and hydrostatic head. Deviation between the effective interfacial area determined by chemical methods and the geometrical interfacial area is largely dependent on the properties of the reaction system such as rate constant, diffusivity and solubility, the operating conditions, bubble size, and bubble size distribution.

It can be seen that even though the chemical method is a common technique for determination of interfacial area, systematic investigation of the effects of the liquid phase properties on the interfacial area is extremely difficult. It is also difficult to measure the local rates of absorption.

The method seems to be highly dependent on the reaction chosen and also the geometry of the reactor. Depending on the application, a suitable reaction has to be chosen with great care, and the experiments can be time consuming. The results are not suitable for obtaining information of a more general nature, as the results are specific to the property of the system. It seems, however, to be the only method which does not require verification by any other kind of measurement, and yields an overall value of the interfacial area from a single measurement.

2.2 Photographic Method

The photographic method has been used innovatively in the two-phase flow measurements of various parameters. This method involves, first, the determination of the mean particle diameter of the dispersion which could be either a droplet or a bubble. The specific interfacial area is then calculated from the relation:

$$a_i = 6 \frac{\alpha}{D_{sm}} \tag{17}$$

where D_{sm} is the Sauter mean diameter.

The above relation gives good results for the case of spherical bubbles. However, for non-spherical bubbles, the projected area and the perimeter for each bubble under consideration is to be obtained. Hence, in this case two Sauter mean diameters are obtained, one based on the projected area and the other based on the perimeter. The shape factor is then calculated based on the ratio of the perimeter of the projected non-spherical bubble to that of the spherical bubble having the same projected area. With this information the interfacial area in the case of non-spherical bubbles can be obtained.

The photographic method seems to be a very expensive method. Rapid advances have been made in terms of the availability of equipment including sophistication combined with ease of use. These advances include the high-speed movie camera and the high-speed video camera. High-speed movie cameras offer the advantage of a better resolution at a considerably lower cost than a video camera. But it has a disadvantage in that it needs an additional digitizer or a projector for analysis. Instant analysis is also not possible due to the time involved in film processing. Speeds up to 60,000 frames per second are available in these types of cameras. The video cameras have an advantage in that there is no processing time and, hence, the results can be analyzed almost instantaneously. But the tremendous cost involved, which can be almost four times that of a movie camera, offsets this advantage on most occasions. The resolution also leaves much to be desired.

It is, however, to be borne in mind that it becomes absolutely necessary to conduct experiments in transparent sections in order to enable us to use the photographic method. Photographs taken through a transparent wall are representative of the conditions at the focal point and may not be representative of those over the entire cross section. This section of the experimental setup must be carefully chosen to minimize the effects of refraction and reflection, as they could have disastrous effects on the end results. It also appears that selection of the lighting equipment is something of a trial and error process before yielding photographs of the right quality. Analysis of photographs can be very tedious, time consuming, and at times even subjective. It also seems unlikely that a large body of data can be generated by this method.

Studies on the determination of the interfacial area by the photographic method have been conducted by various investigators [18,25,34,49-56]. Burgess

and Calderbank [52] have shown that the photographic method yields interfacial areas which are more than twice those obtained by other methods. Kawecki et al. [53]. applied the photographic technique so that a continuous stream of the liquid and dispersed gas was withdrawn from the apparatus into a translucent rectangular chamber, and photographs were taken through the chamber wall. As pointed out by Reith [54], however, the procedure cannot be used with higher gas void fractions because of coalescence of bubbles during transfer from the apparatus into the chamber. Instead of photographing through the wall, a special probe can be placed inside the vessel as suggested by Weiss and Ziegel [55]. Only small volumes can be sampled by such a device and, also, especially at higher gas void fractions, the alteration of the flow conditions by the probe can lead to non-representative results. Landau et al. [25] used diffused side lighting for the photographs. Information regarding bubble size and shape was obtained from photographs with the aid of a digitizer. Bubble contours were traced with a stylus on an enlarged print placed on the digitizer. They obtained two Sauter mean diameters, one based on the perimeter and the other based on the projected area. In addition, Landau et al. [25] have shown that the photographic technique, when applicable, can be used in combination with a suitable means for photographic analysis to provide additional information on the dispersion, such as mean bubble diameter, bubble size distribution and shape factor.

Gunn and Doori [56] have compared the photographic method and the electrical probe method to study bubbles in a fluidized bed. A 16 mm cine camera was used at a film speed of 24 frames per second. A digitizer was used by them, as by most other investigators, for analysis. They have studied the volumetric bubble flow rate, the mean equivalent diameter, the bubble velocity and the effects bubble orientation near a probe. They, in fact, compared the

bubble measurements by the optical and electrical methods with very good results.

2.3 Light Attenuation Method

The method of light attenuation to measure the interfacial area was first used by Vermeulen et al. [57] and later by Calderbank [58]. The theory for the attenuation of a light beam passing through dispersion is well established [18,58-63].

In this method, a narrow beam of light travels through the fluid containing bubbles or drops, and the intensity, I, of the beam leaving the fluid is measured with a photoelectric detector such as a photodiode or photomultiplier. The access to the detector is carefully collimated to be in line with the original beam. When the beam passes through a droplet or bubble, it is scattered, and this leads to a reduction in the intensity received, as compared to the intensity I_o received in the absence of the bubbles or drops. I is related to I_o through the classical photo-extinction law by

$$\frac{I}{I_o} = \exp\ (-\beta \ell) \tag{18}$$

where ℓ is the distance the light beam travels through the fluid, and β is the attenuation coefficient.

There are three basic assumptions in evaluating the attenuation coefficient β. They are as follows:

1. There is no interaction between the scattering of bubbles or droplets. This condition can be met for dispersed two-phase flow of volumetric concentration less than ten percent composed of small fluid particles randomly spaced and separated by several fluid particle diameters.

2. The dispersed phase should be limited to spherical fluid particles. There are great differences in the scattering behavior of spherical and non-spherical fluid particles. Thus, the solution for scattering cross sections presently available for spherical fluid particles is a rather poor approximation of the total scattering cross section for large diameter non-spherical fluid particles.
3. Finally, it is assumed that there are no effects of forward scattering.

In view of the above assumptions, the attenuation coefficient is expressed as

$$\beta = \frac{\pi n}{8} \int_0^\infty D^2 f(D)\, S_{app}(2\pi D/\lambda)\, dD \tag{19}$$

where n is the fluid particle number density, D is the fluid particle diameter, f(D) is the particle size distribution, λ is the wave length, and S_{app} is the apparent scattering coefficient.

Noting that the interfacial area concentration can be expressed by

$$a_i = \frac{\pi n}{2} \int_0^\infty D^2 f(D)\, dD \tag{20}$$

from Eqs. (19) and (20), n can be eliminated to obtain a relation between β and a_i. Thus,

$$\frac{\beta}{a_i} = \left(\frac{1}{4}\right) \frac{\int_0^\infty D^2 f(D)\, S_{app}(2\pi d/\lambda)\, dD}{\int_0^\infty D^2 f(D)\, dD} \tag{21}$$

In general, the apparent scattering coefficient depends on the real scattering coefficient, $S_n\ (2\pi D/\lambda)$, and the geometry of the actual

experimental apparatus. To determine the scattering coefficient, the normalized extinction cross section which consists of scattering and absorption cross-sections are used. Neglecting the absorption cross section with respect to the scattering cross-section, Stravs and von Stockar [64] showed that

$$S_{app}(2\pi D/\lambda) \simeq S_n(2\pi D/\lambda) \tag{22}$$

The theoretical expression of S_n for an air bubble in water was derived by Marston et al. [65]. Stravs and von Stockar [64] showed that for a sufficiently large spherical gas bubble, the scattering coefficient rapidly approaches its final value of 2 with increasing values of $(2\pi D/\lambda)$. This means the bubble removes an amount of energy from the incident light beam as if it were a completely absorbing disc of twice its projection area. In reality, one-half of this energy is reflected backwards, whereas the other half is diffracted forward around the bubble. Furthermore, as shown by Stravs and von Stockar [64] with light, where $2\pi D/\lambda > 700$, the diffracted energy is confined in such a narrow angle that under normal measuring conditions, it will be measured together with non-disturbed parallel light. This reduces the apparent scattering coefficient S_{app} to 1. Thus,

$$S_{app} \simeq S_n \simeq 1.0 \tag{23}$$

With Eq. (23), Eq. (21) reduces to

$$\beta = \frac{a_i}{4} \tag{24}$$

indicating that the attenuation coefficient ß is equal to one-fourth of the interfacial area concentrations, which is four times larger than the projection area of the bubble size distribution. Furthermore, combining Eq.

(24) with the photo-extinction law expressed by Eq. (18) leads to the following equation [58-60]:

$$I = I_o \exp (- a_i \ell/4) \tag{25}$$

In principle, measuring I, I_o and ℓ, Eq. (25) allows the line-averaged interfacial area concentration, a_i. However, it is important to note here that in arriving at Eq. (25) a series of assumptions have been made regarding the interaction between scattering of fluid particles, the particle shape, the effects of forward scattering, and the particle size D in relation to the wavelength λ. These assumptions limit the applicability of the light attenuation technique to optically dilute, transparent, dispersed two-phase flow with a volumetric concentration of less than a few percent. The method becomes inaccurate as the bubble or droplet concentration increases.

In fact, Eq. (25) has been extensively tested [66] and found to hold only up to

$$\ln \left(\frac{I_o}{I}\right) = \frac{a_i \ell}{4} < 5 \tag{26}$$

Above this value multiple scattering becomes important. This severe limitation of the light attenuation technique has evidently prevented its widespread use in dispersed two-phase flow. For example, Ohba and Itoh [62] showed a thousandfold attenuation in intensity for bubbly two-phase flow at a void fraction of about 30%. This implies a considerable number of inaccuracies in the measurements of the interfacial area concentrations at a void fraction of this magnitude and higher, although the method can be effectively used at lower void fractions of less than 10%. Evidently, the method cannot be applicable for horizontal, bubbly, two-phase flow, where the

local void fraction toward the top of the pipe may reach as high as 60 ~ 65% corresponding to the maximum packing condition.

2.4 Ultrasonic Attenuation Method

For bubbly flows, the ultrasonic attenuation method as described by Stravs and von Stockar [64], Jones et al. [67], Delhaye [68] and Bensler et al. [69] looks promising because of its simplicity and versatility. It compares fairly well with the photographic method and the light attenuation method at relatively low void fractions.

The interfacial area measurement by this method is based on the principle of energy attenuation as described in the preceding section. For the ultrasonic attenuation method measurements, a plane wave of ultrasound pulse is used instead of the visible light beam. As shown by Stravs and von Stockar [64], Eqs. (18) through (22) are valid in this technique, too. However, in the case of ultrasonic pulse attenuations, S_n varies with the bubble size, and the theoretical expression of S_n for an air bubble in water has been given by Nishi [70]. With a known value of S_n as a function of the dimensionless size parameter $2\pi D/\lambda$, the interfacial area concentration can be calculated from Eqs. (21) and (22) as follows:

$$a_i = 4\beta \frac{\int_0^\infty D^2 f(D)\, dD}{\int_0^\infty D^2 f(D)\, S_n(2\pi D/\lambda)\, dD} \tag{27}$$

It is evident from Eq. (27) that one must know the bubble size distribution $f(D)$ in order to calculate a_i from the measured value of β from Eq. (18). However, the bubble size distributions are generally difficult to obtain, whereas the Sauter mean diameter D_{sm} may be found by a simultaneous

measurement of the void fraction α and the interfacial area concentration a_i through Eq. (17). Thus,

$$D_{sm} = \frac{6\alpha}{a_i} \tag{28}$$

Stravs and von Stockar [64] used simulated size distribution f(D) over a frequency range from 1 to 5 MHz to show that the attenuation coefficient β calculated from Eq. (19) was in the worst case only 3% greater than a β value based on D_{sm}:

$$\beta^* = (\frac{\pi n}{8})\ S_n(2\pi D_{sm}/\lambda) \int_0^\infty D^2 f(D)\ dD = (\frac{a_i}{4})\ S_n(2\pi D_{sm}/\lambda) \tag{29}$$

β is approximated by β^*. Thus,

$$\beta \simeq (\frac{a_i}{4})\ S_n(2\pi D_{sm}/\lambda) \tag{30}$$

which can be rearranged to solve for a_i as

$$a_i = \frac{4\beta}{S_n(2\pi D_{sm}/\lambda)} = \frac{4\beta}{S_n(12\pi\alpha/a_i\lambda)} \tag{31}$$

From Eqs. (31) and (28), it follows that by knowing the local Sauter mean diameter, D_{sm}, or the local void fraction, α, one may determine the interfacial area concentration, a_i, from the measured attenuation coefficient, β, from Eq. (18).

Stravs and von Stockar [64] reported experimental results showing that for gas-liquid dispersions the interfacial area concentrations determined with the ultrasonic pulse attenuation method differed from those determined with the light attenuation method by approximately 5%. Bensler et al. [67] indicated that the ultrasonic pulse attenuation method compared fairly well

with the photographic technique in the determination of specific interfacial areas in bubbly two-phase flows with a low void fraction.

As in the case of the light attenuation method, the ultrasonic pulse attenuation method has a limited success at relatively low void fractions. At high void fractions, the scattering and refraction at multiple interfaces becomes a very serious problem. Since the measurements of interfacial areas by the ultrasonic attenuation method can be made for non-transparent fluids in an opague flow channel where measurements by the light transmissions method fails, this method appears to be a powerful new technique over the light attenuation technique for measuring the interfacial area in bubbly two-phase flow.

2.5 Summary and Concluding Remarks

The chemical absorption method is the most widely used technique and is applicable to all two-phase flow patterns. The value of the interfacial area is obtained by sampling and chemical analysis of concentrations. It is a global measurement over a certain length of a flow channel. Therefore, it does not give detailed local information on the interfacial area concentration. It is limited to steady-state flow without phase change. The experimental setup is cumbersome and time consuming. Furthermore, the errors associated with this method may be large depending on the experimental conditions.

The photographic method is applicable to relatively low concentration, dispersed two-phase flow. It involves the actual measurement of the fluid particle size from pictures of the flow. The combination of the fluid particle size and information on the void fraction yields the interfacial area. The method can be used for the case where the phase change occurs. However, it requires a transparent test section. Analysis of photographs may

be very time consuming and highly expensive and even subjective in nature. The method seems to be useful when used in conjunction with other methods to provide additional information on the dispersion.

As in the case of the photographic method, the light attenuation method requires a flow channel with transparent walls. Basically, the attenuation of a visible light beam crossing a two-phase mixture is measured; and, relating the attenuation to the concentration of fluid particles, the interfacial area is calculated. In this method the fluid particle size should be larger than the incident wavelength, and multiple reflections reaching the detector should be negligible. These assumptions limit the light attenuation method to an optically dilute, transparent, dispersed, two-phase flow with a volumetric concentration of less than a few percent. The method becomes inaccurate as the bubble or droplet concentration increases.

For bubbly flows the ultrasonic attenuation method is a relatively new technique for interfacial area measurements. It involves the measurement of pulse amplitude attenuation of an ultrasonic beam coupled with a sound scattering theory for calculating the interfacial area concentration. Although the photographic and the light attenuation methods can not be used with opaque channel walls and are limited to transparent fluids, the ultrasonic technique is not restricted to such conditions. However, presently it can be used only for relatively low void fractions.

In conclusion, the presently available methods summarized above for measuring the interfacial area concentration are effective for certain idealized cases. Only an average interfacial area can be measured by the chemical absorption method. The photographic and light attenuation methods cannot be used with opaque walls and are limited to transparent bubbly flows. The ultrasonic method is not restricted to such conditions, and thus expands

the measurement of the interfacial area concentration beyond the presently available range of fluids and non-opaque systems. However, the ultrasonic attenuation method is limited to low void fraction bubbly systems. In view of the intention of the present investigation to measure local interfacial variables in a horizontal bubbly two-phase flow with local void fractions possibly ranging from zero to 60 ~ 65%, it is inevitable that a probe method must be used. An evaluation of potential probe methods resulted in the selection of the electrical resistivity probe because of the relatively simple instrumentation and the positive results for conducting liquids reported in the literature.

3. DOUBLE-SENSOR RESISTIVITY PROBE METHOD

3.1 Measurement Principle

The electrical resistivity probe method was first proposed by Neal and Bankoff [71] for the determination of bubble size and velocity in vertical bubbly flows. Since then the double-sensor resistivity probe has been used by Park et al. [72], Rigby et al. [73] for the determination of bubble parameters in three-phase fluidized beds, by Hoffer and Resnick [74] for steady- and unsteady-state measurements in liquid-liquid dispersions, by Burgess and Calderbank [52] for measurement of bubble parameters in single-bubbly flow, by Serizawa et al. [75], Herringe and Davis [76], for the study of structural parameters as well as of structural development of gas-liquid bubbly flows, and by Veteau [19] for the measurement of local interfacial area concentration.

In principle, this method consists of the instantaneous measurement of local electrical resistivity in the two-phase mixture by means of a sensor electrode. In an air-water flow the air can be considered as electrically insulating, whereas water is electrically conducting. When the sensor is in

contact with the liquid, the circuit is closed. On the other hand, when it is in contact with a bubble, the circuit will open. Since the circuit is open or closed depending on whether the sensor is in contact with gas or liquid, the voltage drop across a sensor fluctuates between a V_{min} and a V_{max}. In the case of a double-sensor probe method, each sensor and return electrodes are connected to their own measuring circuits and, therefore, each sensor is used independently as a phase identifying device. Furthermore, from the timing of the shift in the voltage between V_{min} and V_{max}, the time when the gas-liquid interface passes the sensor can be recorded. Therefore, two pieces of parallel and independent information related to the phase identification and the passing time of the gas-liquid interface are obtained. A typical time history record of signals from a double-sensor electrical resistivity probe in bubbly flow is illustrated in Figure 3.1.

As seen from the figure, the signals deviate from the ideal two-state square wave signals. This deviation is largely due to the finite size of the sensor and the possible deformation of the interface before the sensor enters from one phase to the other. The trailing edges are generally steeper than the leading edges. This difference is probably due to the wetting of the sensor by the residual liquid when the sensor is in the gas phase. In order to condition the voltage output to ideal square wave type signals, a proper threshold voltage has to be used as a triggering criterion. The value of the threshold voltage can be obtained by processing the data for void fraction and by comparing the data with other reference measurement methods. In the present study, the threshold voltage is determined by a calibration procedure by comparing the average void fraction measured by the quick-closing valve technique and the integrated value of the local void fraction over the pipe cross-section.

3.2 Double-Sensor Resistivity Probe Design and Signal Processing

A typical double-sensor resistivity probe is shown in Figure 3.2. It consists of two identical stainless steel wire sensors of 0.25 mm in diameter. Their tips are 2.5 mm apart from each other. They are completely insulated from the environment except at their tips. The tips are sharpened to a fine needle point to prevent deformation of bubbles on impact with the sensors. The two sensors are placed next to each other but insulated from each other. The body which holds the sensor acts as the return electrode. These two sensors are welded onto gold plated wires of 0.8 mm diameter. The complete assembly fits into a probe holder from which coaxial cables run to the electronic circuit. The coaxial cables are used to minimize noise in the signals. The electronic circuit uses a 4.5 V DC power supply. Variable resistors are used to enable adjustment of the maximum and minimum voltage signals.

It was found that the proper distance, L, between two sensors was critical for analyzing the experimental data. Preliminary experiments were conducted to determine a proper distance between two probe tips. The distance was dictated by possible bubble size and bubble velocity. It was decided that 2.5 mm was the appropriate separation distance for the horizontal flow. It is to be noted that a very small distance results in inaccuracies in time duration measurements, since it requires very high sampling frequencies or very small bubble velocities. During the present experiments a sampling rate of 20 kHz was used. On the other hand, if the distance is too large, then there is a strong possibility of misinterpretation of signals since multibubble contact may occur between two signals originating from the same bubble. Even though most investigators in the past have used a distance of 5 mm or higher in their vertical bubbly flow experiments, it was found that 5 mm was too large for the

horizontal two-phase flow experiments, since maximum packing of bubbles almost always occurs toward the top of the pipe, which requires a smaller separation distance.

As illustrated in Figure 3.1, the experimental data was obtained in the form of a voltage signal as a function of time from the front and rear sensors of a probe. The correct interpretation of data involves identification of gas and liquid phases. The first step is to set a threshold voltage at which the signal representing the beginning of the gas phase for an isolated bubble can be identified. Earlier investigators of the resistivity probe have different methods to set the threshold voltage. For example, Serizawa et al. [75] used a preset threshold voltage to transfer the probe signals into square wave signals, and the same threshold voltage was used throughout the experiments. However, in the present study it was observed that the threshold voltage level may drift during the experiments due to the probe contamination. This difficulty was overcome by dividing the data into several blocks within the total sampling time domain. In principle, the threshold voltage, V_T, and the slope, dV/dt, were used together in the present investigation to distinguish the phases. A linear programming method was developed to reach a desired convergence.

Initially the maximum and minimum voltages for each data block for each sensor were determined. The threshold voltage was then determined by

$$V_T = B_o (V_{max} - V_{min}) + V_{min} \tag{32}$$

where $0 \leq B_o \leq 1$. Since the values of V_{max} and V_{min} were fixed for each data block, it is the variation in the value of B_o that results in a varying threshold voltage.

As an isolated bubble contacts the previously wetted probe, output signals increase from the value of a near V_{min} to a near V_{max}, and decrease abruptly to the value of V_{min} as the bubble moves away. Identification of such a bubble is straightforward. However, for closely compacted bubbles that are observed in a horizontal bubbly flow, the time duration of the liquid phase contacting a probe sensor is very short. Hence, before the sensor tip becomes totally wet, it could be in contact with another bubble. In this case the voltage signal varies between a local minimum above the threshold voltage and the gas level. To identify such a bubble the threshold voltage and slope of the signal were used in combination for distinguishing phases.

The slope corresponding to a value

$$\frac{dV}{dt} = \frac{(V_{max} - V_{min})\ B_o}{E} \tag{33}$$

was used as a criterion. A value of E=12 was found to give the best result for our case. When the sensor output signal reaches a local minimum value above the threshold voltage and the absolute value of the local slope at the neighborhood of this point is greater than the criterion, this point is treated as the commencement of the gas phase. The time duration in which the sensor is in the gas phase is used to determine the local void fraction. The local void fraction obtained in different locations is then integrated over the entire cross section to obtain the average void fraction.

After the determination of the phase, the next step is the identification of signals originating from the same bubble. In this case, the right selection of two closely corresponding signals from each sensor is important, since two signals detected by both front and rear sensors do not always correspond to the same bubble, and the residence time intervals of gas or

liquid phase at the sensors are not exactly the same. The signal validation was made by judging whether the following series of conditions are satisfied:

1. For a forward motion of the bubbles, the front sensor signal rises or falls before the rear sensor signal does. Therefore, referring to Figure 3.1, the condition is given by

$$t_{f(2j-1)} < t_{f(2j)} \text{ and } t_{r(2j-1)} < t_{r(2j)};\ j=1,\ldots,\ N \tag{34}$$

where f and r, respectively, denote the front and rear sensors. $t_{(2j-1)}$ is the time the front and rear sensor tips enter into the bubble, and t_{2j} is the time sensor tips enter into the liquid phase. N is the number of bubbles passing through a given sensor in the total sampling time T.

2. The residence time of a bubble, i.e., the width of the signals, the amplitude and the height above the threshold voltage of the signals for the front and rear sensors should be comparable to ensure that the both sensors detect the same bubble. Hence, the following conditions should be also satisfied:

$$(t_{f(2j)} - t_{f(2j-1)}) \simeq (t_{r(2j)} - t_{r(2j-1)});\ j=1,\ldots,\ N \tag{35}$$

$$V_f(t_{f(2j)}) - V_f(t_{f(2j-1)}) \simeq V_r(t_{r(2j)}) - V_r(t_{r(2j-1)});\ j=1,\ldots,\ N \tag{36}$$

and

$$V_f(t_{f(2j-1)}) - V_{fT} \simeq V_r(t_{r(2j-1)}) - V_{rT};\ j=1,\ldots,\ N \tag{37}$$

3. The time difference between the rear and front sensor should be limited by the following condition

$$\Delta t_{min} \leq t_{r(2j)} - t_{f(2j)} \leq \Delta t_{max} \tag{38}$$

$$\Delta t_{min} \leq t_{r(2j-1)} - t_{f(2j-1)} \leq \Delta t_{max} \tag{39}$$

where Δt_{min} and Δt_{max} are the time limits corresponding to the maximum and minimum bubble velocities, respectively. The maximum and minimum bubble velocities are determined from experimental conditions.

3.3 Local Void Fraction

The local void fraction at any location r can be obtained by either front or rear probe sensor tips. It is defined as a time average of the concentration $\delta(r,t)$ by

$$\alpha(r) = \lim_{T\to\infty} \frac{1}{T} \int_0^T \delta(r,t)\, dt \tag{40}$$

where δ, as a function of space coordinate r and time t, equals one if the probe tip is in gas and zero if the tip is in the liquid phase. As the signal is given in discrete form, Eq. (40) can be written from Figure 3.1 either for the front or rear probe as follows:

$$\alpha(r) = \frac{1}{T} \sum_{j=1}^{N} (t_{2j} - t_{2j-1}) \tag{41}$$

3.4 Local Bubble Interface Velocity and Velocity Spectrum

The local bubble interface velocity is determined from the signals of two sensors. A bubble interface which contacts the first sensor will in general subsequently contact with the second sensor. The time delay between the two contact signals is a measure of the bubble interface velocity. The bubble interface velocity component in the axial direction at any location r can be expressed as

$$u_b = \frac{L}{\Delta t} \tag{42}$$

where L is the distance between two sensor tips, and Δt is the time delay for an interface, which contacts the rear and front sensor tips as illustrated in Figure 3.1.

The time delay can be determined by the cross-correlation method or by the multi-channel technique [75]. The cross-correlation method gives the most probable time delay between the two sensor output signals, while the multichannel technique gives the spectrum of the time delay for each bubble interface.

In the present study both the multichannel method and cross-correlation techniques are used in the determination of local bubble interface velocity. In the multichannel method, the bubble transport time signals are processed through a computer program to identify signals from the same bubble. This process thus eliminates miscounting of bubbles. The interface velocity for a specified j'th bubble interface is then given by

$$u_{bj} = \frac{L}{\Delta t_{(2j-1)}}, \qquad j=1, 2, \ldots, N \tag{43}$$

where the index j refers to a j'th bubble. Considering the bubble deformations we used the bubble leading surface velocity as a representative of a bubble surface velocity. Then using the multi-channel method, the bubble velocity signals are proportionally transferred into an amplitude pulse. The maximum and minimum values of these amplitude pulses are then divided into equally spaced channels. The amplitude pulses are then counted into their respective channels to generate a bubble velocity spectrum at a given probe radial position.

The local mean bubble interface velocity component in the flow direction, $u_b(r)$, and the standard deviation of bubble velocity spectrum are given by:

$$u_b(r) = \frac{\sum_{k=1}^{N_k} n_k \, u_{bk}(r)}{\sum_{k=1}^{N_k} n_k} \tag{44}$$

$$S(r) = \left[\frac{\sum_{k=1}^{N_k} n_k [u_{bk}(r) - u_b(r)]^2}{\sum_{k=1}^{N_k} n_k}\right]^{1/2} \tag{45}$$

where u_{bk} is the instantaneously measured local axial bubble velocity in the k'th channel, n_k is the total count for the k'th channel, and N_k is the number of channels.

The cross-correlation function, which gives the most probable time delay, is also computed. If $u_f(t)$ and $u_r(t)$ are two signals from the front and the rear sensors respectively, then the cross-correlation function $F_{u_f u_r}(\Delta t_m)$ is given by

$$F_{u_f u_r}(\Delta t_m) = \frac{1}{T} \int_0^T u_f(t-\Delta t_m) \, u_r(t) \, dt \tag{46}$$

The maximum value of $F_{u_f u_r}(\Delta t_m)$ yields the most probable time delay Δt_m, from which the bubble velocity is determined through the use of Eq. (42).

3.5 Local Interfacial Area Concentration

The local interfacial area concentration at any spatial location r is given by Ishii [3] as

$$a_i(r) = \frac{1}{T} \sum_{j=1}^{N_i} \frac{1}{|\vec{v}_i \cdot \vec{n}_i|_j} \tag{47}$$

where T, v_i and n_i are the sampling time, interfacial velocity and unit normal vector of the interface. N_i is the total number of interfaces passing within the sampling time, T. Physically this local interfacial area concentration represents the probability of the interface occurring at that point.

The form of Eq. (44) indicates a possible measurement technique for determining the local interfacial area concentration. Basically it requires the measurement of the interfacial velocity and the surface direction at the point. A simplified double-sensor resistivity probe suggested by Herringe et al. [76], Veteau [18], Veteau and Charlot [17], Kataoka et al. [77] assumes a unidirectional flow of spherical particles. Under this condition, the local interfacial area concentration becomes

$$a_i(r) = \frac{2}{T} \sum_{j=1}^{N_i} \frac{1}{|u_{bj}(r)|} \tag{48}$$

where the u_{bj} is the passing velocity of the j'th interface measured through the double-sensor probe in the flow direction. This model has been applied, and $a_i(r)$ or the implied mean bubble size has been experimentally measured for two-phase bubbly flow [76,18].

Considering the velocity fluctuations due to turbulences or fluid particle motions, Kataoka et al. [77] suggested an improved statistical model to relate term $|v_i.n_i|_j$ appearing in Eq. (47) to measurable quantities. In this model it was assumed that the direction of the interface velocity fluctuates within a maximum angle of θ_o from the axial direction with equal probability. Then this angle θ_o was related to the root mean square of fluctuating components of the velocity which can be measured by the same

double-sensor probe simultaneously with the measurement of the sensor passing velocity u_{bj}. Then the local interfacial area concentrations is given by

$$a_i(r) = \{\frac{2}{T} \sum_{j=1}^{N_i} \frac{1}{|u_{bj}(r)|}\} \; C(a_o) = \frac{2}{LT} \sum_{j=1}^{N} [\Delta t_{(2j-1)} + \Delta t_{(2j)}] \qquad (49)$$

where

$$C(\alpha_o) = \{1 - \cot(\frac{\alpha_o}{2}) \ln [\cos(\frac{\alpha_o}{2})] - \tan(\frac{\alpha_o}{2}) \ln [\sin(\frac{\alpha_o}{2})]\}^{-1} \qquad (50)$$

The angle α_o is given approximately by

$$\frac{\sin 2\alpha_o}{2\alpha_o} \simeq \frac{1-S^2/u_b^2}{1+3S^2/u_b^2} \qquad (51)$$

where S is the root mean square of the fluctuating component of the sensor passing velocity, which is conveniently expressed by Eq. (45).

Knowing the value of α_o, the time-averaged local interfacial area concentration can be calculated from the measured values of $u_b(r)$ at any location r. The measured value of $u_b(r)$ is given by Eq. (42), whereas the value of α_o can be estimated from measured values of statistical parameters of interfacial velocity as given by Eq. (51). It is to be noted that the root mean square of fluctuations of the axial component of interfacial velocity is assumed to be the root mean square of two other velocity component fluctuations, i.e., unidirectional assumption. Studies carried out by Hilgert and Hofmann [78] on bubble columns in a vertical pipe using an ultrasonic doppler technique have shown that the magnitude of axial component root mean square bubble velocity fluctuation is nearly equal to the radial component of root mean square of fluctuation of bubble velocity. In the present study Eq. (49) will be used to determine the local interfacial area concentration for the horizontal bubbly flow experiments.

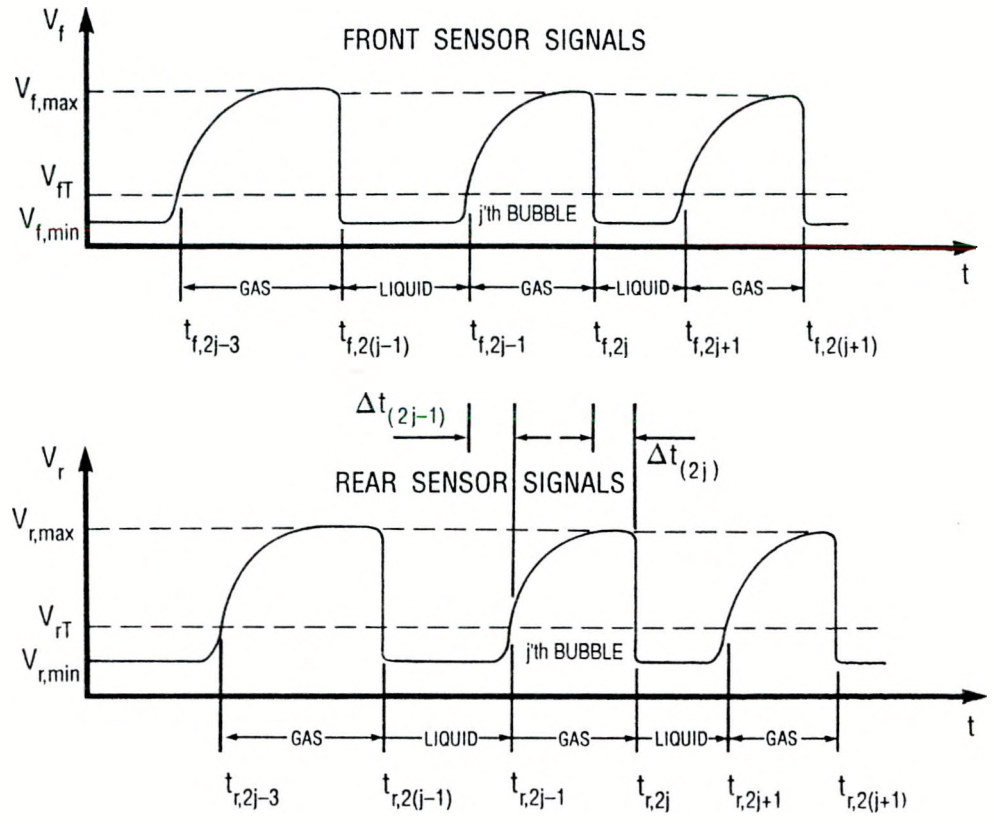

Figure 3.1 A typical Time History Record of Signals from a Double-Sensor Electrical Resistivity Probe on a Bubbly Two-Phase Flow.

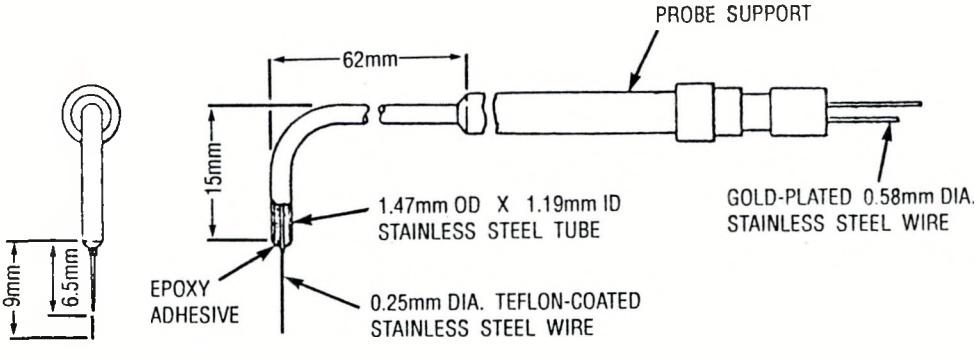

Figure 3.2 Double-Sensor Electrical Resistivity Probe Design.

4. EXPERIMENTAL SETUP AND PROCEDURE

4.1 Description of Flow Loop

A horizontal flow loop was designed and built for investigating the interfacial structure of horizontal two-phase flow. The overall loop schematic is illustrated in Figure 4.1. The loop basically consists of various flanged lengths of 50.3 mm ID circular Pyrex glass tubings with pressure taps installed between them. However, smaller or larger diameter test sections can be easily fitted to the loop. The over-all test section is about 15.4 m in length.

The entire test section is all transparent, so that flow visualization, high-speed photography, and high speed cinematography are possible. It is designed such that various local instrumentations for two-phase flow measurements and different mixing chambers can be easily accommodated. In designing the loop, a special emphasis is placed on investigating geometric scaling and phenomenological modeling for a developing horizontal two-phase flow and the effects of entrance mixing geometry.

Because of the large number of flanged joints in the test section, considerable care is taken in the alignment and matching of the joints. This would minimize the flow disturbances caused by a joint. All flanged joints are sealed by the use of O-rings to ensure an even and leak proof joint. In order to support and level the entire test section, an elaborate unistrut support structure is constructed. The support structure consists of one main rail, oriented parallel to and below the test section. This main rail is supported by many support arms, located at 1.2 m intervals. Each of the support arms heights is adjustable for leveling purposes. The glass test section is supported on the unistrut main rail by specially constructed maple wood blocks. The wood blocks have a semicircle machined out of the top side,

with a diameter the same as that of the outside diameter of the glass test section. This allows the glass test section to rest on the top of the wood block and be securely clamped in place, and so no movement is possible. The wood blocks are evenly distributed along the glass test section length as required for sufficient support.

Air and water are used as coupling fluids. The air enters the mixing chamber from a 90° vertical leg and is injected into the water flow through a cylindrical porous media to achieve a uniform mixing and a quick development of a bubbly two-phase flow pattern. The porous media is made of pregraded, sintered powder to obtain the desired porosity. Three different sizes of porous media are used. The experimental results presented in this report are based on 100 micron porosity. The cylindrical porous media is centered in the glass test section, and directs the air flow from 90° to an axially aligned downstream direction. The water enters the mixing chamber from upstream, with the same central axis as the downstream glass test section. All flow paths for the air and water are designed to be as smooth as possible in order to minimize single-phase flow disturbances in the areas immediately before mixing. A schematic of the mixing chamber is presented in Figure 4.2.

After exiting the test section, the two-phase mixture enters an air-water separator. The separator is constructed from 0.4 m^3 circular tank. Aluminum baffles are fastened inside the separator tank to assist the separation process and to prevent the possibility of vortex formation. Once separated, the air is vented to the atmosphere, and the water is returned to the water storage tank. The water storage tank is kept sealed at all times in order to prevent any contamination of the water with foreign debris.

The water flow was supplied by a stainless steel centrifugal pump. The pump has a 20 hp motor and delivers 750 gpm at 1800 rpm. A Toshiba Transistor

Inverter model VFP-2220P1 motor control is used to control the pump speed. The inverter allows the pump's output capacity to be regulated from 0 to 100 percent of its rated capacity. The pump delivers water from a 500 gallon circular water storage tank to a system of flow regulating valves. All water supply piping is made up of schedule 40 and schedule 80 polyvinyl chloride piping. After the regulating valves, the water passes through a system of three water flow meters. These flow meters are of the paddle wheel type and are assembled in a parallel configuration and have a range of 0 to 750 gpm. They are electrically connected to a digital flow analyzer. The water then passes through a pneumatically controlled butterfly valve and then into the two-phase flow mixing chamber. The butterfly valve is used to shut off the water flow to the mixing chamber and test section during the period of average void fraction measurements.

The air flow is supplied by a centrally located university air compressor. The central air compressor has a 450 CFM capacity. An additional 100 hp air compressor with 450 CFM capacity is also available if necessary. The central compressor supplies air to the laboratory through a 6 inch diameter steel pipe at 115 psi. Before the air enters the 0.9 m^3 circular air storage tank, it passes through a 0.5 micron Arrow model F4 air filter and then through a Norgren model R18 regulator. The air regulator is used to reduce air flow fluctuations emanating from the air compressor or air supply piping. The air flow regulator is set so that the air pressure in the air storage tank is about 100 psig, or about 10 psig less than the air supply piping. From the air storage tank the air then passes through a second Arrow air filter with a 0.3 micron filter element. The air then goes through a second Norgren air pressure regulator, where the air pressure is reduced to

the flow loop operating pressure. This pressure depends on the two-phase flow conditions desired.

The air flow rate is measured by two turbine flow meters. One of the flow meters has a 1/2 inch inside diameter and the other had a 2 inch inside diameter. The larger flow meter has the capacity to measure up to 300 CFM. The two flow meters were connected in a parallel configuration and the appropriate flow meter is used, depending on the desired air flow rate. The output signal of the flow meters is connected to a Masstrol digital flow analyzer. After the flow meters, the air flow passes through a pneumatically controlled ball valve and then enters the two-phase mixing chamber. The pneumatically controlled ball valve is used to shut off the air flow during the period of average void fraction measurements.

The last 1.5 m of the test section incorporates two quick-closing valves which are used for average void fraction measurements. These valves, which are pneumatically operated and electrically controlled, have a very high response time in the order of milliseconds and are synchronized through a common electrical switch to ensure simultaneous operation. The distance between the valves is long enough to minimize any experimental error. During experimental runs operation of the quick-closing valves and measurement of the mass of water entrapped yields the average void fraction.

To protect the system against pressure surges the following features are incorporated:

- Two more quick-closing valves are added, one in the water line and one in the air line to cut off supply of water and air, respectively. A fifth quick-closing valve is installed to bypass flow of water from the pump to the tank. All of these valves are also pneumatically operated

and electrically controlled. The five valves are connected to a common electrical connection to ensure complete synchronization.

- Two relief valves are installed in the single-phase liquid line after quick-closing valve to relieve excess pressure.
- Two air pressure relief valves of the pop-up type relieve excess pressure in the air-line after quick-closing valve.

Pressure transducers of the diaphragm type are utilized for both absolute and differential pressure measurements. The pressure drop in the test section is measured at six intervals with high frequency transducers located at 1.55 m apart from each other. The absolute pressure transducers are located at two locations in the test section, 6.70 m and 8.22 m downstream of the mixing chamber, respectively.

Experiments in the laboratory are interfaced with a data acquisition system utilizing a Zenith PC/AT computer with Metrabyte DASH-16F 16-channel multifunctions high-speed analog/digital I/O expansion board, and a Labtech notebook software. The data, which can be taken at 100 kHz, can be stored on magnetic media and analyzed off-line by the computer in the laboratory or on the main-frame computer.

4.2 Experimental Procedure

The experiments were carried out under fully developed bubbly flow conditions by variation in the liquid flow rate, gas flow rate and the radial position of the probe. The superficial liquid velocities ranged from 2.80 m/s to 5.92 m/s, and the superficial gas velocities covered a range from 0.23 m/s to 1.97 m/s. At each fixed liquid superficial velocity, the gas superficial velocity was increased as long as the flow-pattern was bubbly. Evidence of slug flow was indicated in the output signals and discarded from evaluation. Liquid superficial velocities higher than indicated above could not be reached

due to pressure limitations of the pyrex-glass test loop. During the operation of the quick-closing valves, the pressure reached sizable proportions of the loop pressure limitations. The temperature of the water was maintained at room temperature by adding tap water to the storage tank.

The mounting and traversing mechanism for the resistivity probe is shown in Figure 4.3. The probe was inserted through a probe support located at the bottom of a rectangular plexi-glass test section. The test section was 15 cm in length, 15 cm in height and 7.5 cm in width. A Vernier with graduations to an accuracy of 0.0254 mm was used to traverse the probe in a direction perpendicular to the axis of the tube. As shown in Figure 4.4 twenty-three locations were selected through the pipe diameter of 50.3 mm. The increments were smaller as the probe traversed toward the wall at the upper half of the tube.

For each preset experimental condition the data including 23 probe locations, pressure drops at six intervals, and the absolute system pressure at two locations were recorded. At the end of each experimental run the quick-closing valves were operated to measure average void fraction. Experiments were interfaced with a data acquisition system utilizing a Zenith PC/AT computer with a Metrabyte DASH-16F 16-channel multi-function high-speed analog/digital I/O expansion board, and a Labtech Notebook software.

Due to the large volume of data generated the sampling rate was kept at 20 kHz for each sensor, and the sampling time was 1 second. It was found that this combination provided a sufficiently large volume of data for any statistical analysis. It is to be noted that the total sampling time may seem very short when compared to earlier investigations carried out on vertical bubbly two-phase flows. However, it is also to be noted that in a horizontal bubbly two-phase flow the velocities are very high and it becomes essential to

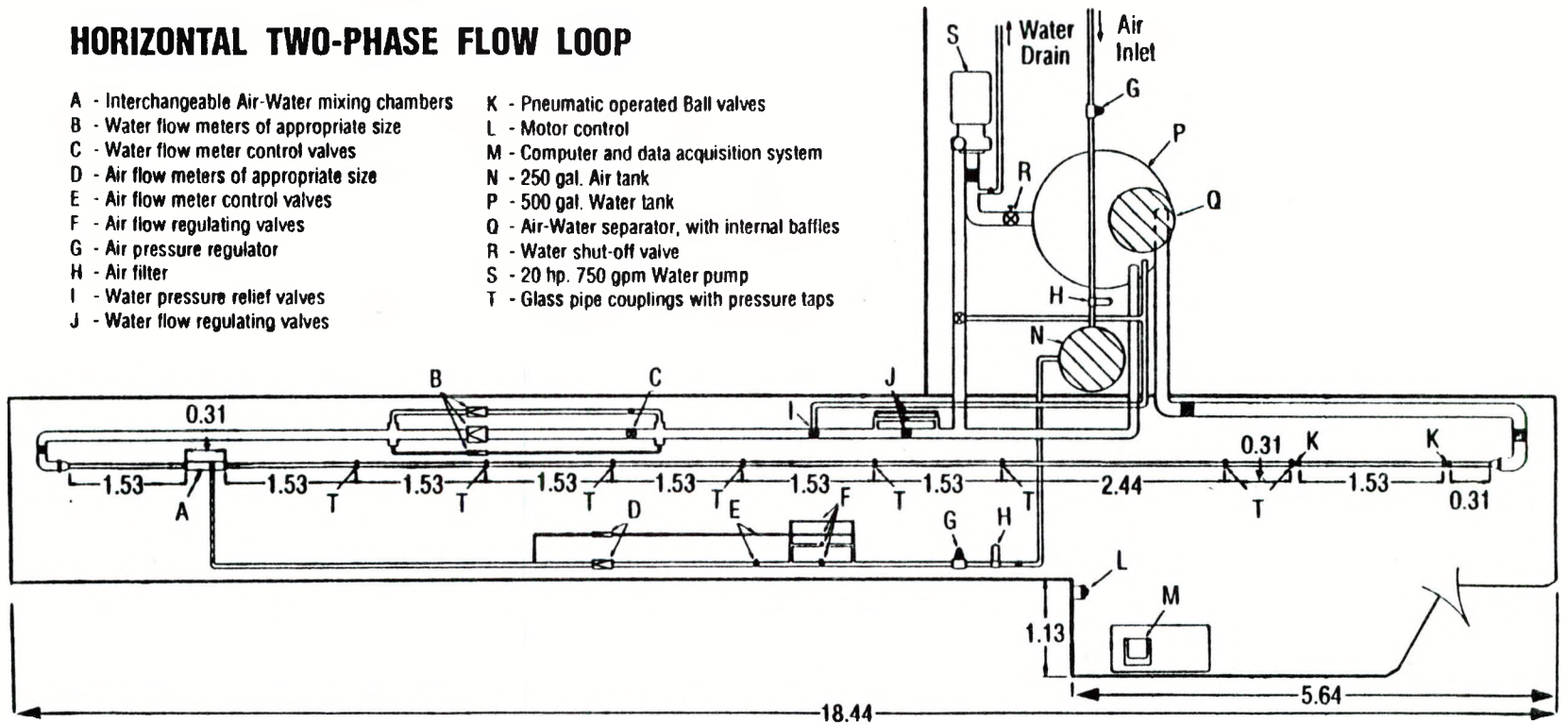

Figure 4.1 Schematic of Experimental Flow Loop.

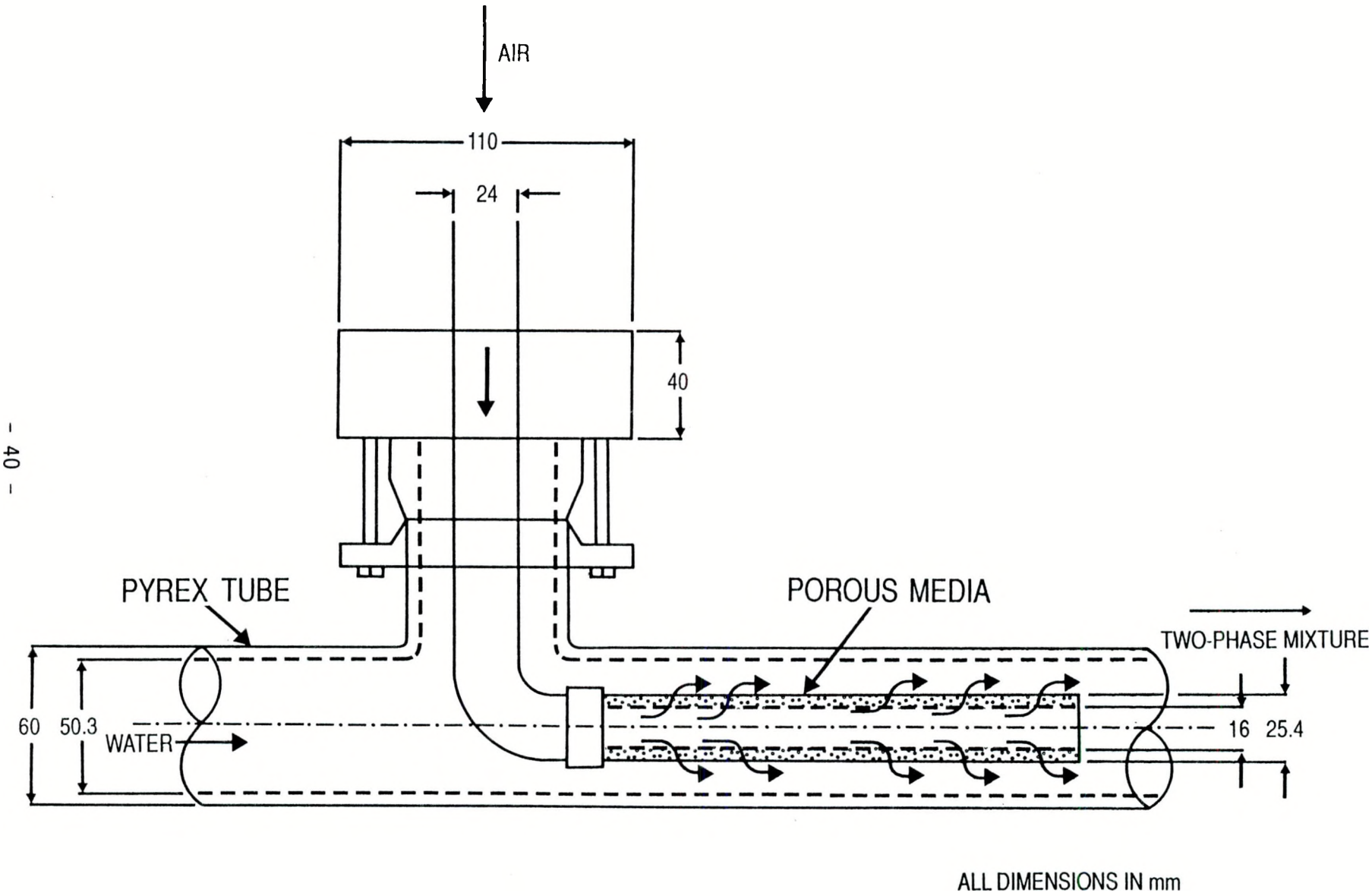

Figure 4.2 Schematic of Air-Water Mixing Chamber.

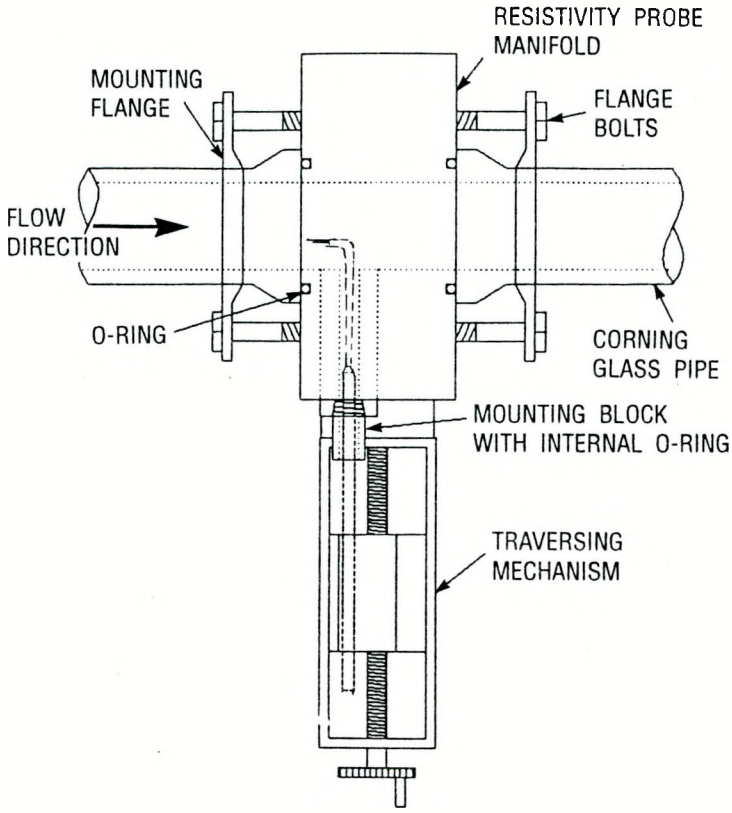

Figure 4.3 Mounting and Traversing Mechanism.

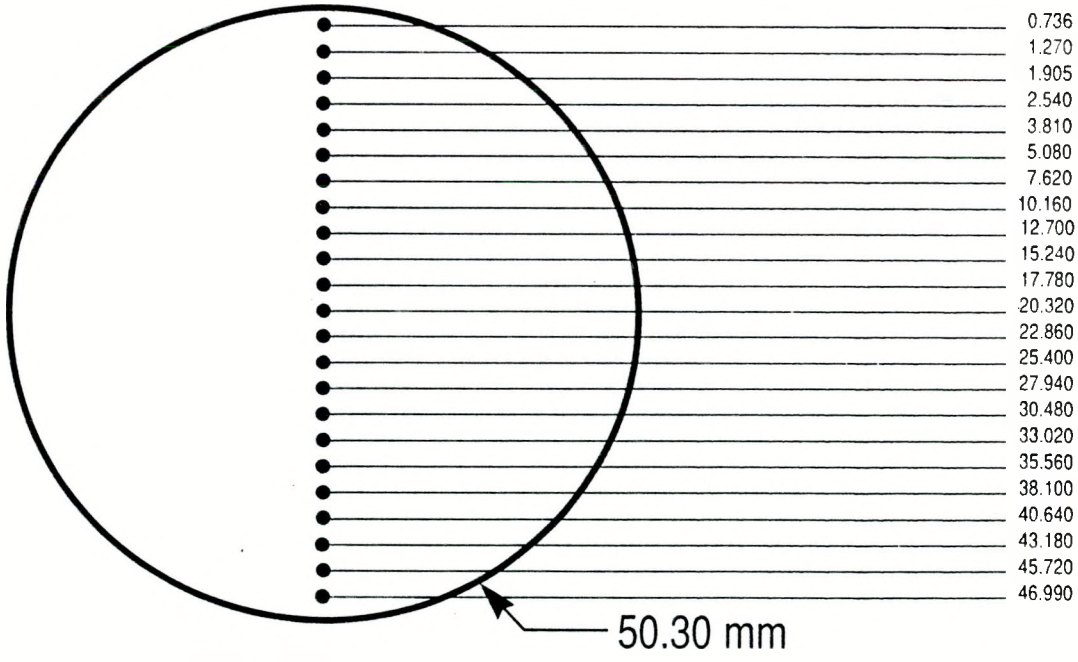

Figure 4.4 Various Probe Positions Along Diameter of Test Section.

have a sampling rate as high as possible to record all the bubbles. This simultaneously leads to a shorter sampling time due to overall limitations on the data acquisition system.

5. EXPERIMENTAL RESULTS AND DISCUSSIONS

5.1 Flow Conditions

The flow conditions investigated are summarized in Table 5.1. The superficial liquid velocities of 2.80 to 5.92 m/s were used with average axial air superficial velocities from 0.23 to 1.97 m/s. The detailed experimental data is given in Appendix A.

5.2 Experimental Results and Discussions

5.2.1 Local Void Fraction Distribution

The local void fractions were obtained independently with both front and rear sensors of the probe using the average void fraction as a convergency criterion to decide the threshold voltage. Then Eq. (41) was used to calculate the local void fractions. The profiles of local void fraction measured from both the front and rear sensors are shown in Figures 5.1 to 5.28 for superficial liquid and gas velocities ranging from 2.80 to 5.92 m/s and 0.23 to 1.97 m/s, respectively. Figures 5.28 to 5.40 illustrate local void fraction profiles at several flow parameter values of $\langle j_g \rangle$ and $\langle j_f \rangle$. In Figures 5.28 to 5.40 only the front sensor measurements are used. The following observations can be made from these figures:

a) The void fraction distributions obtained by front and rear sensors are surprisingly close to each other, indicating the consistency in the signal processing methodology.

b) It is evident from Figures 5.1 to 5.28 that the bubbles tend to migrate toward the upper wall under the dominating influence of buoyancy force. Thus, the void fraction under all test conditions generally showed a distinct peak near the top wall at about $r/R \simeq 0.8 \sim 0.9$. However, close to the wall, the wall viscous layer causes a larger hydraulic resistance of the liquid path between bubble and wall, inducing a steep decrease in the void fraction distribution toward the wall. This phenomenon is exactly similar to the one that has been observed in vertical bubbly two-phase flows [19, 75, 79-81].

c) Although the void fraction distributions tend to flatten as the average void fraction increases, the distinct peak always occurs in relatively the same location. The fact that the peak void fraction in all cases never exceeds $0.60 \sim 0.65$ indicates that a maximum packing exists in the channel. Above the maximum packing limit, coalescence of bubbles occurs resulting in larger slug bubbles.

d) As illustrated in Figures 5.29 to 5.35 the effect of increasing the gas flow rate is to increase the average void fraction and to flatten the void fraction distribution toward the bottom channel wall. Again, there was no noticeable change at the peaking positions.

e) The effect of increasing liquid flow rate is to decrease the average void fraction, Figures 5.36 to 5.40. However, there were no noticeable differences in the peaking positions, but there was a significant decrease in the value of the maximum void fraction.

5.2.2 Local Interfacial Area and Bubble Size Distributions

Figures 5.1 to 5.28 show the local interfacial area concentration profiles based on Eq. (49). Figures 5.41 to 5.51 demonstrates effects of flow parameters on local interfacial area concentrations. It is interesting to

note that the interfacial area concentration distributions have similar characteristics to those of the the void fraction distributions. The interfacial area reaches a maximum at about the same location as the void fraction peak. Increasing the gas flow or decreasing the liquid flow would increase the local and overall interfacial area concentration and tend to flatten the interfacial area concentration profile.

It is important to note that the local interfacial area concentration in horizontal bubbly two-phase flow may become as high as 800 ~ 900 m^2/m^3 toward the top of the channel. This range of the interfacial area concentration has never been reported for vertical bubbly flow. The higher values suggest that in this type of bubbly flow the interfacial transport of mass, momentum and heat transfer is much higher near the top portion of the tube wall.

The interfacial area concentration is strongly affected by bubble sizes, since the surface to volume ratio of a small bubble is larger than that of a larger bubble. Furthermore, when the bubbles are not spherical, the volume to surface areas also depend on the shape of the bubble at the same void fraction.

The profiles of the interfacial area concentration and the void fraction can be used to determine the Sauter mean bubble diameter variations along the cross section. The definition of the Sauter mean bubble diameter assumes spherical bubbles and is given by

$$D_{sm} = \frac{\sum_{k=1}^{N_k} n_k D_k^3}{\sum_{k=1}^{N_k} n_k D_k^2} \qquad (52)$$

where n_k is the number of bubbles of size D_k, and N_k is the total bubble size classes.

On the other hand the void fraction and the interfacial area concentration can be expressed, respectively, as

$$\alpha(r) = \frac{\sum_{k=1}^{N_k} n_k V_k}{V_T} = (\frac{\pi}{6}) \frac{\sum_{k=1}^{N_k} n_k D_k^3}{V_T} \tag{53}$$

and

$$a_i(r) = \frac{\sum_{k=1}^{N_k} n_k A_k}{V_T} = \frac{\pi \sum_{k=1}^{N_k} n_k D_k^2}{V_T} \tag{54}$$

where V_k is the volume of a typical bubble of size D_k in a given class k, A_k is the surface area of a typical bubble in the same class size, and V_T is the total mixture volume.

From Eqs. (52), (53) and (54) it can be shown that

$$D_{sm}(r) = \frac{6\alpha(r)}{a_i(r)} \tag{55}$$

Based on Eq. (55), Sauter mean diameter distributions for the present experimental conditions are illustrated in Figures 5.52 to 5.79 at various gas and liquid fluxes. The effect of gas flow and liquid flow on the Sauter mean diameter are shown in Figures 5.80 to 5.91. From this figure it may be observed that the Sauter mean diameters are in the range of 2 mm to 4 mm depending on the location and flow conditions. The profiles show relatively small variations over most of the flow channel cross-section except near the wall region. The bubble size tends to reduce close to the wall region. Generally there is no bubble size peaking found as reported for vertical bubbly flow by Michiyoshi and Serizawa [82], Matsui [83] and Liu [80]. The bubble diameter generally shows an increase with the gas flow rate, although the influence is not significant. By comparing two figures it may be observed

that increasing liquid flow rate results in a more homogeneous distribution of the bubbles.

Figure 5.92 illustrates the variation in the average interfacial area concentration as a function of the averaged void fraction. Considering small variations in the Sauter mean diameter, this behavior is not surprising from Eq. (55).

5.2.3 Local Bubble Interface Velocity

The local bubble interface velocity in the axial direction was determined from the signals of two resistivity probe tips using Eq. (44).

The mean local bubble velocity distributions calculated from the bubble velocity spectrum and also from the cross-correlation method are shown in Figures 5.1 to 5.28. The effect of gas flow and liquid flow on bubble velocity distribution are shown in Figures 5.93 to 5.104. The bubble velocity spectrum at every local position covered a range of bubble velocities approximately following a Poisson distribution. A typical velocity spectra is also illustrated in Figure 5.105. The following observations can be made from these figures.

a) There was no evidence to suggest a proportionate correspondence between local void fraction and bubble velocity distributions as suggested by Van der Welle [84] and Beattie [85] for the vertical flow. There were no peaks in bubble velocity profiles corresponding to those observed toward the top wall peeking void and interfacial area concentration profiles. On the contrary, the velocity profiles show a fairly uniform distribution over a large portion of the flow area, except for the wall region.

It can be observed that an increase in either the liquid flow rate or gas flow rate increases the bubble velocity. The mean bubble velocity near the

upper wall decreases indicating the same tendency as that found in vertical bubbly flows.

Verification of the measured velocities was undertaken by comparing the averaged values u_b and u_g based on the probe measurements and the measured gas volumetric flow rates Q_g, respectively. u_b and u_g are defined as follows:

$$\bar{u}_b \equiv \frac{\int_A \alpha\, u_b\, dA}{\int_A \alpha\, dA} = \frac{\langle \alpha\, u_b \rangle}{\langle \alpha \rangle} = \frac{\langle j_b \rangle}{\langle \alpha \rangle} \tag{56}$$

$$\bar{u}_g \equiv \frac{\dot{Q}_g}{\langle \alpha \rangle\, A} = \frac{\langle j_g \rangle}{\langle \alpha \rangle} \tag{57}$$

where the brackets, < >, denote area averaged values from integration, and Q_g is the volumetric flow rate of the air.

The corresponding values of the velocity from Eq. (1) were determined by numerical integration, and the values are listed in Table 5.2. Furthermore the deviation of u_b with respect to u_g and of $\langle j_b \rangle$ with respect to $\langle j_g \rangle$ which are, respectively, defined as

$$\Delta\, \bar{u}_b = \left(\frac{\bar{u}_b - \bar{u}_g}{\bar{u}_g}\right) \times 100\% \tag{58}$$

and

$$\Delta\, \langle j_b \rangle = \left(\frac{\langle j_b \rangle - \langle j_g \rangle}{\langle j_g \rangle}\right) \times 100\% \tag{59}$$

are also listed in Table 5.2. The mean deviation between the values obtained from integration of the local flow parameters and those obtained from flow rate measurements is $\pm$ 5.7%. The integrated values are generally lower. This may be explained partially by the fact that we expect the measured values of velocity to be slightly low, both because of possible deflexion of the bubbles

when they hit the probe tips and because of missing the smallest size bubbles. In all cases, the difference is less than 12% of the value calculated from the overall gas flow rate, with only 5 of the total 28 experimental runs showing a deviation greater than 10%.

The above comparison justifies the reliability of the double-sensor resistivity probe technique for measuring local void fractions and axial velocity components.

Based on the bubble velocity and void fraction measurements, a drift-flux presentation is illustrated in Figure 5.106. As suggested by Ishii [3] and Wallis [2] it is given by

$$\bar{u}_g = \bar{u}_{gj} + c_o \langle j \rangle \tag{60}$$

where $\bar{u}_{gj}$ is the weighted mean drift velocity of the gas phase, and c_o is the distribution parameter. Figure 5.106 indicates a linear relationship between $\bar{u}_g$ and $\langle j \rangle$, which can be used to determine $\bar{u}_{gj}$ and c_o. Regression analysis on data yields $c_o = 1.05$ and $\bar{u}_{gj} = 0.13$ m/s It is to be noted that such a representation was obtained from our air-water bubbly flow data which is far from the origin. Therefore, it has the limitations of our data range. It should be checked further for a wider data range.

5.2.4 Bubble Chord-Length and Bubble Frequency Distributions

The local bubble chord length was determined from the bubble residency time measured from the front probe, τ, and from the bubble velocity, u_b, as follows:

$$\ell_{c\ell} = u_b \tau \tag{61}$$

A typical bubble chord-length distribution is illustrated in Figure 5.107. For each experiment, this type of figure has been produced to verify the order of Sauter mean diameter values obtained from Eq. (55).

The local bubble impaction rate or bubble frequency, which is the number of bubbles detected by the front probe in unit time at a specific location, can also be obtained from the experimental data. Bubble impaction rate distributions are shown in Figures 5.1 to 5.28. The influence of gas and liquid flow on the bubble frequency are shown in Figures 5.108 to 5.104. It is important to note from these figures that the bubble impaction rate distribution has the same behavior as that of the local void fraction distribution. Due to the buoyancy effect, the uniformly generated and distributed bubbles move into the upper sections and crowd together near the top wall of the horizontal flow channel. A distinct peak of bubble impaction rates close to the top wall can be observed in all flow conditions even though the bubble impaction rate profile tends to flatten as the average void fraction is increased. A very high bubble frequency on the order of 1800 1/s may be observed toward the top of the tube. This might explain the high void fractions and interfacial areas observed in the present horizontal bubbly flow experiments.

6. SUMMARY AND CONCLUSIONS

The internal phase distribution of cocurrent, air-water bubbly flow in a 50.3 mm diameter transparent pipeline has been experimentally investigated by using double-sensor resistivity probe technique. Liquid and gas volumetric superficial velocities ranged from 3.11 to 5.92 m/s and 0.23 to 1.97 m/s, respectively, and average void fractions ranged from 0.9 to 30%. The local values of void fraction, interfacial area concentration, mean bubble diameter, bubble interfacial velocity, bubble chord-length and bubble frequency distributions were measured.

The experimental results indicated that the void fraction, interfacial area concentration and bubble frequency have local maxima near the upper pipe wall, and that the profiles tended to flatten with increasing void fraction. For the horizontal bubbly flow, the observed peak void fraction can reach 0.65, and the peak interfacial area concentration can go up to 1000 m^2/m^3, whereas the bubble frequency may reach a value of 1700/s. It was found that either decreasing the liquid flow at constant gas flow or increasing the gas flow at a fixed liquid flow would increase the local void fraction, interfacial area concentration and the bubble frequency.

The axial bubble interface velocity showed a relatively uniform distribution except near the upper pipe wall, where a sharp reduction in velocity was found. The local bubble interface velocity and the bubble velocity turbulent fluctuations increase with the gas flow.

Using the relation between the local interfacial area concentration, void fraction and the Sauter mean diameter of bubbles, the mean bubble diameter distributions were calculated. It was observed that the mean bubble diameters ranged from 2 to 6 mm depending on the location and flow conditions. The bubble diameter generally increases with the gas flow rate at a given liquid flow rate, although the effect was not found to be significant.

7. ACKNOWLEDGEMENT

The work reported in this report was supported by a grant from the U.S. Department of Energy (DE-FG02-87ER13764).

TABLE 5.1 Experimental Conditions

No.	$\langle j_f \rangle$ (m/s)	$\langle j_g \rangle$ (m/s)	$\langle \alpha \rangle$ %	P (bar)	ΔP_2 (bar)	ΔP_4 (bar)	ΔP_6 (bar)
1	3.74	0.25	5.7	1.22	0.0545	0.0544	0.0542
2	3.74	0.51	10.5	1.23	0.0563	0.0561	0.0559
3	3.83	0.72	15.2	1.28	0.0567	0.0566	0.0564
4	3.74	1.03	18.3	1.27	0.0585	0.0583	0.0581
5	4.05	0.26	6.4	1.24	0.0569	0.0567	0.0565
6	4.05	0.51	10.7	1.26	0.0585	0.0583	0.0581
7	4.05	0.76	15.4	1.27	0.0004	0.0602	0.060
8	4.06	1.04	18.7	1.29	0.0695	0.0602	0.06
9	4.05	1.34	21.0	1.36	0.0563	0.0541	0.0496
10	4.45	0.24	4.7	1.26	0.0611	0.0596	0.0599
11	4.36	0.51	10.3	1.29	0.0550	0.0520	0.0473
12	4.36	0.78	14.1	1.3	0.0617	0.0618	0.0616
13	4.36	1.31	21.5	1.36	0.0656	0.0655	0.0654
14	4.30	1.59	22.5	1.41	0.0651	0.0636	0.0585
15	4.78	0.25	4.3	1.29	0.0619	0.0617	0.0616
16	4.67	0.53	8.7	1.32	0.0801	0.0576	0.0555
17	4.7	0.79	14.3	1.32	0.0669	0.0659	0.0658
18	4.77	1.19	18.2	1.39	0.0688	0.0685	0.0679
19	5.10	0.24	4.3	1.35	0.0653	0.0632	0.0567
20	5.10	0.48	8.0	1.36	0.0679	0.0661	0.0586
21	4.98	0.80	13.9	1.36	0.0674	0.0672	0.0669
22	4.98	1.34	20.4	1.43	0.0716	0.0715	0.0713
23	5.29	0.80	12.5	1.41	0.0705	0.0704	0.0703
24	5.29	1.35	20.8	1.48	0.0749	0.0748	0.0746
25	5.71	0.71	10.6	1.47	0.0748	0.0746	0.0744
26	5.6	1.37	21.3	1.57	0.0785	0.0782	0.078

TABLE 5.2 Experimental Conditions and Comparisons of Velocities

No.	$\langle j_f \rangle$ (m/s)	$\langle \alpha \rangle$ %	$\bar{u}_b$ (m/s)	$\bar{u}_g$ (m/s)	$\Delta\bar{u}_b$ %	$\langle j_b \rangle$ (m/s)	$\langle j_g \rangle$ (m/s)	$\Delta\langle j_b \rangle$ %
1	3.74	5.70	4.01	4.39	-8.9	0.23	0.25	-8.8
2	3.74	10.50	4.49	4.86	-7.6	0.471	0.51	-7.6
3	3.83	15.18	4.50	4.71	-4.4	0.68	0.72	-5.6
4	3.74	18.30	5.10	5.63	-0.4	0.93	1.03	-9.7
5	4.05	6.48	4.25	4.06	-4.7	0.27	0.26	3.8
6	4.05	10.70	4.69	4.77	-1.7	0.50	0.51	-1.9
7	4.05	15.40	5.02	4.94	-1.6	0.77	0.76	1.3
8	4.06	18.70	5.53	5.56	-0.5	1.03	1.04	-0.9
9	4.05	21.00	5.89	6.38	-7.7	1.23	1.34	-8.2
10	4.45	4.70	4.64	5.15	-9.9	0.22	0.24	-9.9
11	4.36	10.30	4.89	4.95	-1.2	0.50	0.51	-1.6
12	4.36	14.10	5.41	5.53	-2.1	0.76	0.78	-2.5
13	4.36	21.50	6.32	6.09	3.7	1.36	1.31	3.8
14	4.36	22.50	6.37	7.07	-9.9	1.43	1.59	-10.1
15	4.78	4.30	5.21	5.88	-11.4	0.22	0.25	-10.4
16	4.67	8.70	5.39	6.09	-11.5	0.47	0.53	-11.3
17	4.70	14.30	5.77	5.52	4.5	0.82	0.79	3.8
18	4.77	18.25	6.17	6.52	-5.4	1.12	1.19	-5.6
19	5.10	4.34	5.49	5.61	-2.1	0.24	0.24	0.0
20	5.10	8.02	5.60	6.05	-7.9	0.44	0.48	-6.4
21	4.98	13.90	6.32	5.76	9.7	0.88	0.80	10.0
22	4.98	20.40	6.26	6.57	-4.7	1.27	1.34	-5.2
23	5.29	12.50	6.78	6.40	5.9	0.849	0.80	-6.1
24	5.29	20.80	7.30	6.49	12.4	1.516	1.35	12.3
25	5.71	10.60	7.03	6.75	4.1	0.75	0.71	4.9
26	5.60	21.80	6.04	6.43	-6.0	1.31	1.37	-5.3

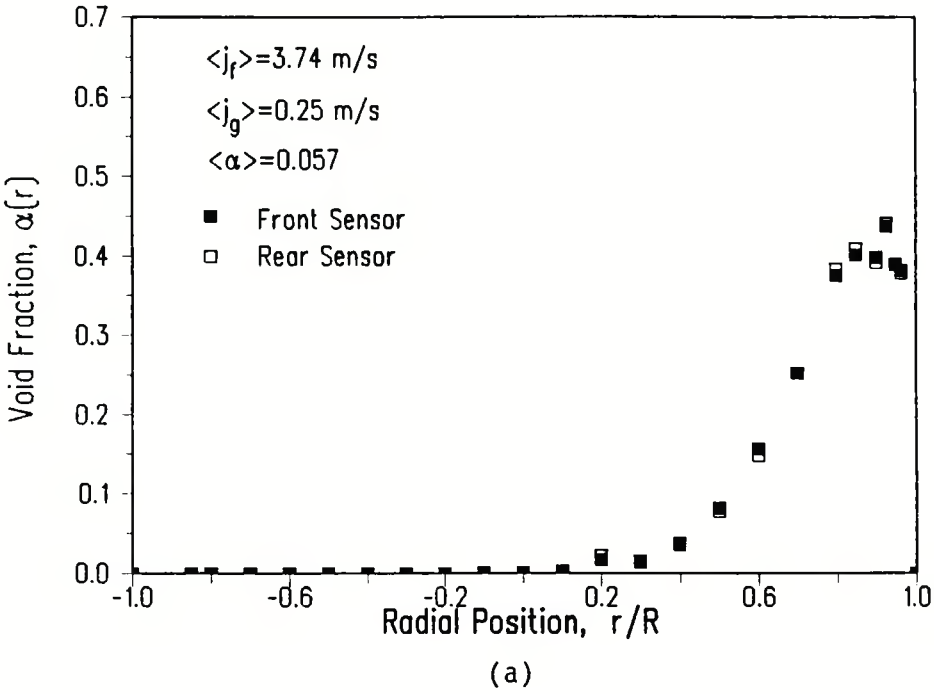

(a)

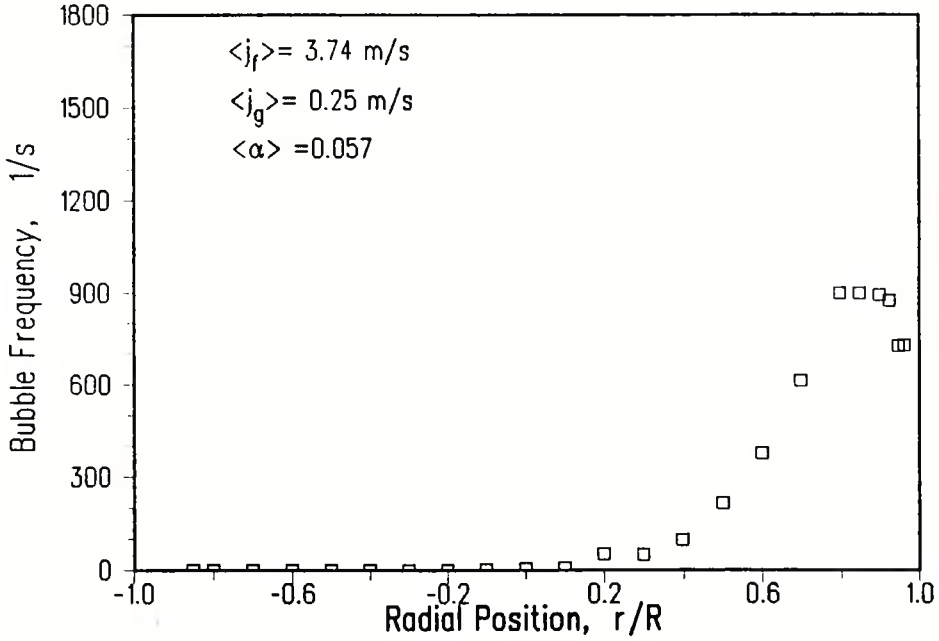

(b)

Figure 5.1 a) Local Void Fraction, b) Bubble Frequency, c) Interfacial Area Concentration, and d) Bubble Velocity Distribution at $\langle j_f \rangle$ = 3.74 m/s, $\langle j_g \rangle$ = 0.25 m/s, $\langle \alpha \rangle$ = 0.057.

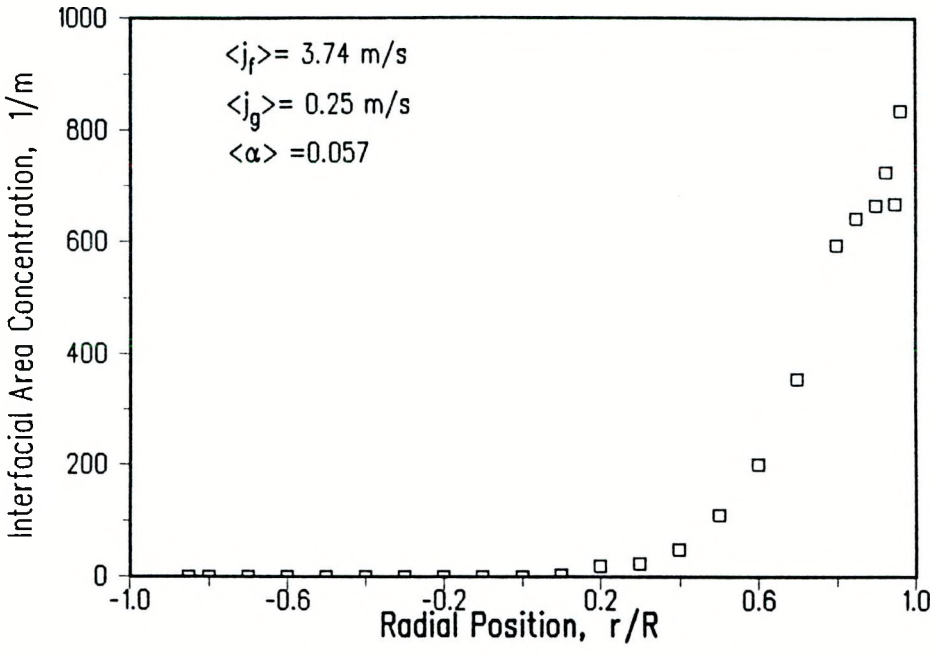

(c)

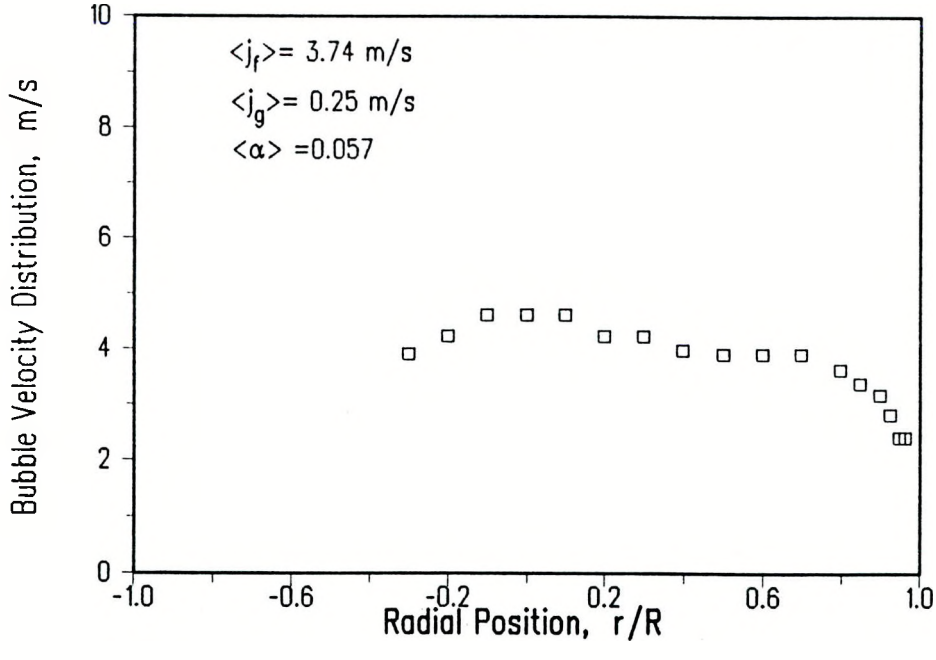

(d)

Figure 5.1 a) Local Void Fraction, b) Bubble Frequency, c) Interfacial Area Concentration, and d) Bubble Velocity Distribution at $\langle j_f \rangle$ = 3.74 m/s, $\langle j_g \rangle$ = 0.25 m/s, $\langle \alpha \rangle$ = 0.057.

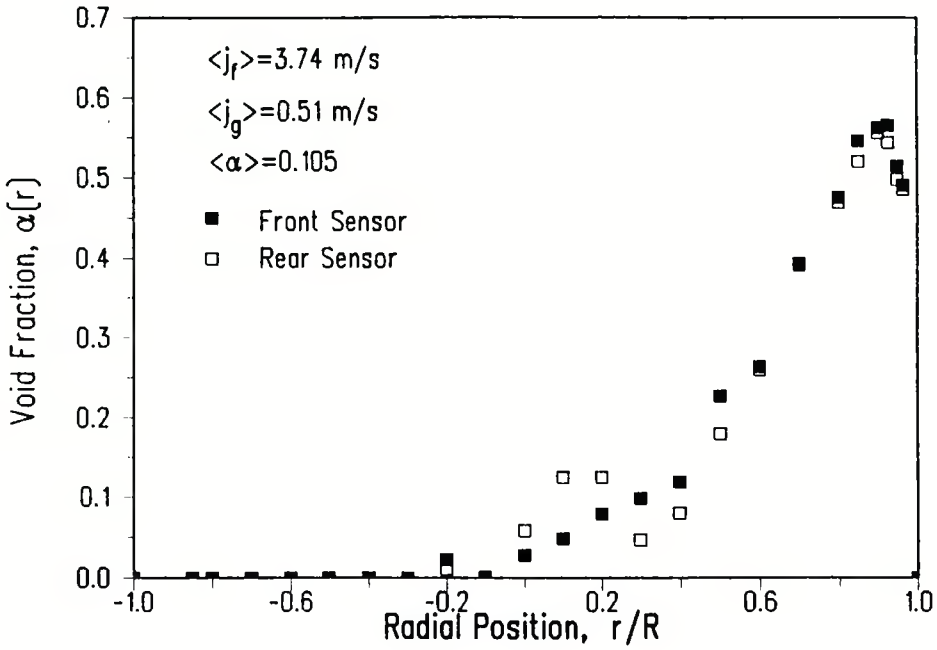

(a)

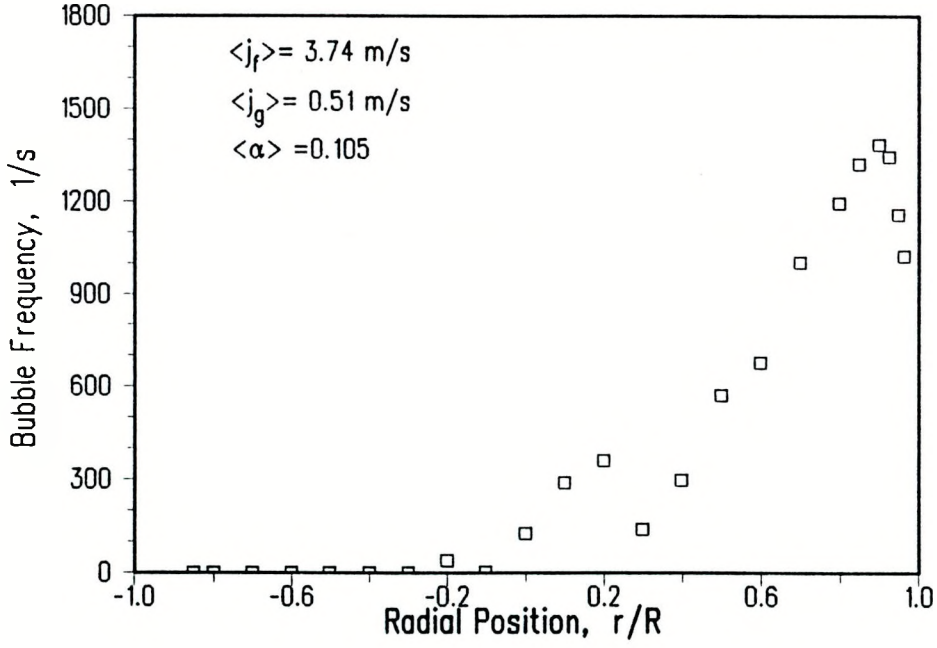

(b)

Figure 5.2 a) Local Void Fraction, b) Bubble Frequency, c) Interfacial Area Concentration, and d) Bubble Velocity Distribution at $\langle j_f \rangle$ = 3.74 m/s, $\langle j_g \rangle$ = 0.51 m/s, $\langle \alpha \rangle$ = 0.105.

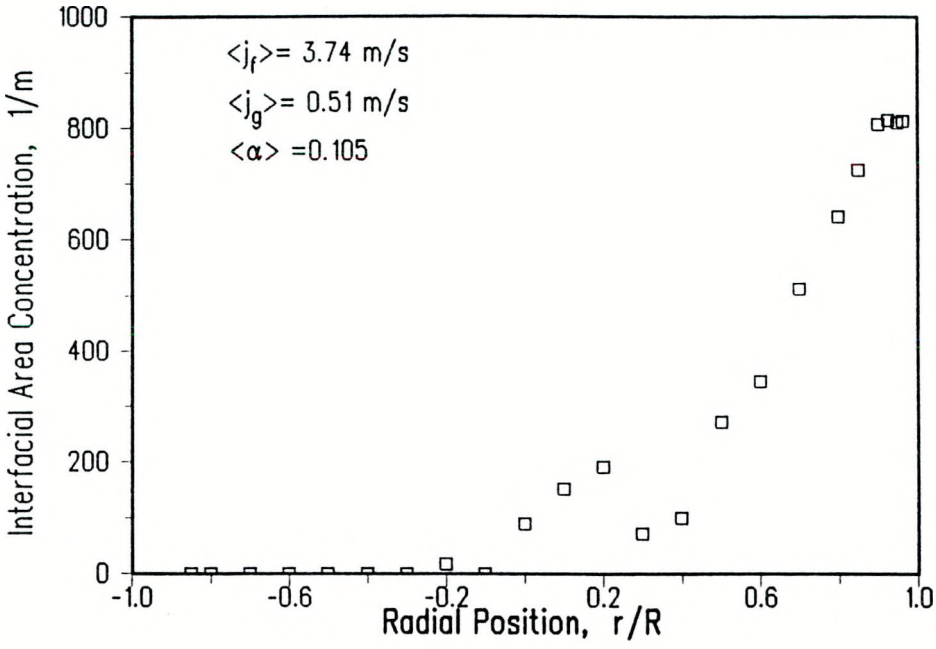

(c)

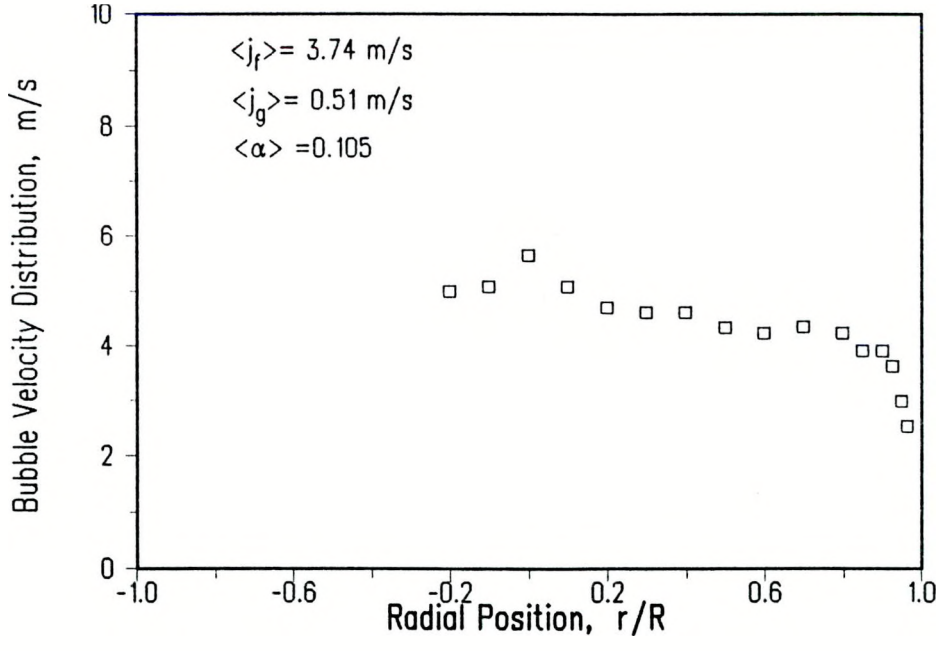

(d)

Figure 5.2 a) Local Void Fraction, b) Bubble Frequency, c) Interfacial Area Concentration, and d) Bubble Velocity Distribution at $\langle j_f \rangle$ = 3.74 m/s, $\langle j_g \rangle$ = 0.51 m/s, $\langle \alpha \rangle$ = 0.105.

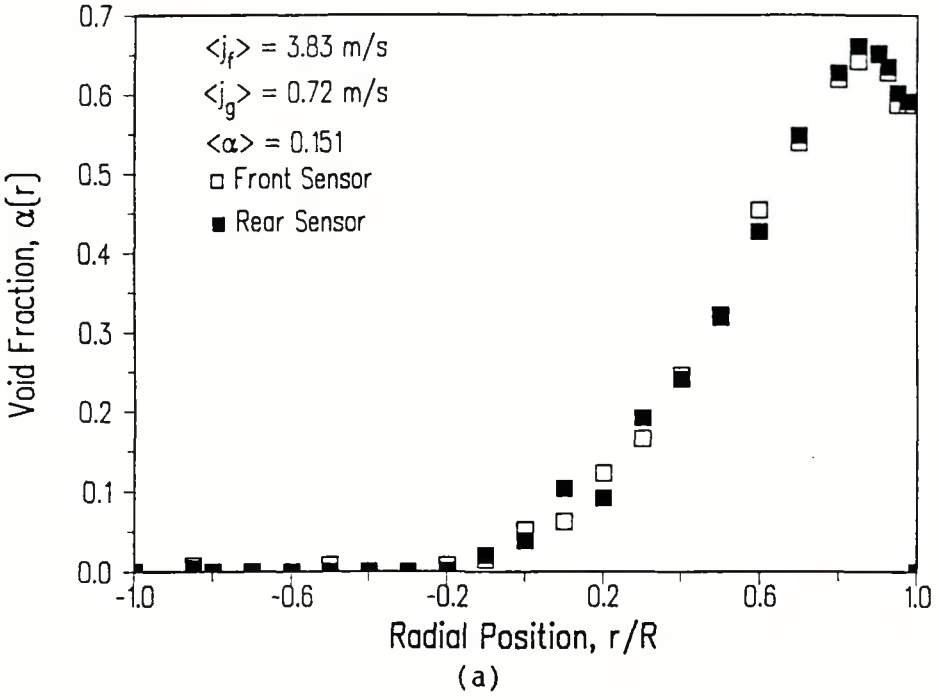

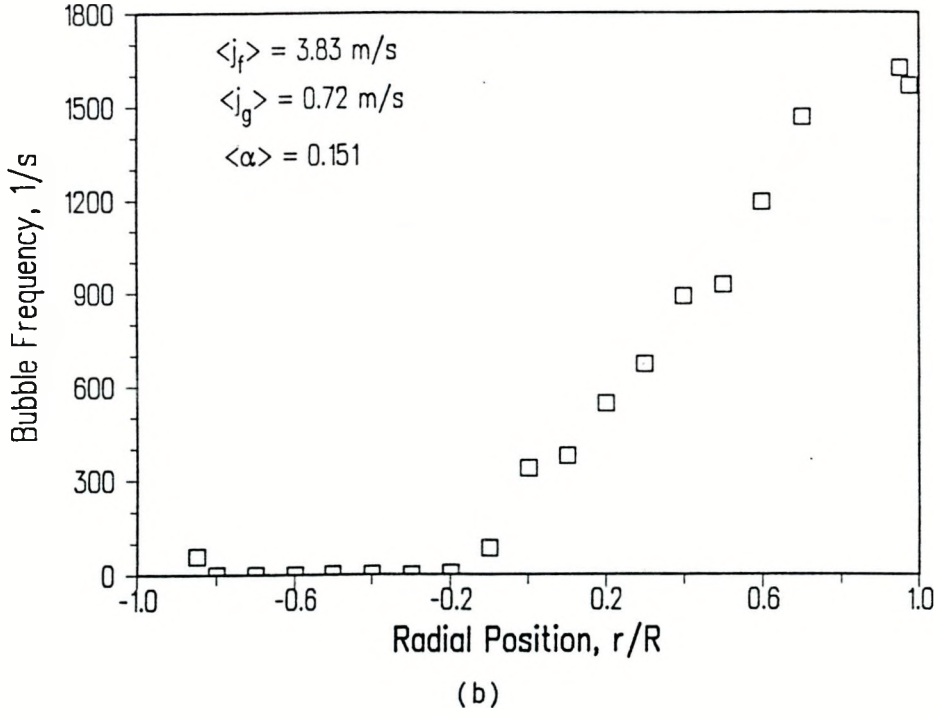

Figure 5.3 a) Local Void Fraction, b) Bubble Frequency, c) Interfacial Area Concentration, and d) Bubble Velocity Distribution at $\langle j_f \rangle$ = 3.83 m/s, $\langle j_g \rangle$ = 0.72 m/s, $\langle \alpha \rangle$ = 0.151.

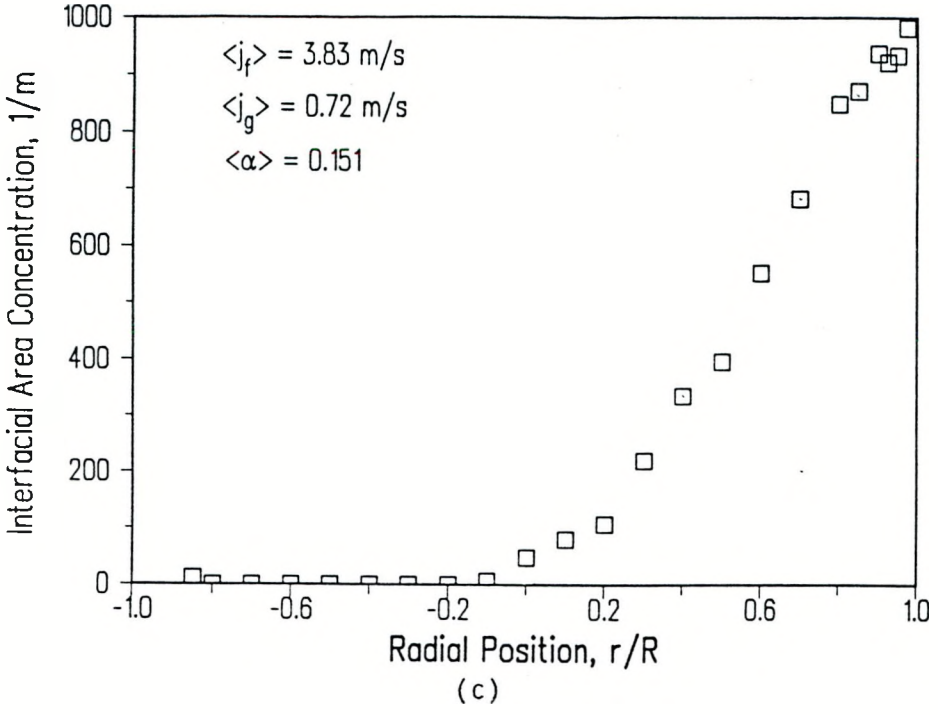

(c)

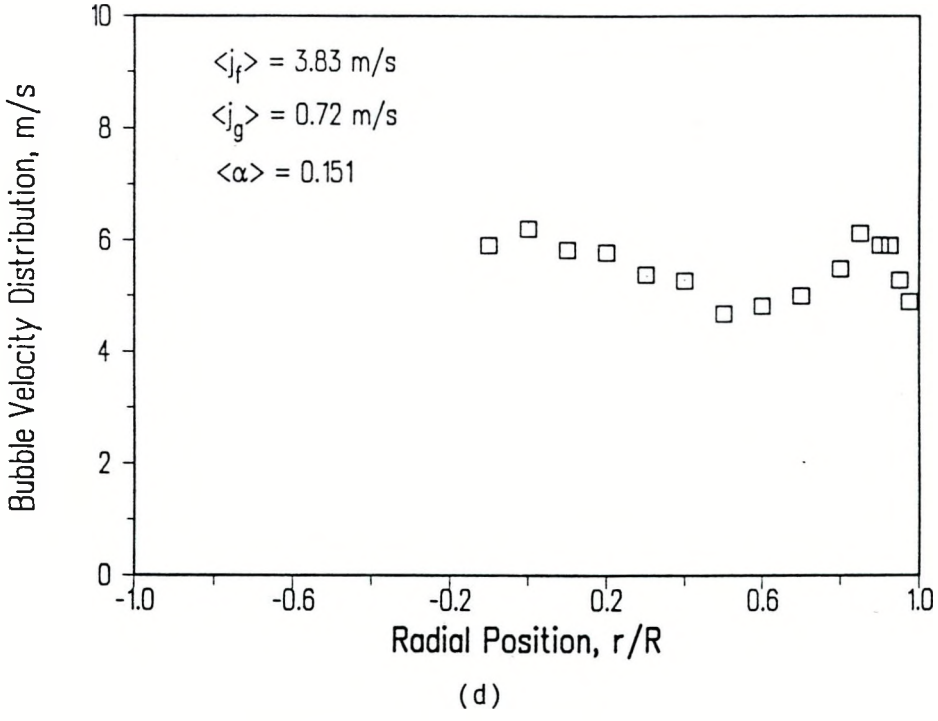

(d)

Figure 5.3 a) Local Void Fraction, b) Bubble Frequency, c) Interfacial Area Concentration, and d) Bubble Velocity Distribution at $\langle j_f \rangle$ = 3.83 m/s, $\langle j_g \rangle$ = 0.72 m/s, $\langle \alpha \rangle$ = 0.151.

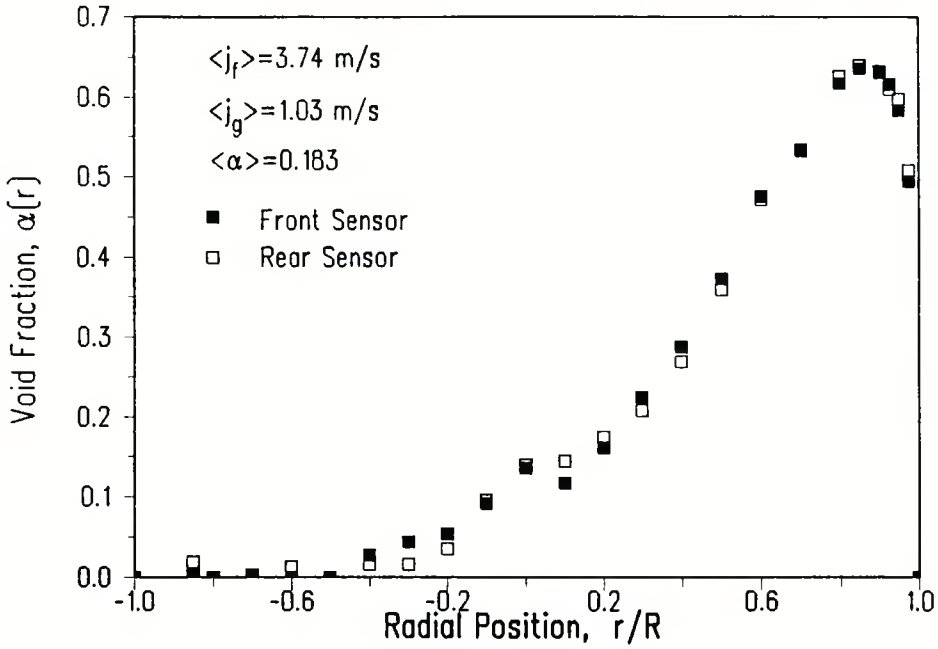

(a)

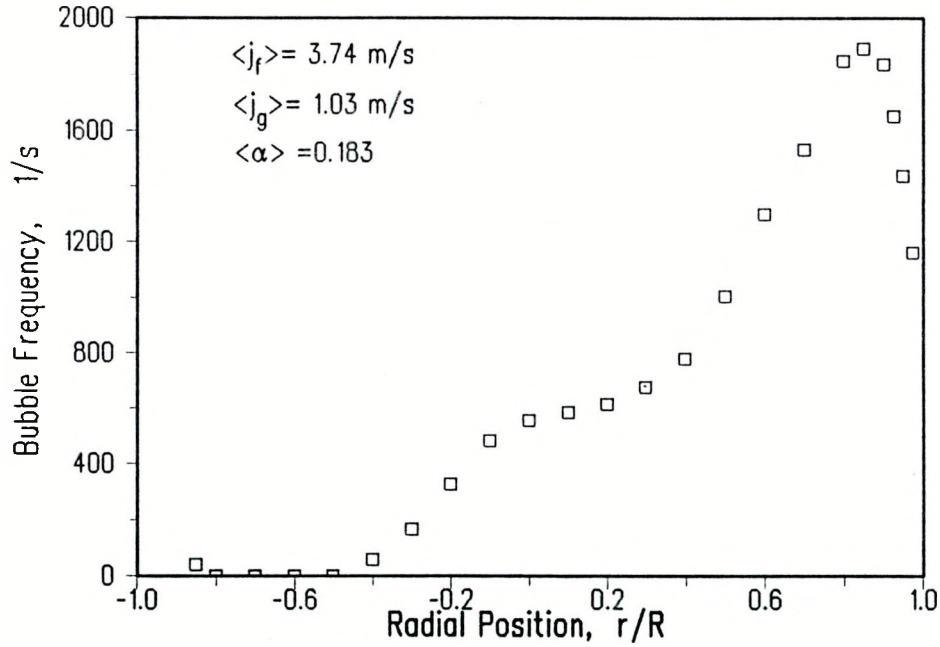

(b)

Figure 5.4 a) Local Void Fraction, b) Bubble Frequency, c) Interfacial Area Concentration, and d) Bubble Velocity Distribution at $\langle j_f \rangle$ = 3.74 m/s, $\langle j_g \rangle$ = 1.03 m/s, $\langle \alpha \rangle$ = 0.183.

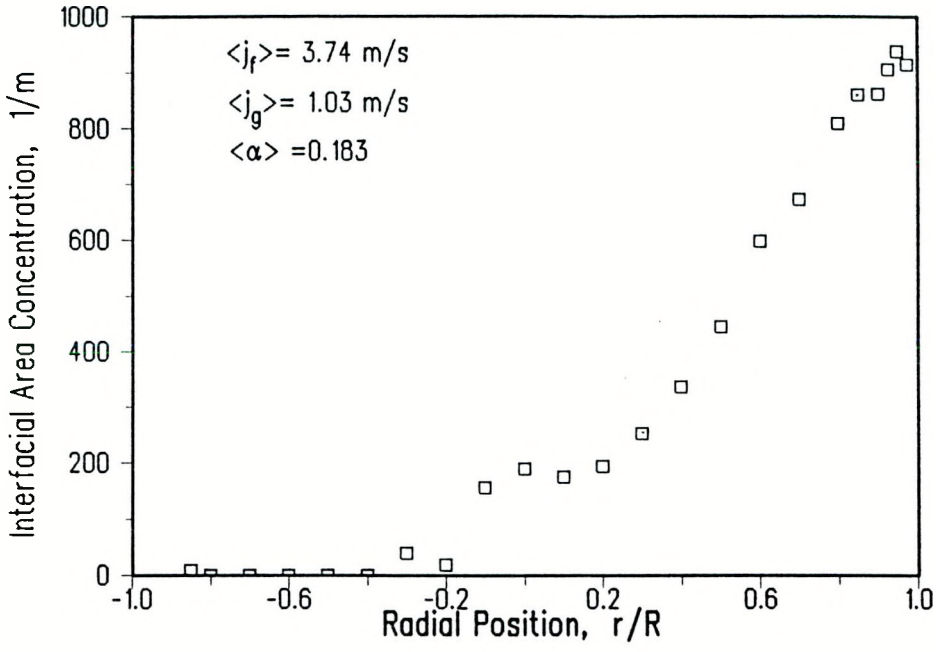

(c)

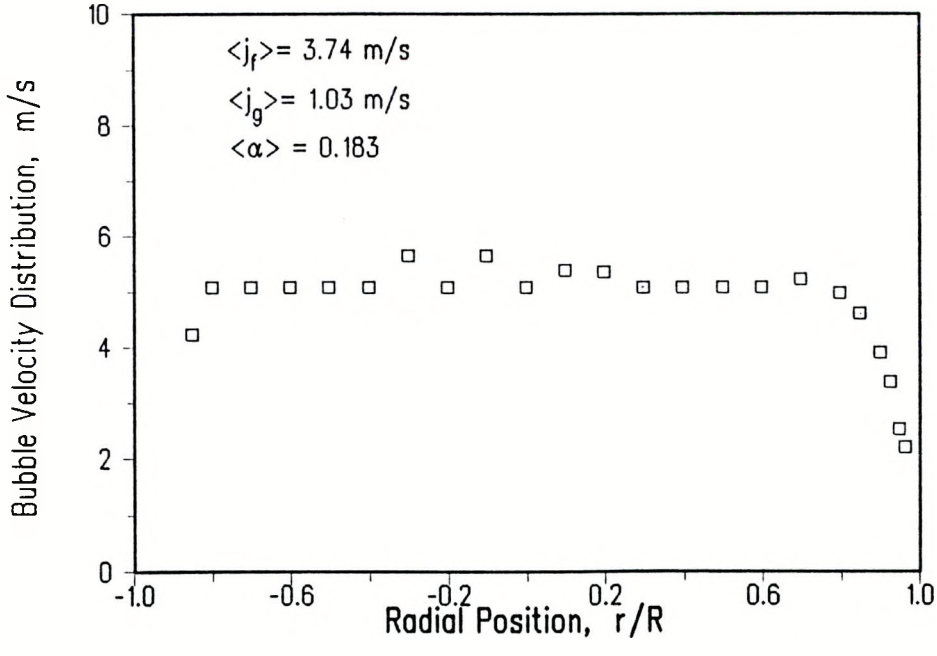

(d)

Figure 5.4 a) Local Void Fraction, b) Bubble Frequency, c) Interfacial Area Concentration, and d) Bubble Velocity Distribution at $\langle j_f \rangle$ = 3.74 m/s, $\langle j_g \rangle$ = 1.03 m/s, $\langle \alpha \rangle$ = 0.183.

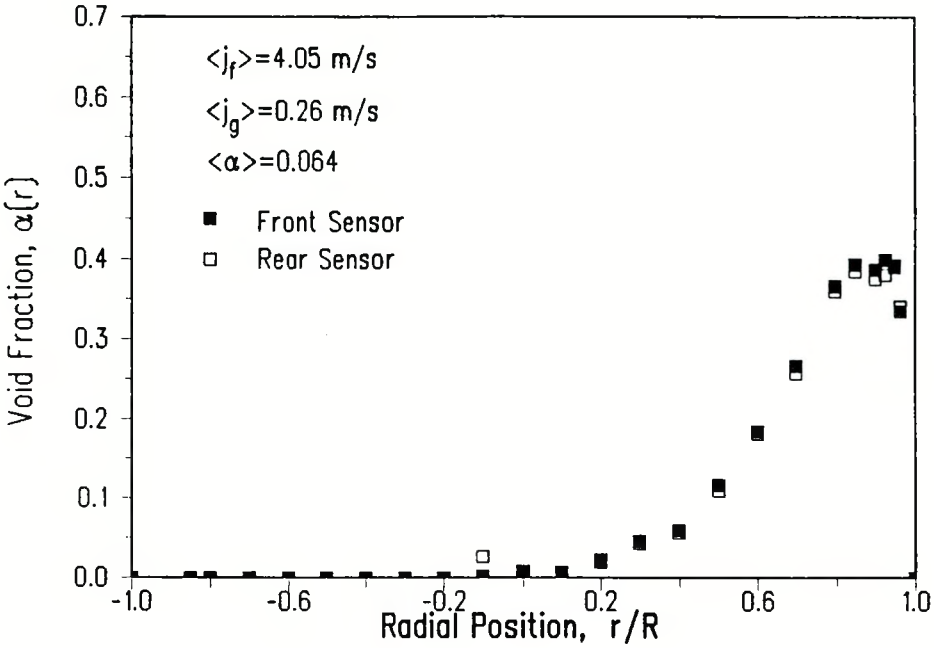

(a)

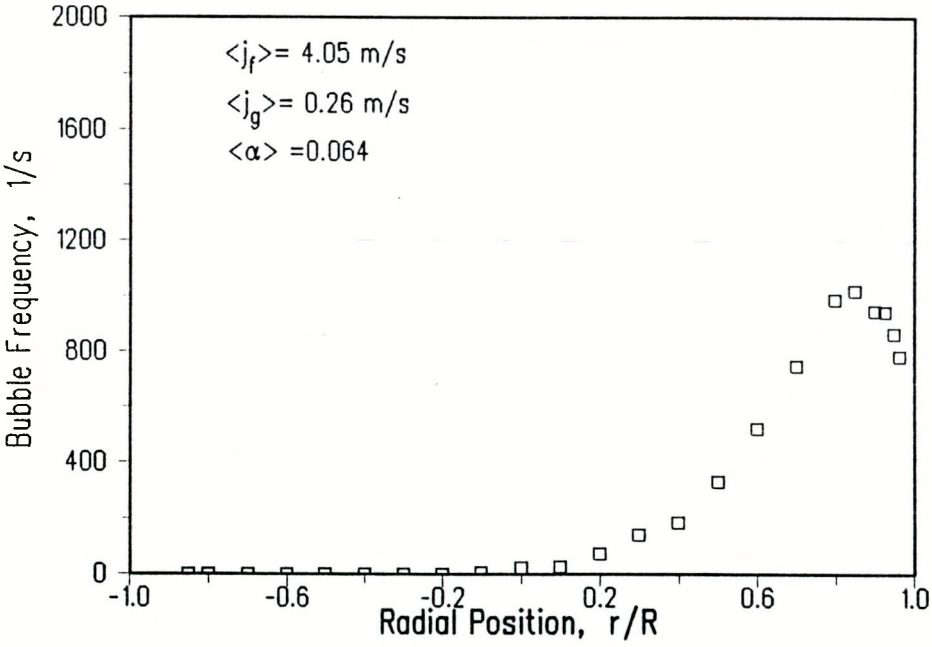

(b)

Figure 5.5 a) Local Void Fraction, b) Bubble Frequency, c) Interfacial Area Concentration, and d) Bubble Velocity Distribution at $\langle j_f \rangle$ = 4.05 m/s, $\langle j_g \rangle$ = 0.26 m/s, $\langle \alpha \rangle$ = 0.064.

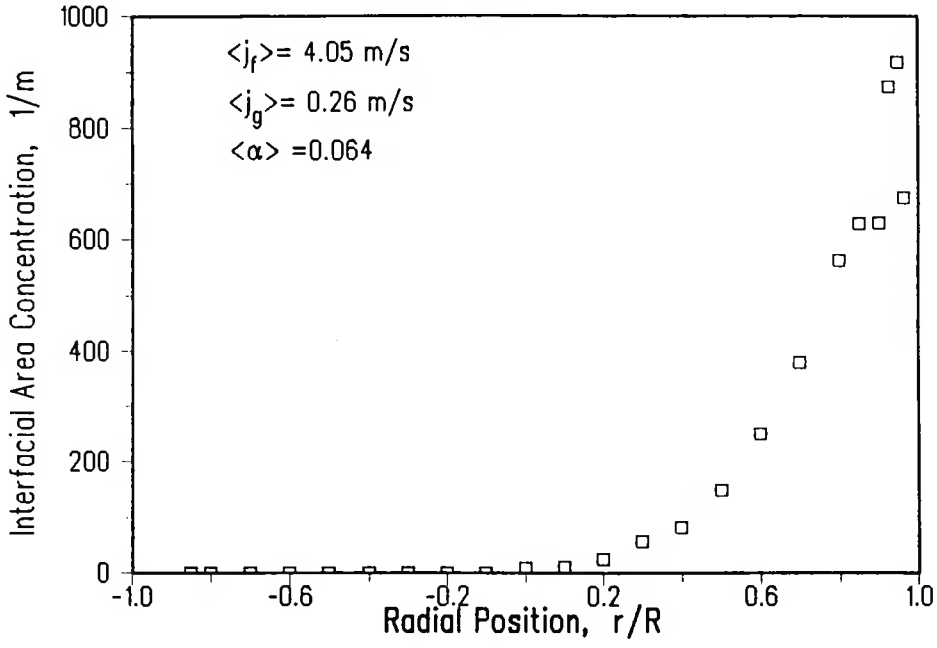

(c)

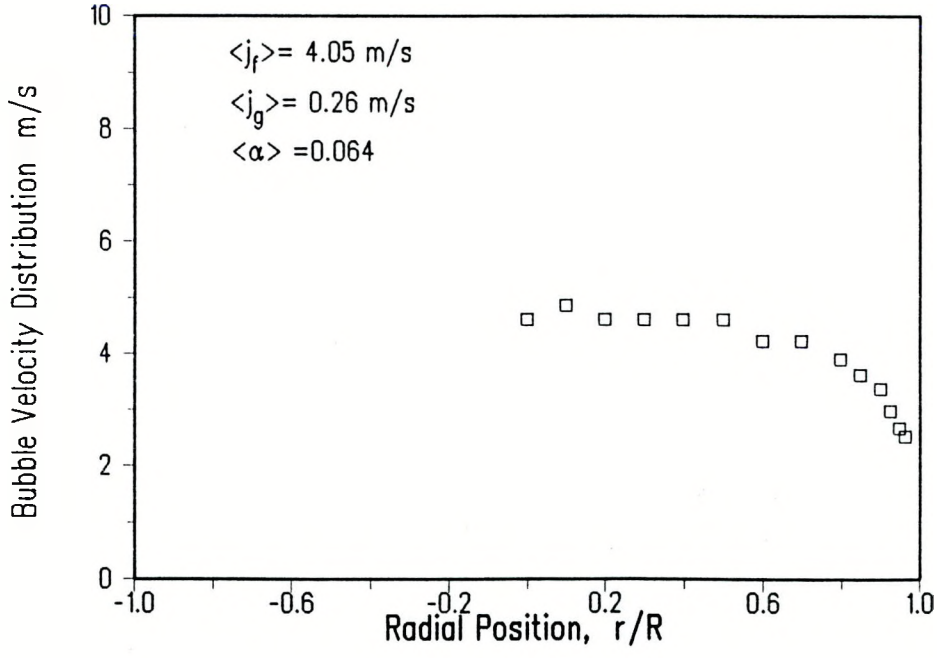

(d)

Figure 5.5 a) Local Void Fraction, b) Bubble Frequency, c) Interfacial Area Concentration, and d) Bubble Velocity Distribution at $\langle j_f \rangle$ = 4.05 m/s, $\langle j_g \rangle$ = 0.26 m/s, $\langle \alpha \rangle$ = 0.064.

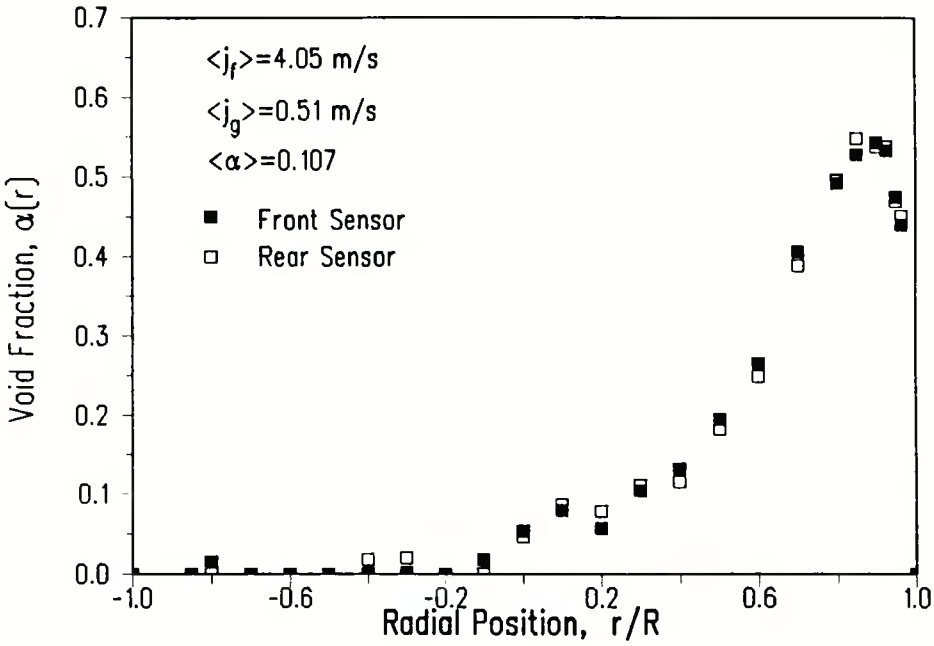

(a)

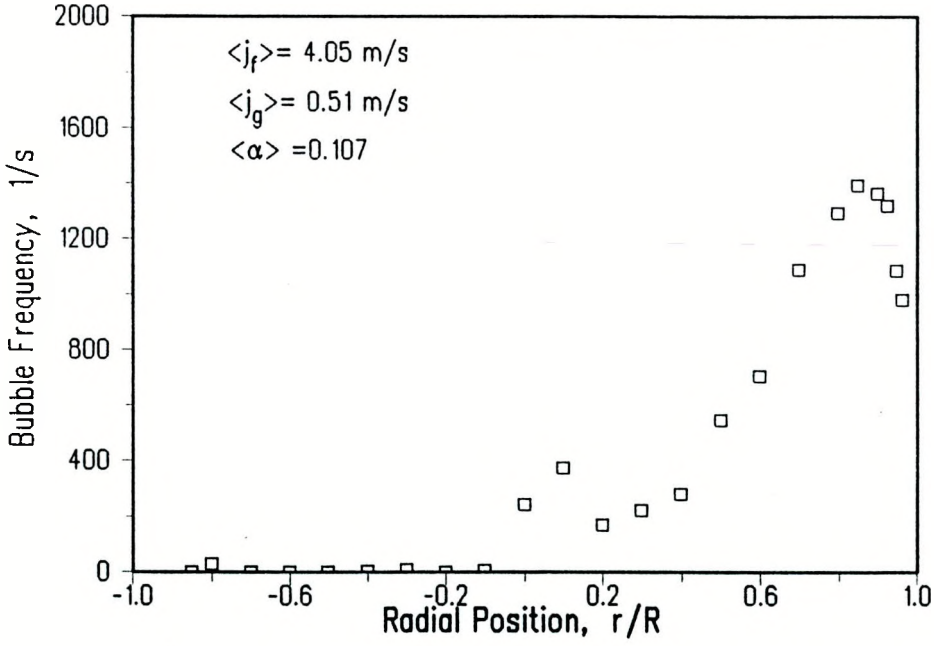

(b)

Figure 5.6 a) Local Void Fraction, b) Bubble Frequency, c) Interfacial Area Concentration, and d) Bubble Velocity Distribution at $\langle j_f \rangle$ = 4.05 m/s, $\langle j_g \rangle$ = 0.51 m/s, $\langle \alpha \rangle$ = 0.107.

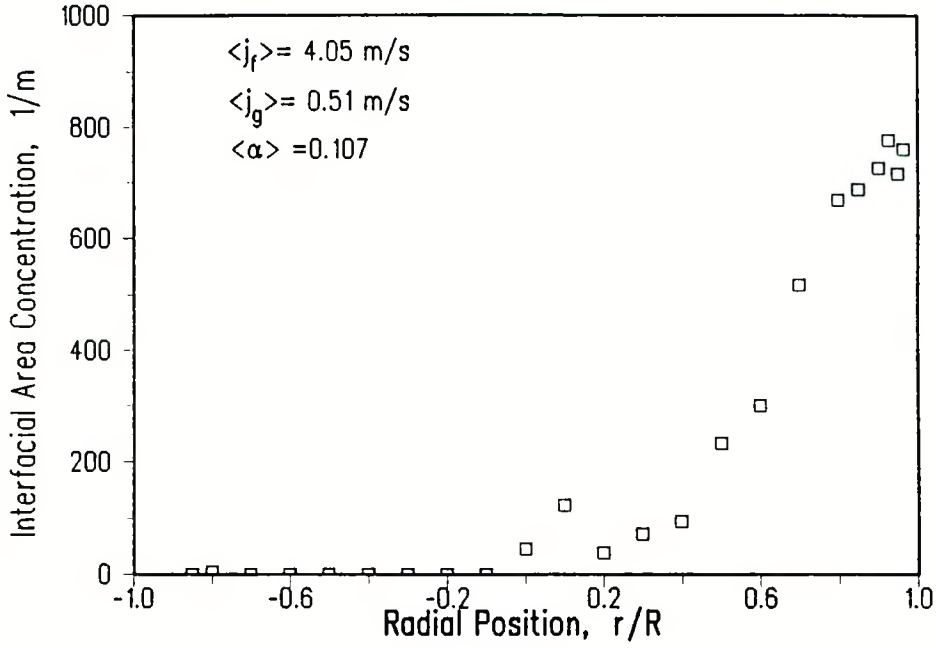

(c)

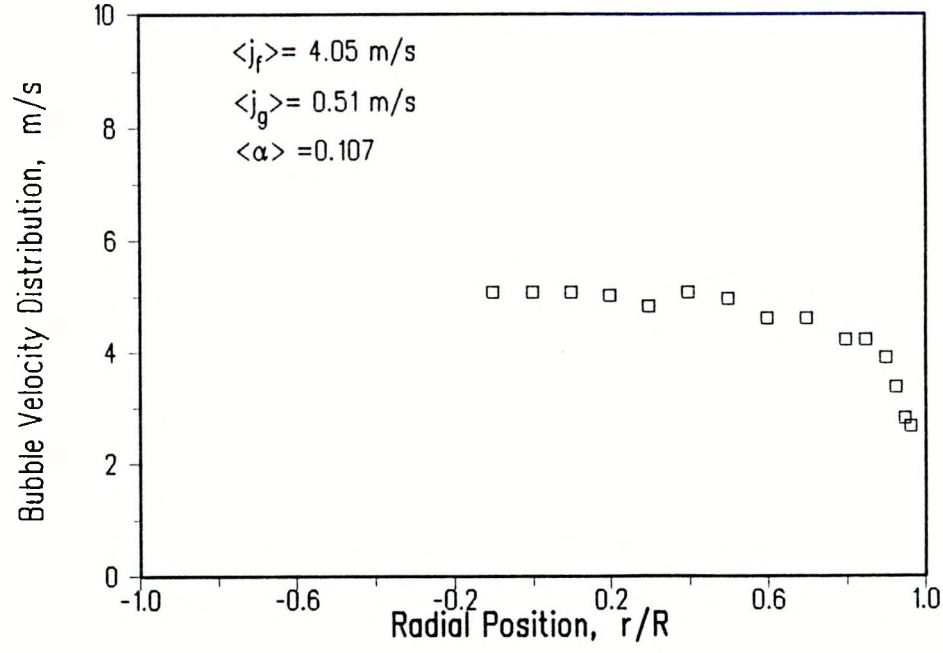

(d)

Figure 5.6 a) Local Void Fraction, b) Bubble Frequency, c) Interfacial Area Concentration, and d) Bubble Velocity Distribution at $\langle j_f \rangle$ = 4.05 m/s, $\langle j_g \rangle$ = 0.51 m/s, $\langle \alpha \rangle$ = 0.107.

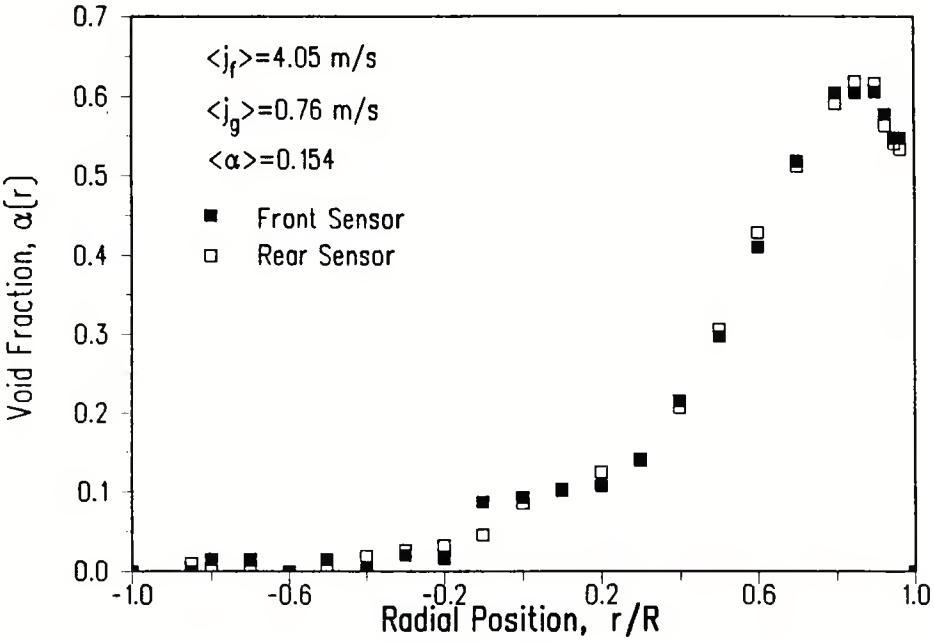

(a)

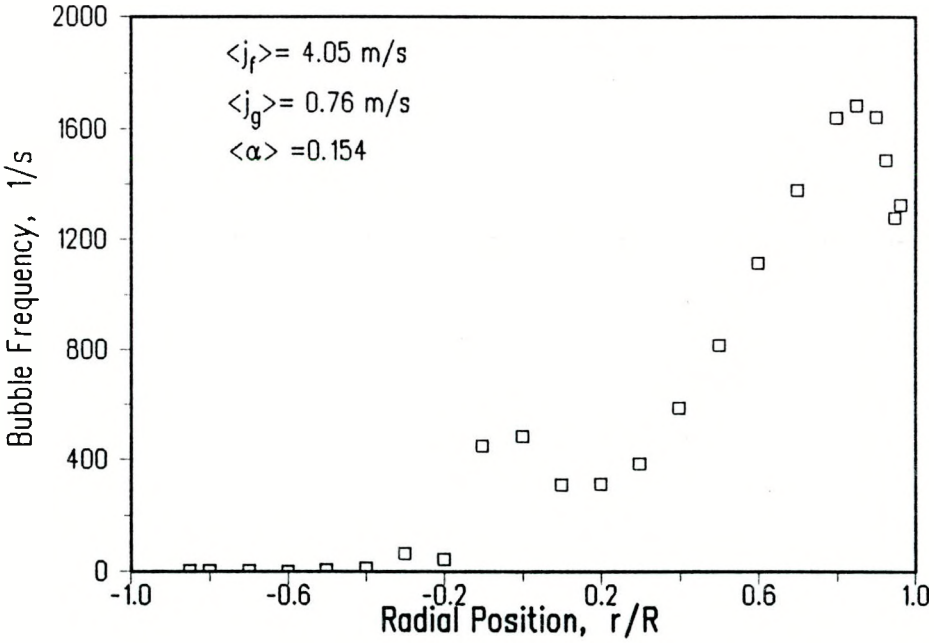

(b)

Figure 5.7 a) Local Void Fraction, b) Bubble Frequency, c) Interfacial Area Concentration, and d) Bubble Velocity Distribution at $\langle j_f \rangle$ = 4.05 m/s, $\langle j_g \rangle$ = 0.76 m/s, $\langle \alpha \rangle$ = 0.154.

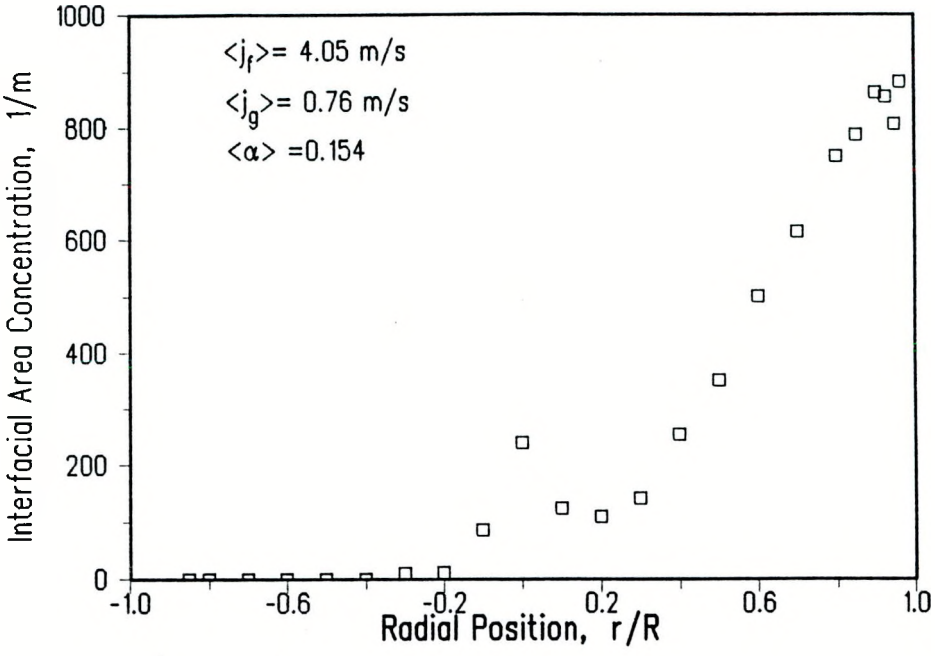

(c)

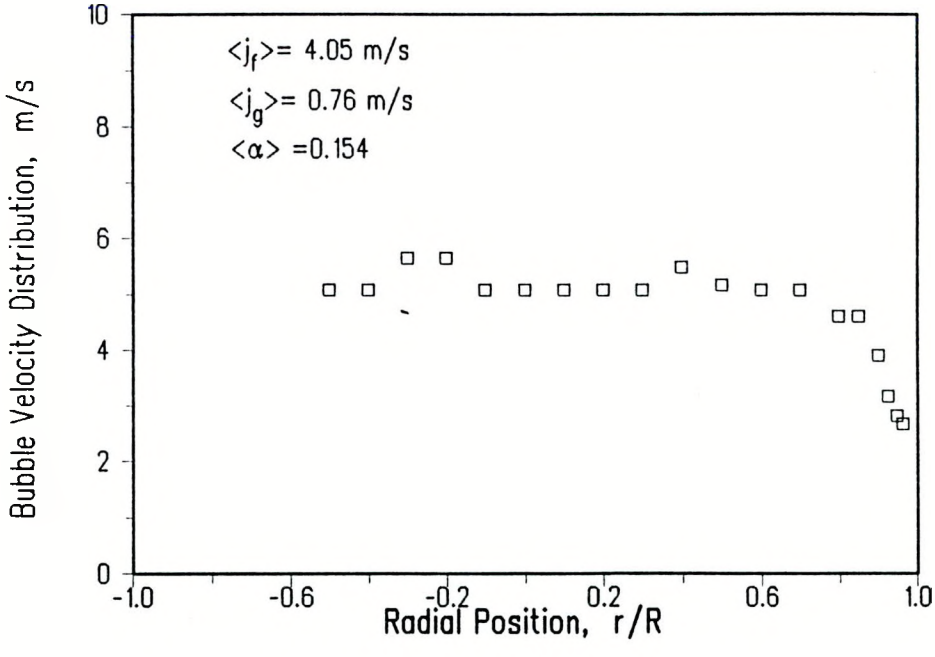

(d)

Figure 5.7 a) Local Void Fraction, b) Bubble Frequency, c) Interfacial Area Concentration, and d) Bubble Velocity Distribution at $\langle j_f \rangle$ = 4.05 m/s, $\langle j_g \rangle$ = 0.76 m/s, $\langle \alpha \rangle$ = 0.154.

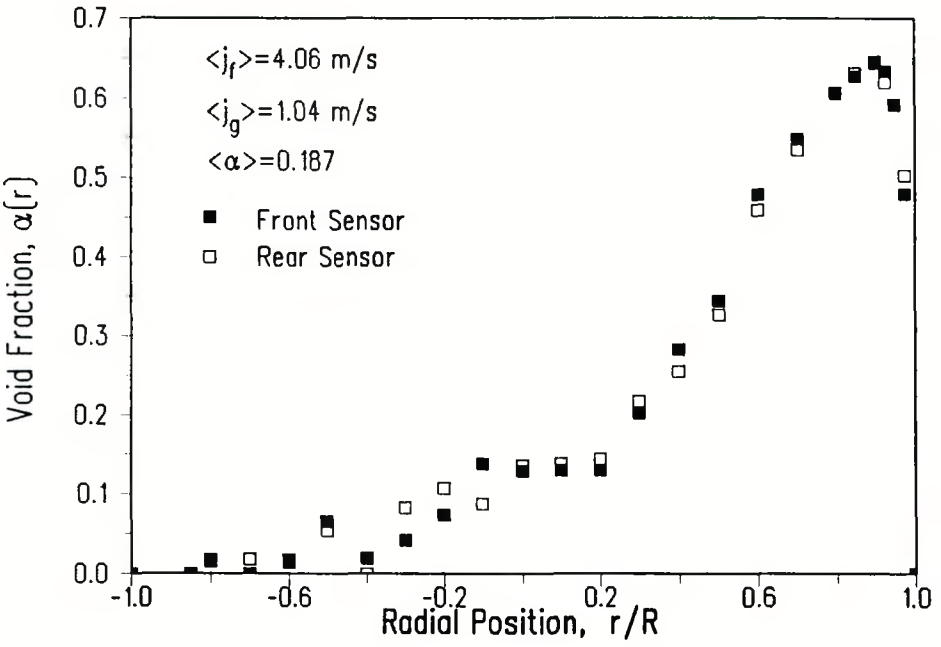

(a)

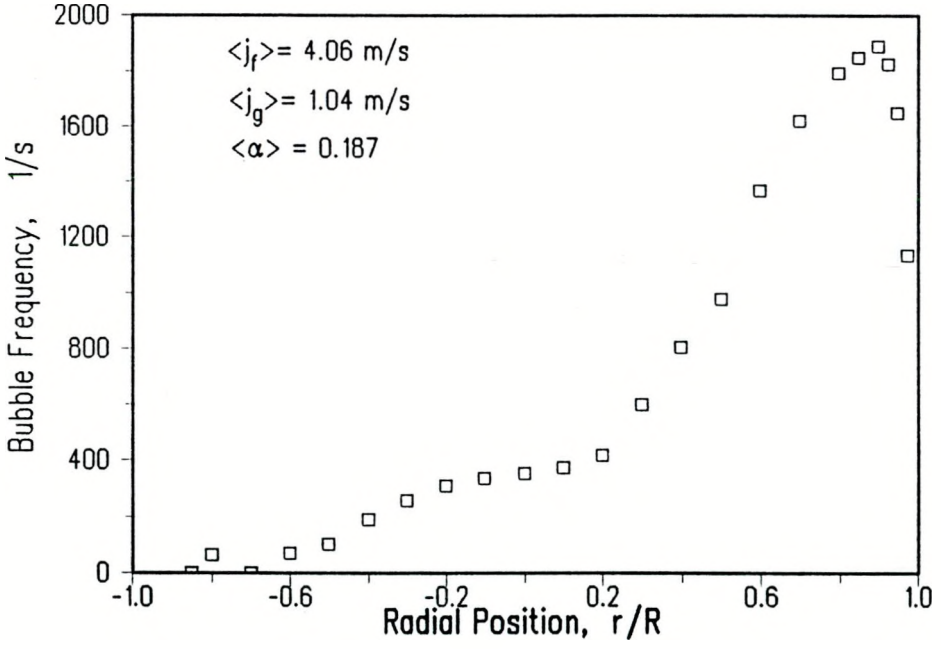

(b)

Figure 5.8 a) Local Void Fraction, b) Bubble Frequency, c) Interfacial Area Concentration, and d) Bubble Velocity Distribution at $\langle j_f \rangle$ = 4.06 m/s, $\langle j_g \rangle$ = 1.04 m/s, $\langle \alpha \rangle$ = 0.187.

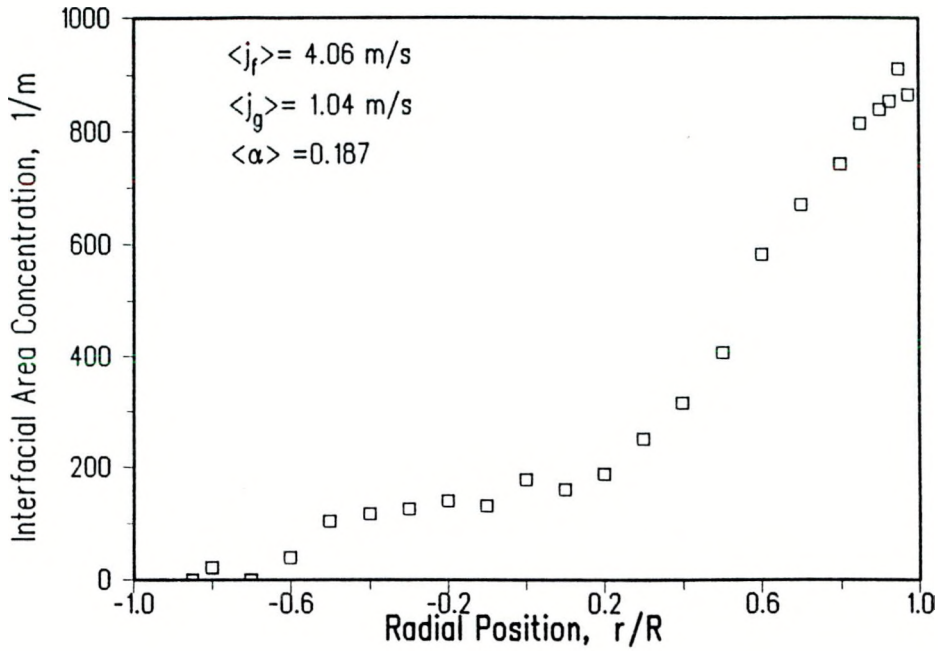

(c)

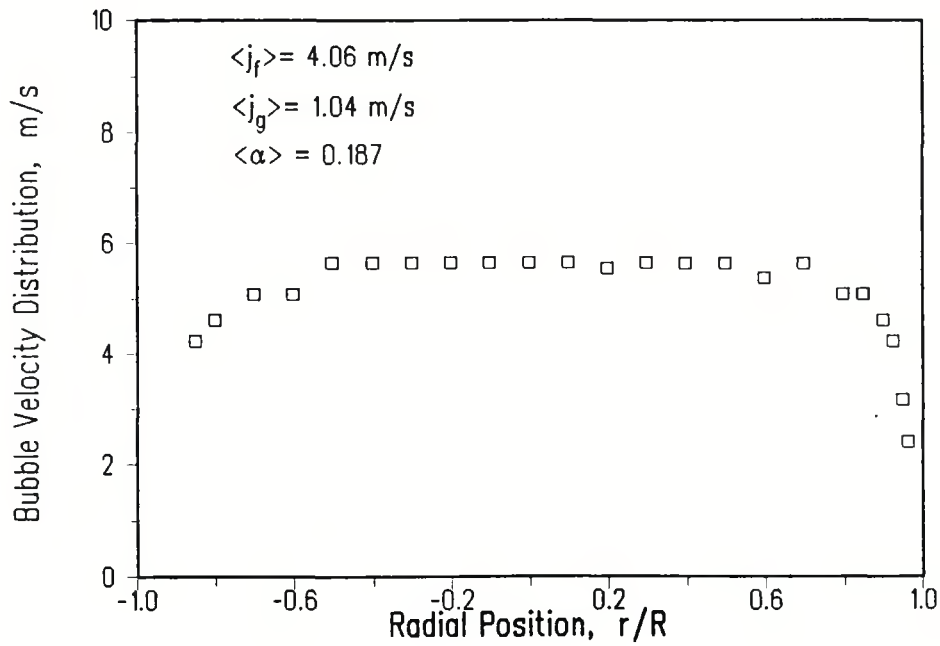

(d)

Figure 5.8 a) Local Void Fraction, b) Bubble Frequency, c) Interfacial Area Concentration, and d) Bubble Velocity Distribution at $\langle j_f \rangle$ = 4.06 m/s, $\langle j_g \rangle$ = 1.04 m/s, $\langle \alpha \rangle$ = 0.187.

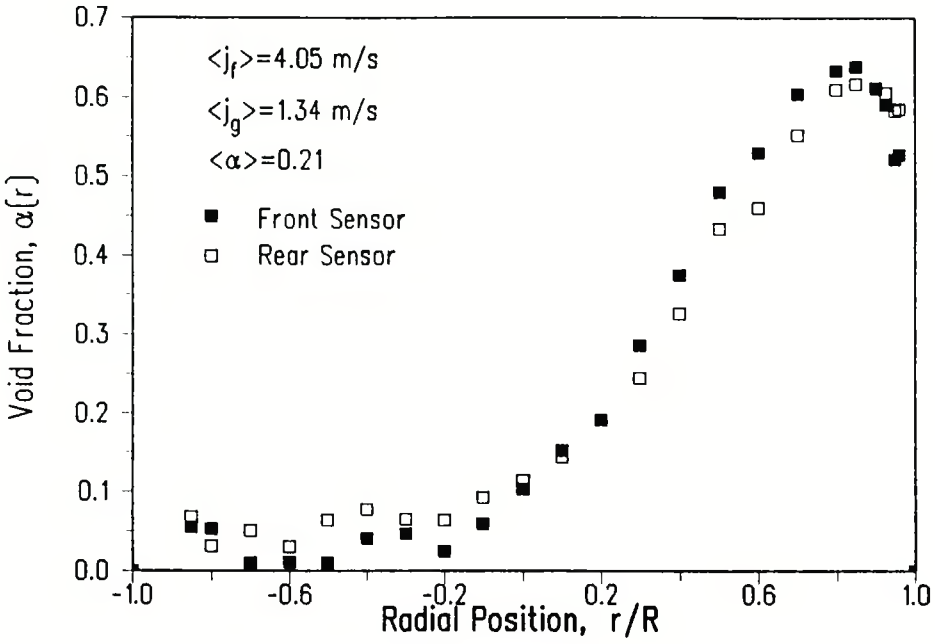

(a)

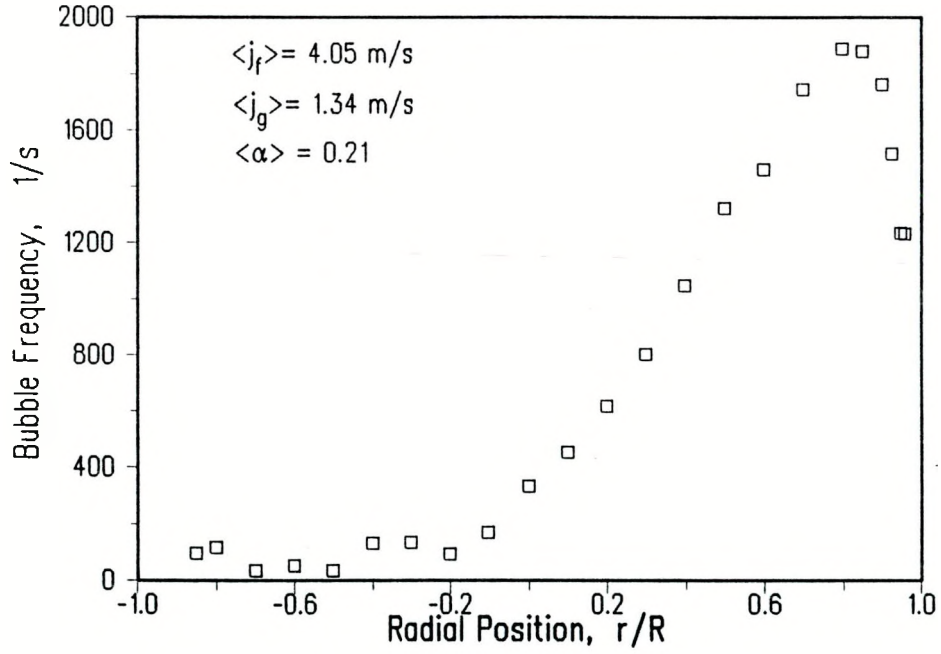

(b)

Figure 5.9 a) Local Void Fraction, b) Bubble Frequency, c) Interfacial Area Concentration, and d) Bubble Velocity Distribution at $\langle j_f \rangle$ = 4.05 m/s, $\langle j_g \rangle$ = 1.34 m/s, $\langle \alpha \rangle$ = 0.21.

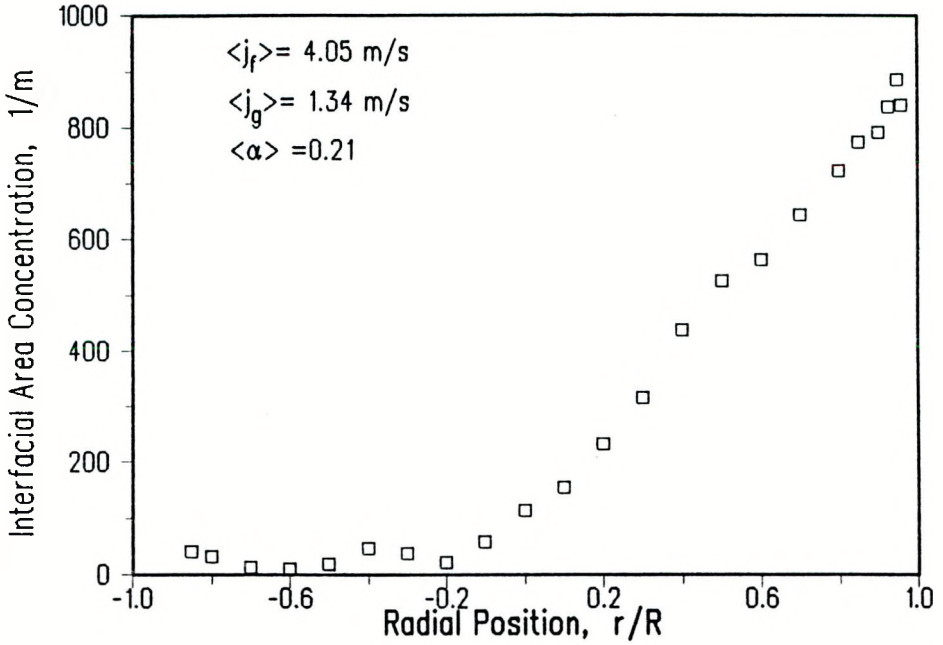

(c)

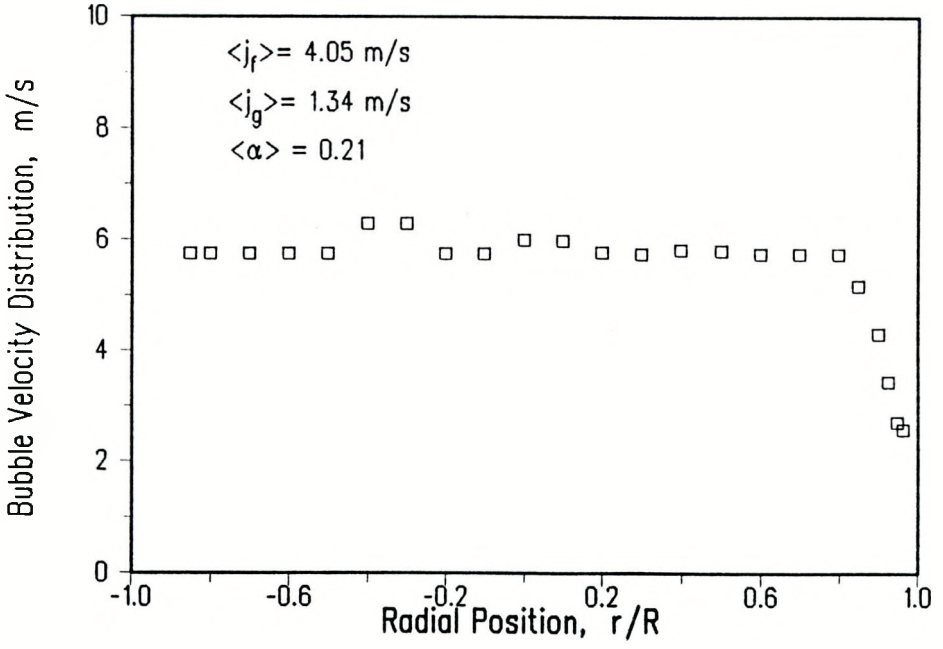

(d)

Figure 5.9 a) Local Void Fraction, b) Bubble Frequency, c) Interfacial Area Concentration, and d) Bubble Velocity Distribution at $\langle j_f \rangle$ = 4.05 m/s, $\langle j_g \rangle$ = 1.34 m/s, $\langle \alpha \rangle$ = 0.21.

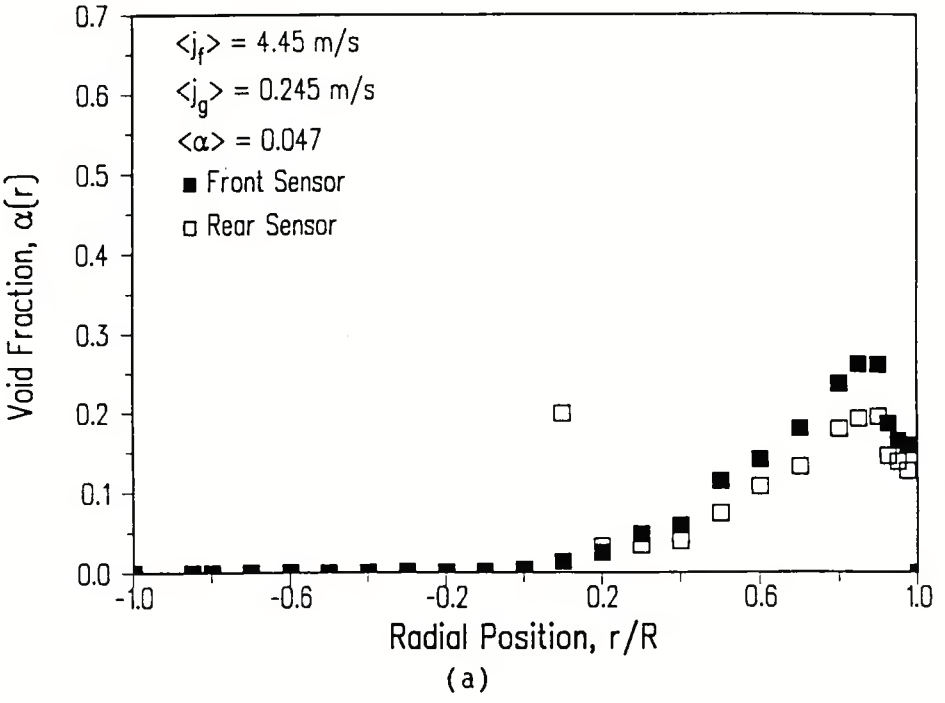

(a)

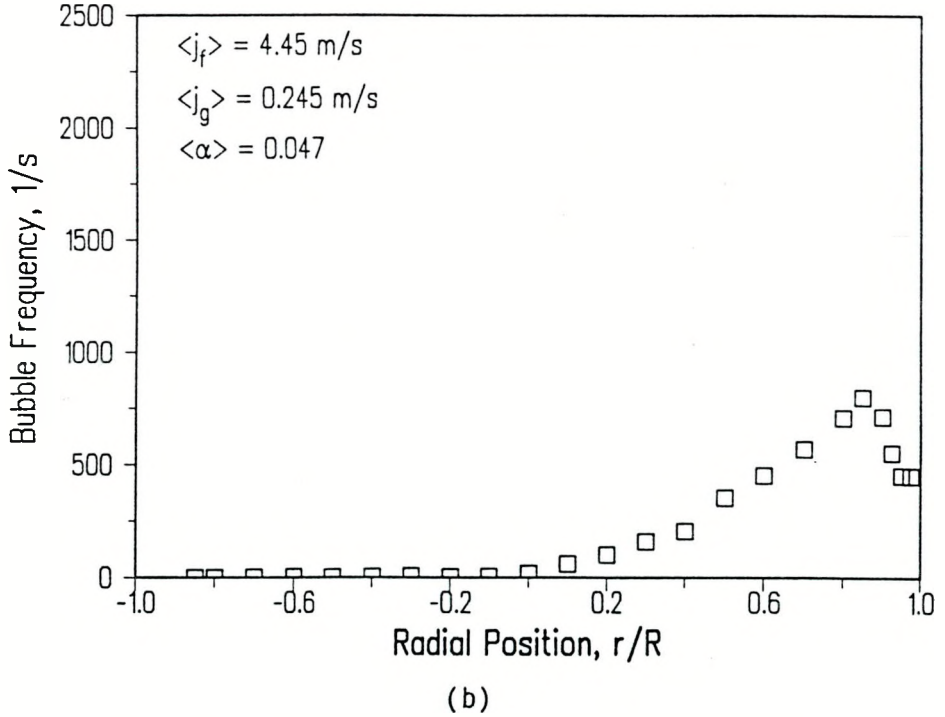

(b)

Figure 5.10 a) Local Void Fraction, b) Bubble Frequency, c) Interfacial Area Concentration, and d) Bubble Velocity Distribution at $\langle j_f \rangle$ = 4.45 m/s, $\langle j_g \rangle$ = 0.25 m/s, $\langle \alpha \rangle$ = 0.047.

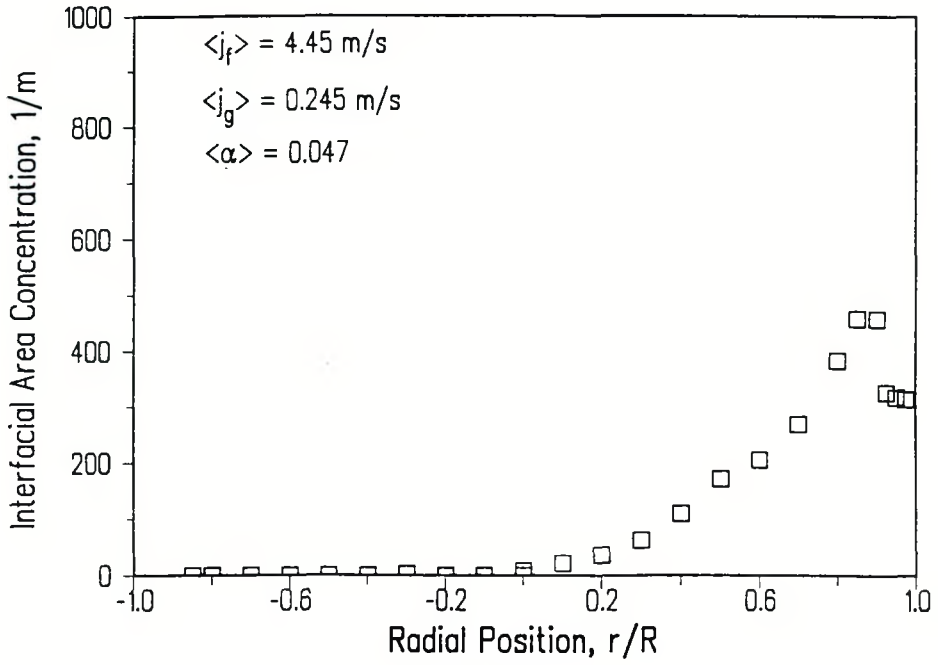

(c)

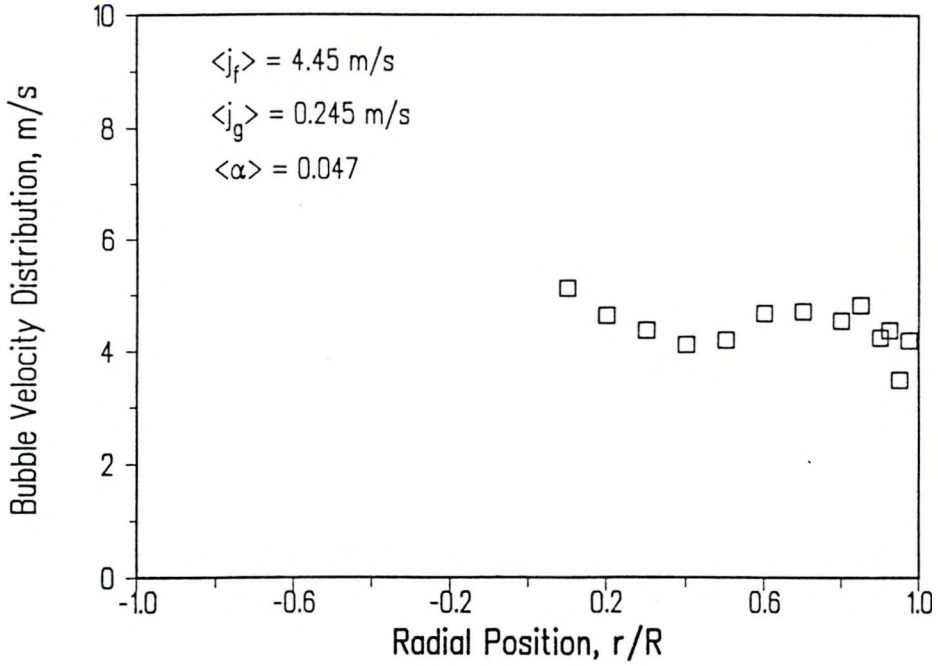

(d)

Figure 5.10 a) Local Void Fraction, b) Bubble Frequency, c) Interfacial Area Concentration, and d) Bubble Velocity Distribution at $\langle j_f \rangle$ = 4.45 m/s, $\langle j_g \rangle$ = 0.25 m/s, $\langle \alpha \rangle$ = 0.047.

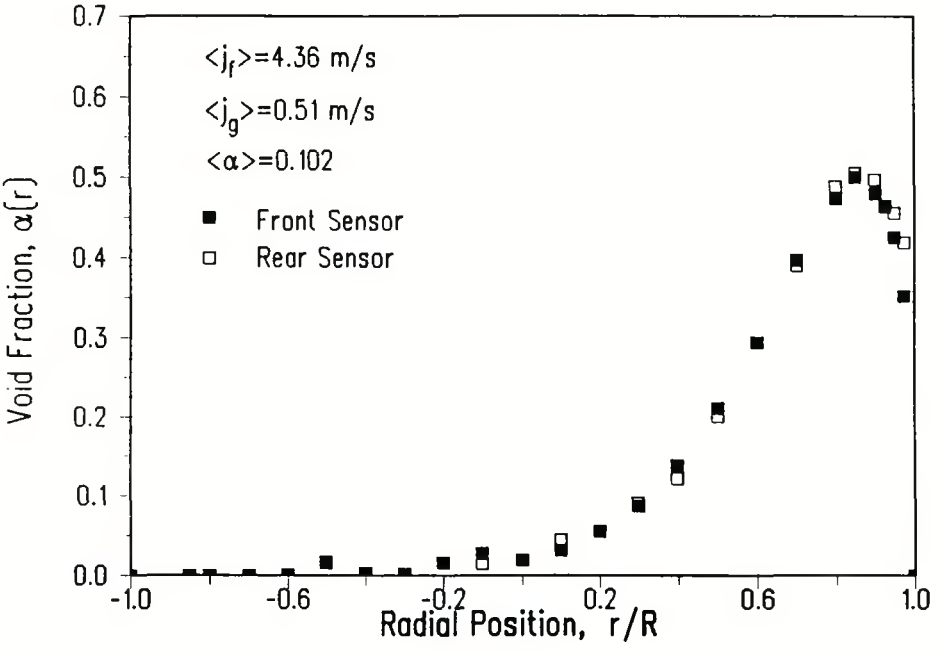

(a)

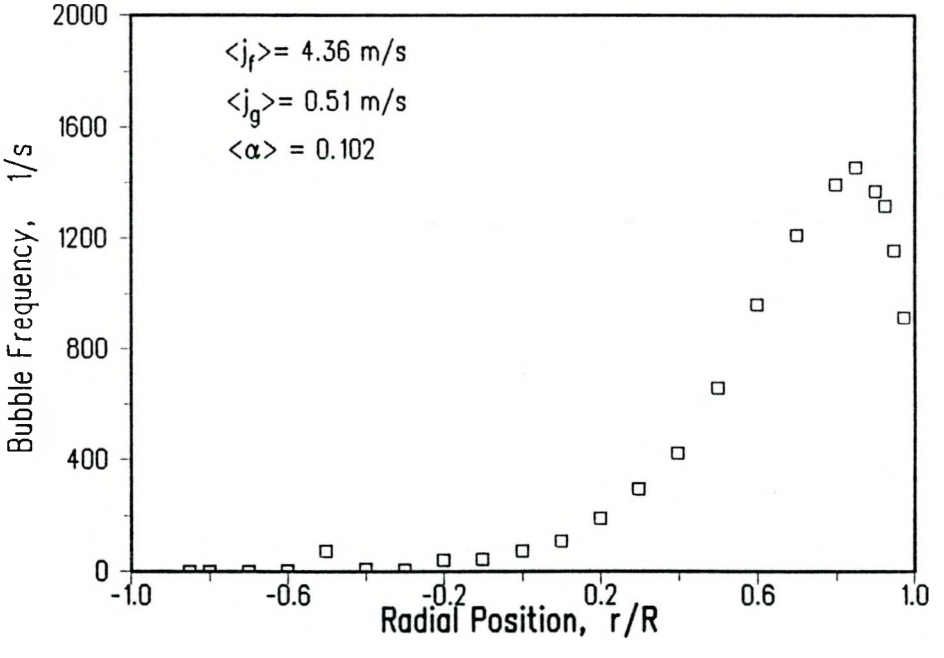

(b)

Figure 5.11 a) Local Void Fraction, b) Bubble Frequency, c) Interfacial Area Concentration, and d) Bubble Velocity Distribution at $\langle j_f \rangle$ = 4.36 m/s, $\langle j_g \rangle$ = 0.51 m/s, $\langle \alpha \rangle$ = 0.102.

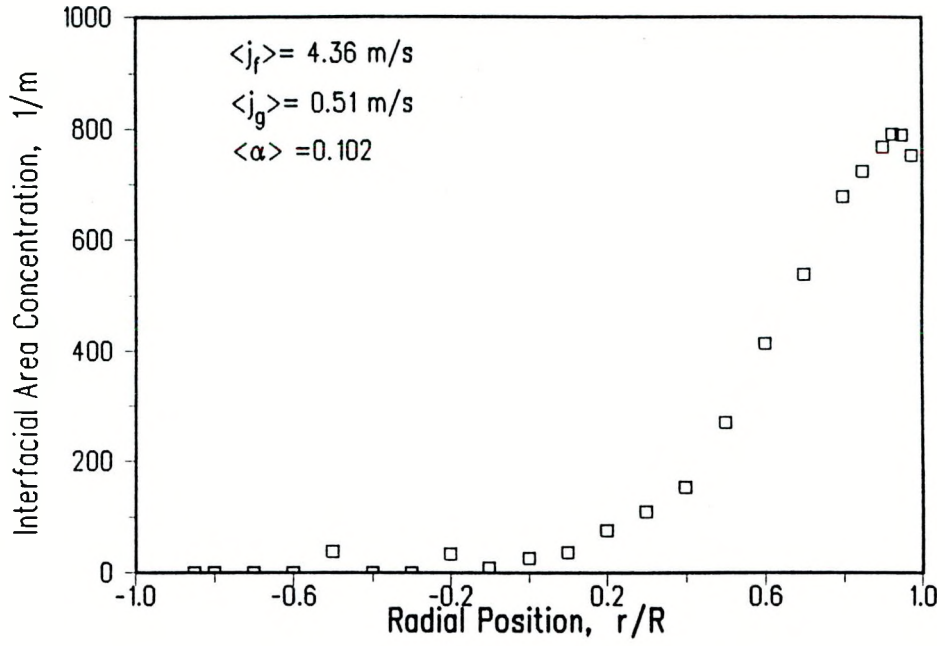

(c)

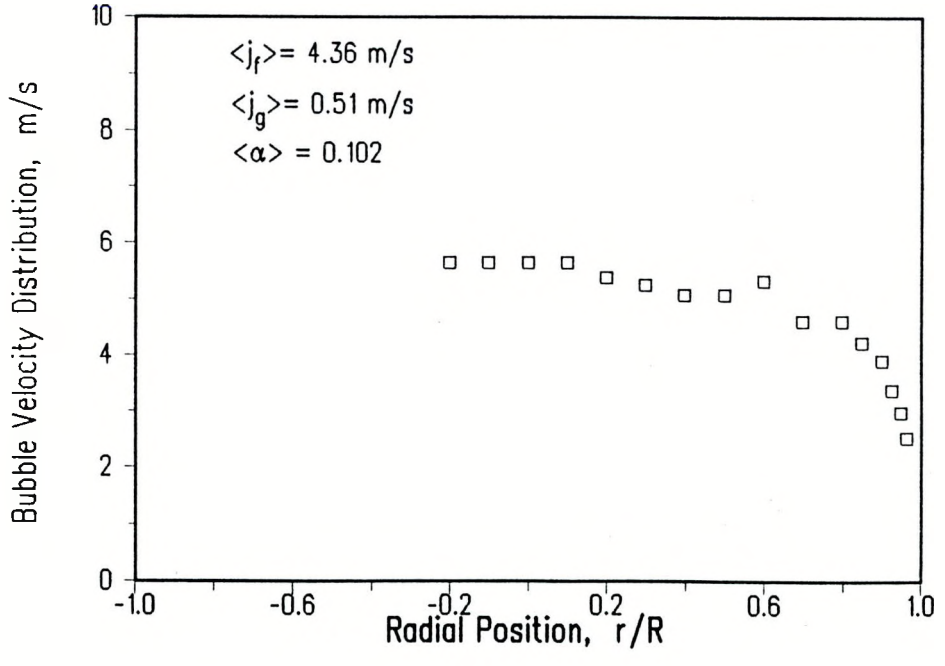

(d)

Figure 5.11 a) Local Void Fraction, b) Bubble Frequency, c) Interfacial Area Concentration, and d) Bubble Velocity Distribution at $\langle j_f \rangle$ = 4.36 m/s, $\langle j_g \rangle$ = 0.51 m/s, $\langle \alpha \rangle$ = 0.102.

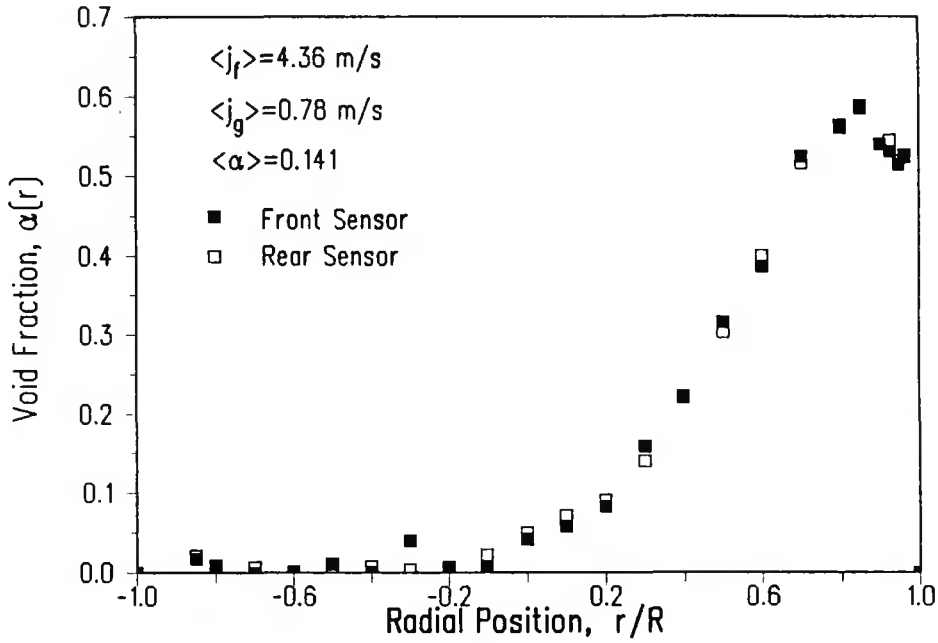

(a)

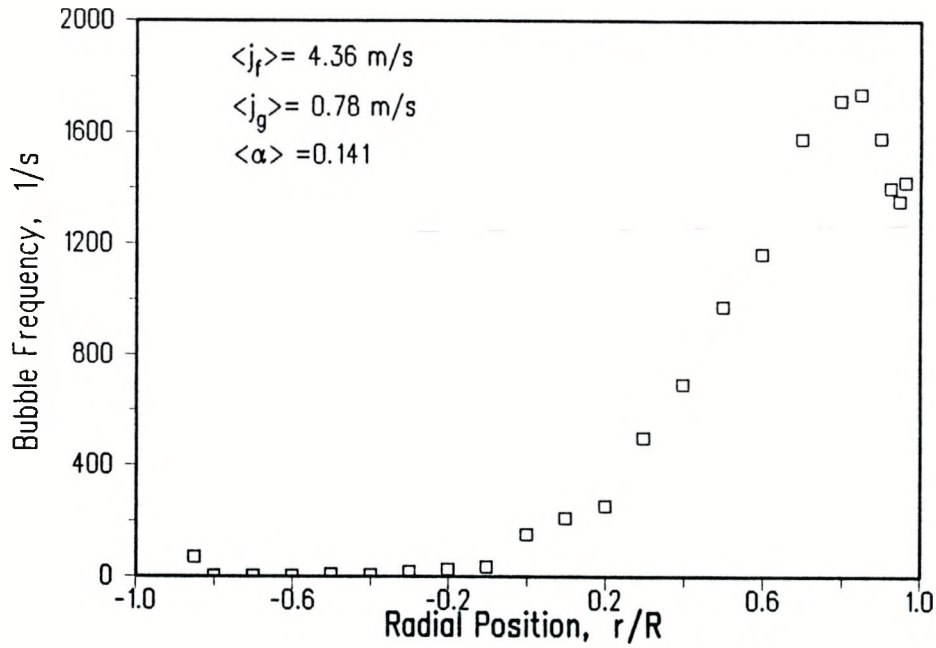

(b)

Figure 5.12 a) Local Void Fraction, b) Bubble Frequency, c) Interfacial Area Concentration, and d) Bubble Velocity Distribution at $\langle j_f \rangle$ = 4.36 m/s, $\langle j_g \rangle$ = 0.78 m/s, $\langle \alpha \rangle$ = 0.141.

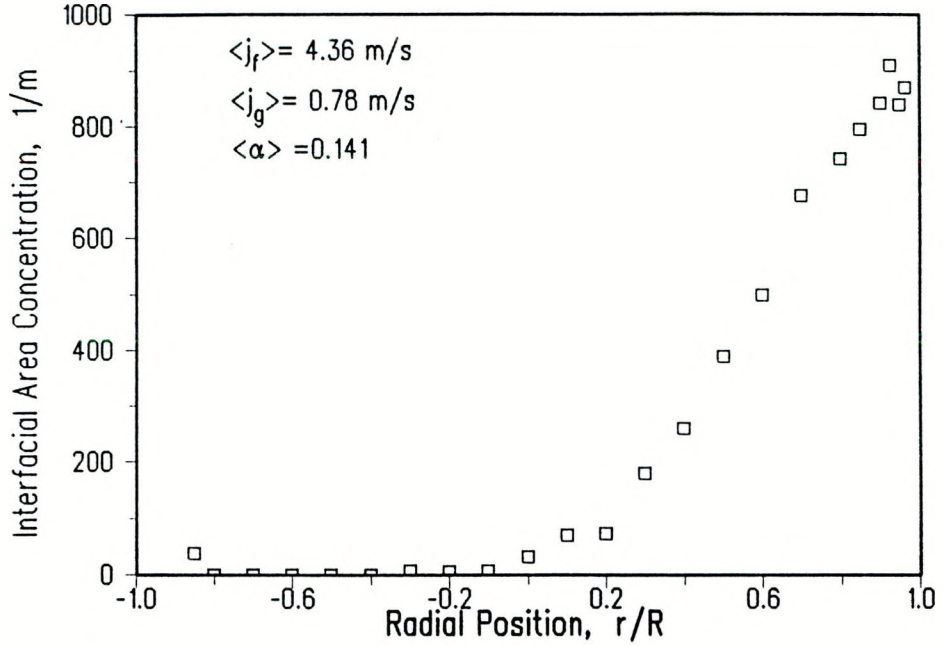

(c)

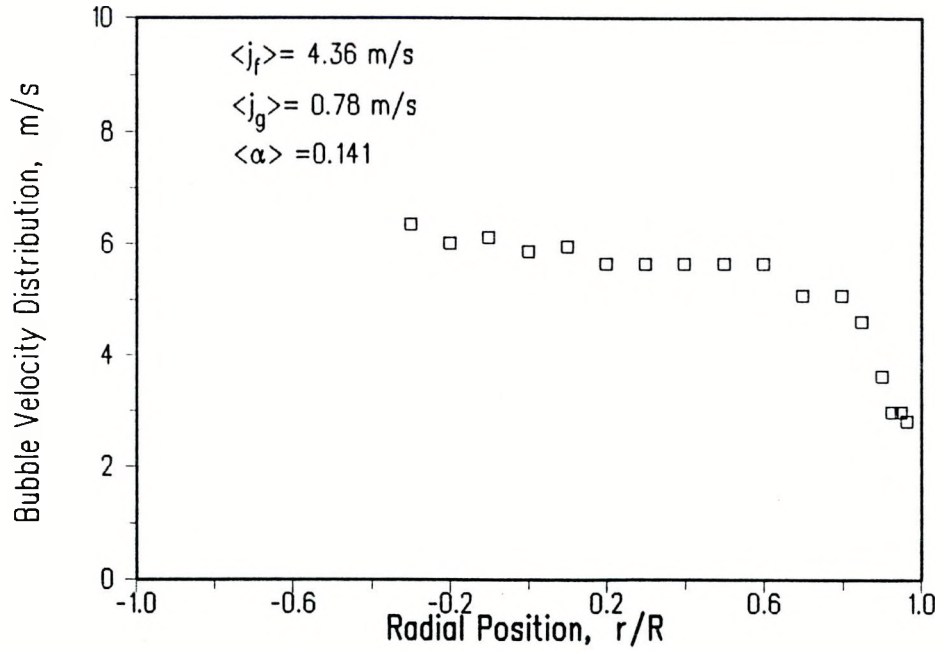

(d)

Figure 5.12 a) Local Void Fraction, b) Bubble Frequency, c) Interfacial Area Concentration, and d) Bubble Velocity Distribution at $\langle j_f \rangle$ = 4.36 m/s, $\langle j_g \rangle$ = 0.78 m/s, $\langle \alpha \rangle$ = 0.141.

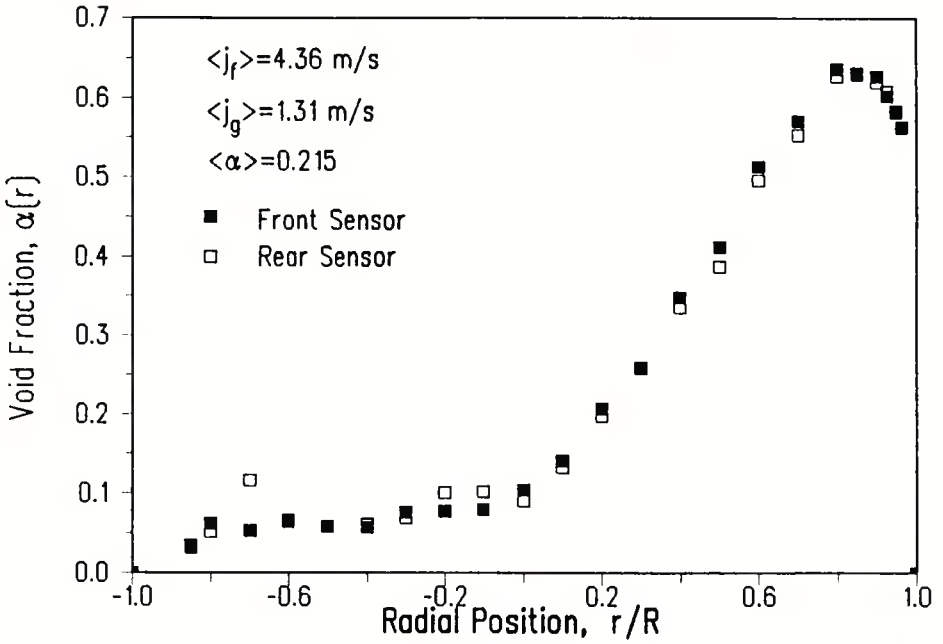

(a)

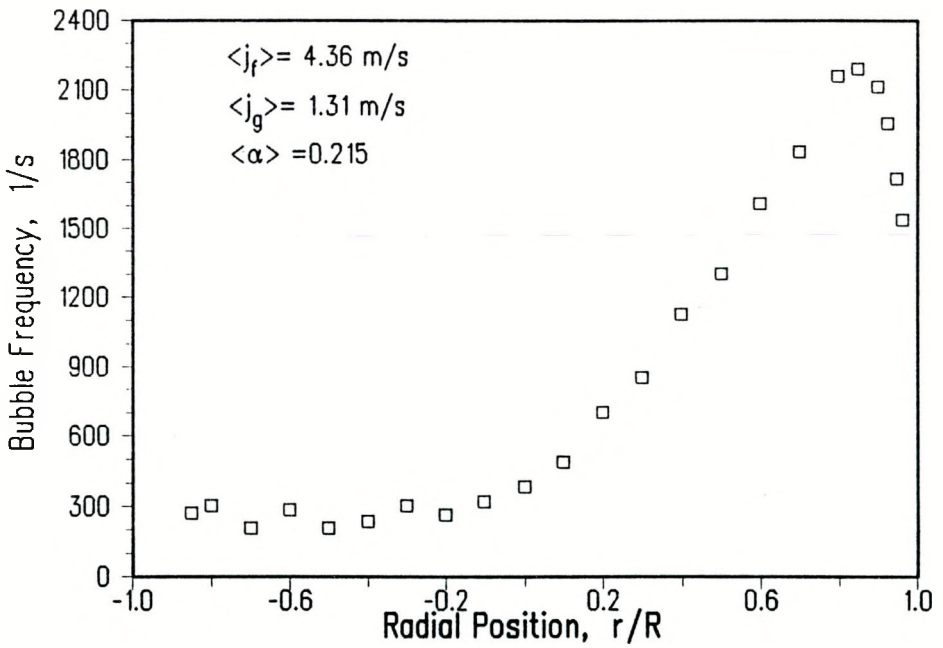

(b)

Figure 5.13 a) Local Void Fraction, b) Bubble Frequency, c) Interfacial Area Concentration, and d) Bubble Velocity Distribution at $\langle j_f \rangle$ = 4.36 m/s, $\langle j_g \rangle$ = 1.31 m/s, $\langle \alpha \rangle$ = 0.215.

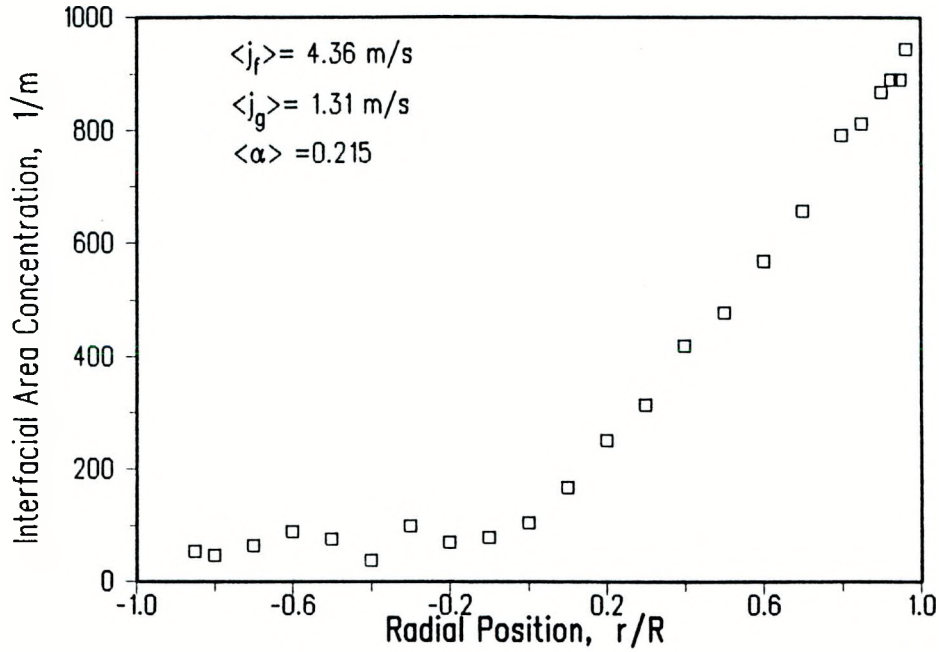

(c)

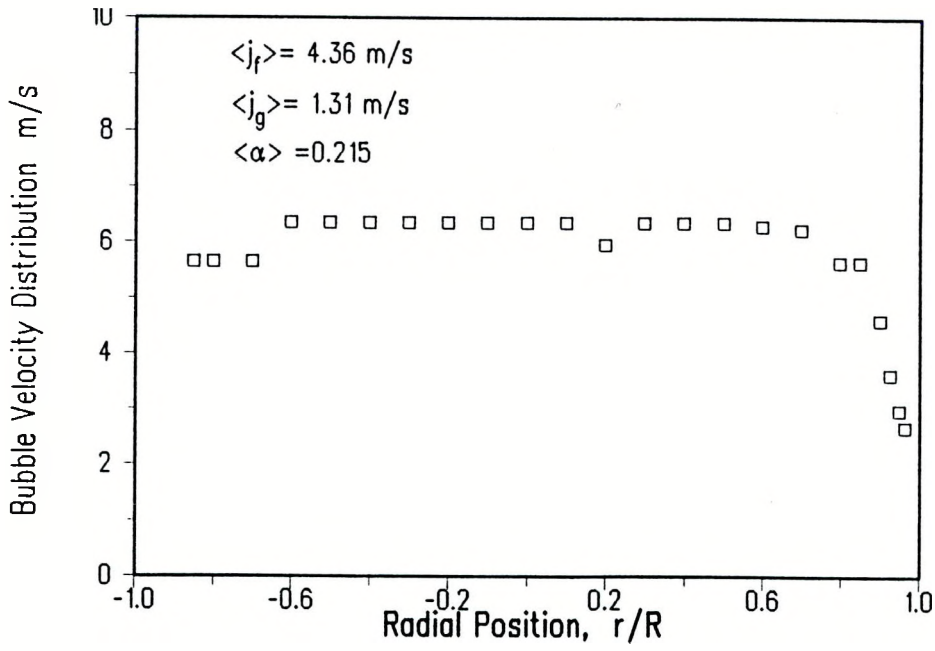

(d)

Figure 5.13 a) Local Void Fraction, b) Bubble Frequency, c) Interfacial Area Concentration, and d) Bubble Velocity Distribution at $\langle j_f \rangle$ = 4.36 m/s, $\langle j_g \rangle$ = 1.31 m/s, $\langle \alpha \rangle$ = 0.215.

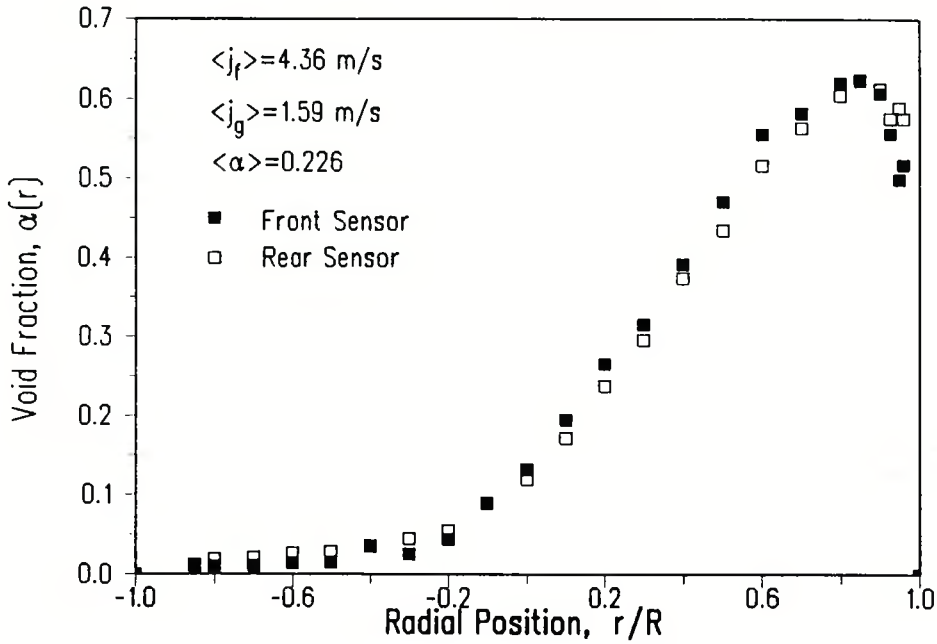

(a)

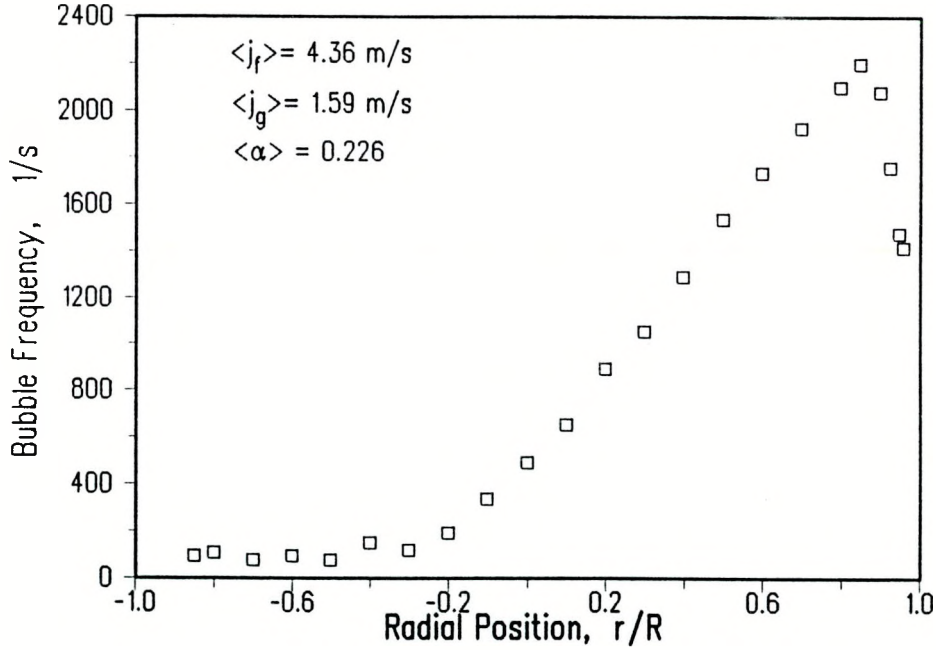

(b)

Figure 5.14 a) Local Void Fraction, b) Bubble Frequency, c) Interfacial Area Concentration, and d) Bubble Velocity Distribution at $\langle j_f \rangle$ = 4.36 m/s, $\langle j_g \rangle$ = 1.59 m/s, $\langle \alpha \rangle$ = 0.226.

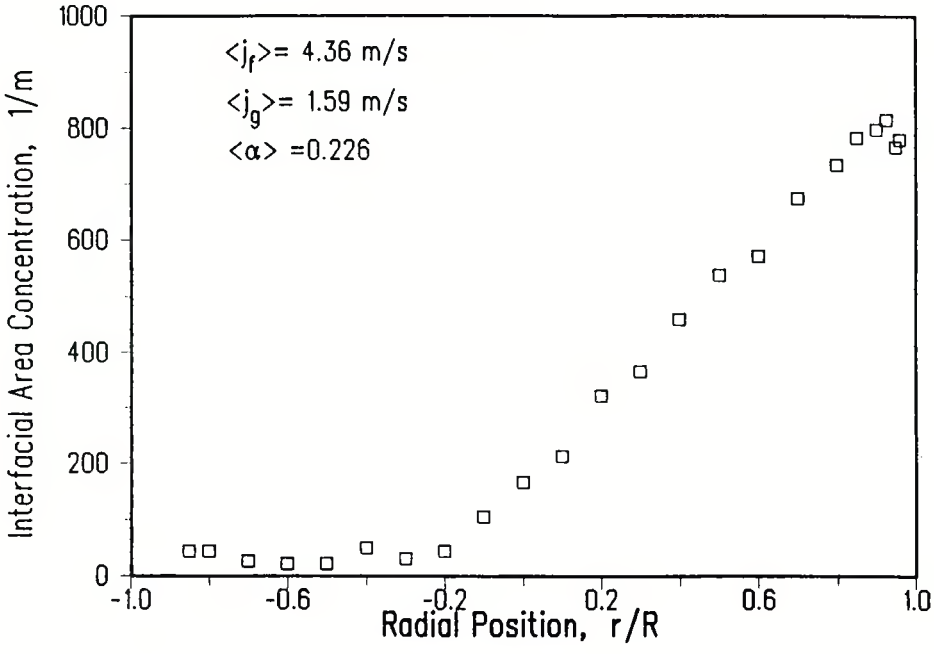

(c)

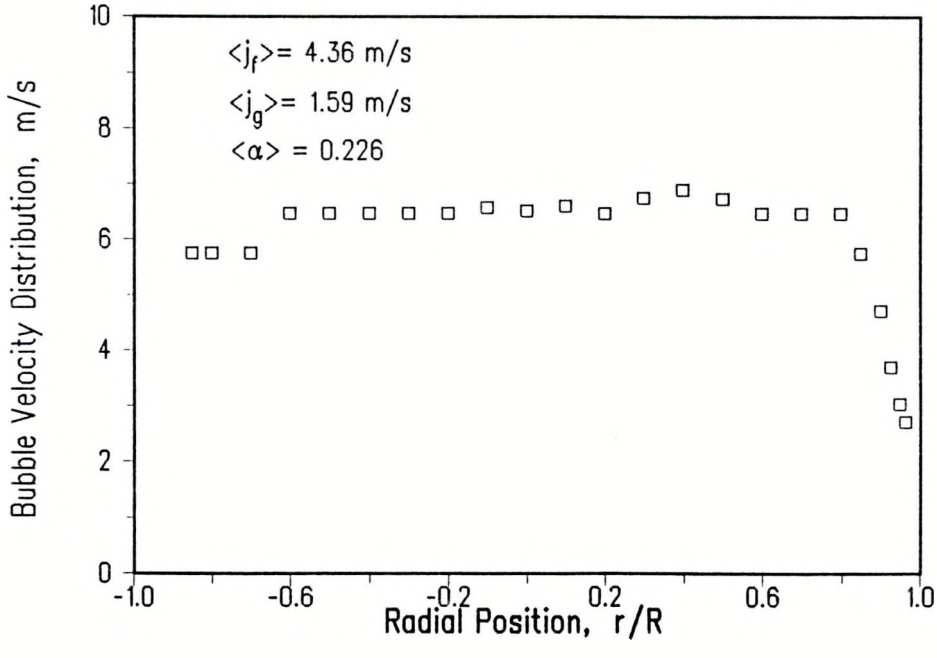

(d)

Figure 5.14 a) Local Void Fraction, b) Bubble Frequency, c) Interfacial Area Concentration, and d) Bubble Velocity Distribution at $\langle j_f \rangle$ = 4.36 m/s, $\langle j_g \rangle$ = 1.59 m/s, $\langle \alpha \rangle$ = 0.226.

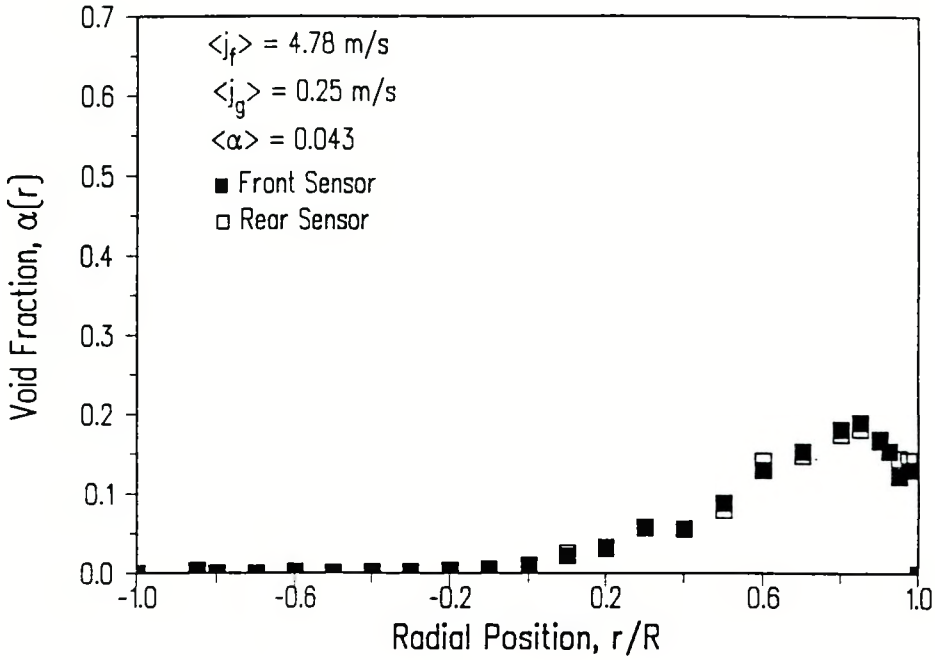

(a)

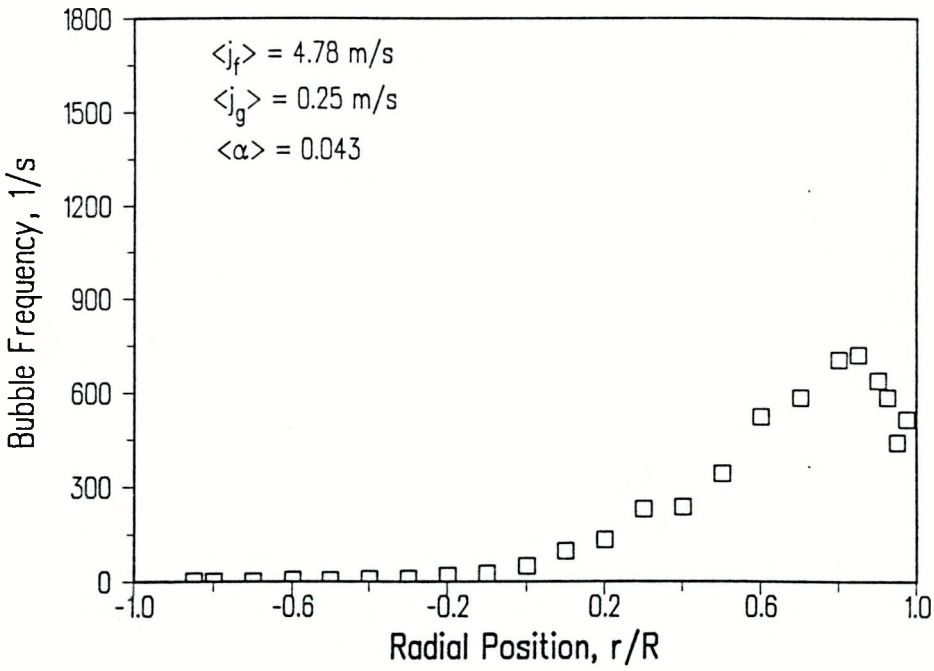

(b)

Figure 5.15 a) Local Void Fraction, b) Bubble Frequency, c) Interfacial Area Concentration, and d) Bubble Velocity Distribution at $\langle j_f \rangle$ = 4.78 m/s, $\langle j_g \rangle$ = 0.25 m/s, $\langle \alpha \rangle$ = 0.043.

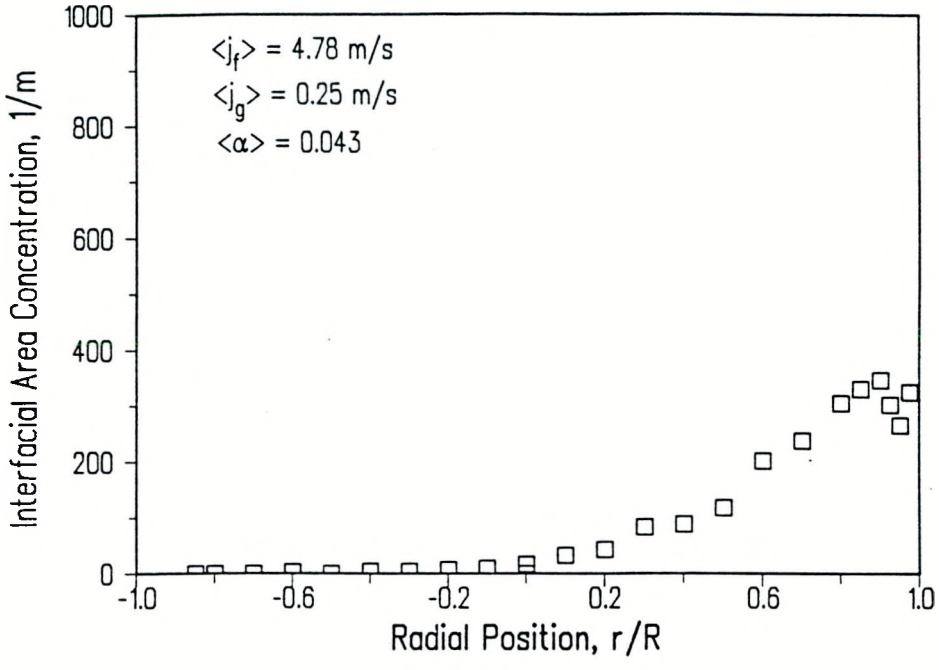

(c)

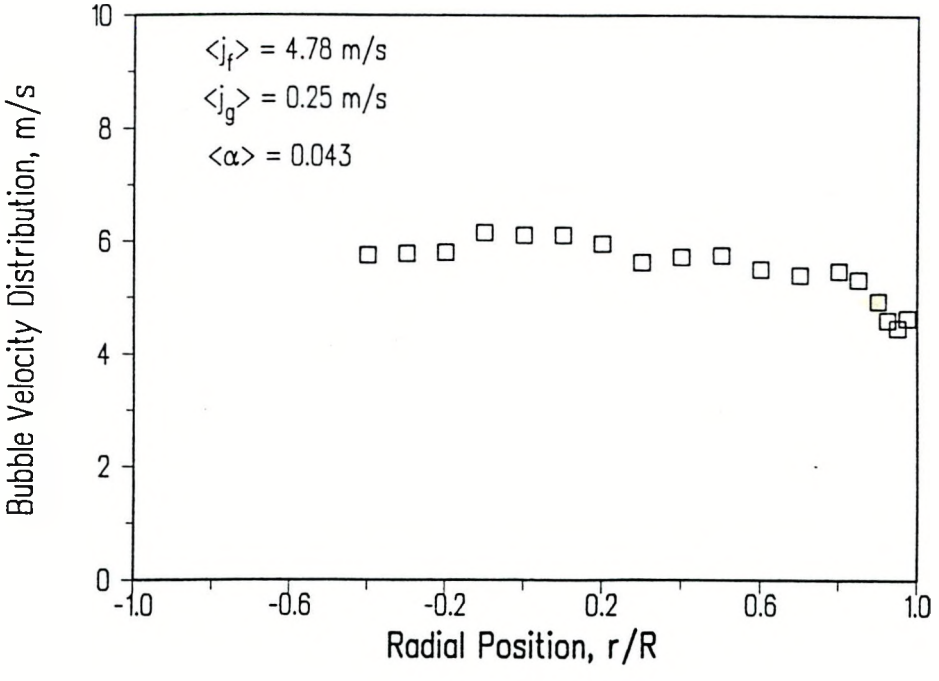

(d)

Figure 5.15 a) Local Void Fraction, b) Bubble Frequency, c) Interfacial Area Concentration, and d) Bubble Velocity Distribution at $\langle j_f \rangle$ = 4.78 m/s, $\langle j_g \rangle$ = 0.25 m/s, $\langle \alpha \rangle$ = 0.043.

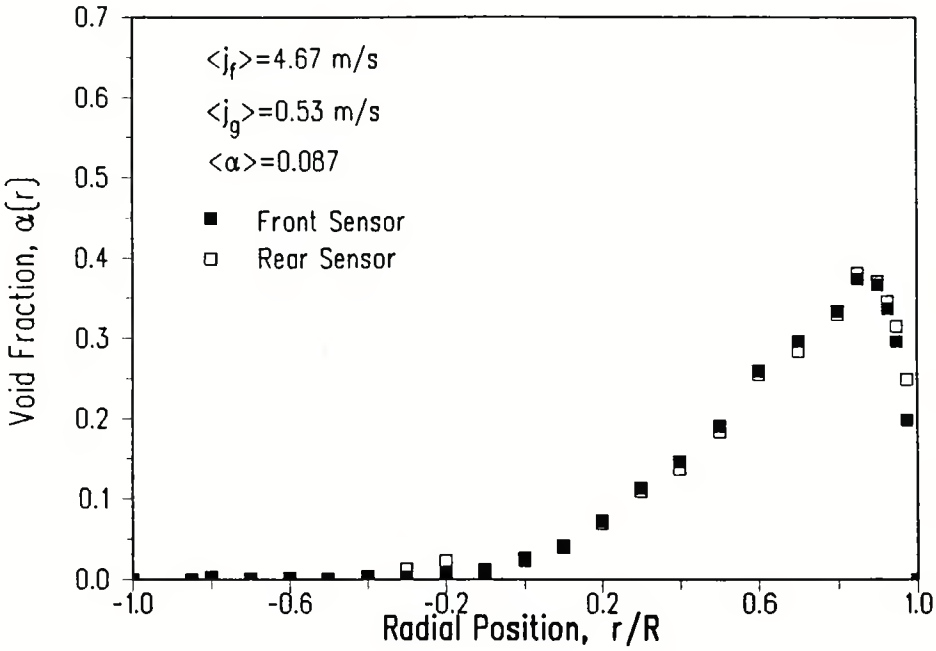

(a)

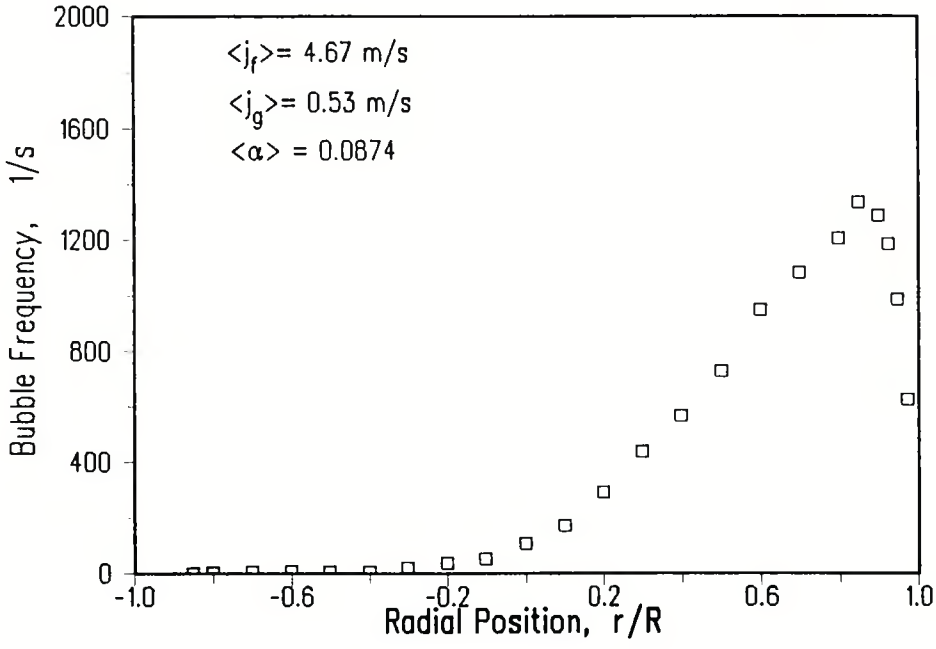

(b)

Figure 5.16 a) Local Void Fraction, b) Bubble Frequency, c) Interfacial Area Concentration, and d) Bubble Velocity Distribution at $\langle j_f \rangle$ = 4.67 m/s, $\langle j_g \rangle$ = 0.53 m/s, $\langle \alpha \rangle$ = 0.087.

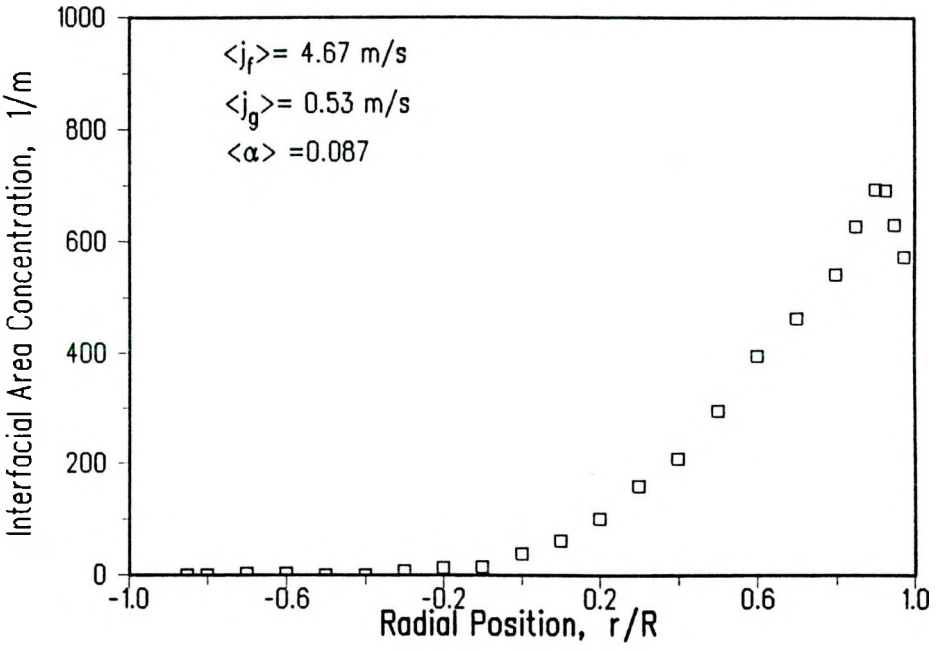

(c)

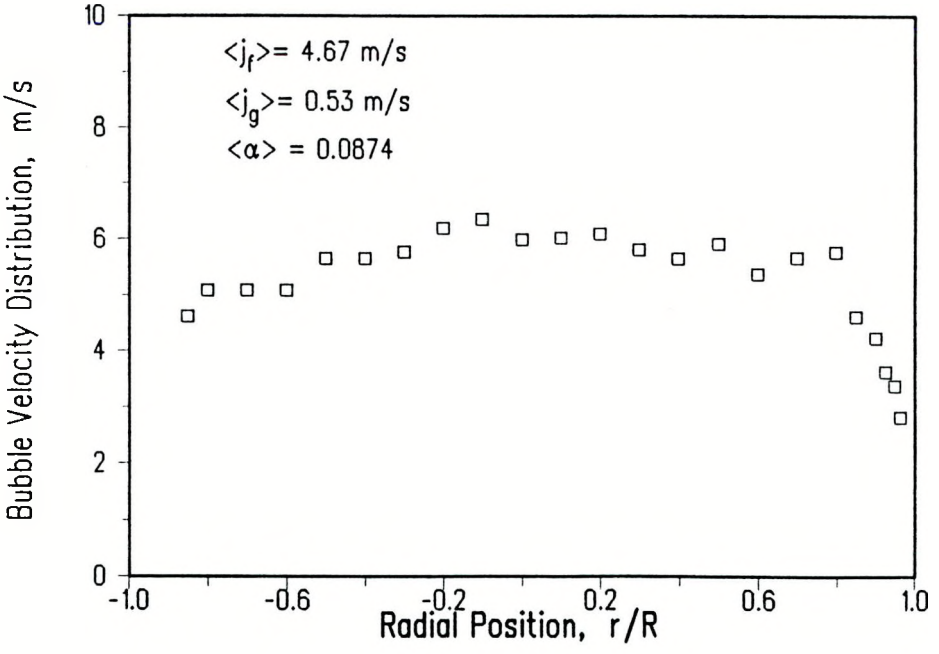

(d)

Figure 5.16 a) Local Void Fraction, b) Bubble Frequency, c) Interfacial Area Concentration, and d) Bubble Velocity Distribution at $\langle j_f \rangle$ = 4.67 m/s, $\langle j_g \rangle$ = 0.53 m/s, $\langle \alpha \rangle$ = 0.087.

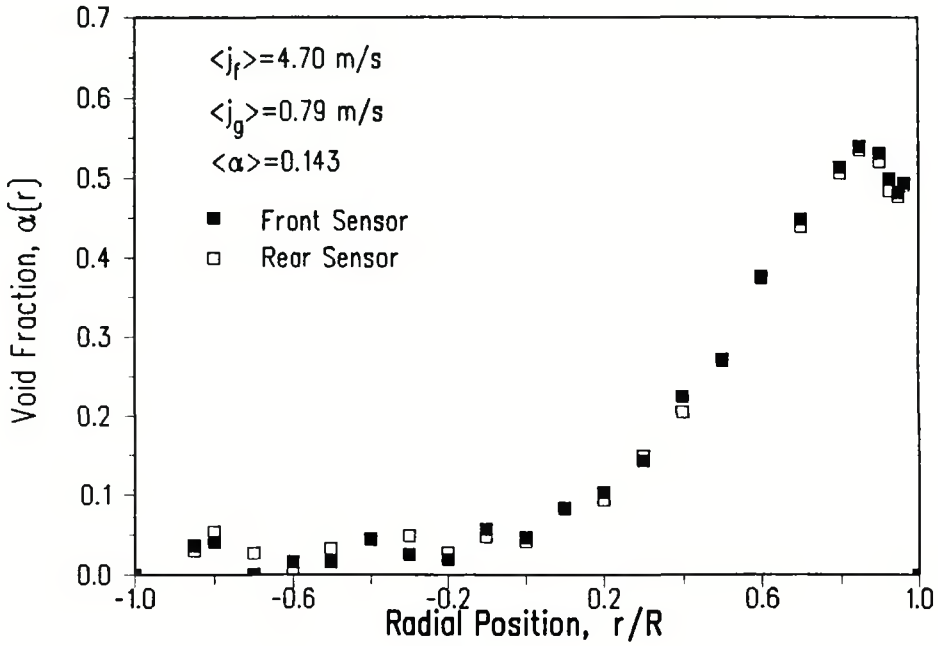

(a)

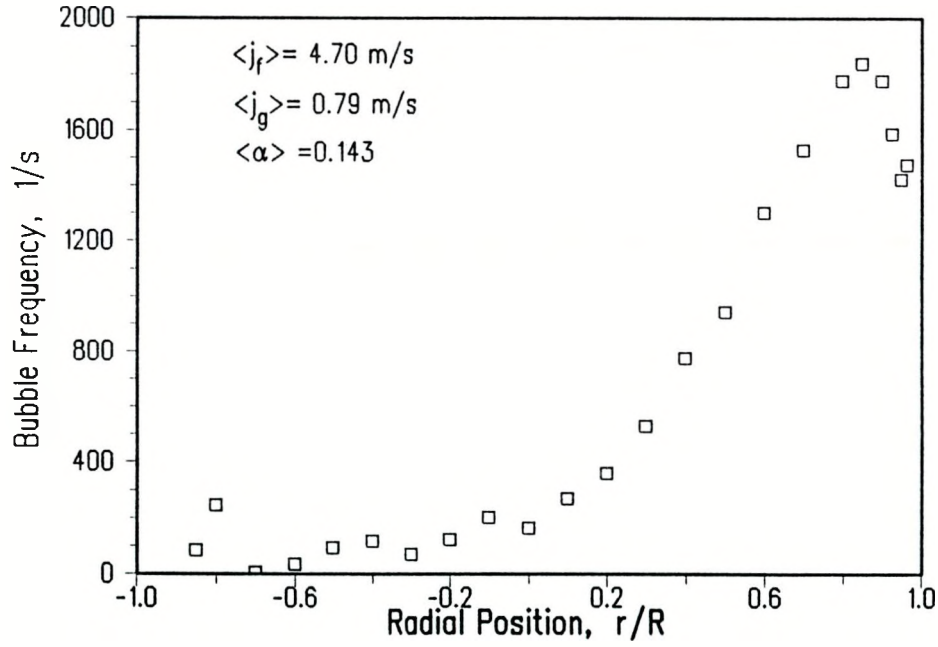

(b)

Figure 5.17 a) Local Void Fraction, b) Bubble Frequency, c) Interfacial Area Concentration, and d) Bubble Velocity Distribution at $\langle j_f \rangle$ = 4.70 m/s, $\langle j_g \rangle$ = 0.79 m/s, $\langle \alpha \rangle$ = 0.143.

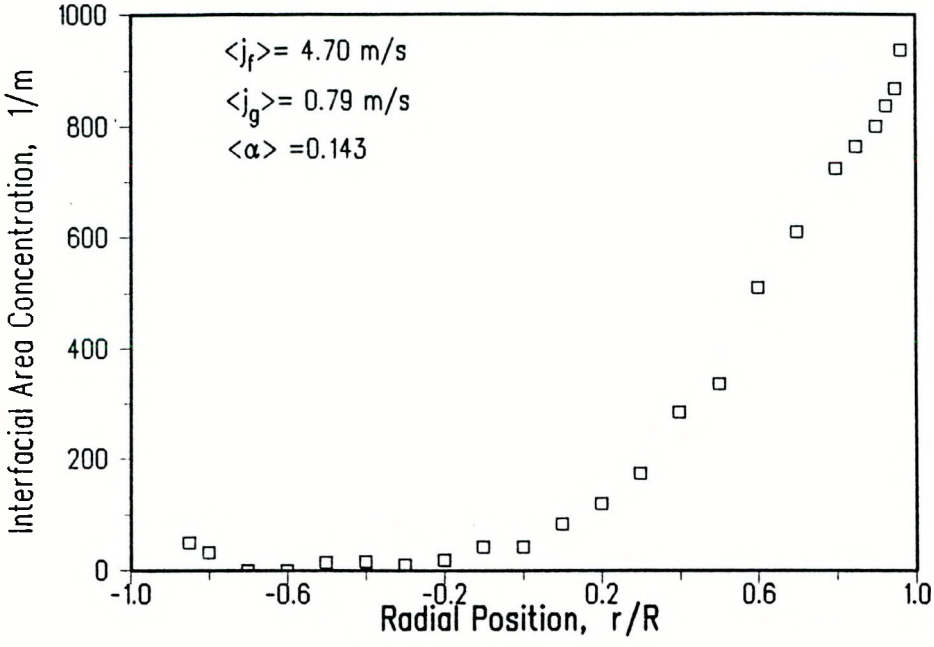

(c)

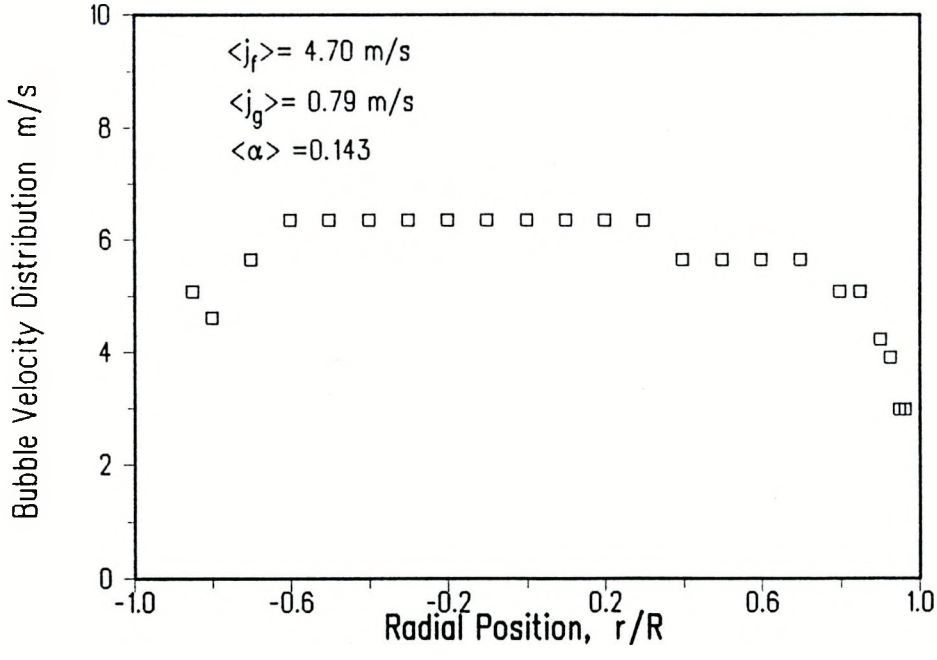

(d)

Figure 5.17 a) Local Void Fraction, b) Bubble Frequency, c) Interfacial Area Concentration, and d) Bubble Velocity Distribution at $\langle j_f \rangle$ = 4.70 m/s, $\langle j_g \rangle$ = 0.79 m/s, $\langle \alpha \rangle$ = 0.143.

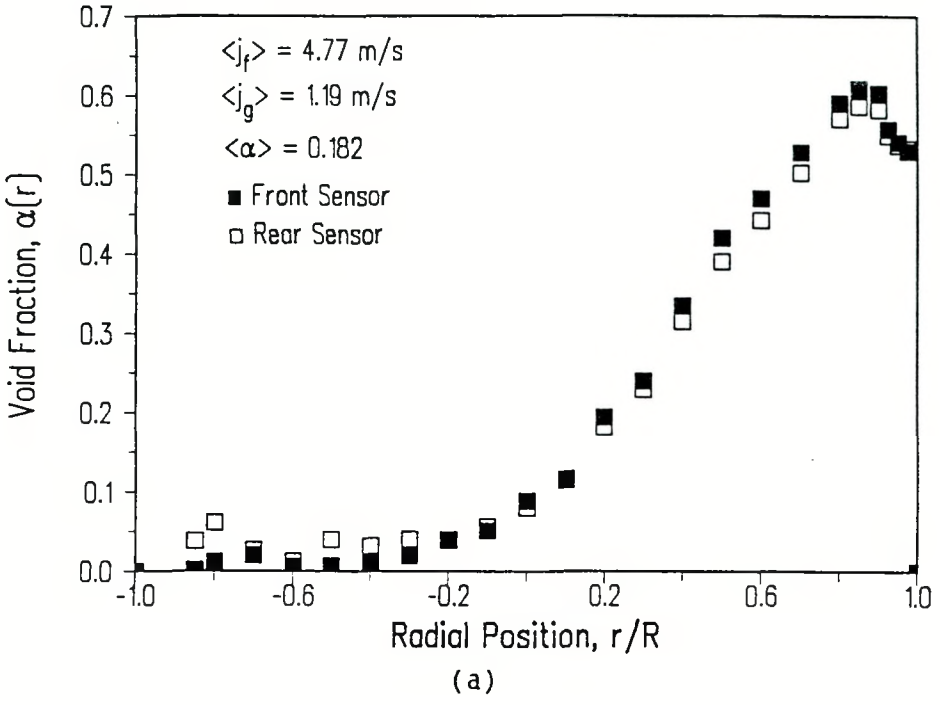

(a)

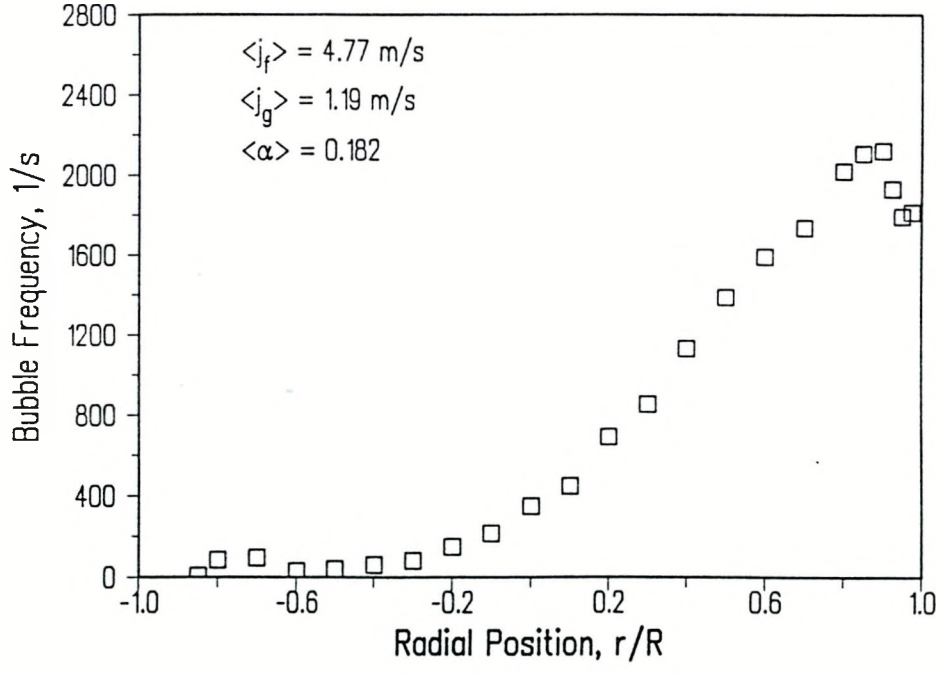

(b)

Figure 5.18 a) Local Void Fraction, b) Bubble Frequency, c) Interfacial Area Concentration, and d) Bubble Velocity Distribution at $\langle j_f \rangle$ = 4.77 m/s, $\langle j_g \rangle$ = 1.19 m/s, $\langle \alpha \rangle$ = 0.182.

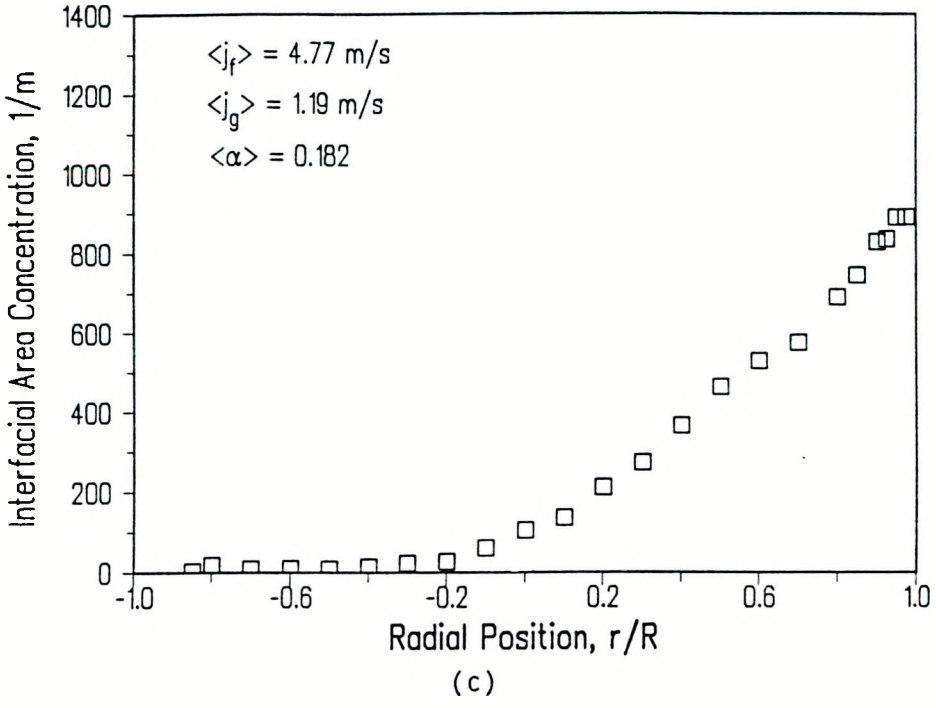

(c)

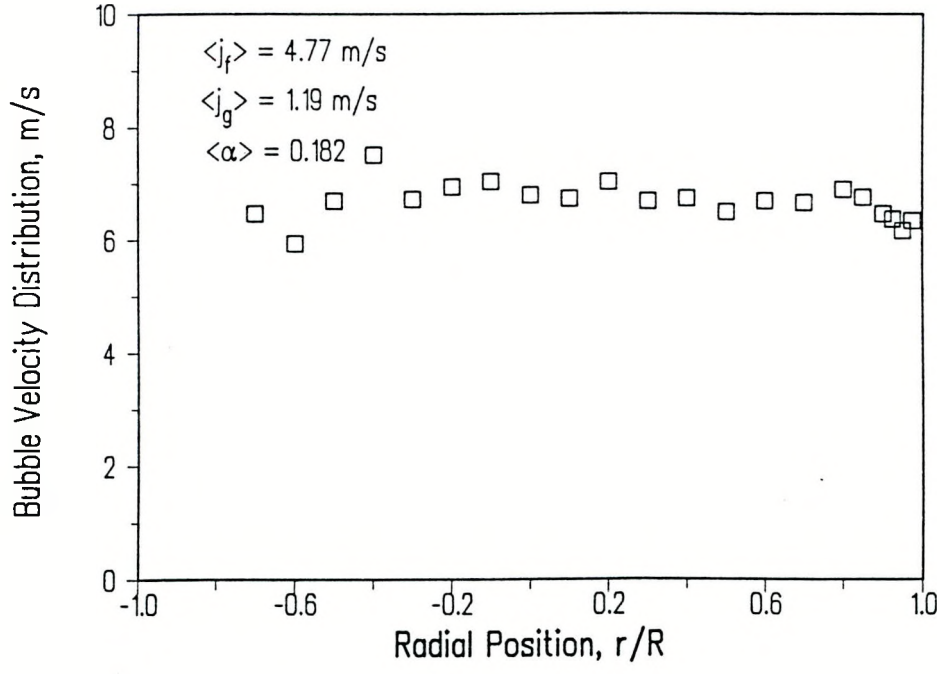

(d)

Figure 5.18 a) Local Void Fraction, b) Bubble Frequency, c) Interfacial Area Concentration, and d) Bubble Velocity Distribution at $\langle j_f \rangle$ = 4.77 m/s, $\langle j_g \rangle$ = 1.19 m/s, $\langle \alpha \rangle$ = 0.182.

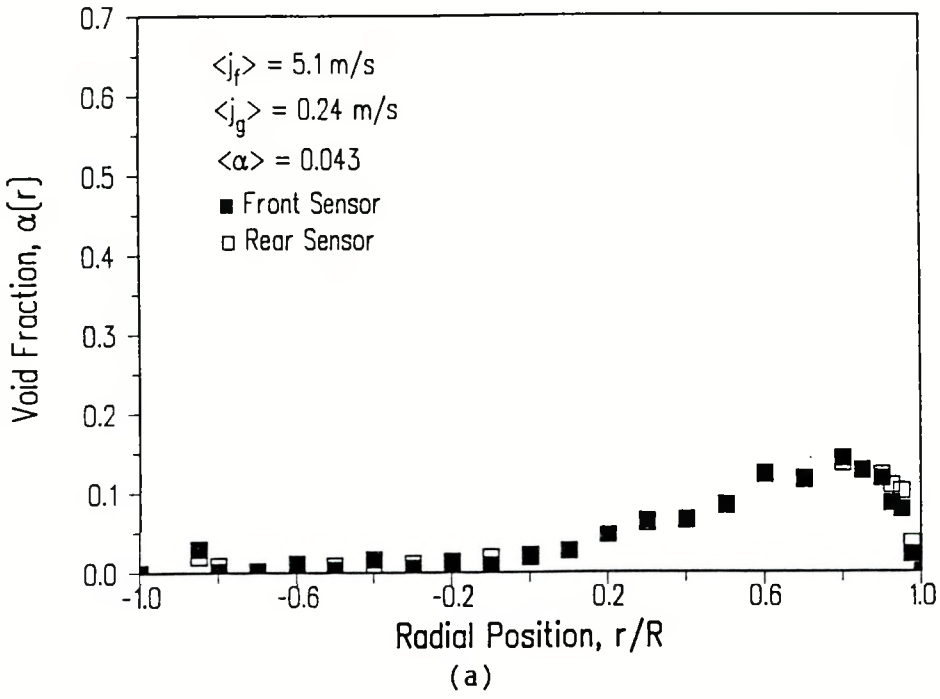

(a)

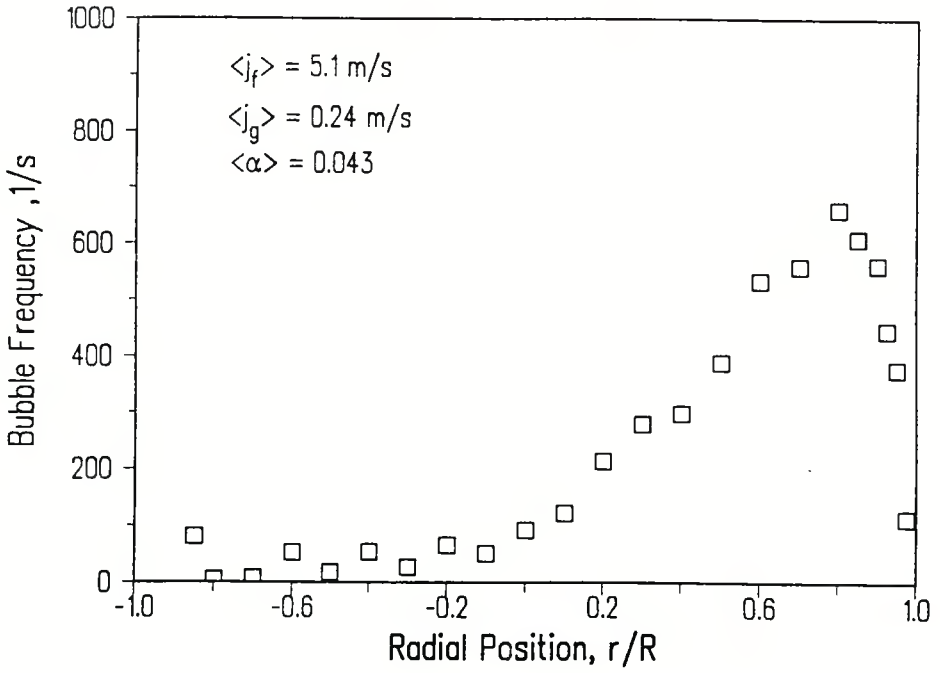

(b)

Figure 5.19 a) Local Void Fraction, b) Bubble Frequency, c) Interfacial Area Concentration, and d) Bubble Velocity Distribution at $\langle j_f \rangle$ = 5.10 m/s, $\langle j_g \rangle$ = 0.24 m/s, $\langle \alpha \rangle$ = 0.043.

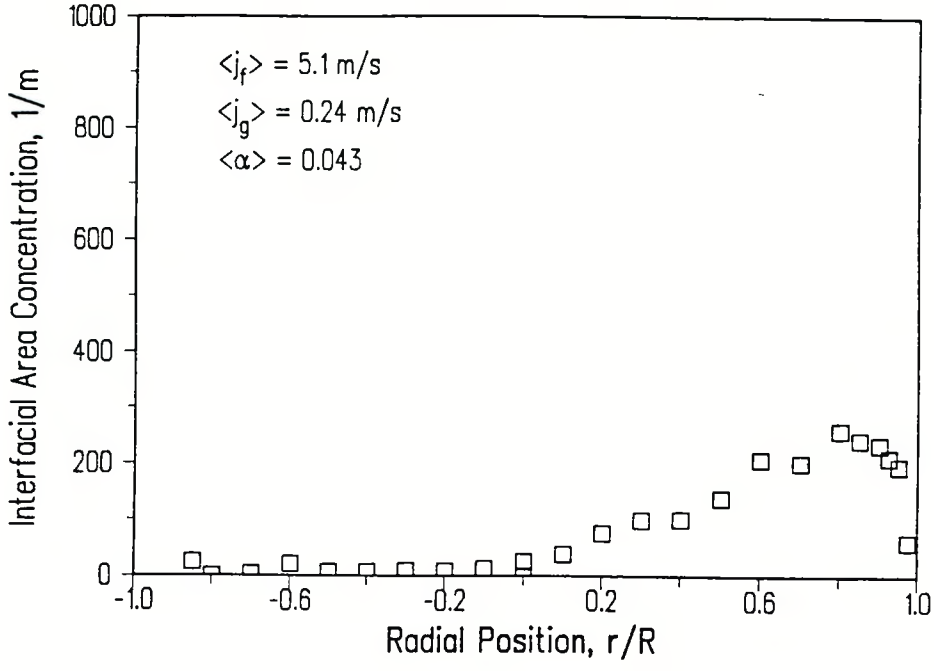

(c)

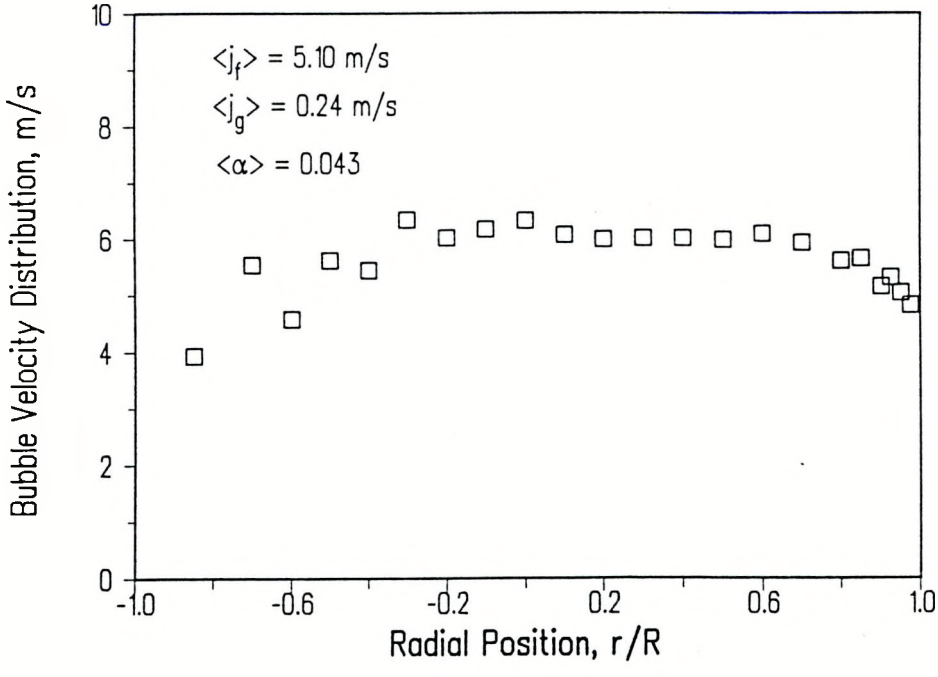

(d)

Figure 5.19 a) Local Void Fraction, b) Bubble Frequency, c) Interfacial Area Concentration, and d) Bubble Velocity Distribution at $\langle j_f \rangle$ = 5.10 m/s, $\langle j_g \rangle$ = 0.24 m/s, $\langle \alpha \rangle$ = 0.043.

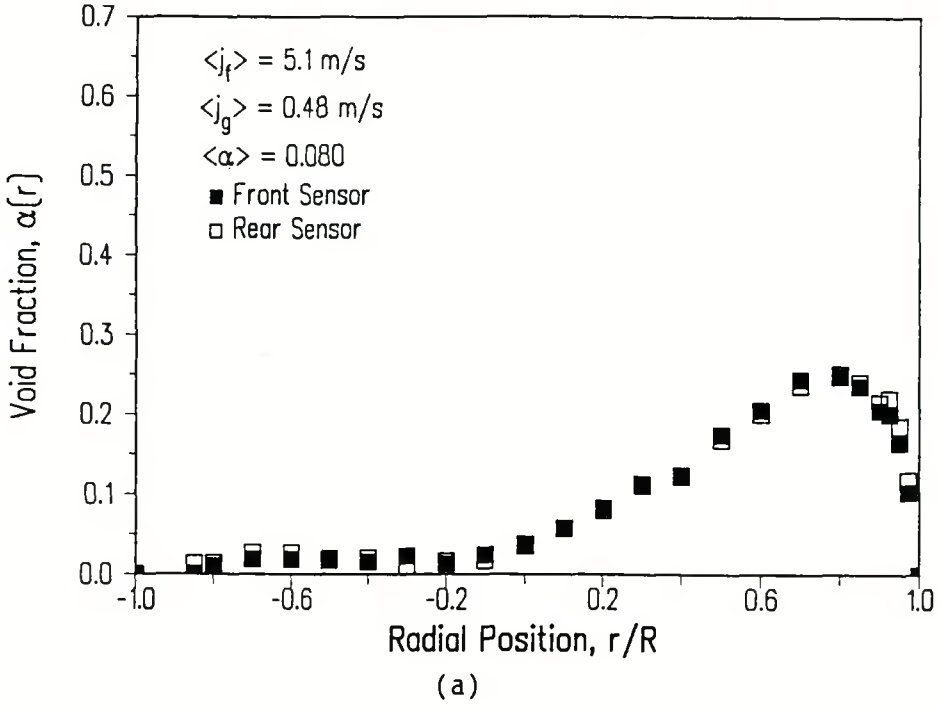

(a)

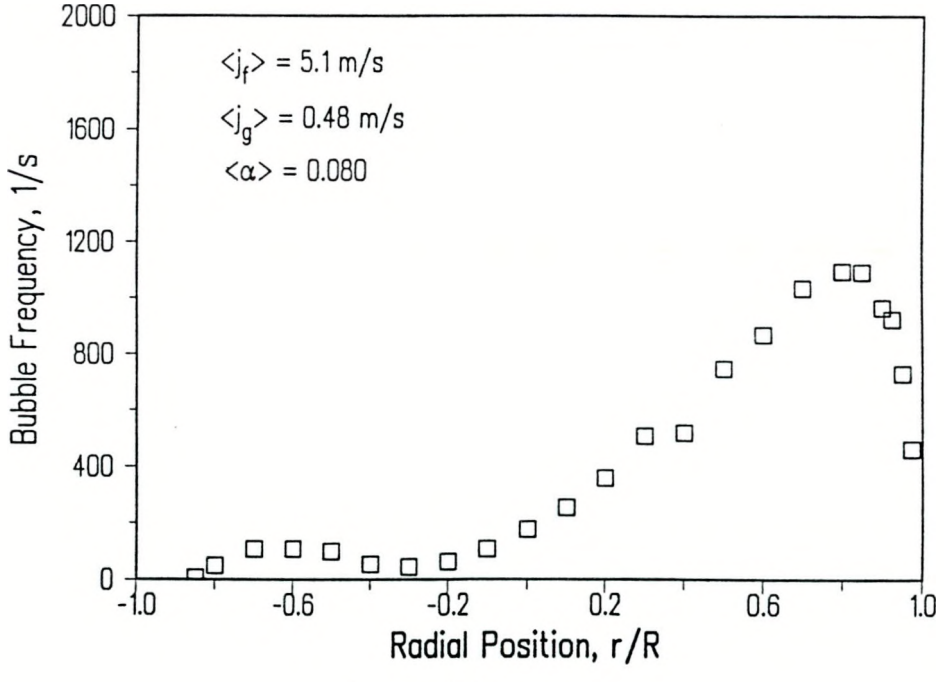

(b)

Figure 5.20 a) Local Void Fraction, b) Bubble Frequency, c) Interfacial Area Concentration, and d) Bubble Velocity Distribution at $\langle j_f \rangle$ = 5.10 m/s, $\langle j_g \rangle$ = 0.48 m/s, $\langle \alpha \rangle$ = 0.080.

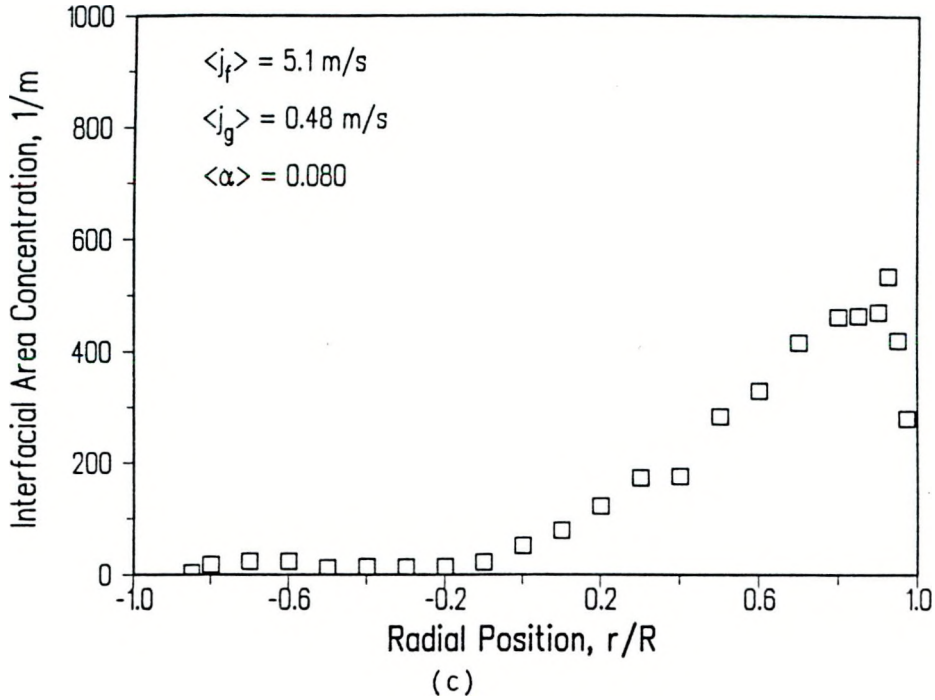

(c)

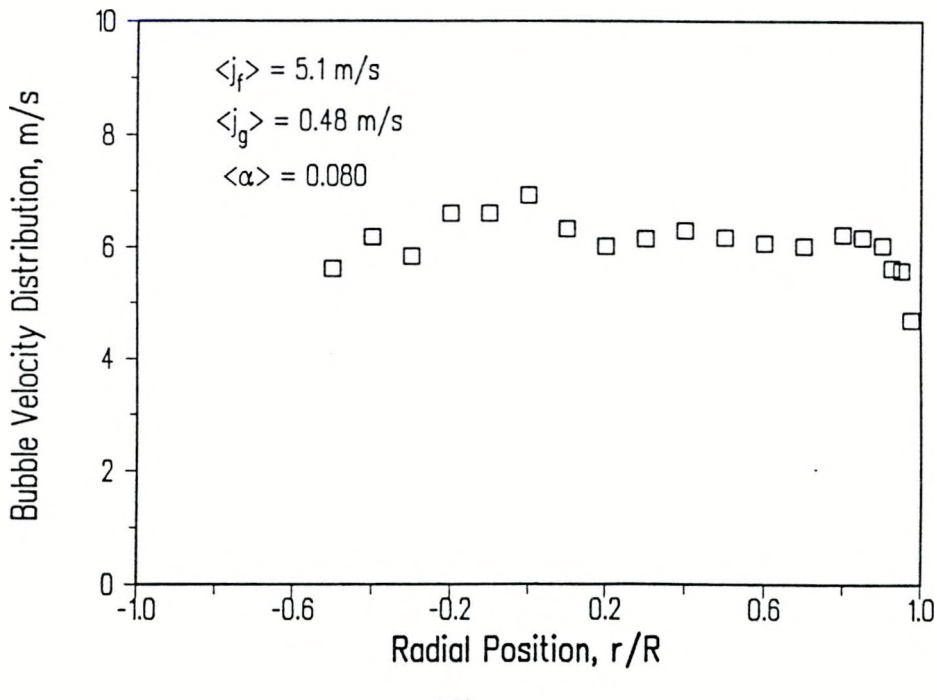

(d)

Figure 5.20 a) Local Void Fraction, b) Bubble Frequency, c) Interfacial Area Concentration, and d) Bubble Velocity Distribution at $\langle j_f \rangle$ = 5.10 m/s, $\langle j_g \rangle$ = 0.48 m/s, $\langle \alpha \rangle$ = 0.080.

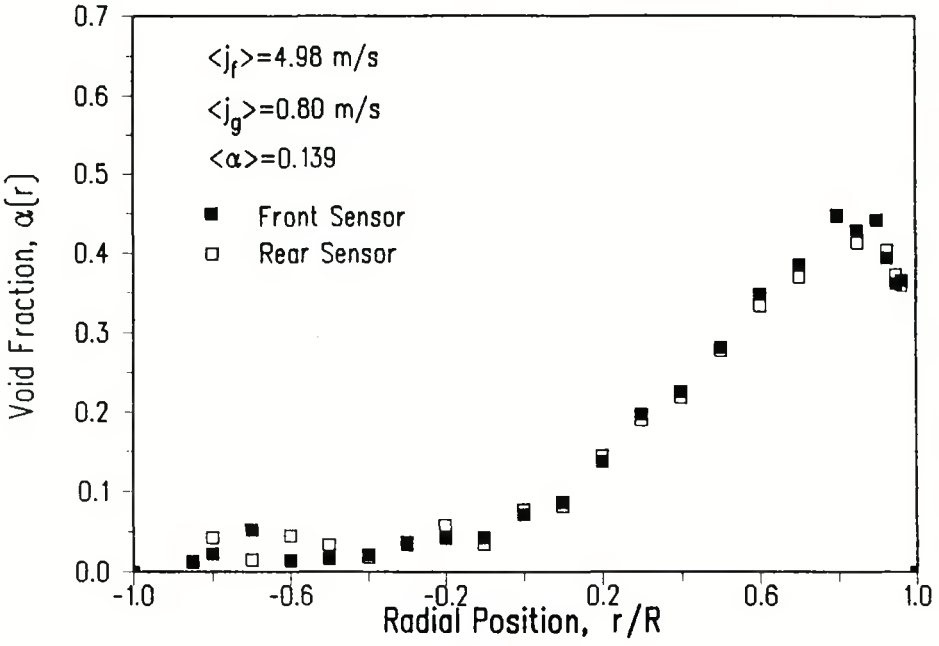

(a)

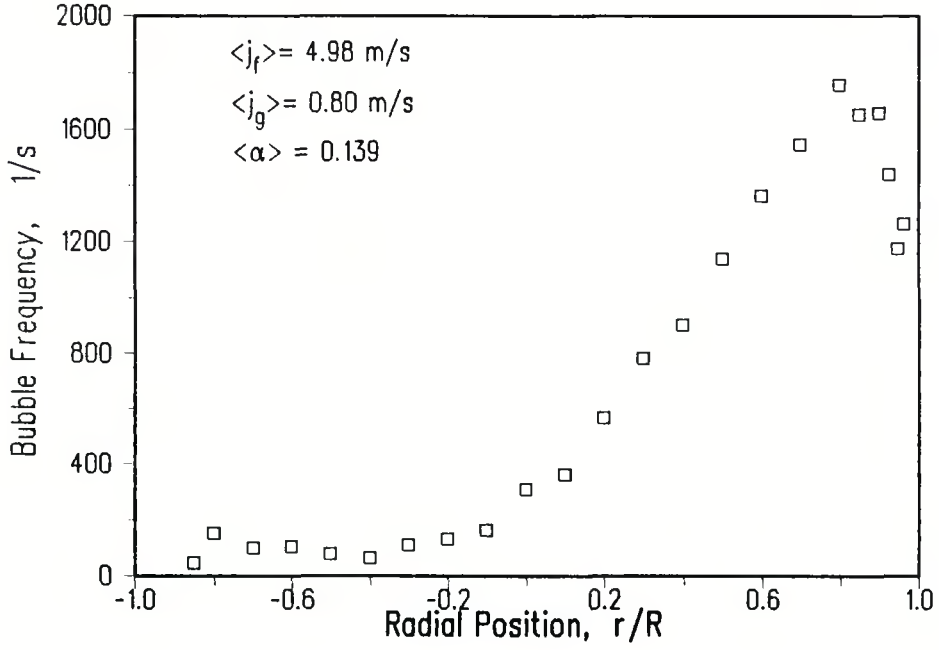

(b)

Figure 5.21 a) Local Void Fraction, b) Bubble Frequency, c) Interfacial Area Concentration, and d) Bubble Velocity Distribution at $\langle j_f \rangle$ = 4.98 m/s, $\langle j_g \rangle$ = 0.80 m/s, $\langle \alpha \rangle$ = 0.139.

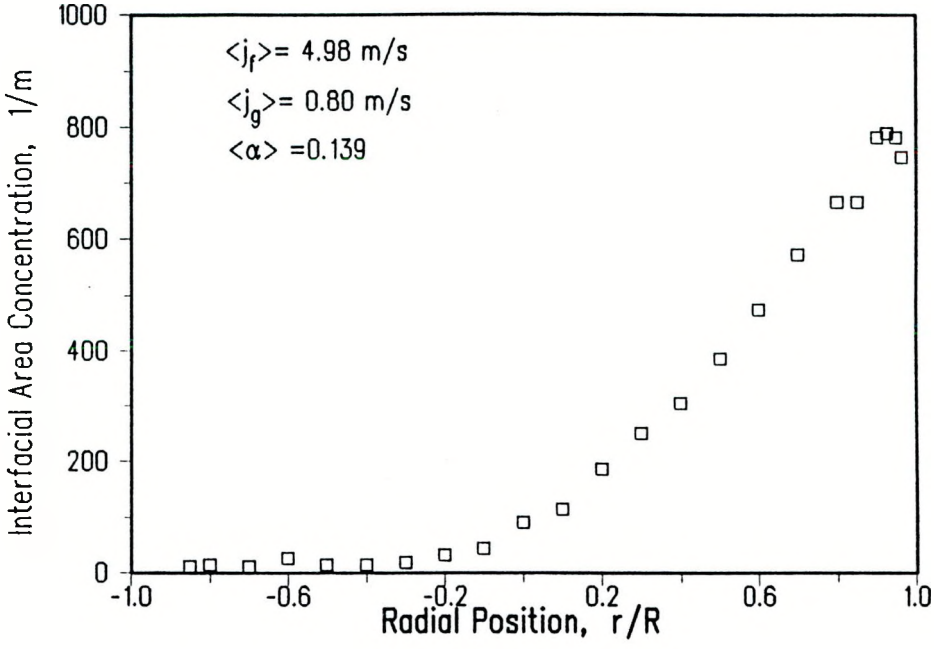

(c)

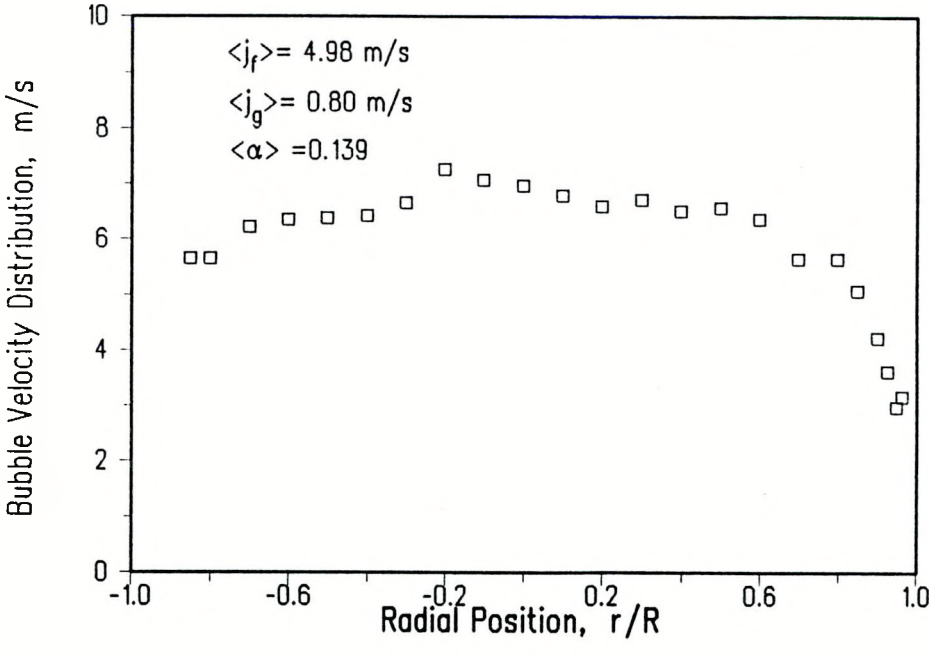

(d)

Figure 5.21 a) Local Void Fraction, b) Bubble Frequency, c) Interfacial Area Concentration, and d) Bubble Velocity Distribution at $\langle j_f \rangle$ = 4.98 m/s, $\langle j_g \rangle$ = 0.80 m/s, $\langle \alpha \rangle$ = 0.139.

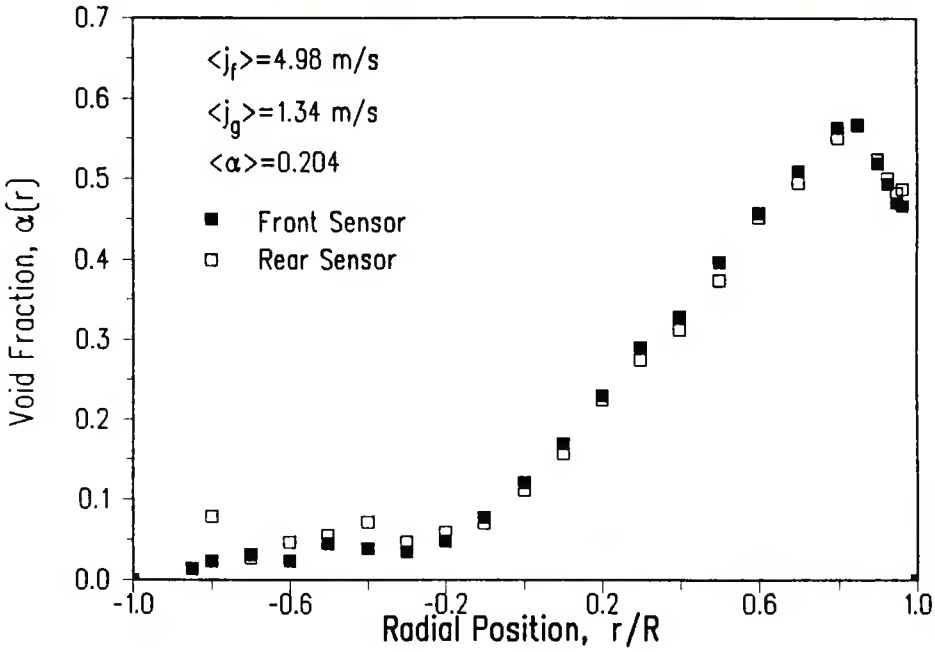

(a)

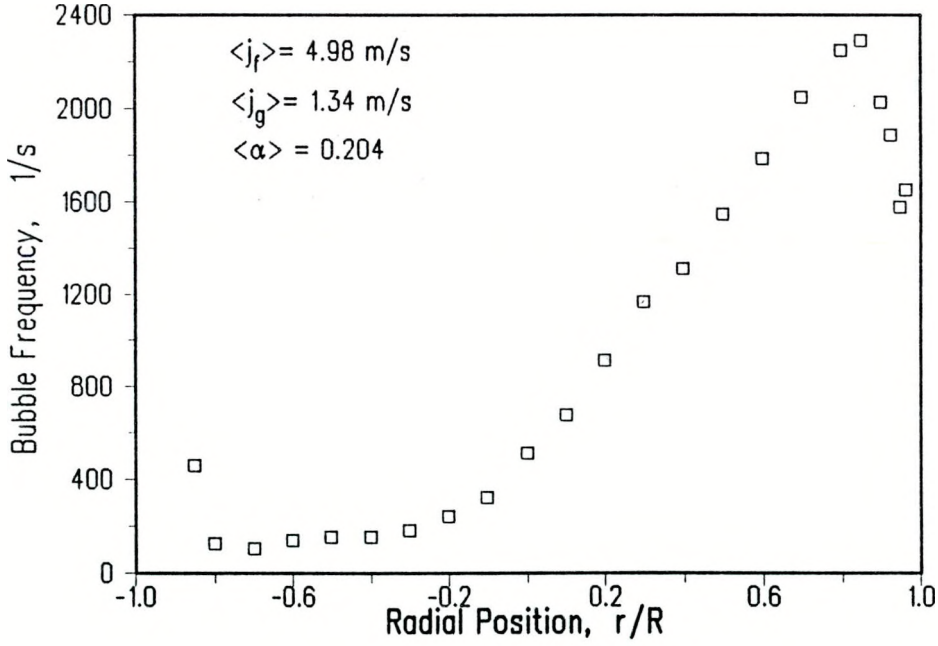

(b)

Figure 5.22 a) Local Void Fraction, b) Bubble Frequency, c) Interfacial Area Concentration, and d) Bubble Velocity Distribution at $\langle j_f \rangle$ = 4.98 m/s, $\langle j_g \rangle$ = 1.34 m/s, $\langle \alpha \rangle$ = 0.204.

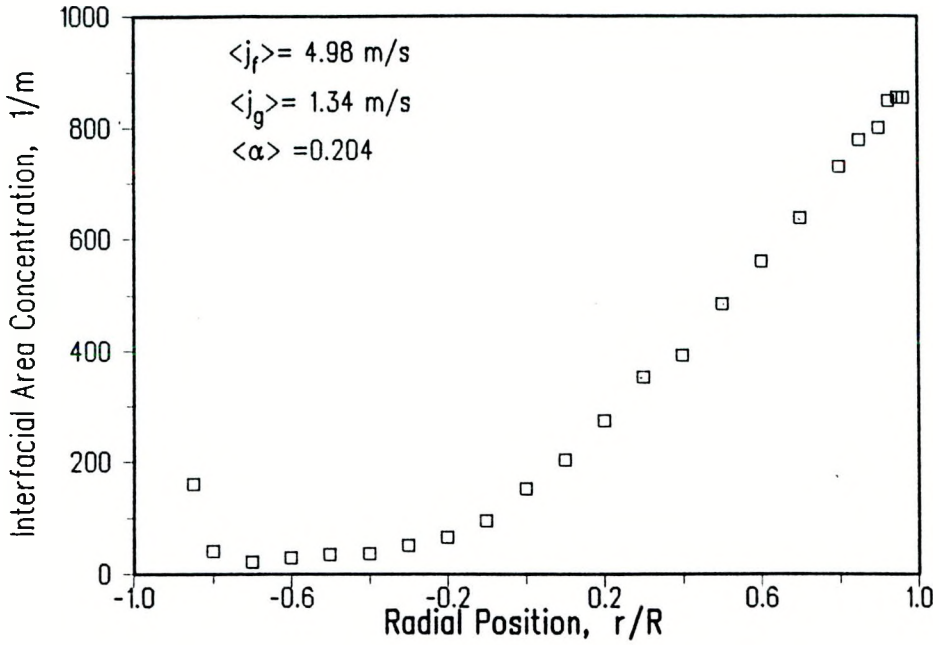

(c)

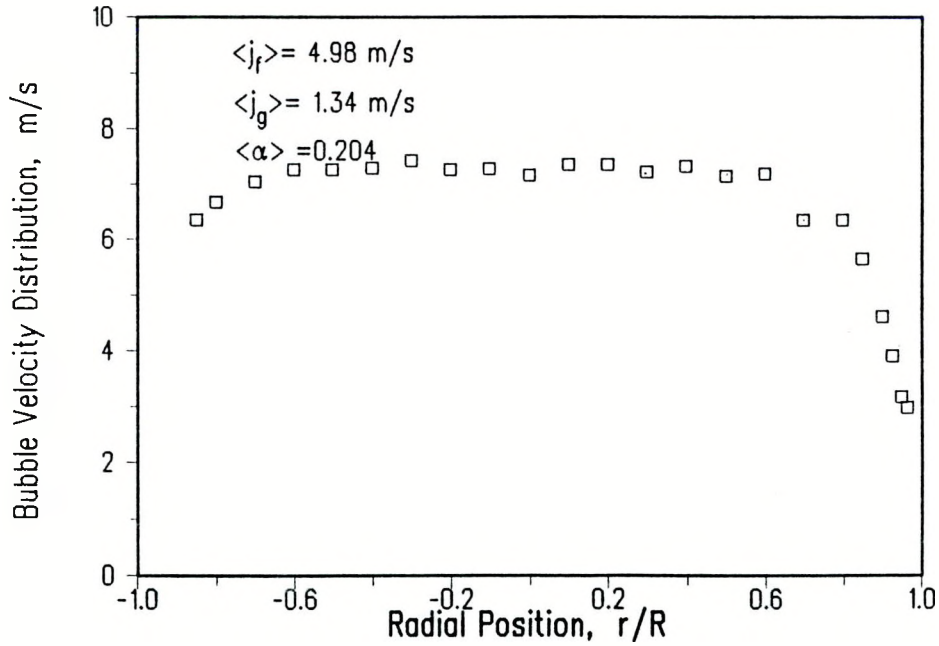

(d)

Figure 5.22 a) Local Void Fraction, b) Bubble Frequency, c) Interfacial Area Concentration, and d) Bubble Velocity Distribution at $\langle j_f \rangle$ = 4.98 m/s, $\langle j_g \rangle$ = 1.34 m/s, $\langle \alpha \rangle$ = 0.204.

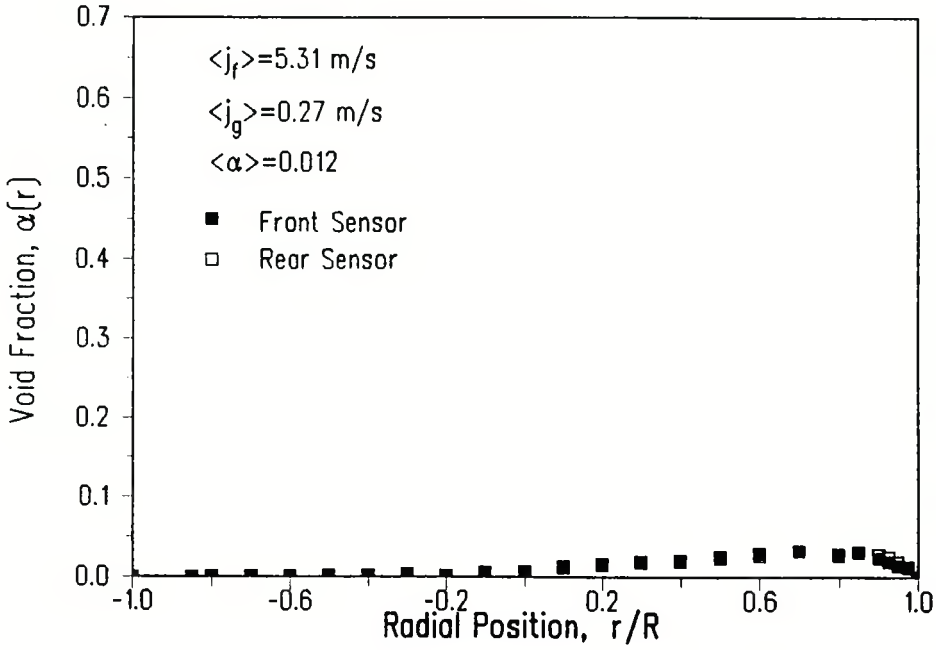

(a)

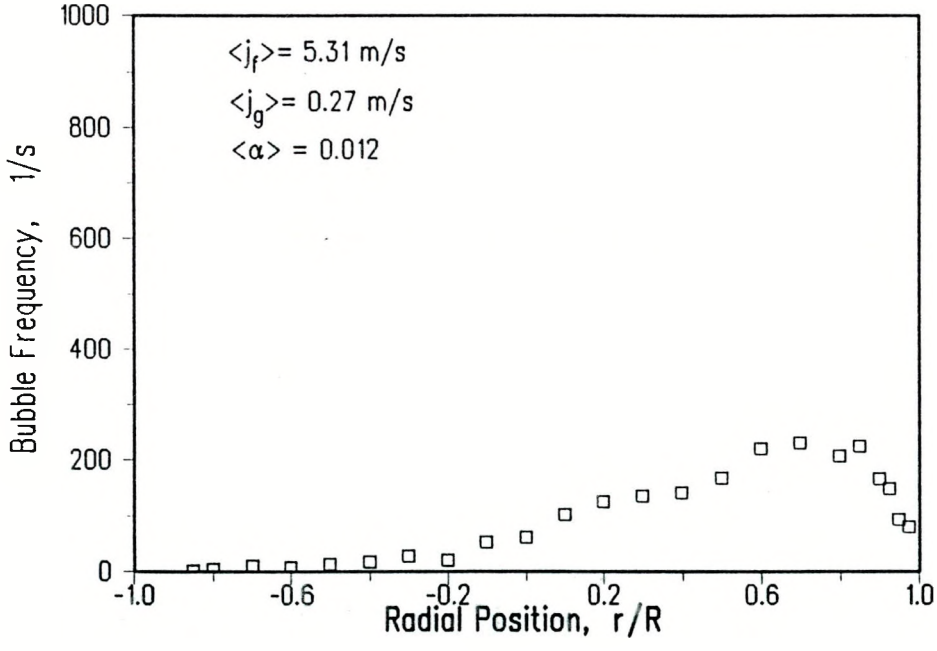

(b)

Figure 5.23 a) Local Void Fraction, b) Bubble Frequency, c) Interfacial Area Concentration, and d) Bubble Velocity Distribution at $\langle j_f \rangle$ = 5.31 m/s, $\langle j_g \rangle$ = 0.27 m/s, $\langle \alpha \rangle$ = 0.012.

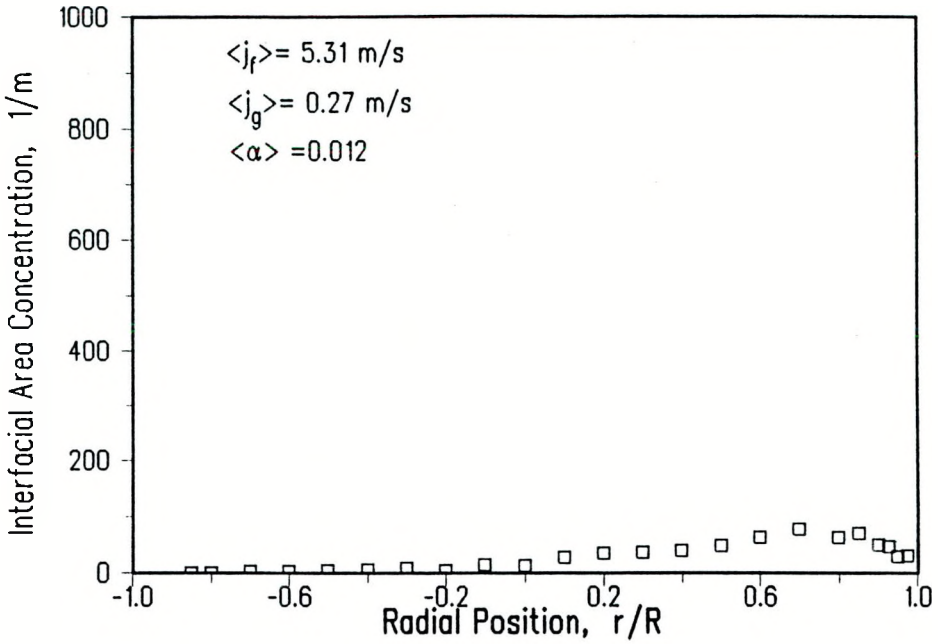

(c)

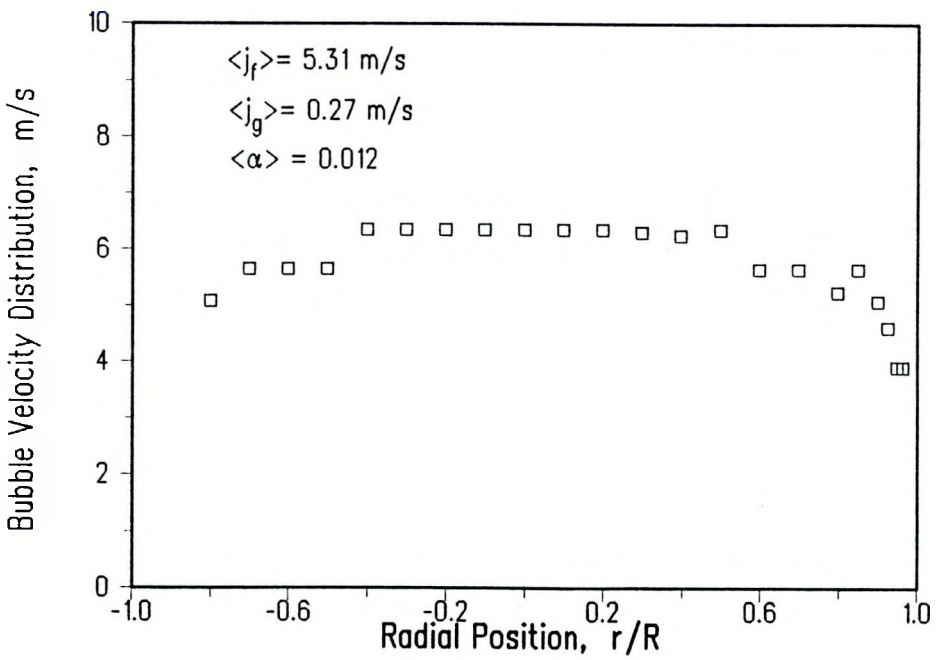

(d)

Figure 5.23 a) Local Void Fraction, b) Bubble Frequency, c) Interfacial Area Concentration, and d) Bubble Velocity Distribution at $\langle j_f \rangle$ = 5.31 m/s, $\langle j_g \rangle$ = 0.27 m/s, $\langle \alpha \rangle$ = 0.012.

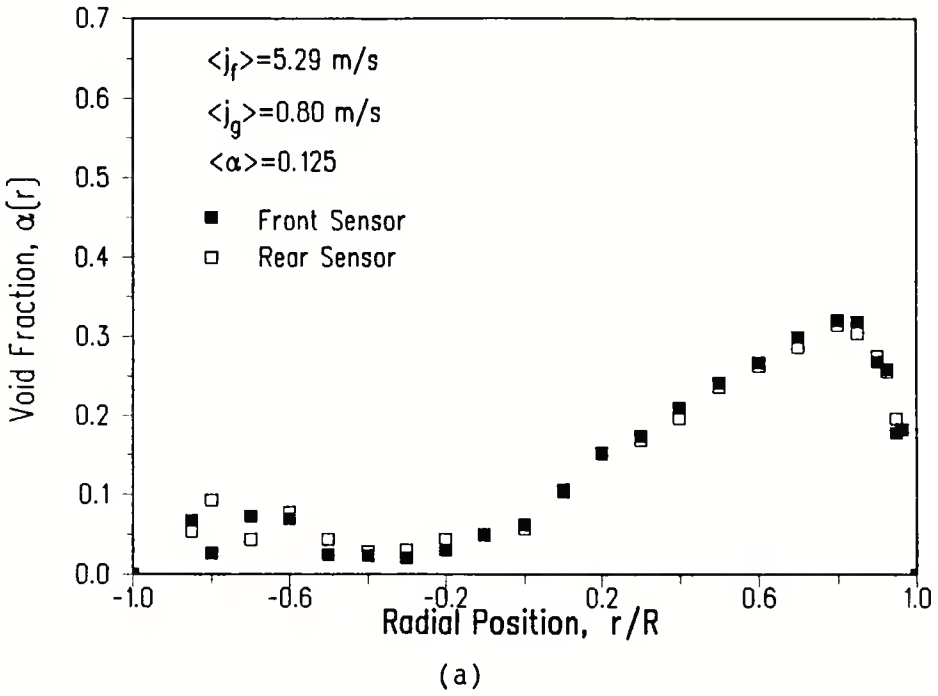

(a)

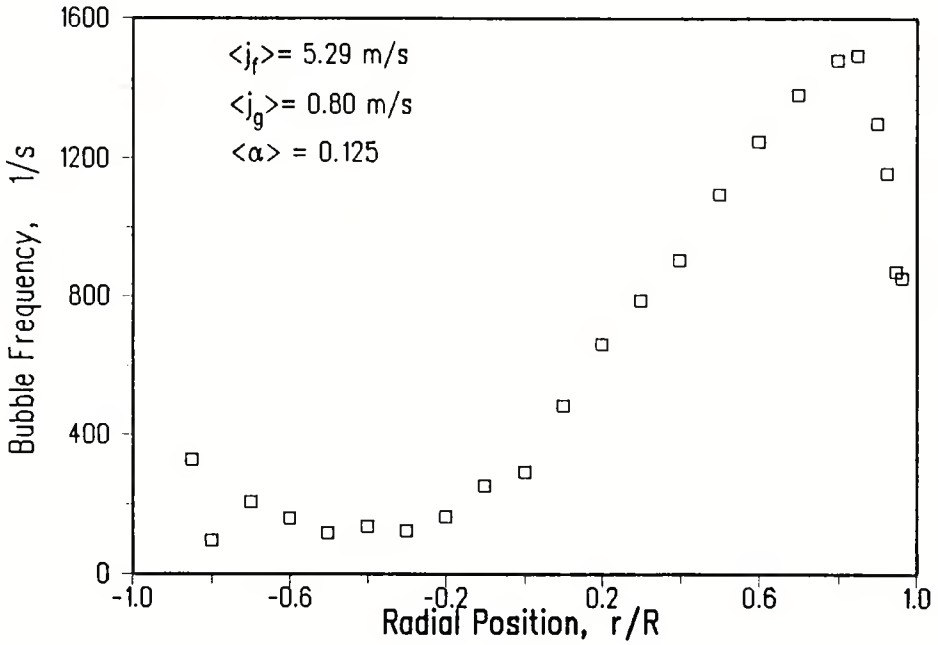

(b)

Figure 5.24 a) Local Void Fraction, b) Bubble Frequency, c) Interfacial Area Concentration, and d) Bubble Velocity Distribution at $\langle j_f \rangle$ = 5.29 m/s, $\langle j_g \rangle$ = 0.80 m/s, $\langle \alpha \rangle$ = 0.125.

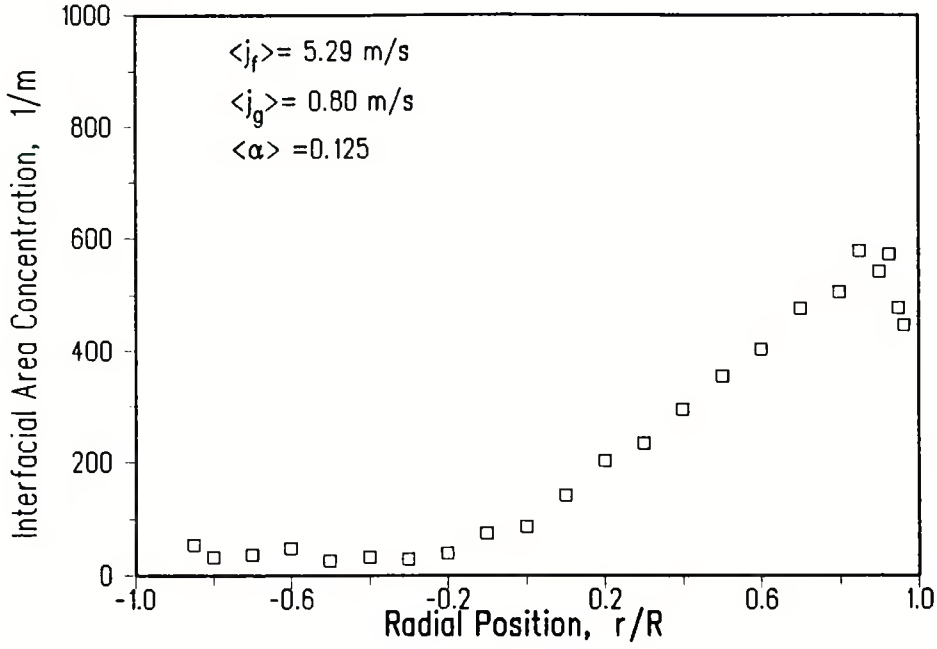

(c)

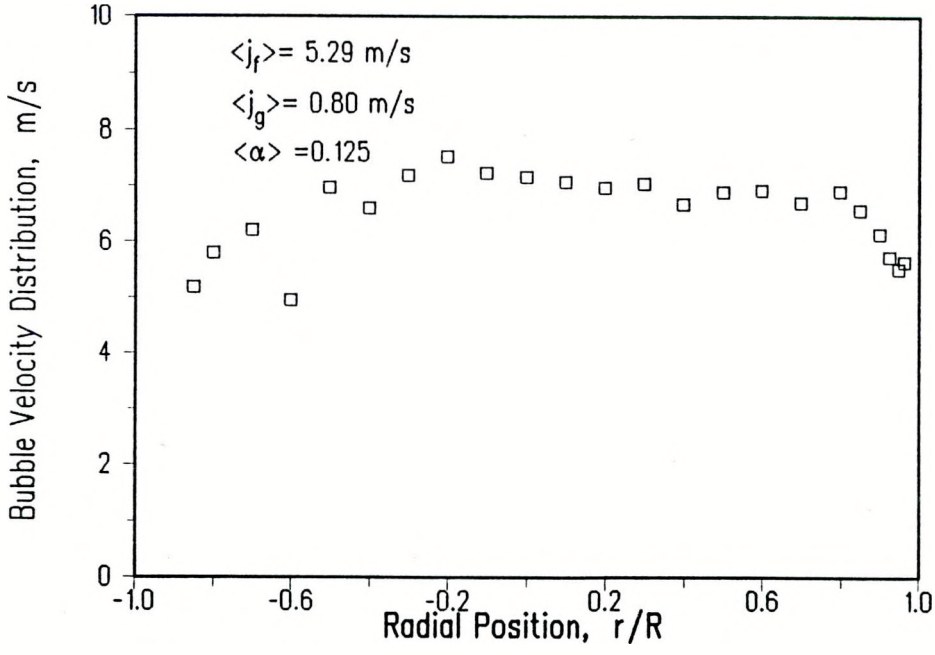

(d)

Figure 5.24 a) Local Void Fraction, b) Bubble Frequency, c) Interfacial Area Concentration, and d) Bubble Velocity Distribution at $\langle j_f \rangle$ = 5.29 m/s, $\langle j_g \rangle$ = 0.80 m/s, $\langle \alpha \rangle$ = 0.125.

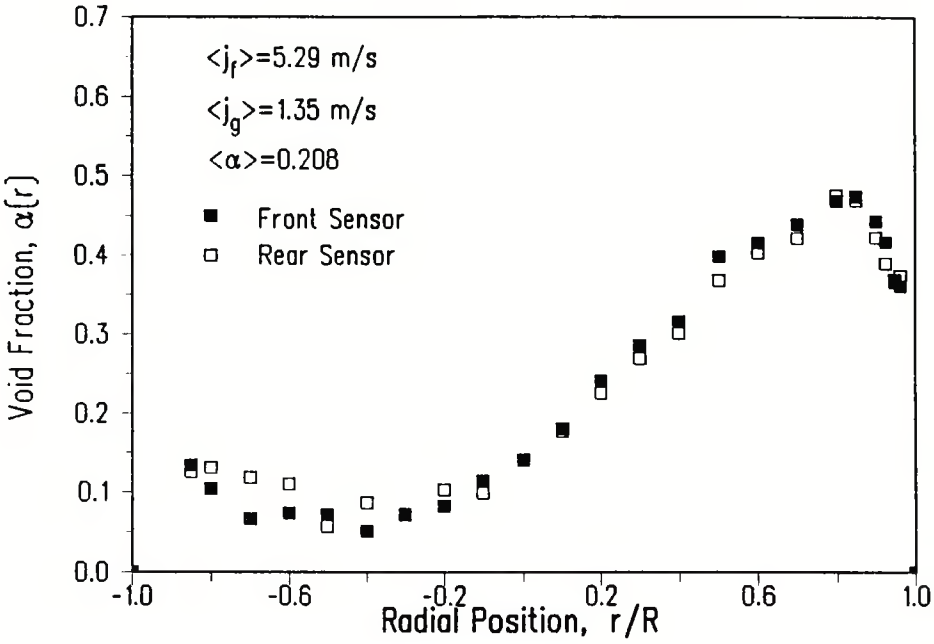

(a)

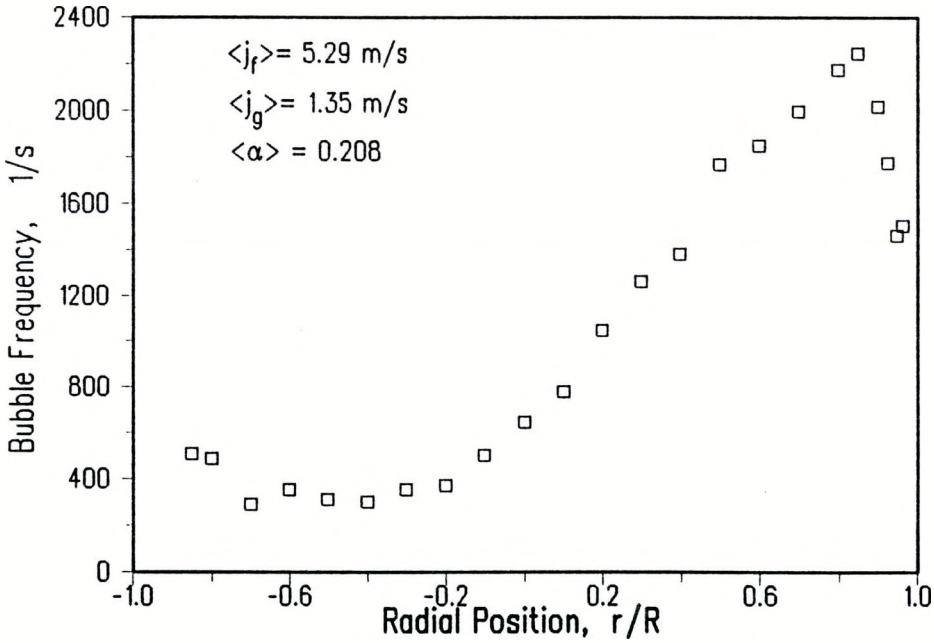

(b)

Figure 5.25 a) Local Void Fraction, b) Bubble Frequency, c) Interfacial Area Concentration, and d) Bubble Velocity Distribution at $\langle j_f \rangle$ = 5.29 m/s, $\langle j_g \rangle$ = 1.35 m/s, $\langle \alpha \rangle$ = 0.208.

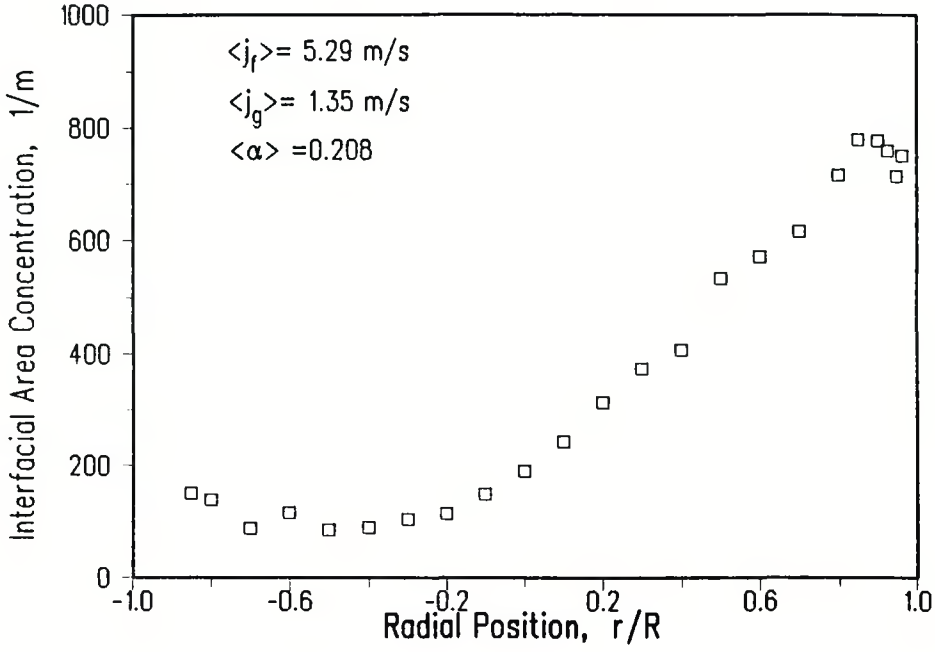

(c)

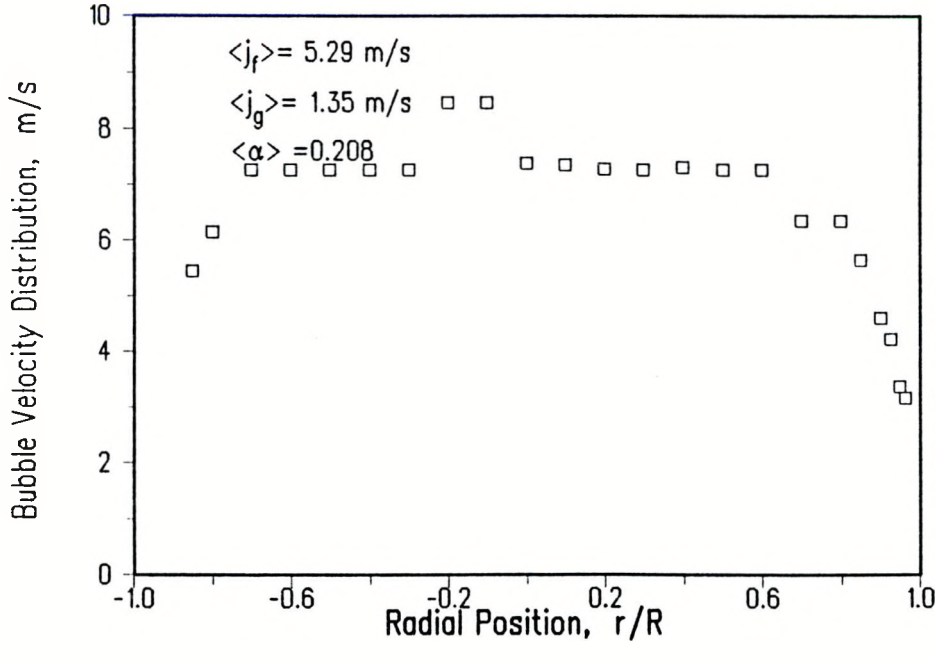

(d)

Figure 5.25 a) Local Void Fraction, b) Bubble Frequency, c) Interfacial Area Concentration, and d) Bubble Velocity Distribution at $\langle j_f \rangle$ = 5.29 m/s, $\langle j_g \rangle$ = 1.35 m/s, $\langle \alpha \rangle$ = 0.208.

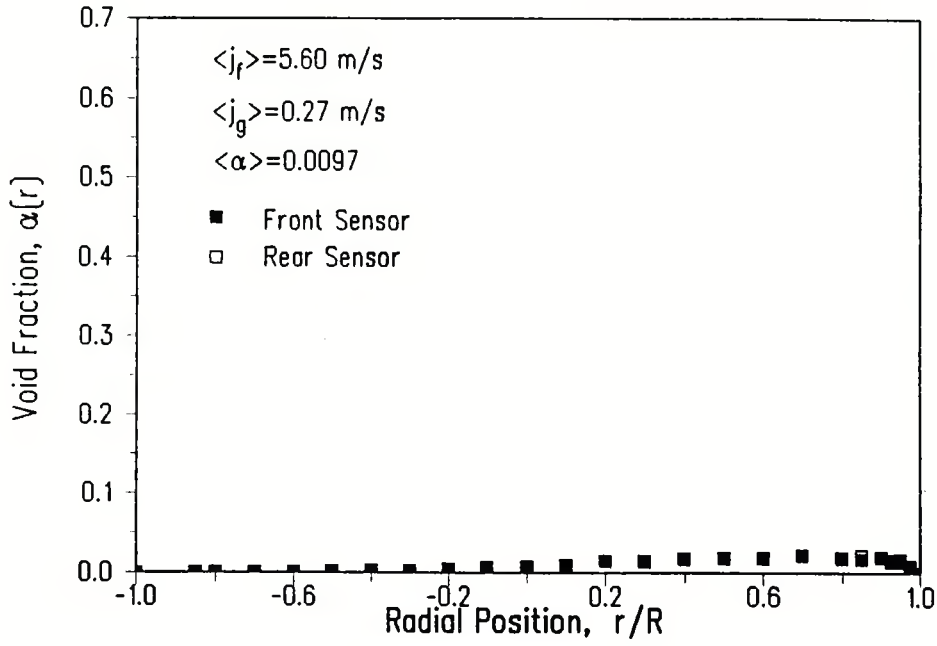

(a)

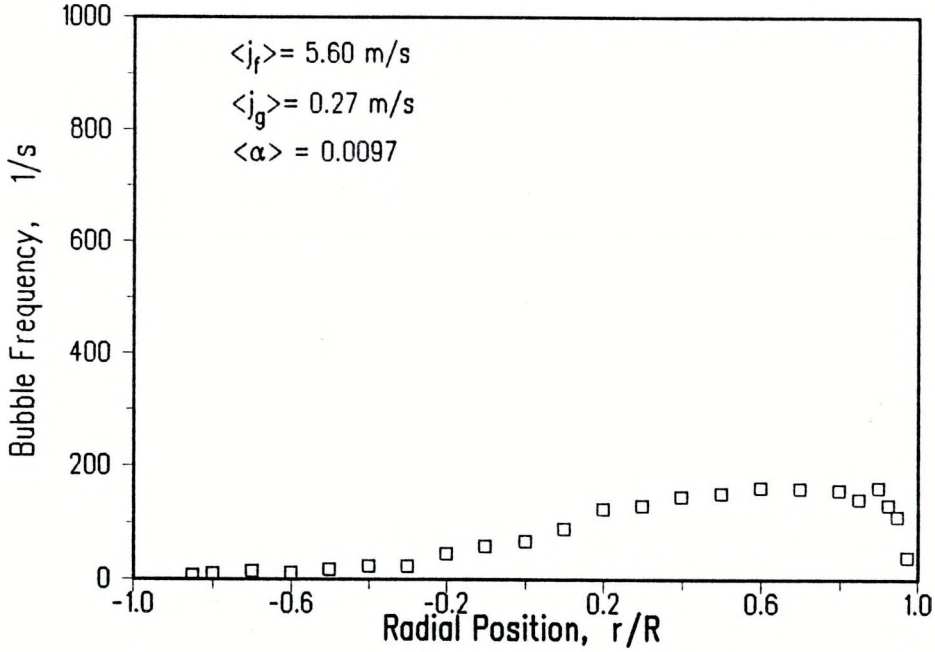

(b)

Figure 5.26 a) Local Void Fraction, b) Bubble Frequency, c) Interfacial Area Concentration, and d) Bubble Velocity Distribution at $\langle j_f \rangle$ = 5.60 m/s, $\langle j_g \rangle$ = 0.27 m/s, $\langle \alpha \rangle$ = 0.0097.

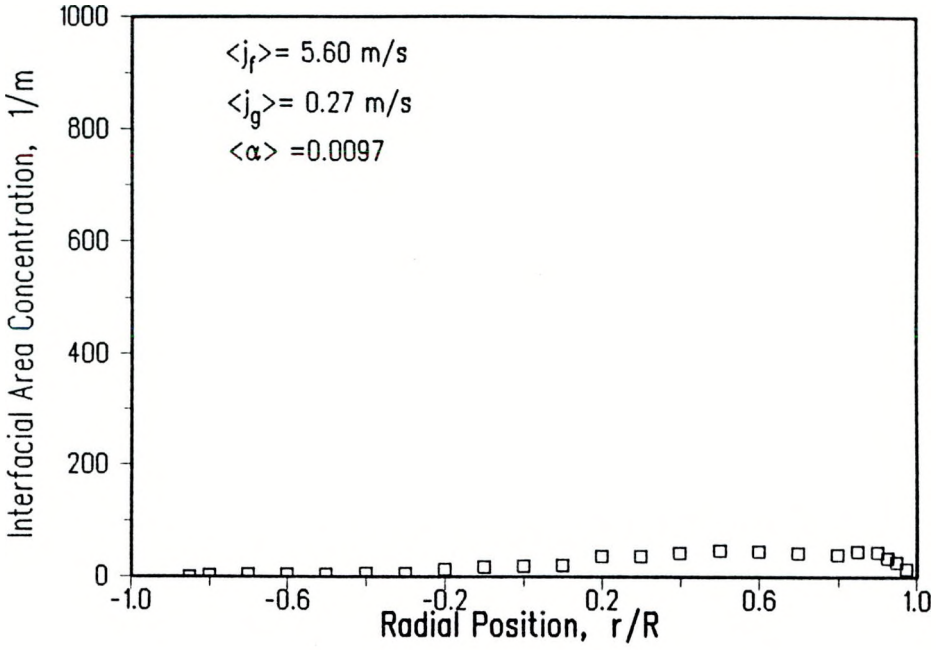

(c)

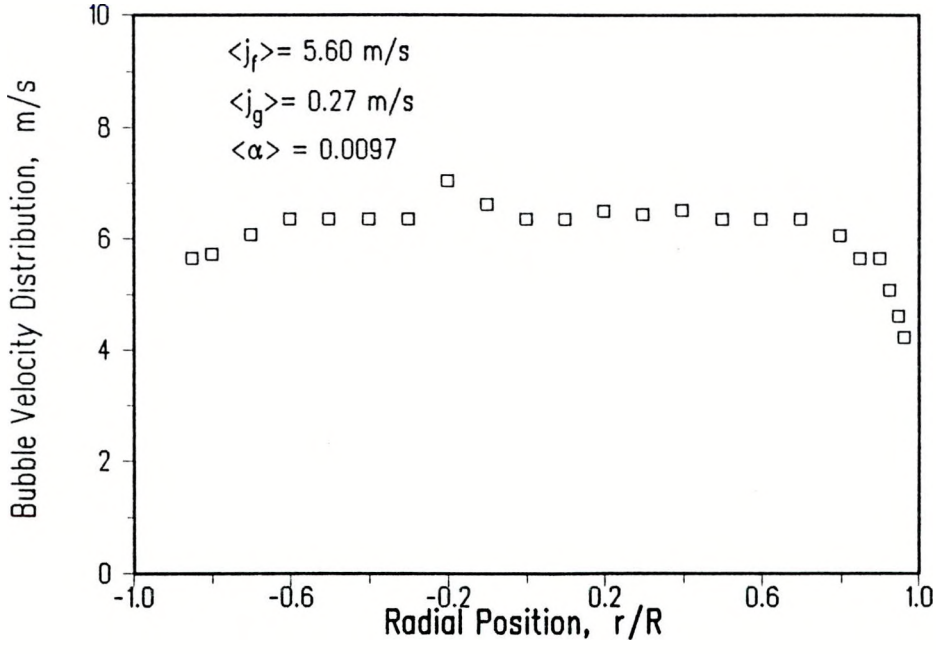

(d)

Figure 5.26 a) Local Void Fraction, b) Bubble Frequency, c) Interfacial Area Concentration, and d) Bubble Velocity Distribution at $\langle j_f \rangle$ = 5.60 m/s, $\langle j_g \rangle$ = 0.27 m/s, $\langle \alpha \rangle$ = 0.0097.

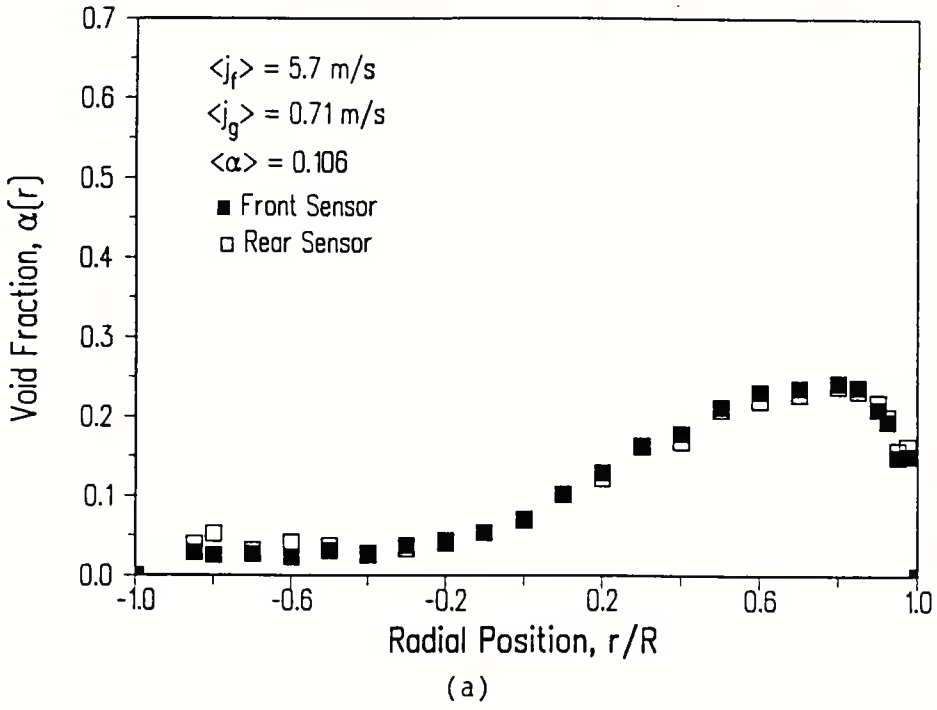

(a)

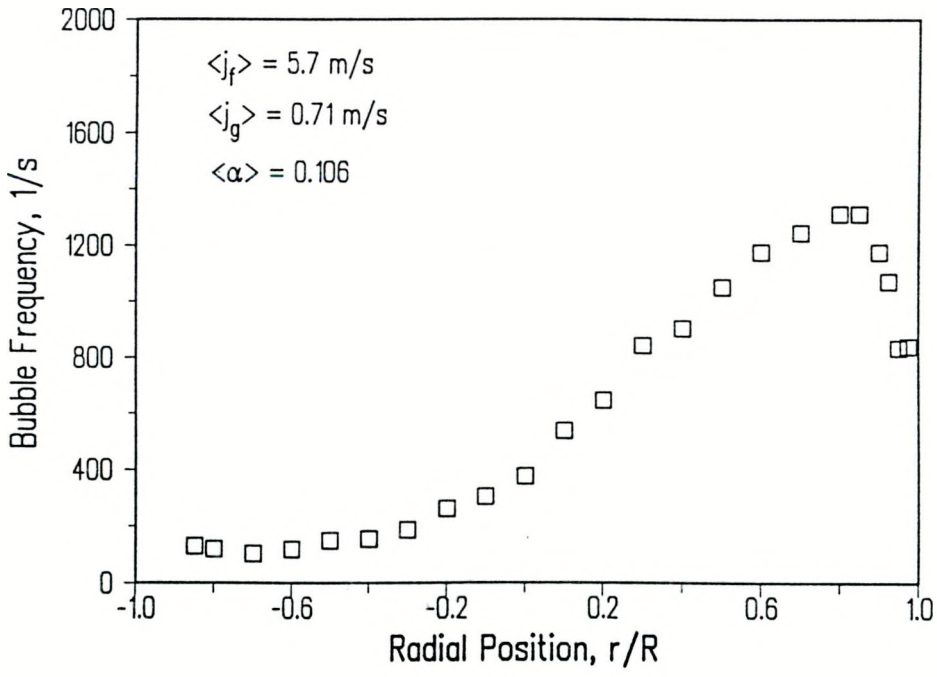

(b)

Figure 5.27 a) Local Void Fraction, b) Bubble Frequency, c) Interfacial Area Concentration, and d) Bubble Velocity Distribution at $\langle j_f \rangle$ = 5.70 m/s, $\langle j_g \rangle$ = 0.71 m/s, $\langle \alpha \rangle$ = 0.106.

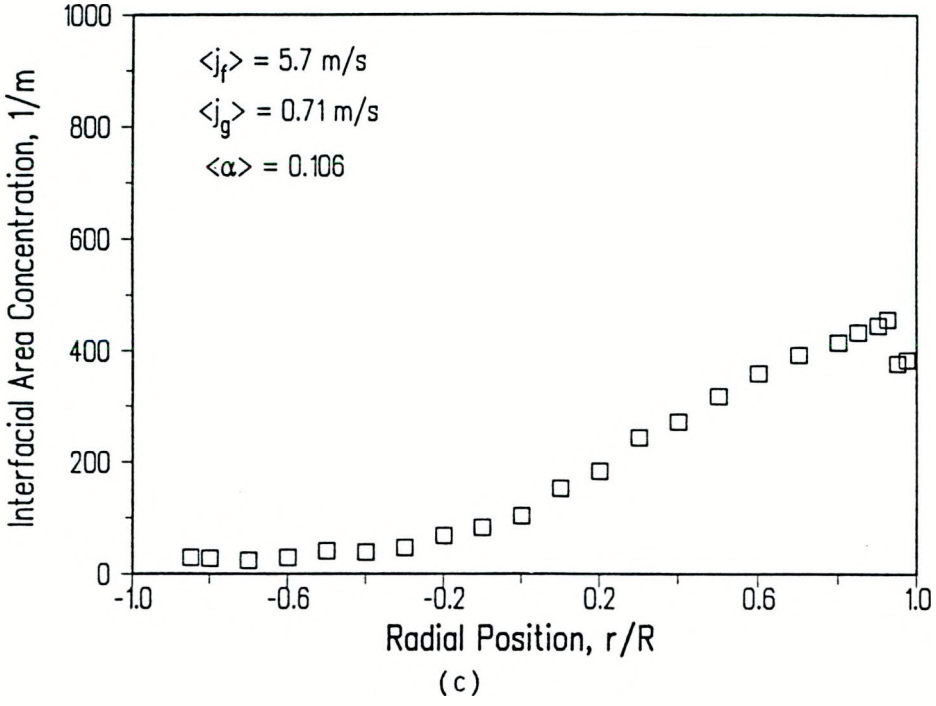

(c)

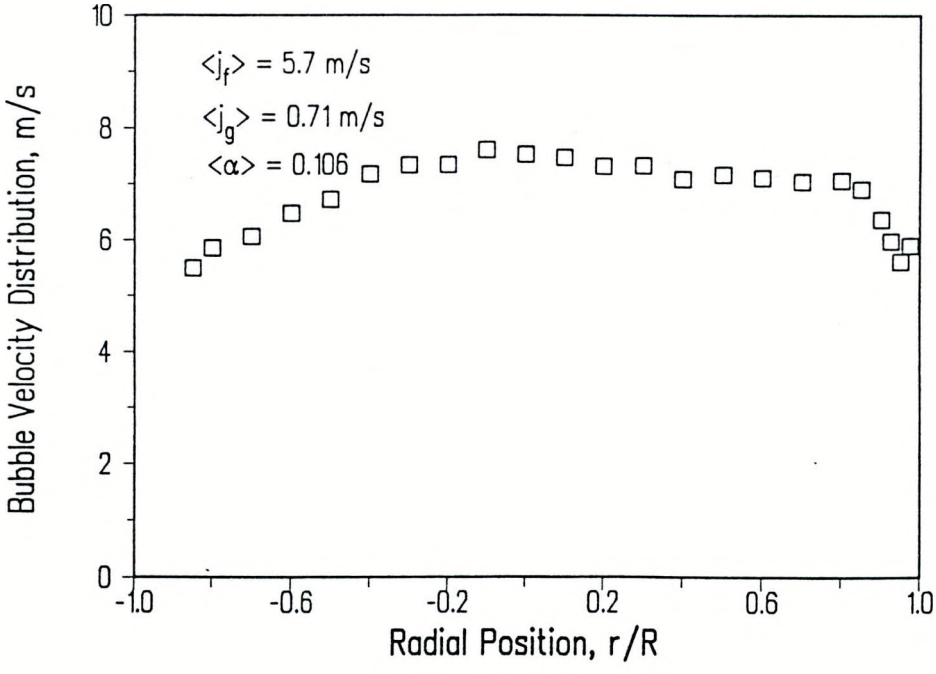

(d)

Figure 5.27 a) Local Void Fraction, b) Bubble Frequency, c) Interfacial Area Concentration, and d) Bubble Velocity Distribution at $\langle j_f \rangle$ = 5.71 m/s, $\langle j_g \rangle$ = 0.71 m/s, $\langle \alpha \rangle$ = 0.106.

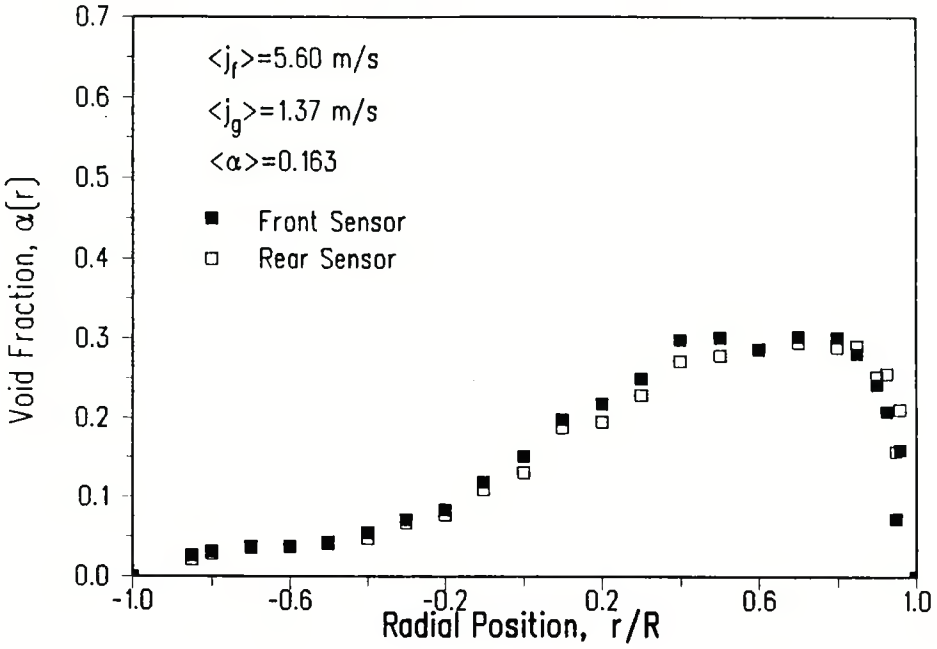

(a)

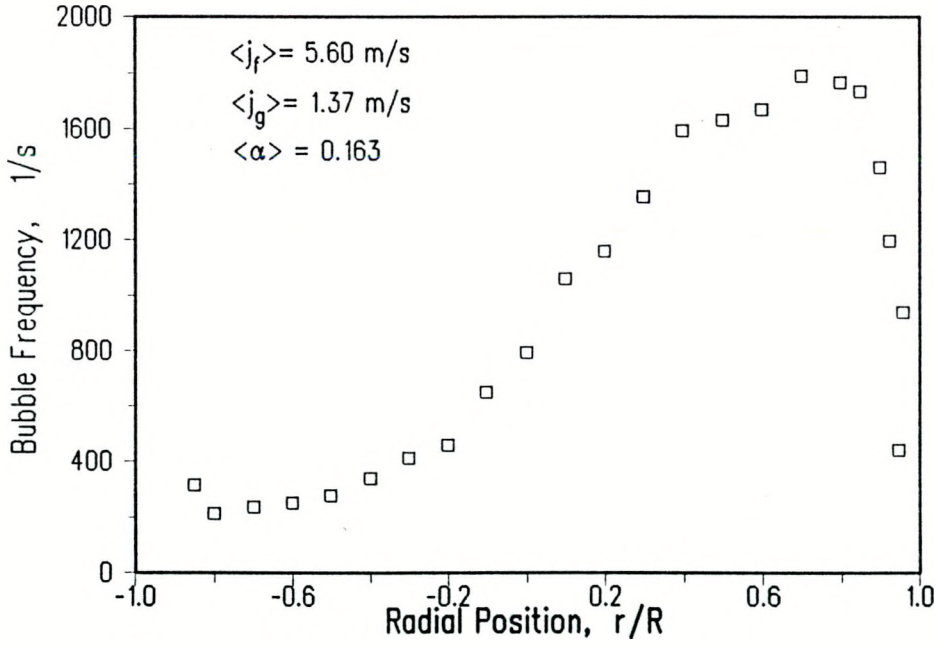

(b)

Figure 5.28 a) Local Void Fraction, b) Bubble Frequency, c) Interfacial Area Concentration, and d) Bubble Velocity Distribution at <j_f> = 5.60 m/s, <j_g> = 1.37 m/s, <α> = 0.163.

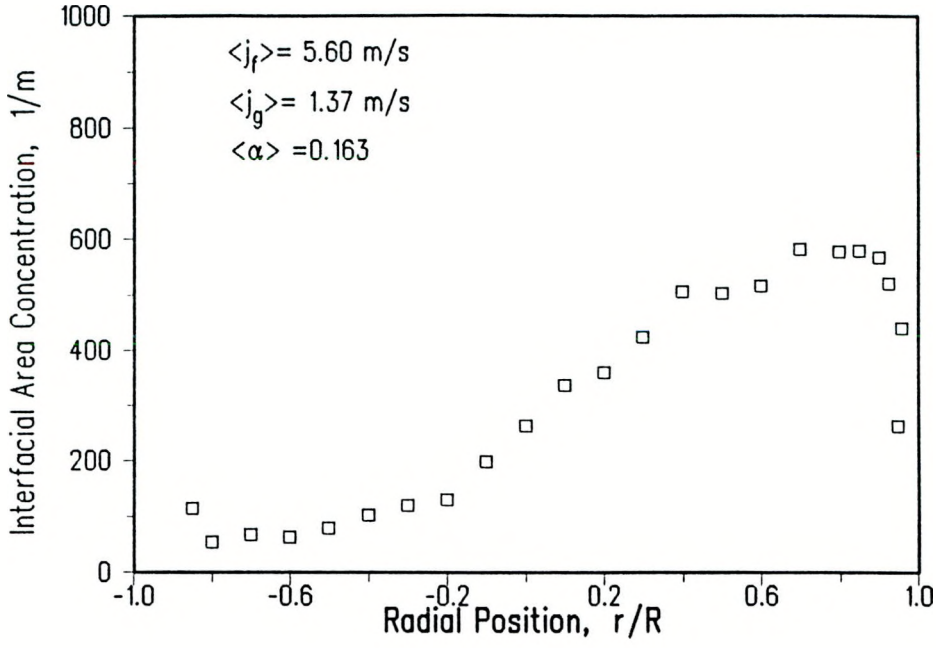

(c)

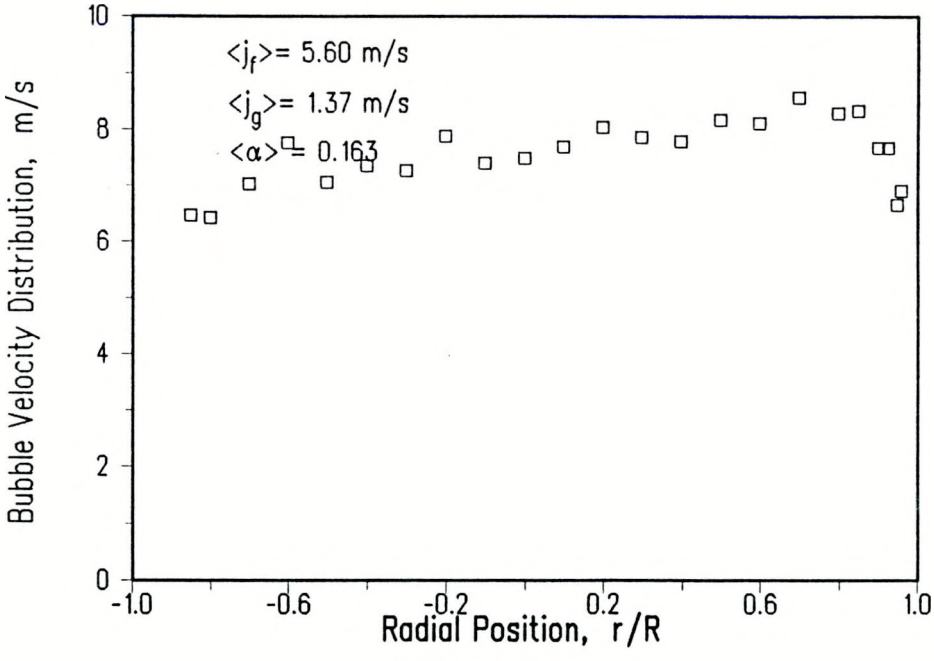

(d)

Figure 5.28 a) Local Void Fraction, b) Bubble Frequency, c) Interfacial Area Concentration, and d) Bubble Velocity Distribution at $\langle j_f \rangle$ = 5.60 m/s, $\langle j_g \rangle$ = 1.37 m/s, $\langle \alpha \rangle$ = 0.163.

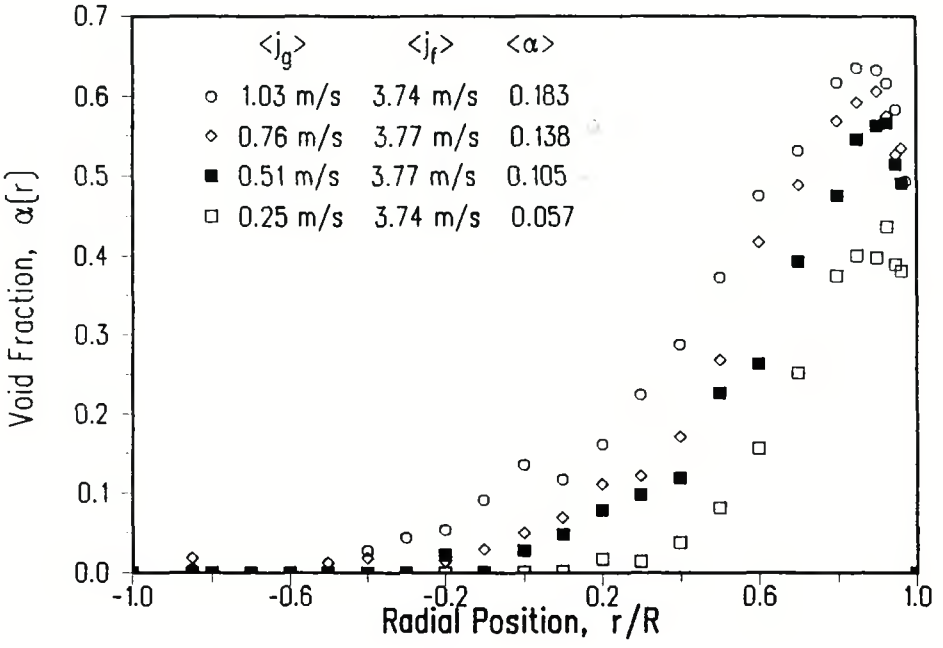

Figure 5.29 Influence of Gas Flow on Local Void Fraction Distribution at $\langle j_f \rangle$ = 3.7 m/s.

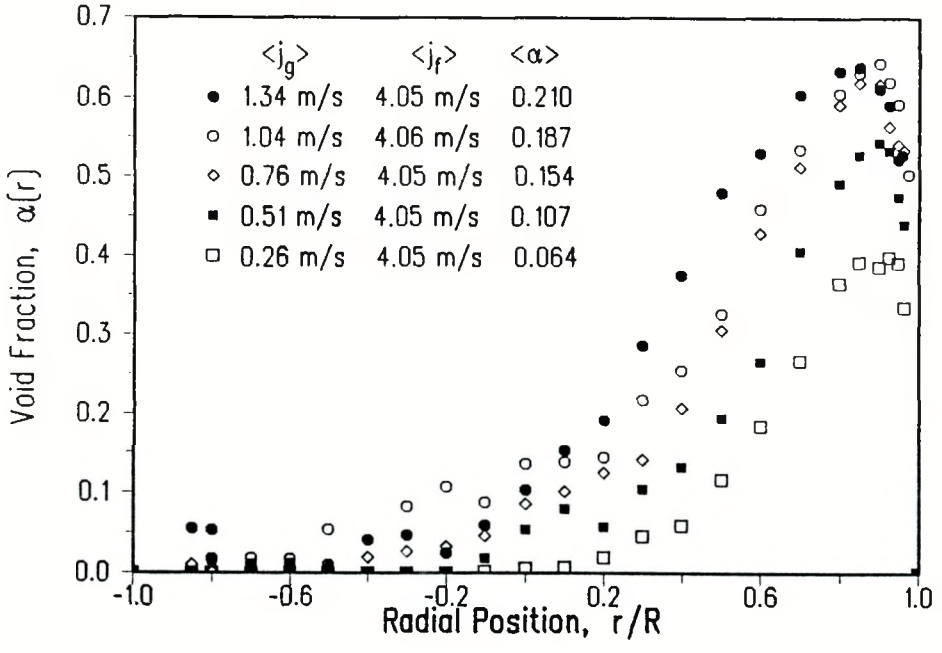

Figure 5.30 Influence of Gas Flow on Local Void Fraction Distribution at $\langle j_f \rangle$ = 4 m/s.

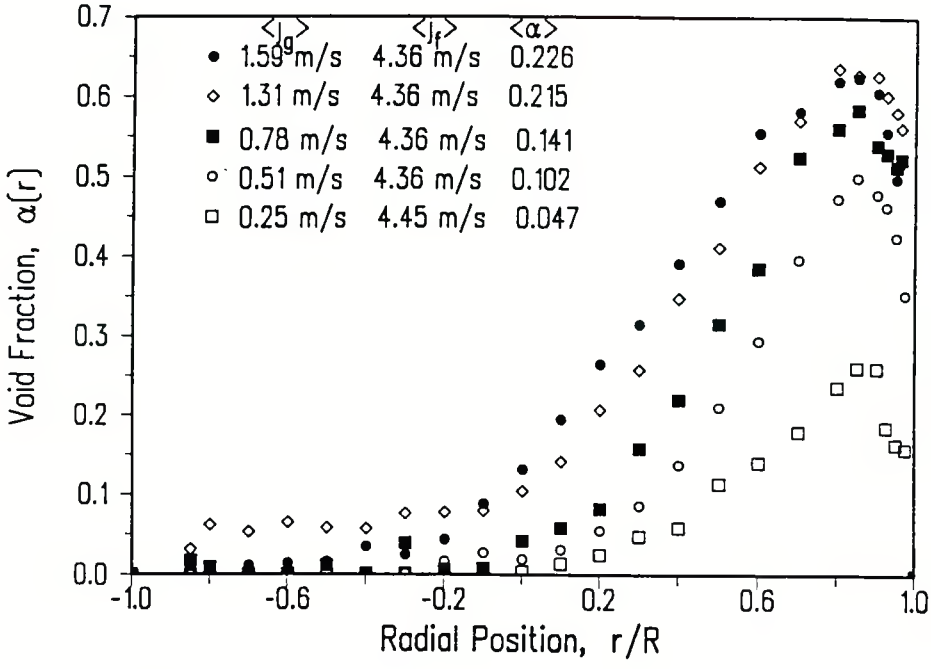

Figure 5.31 Influence of Gas Flow on Local Void Fraction Distribution at $\langle j_f \rangle$ = 4.30 m/s.

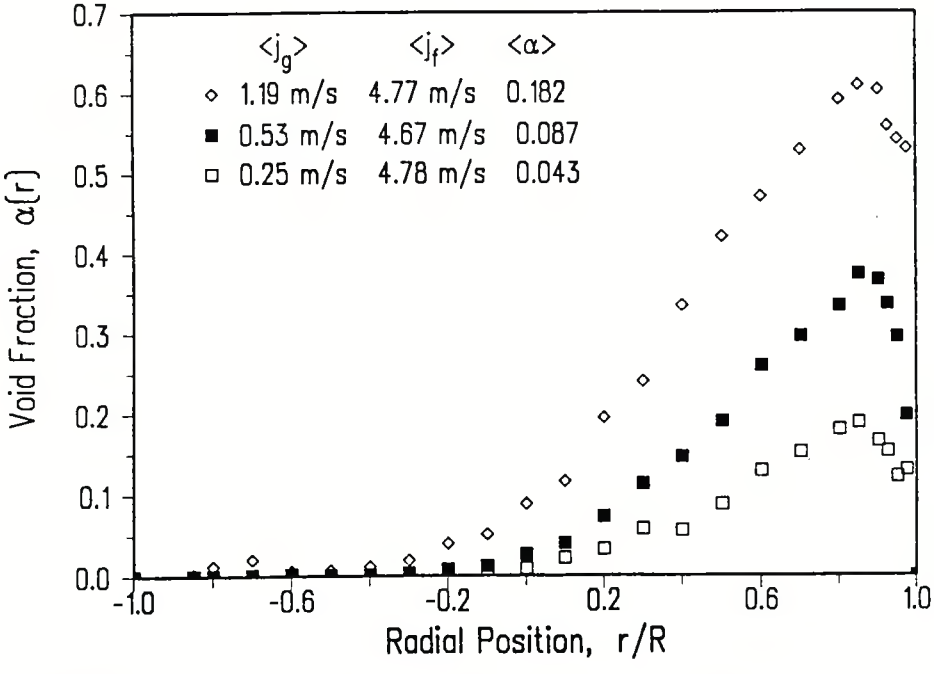

Figure 5.32 Influence of Gas Flow on Local Void Fraction Distribution at $\langle j_f \rangle$ = 4.67 m/s.

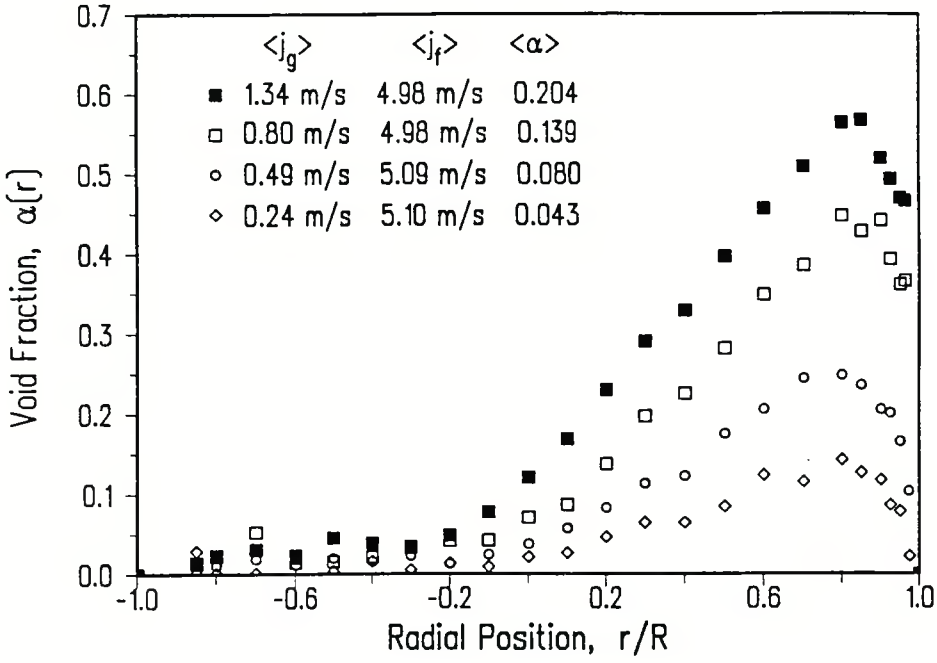

Figure 5.33 Influence of Gas Flow on Local Void Fraction Distribution at $\langle j_f \rangle \simeq 5$ m/s.

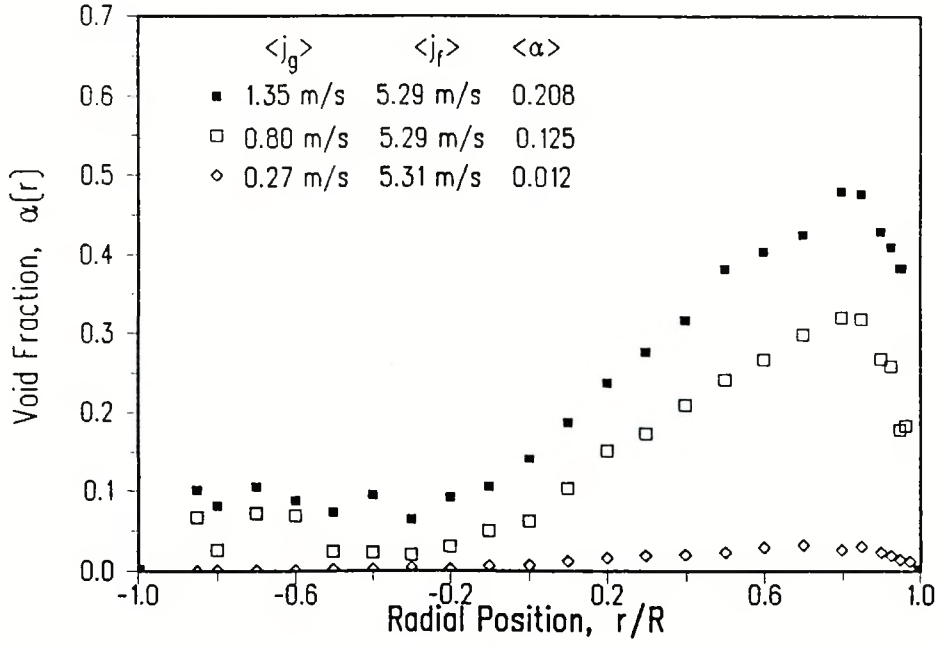

Figure 5.34 Influence of Gas Flow on Local Void Fraction Distribution at $\langle j_f \rangle \simeq 5.3$ m/s.

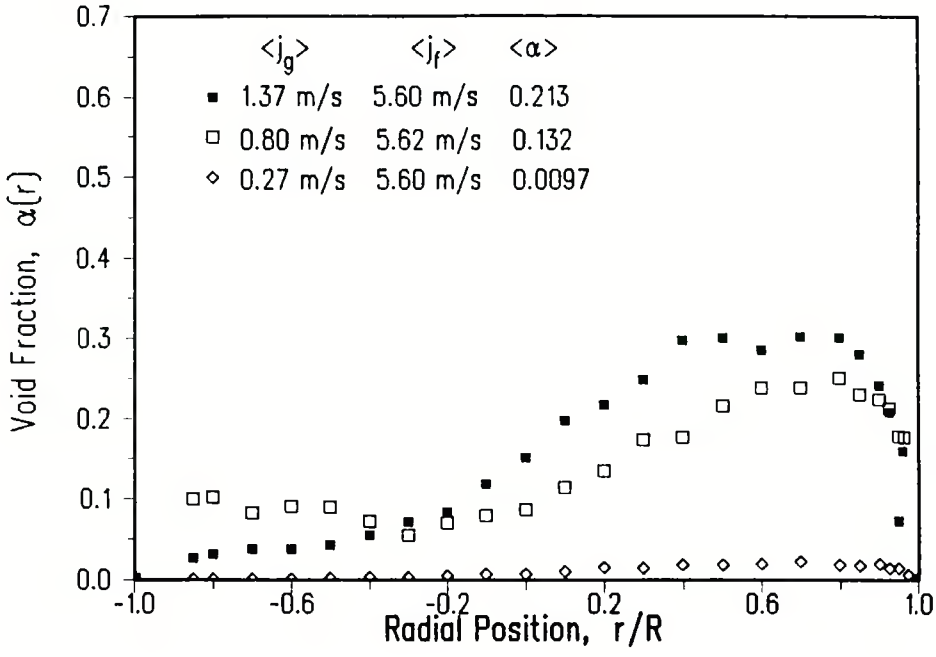

Figure 5.35 Influence of Gas Flow on Local Void Fraction Distribution at $\langle j_f \rangle \simeq 5.6$ m/s.

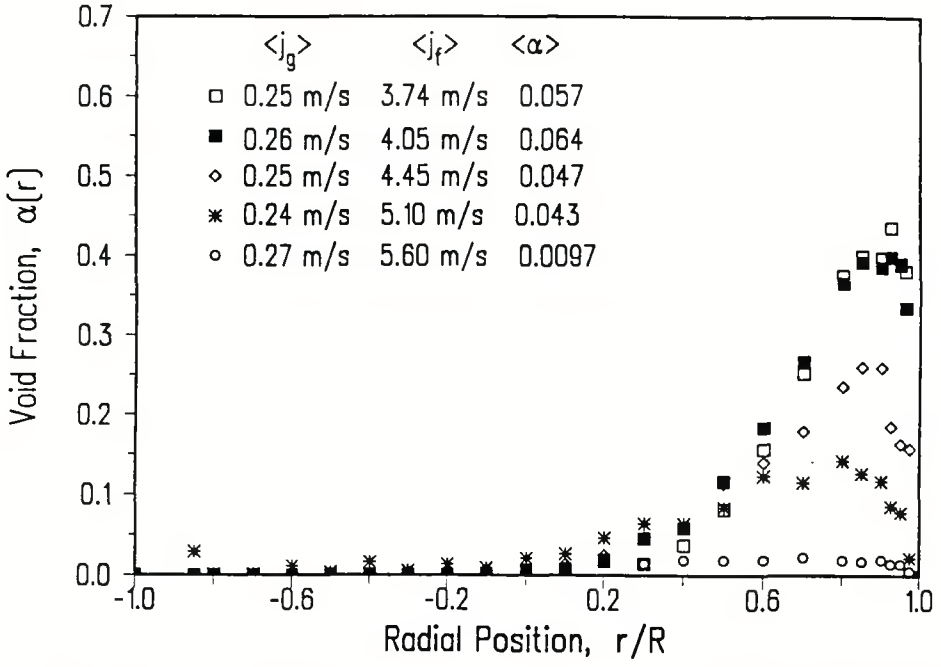

Figure 5.36 Influence of Liquid Flow on Local Void Fraction Distribution at $\langle j_g \rangle \simeq 0.25$ m/s.

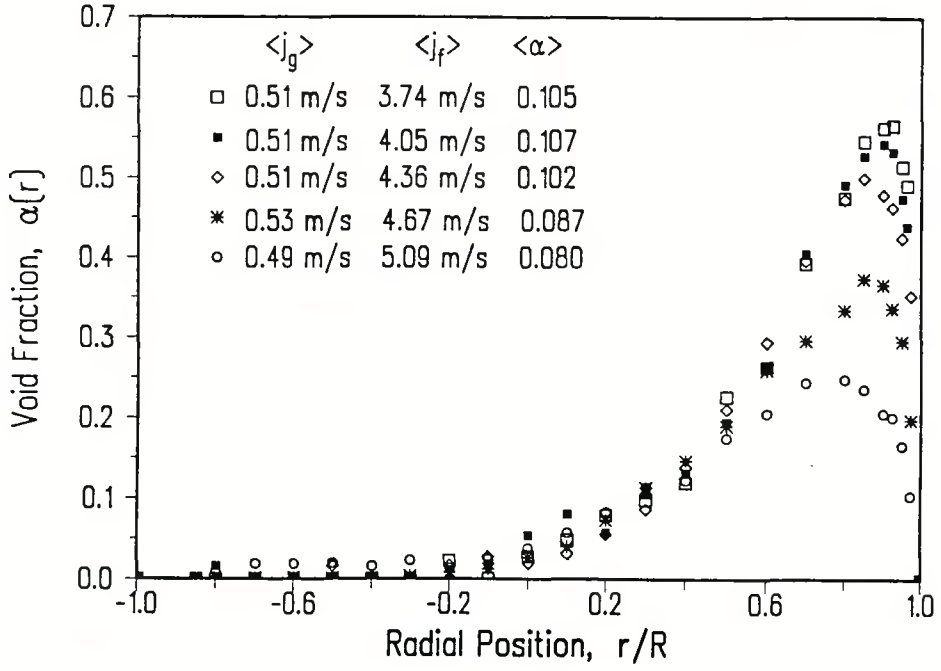

Figure 5.37 Influence of Liquid Flow on Local Void Fraction Distribution at $\langle j_g \rangle \simeq 0.5$ m/s.

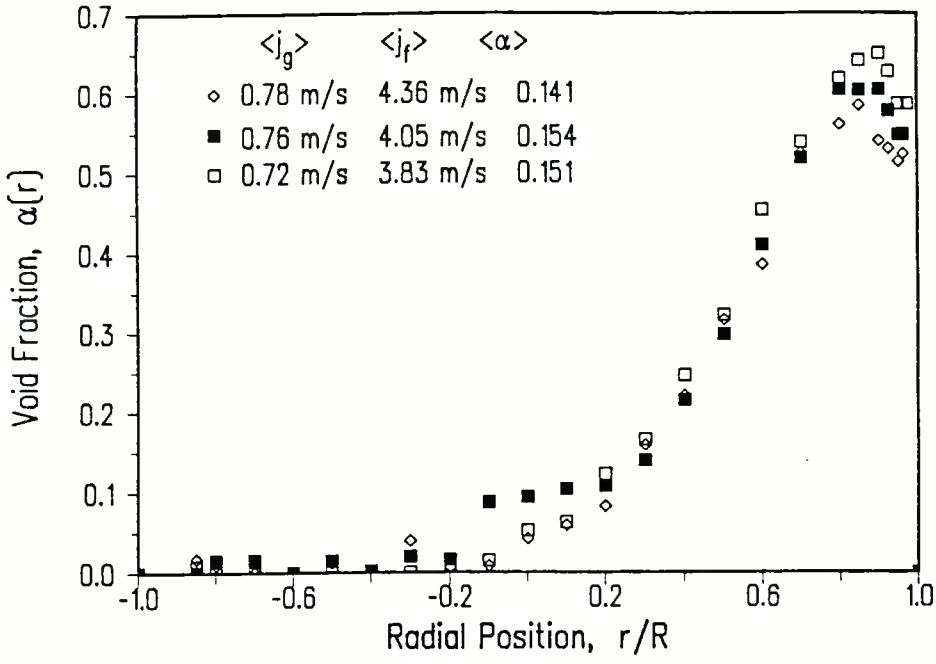

Figure 5.38 Influence of Liquid Flow on Local Void Fraction Distribution at $\langle j_g \rangle \simeq 0.76$ m/s.

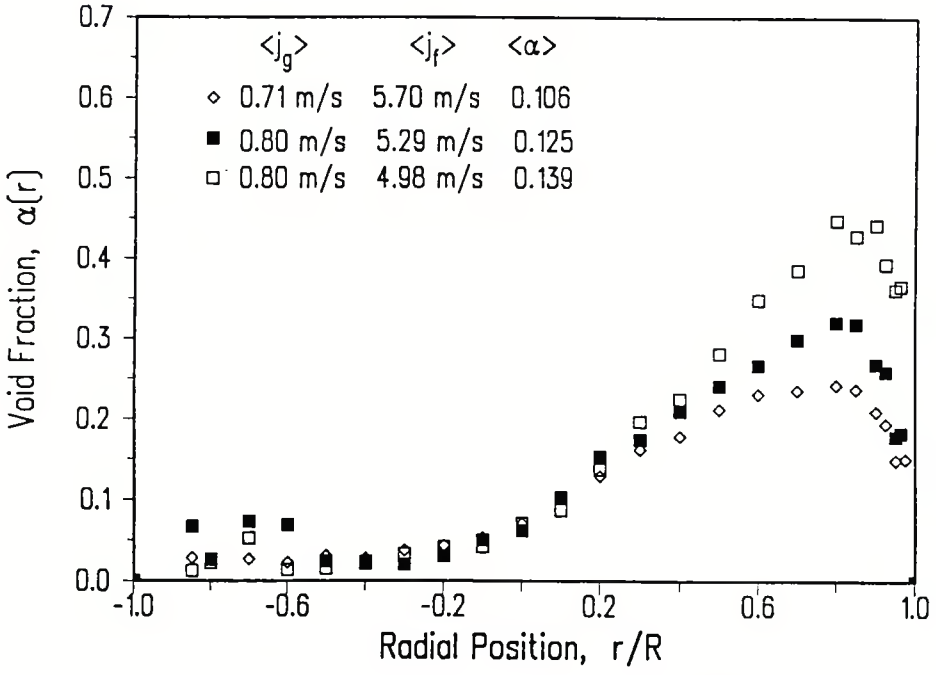

Figure 5.39 Influence of Liquid Flow on Local Void Fraction Distribution at $\langle j_g \rangle \simeq 0.8$ m/s.

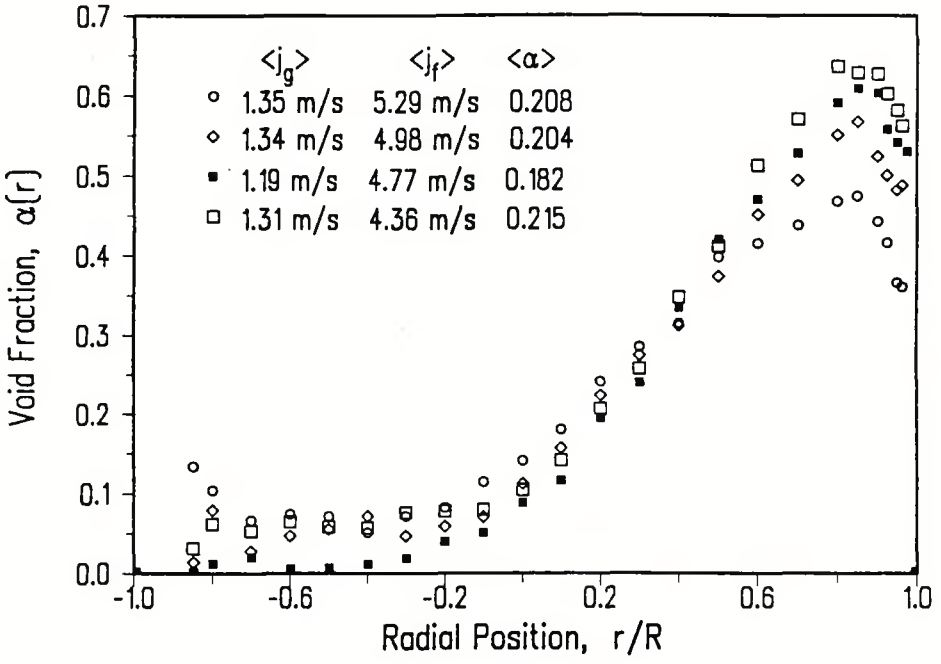

Figure 5.40 Influence of Liquid Flow on Local Void Fraction Distribution at $\langle j_g \rangle \simeq 1.3$ m/s.

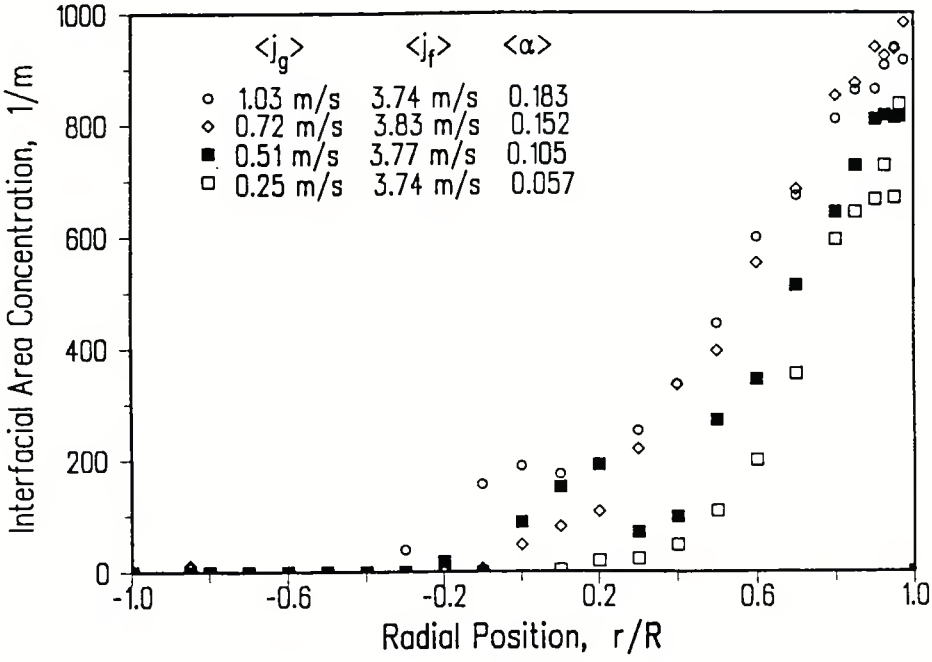

Figure 5.41 Effect of Gas Flow on Local Interfacial Area Concentration Profile at $\langle j_f \rangle \simeq 3.7$ m/s.

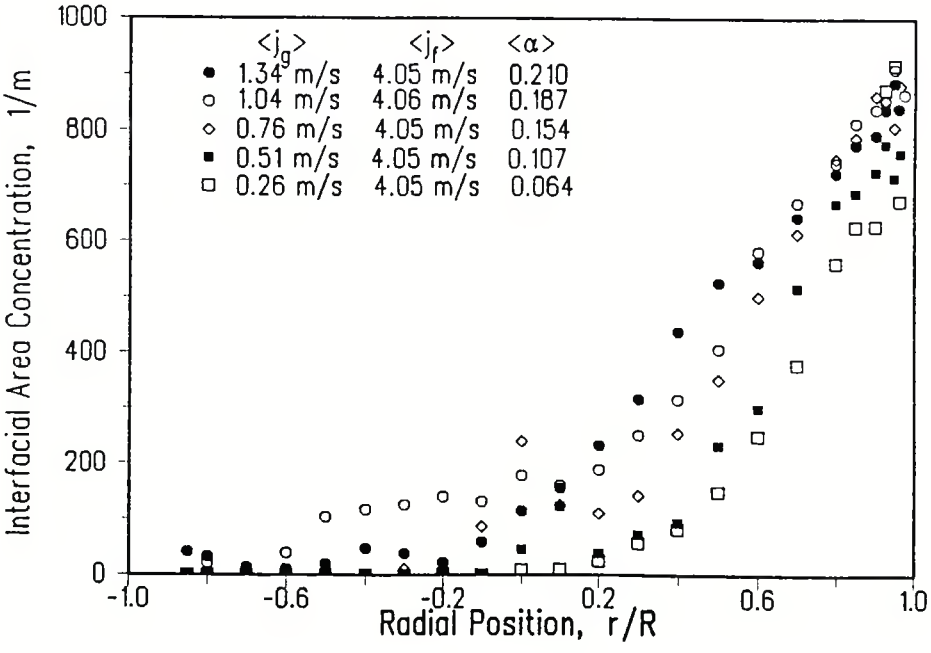

Figure 5.42 Effect of Gas Flow on Local Interfacial Area Concentration Profile at $\langle j_f \rangle \simeq 4$ m/s.

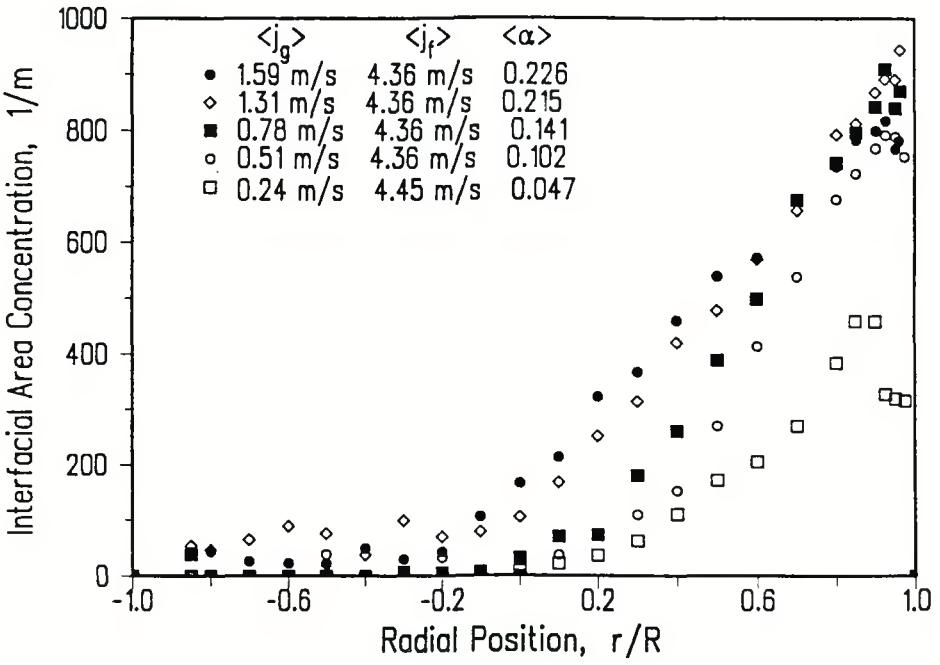

Figure 5.43 Effect of Gas Flow on Local Interfacial Area Concentration Profile at $\langle j_f \rangle \simeq 4.36$ m/s.

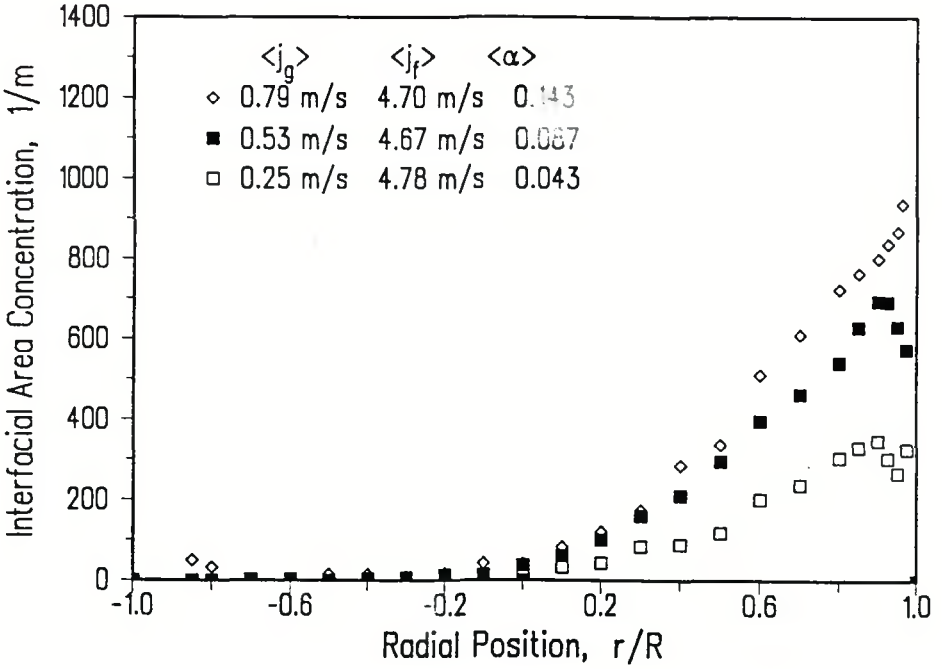

Figure 5.44 Effect of Gas Flow on Local Interfacial Area Concentration Profile at $\langle j_f \rangle \simeq 4.67$ m/s.

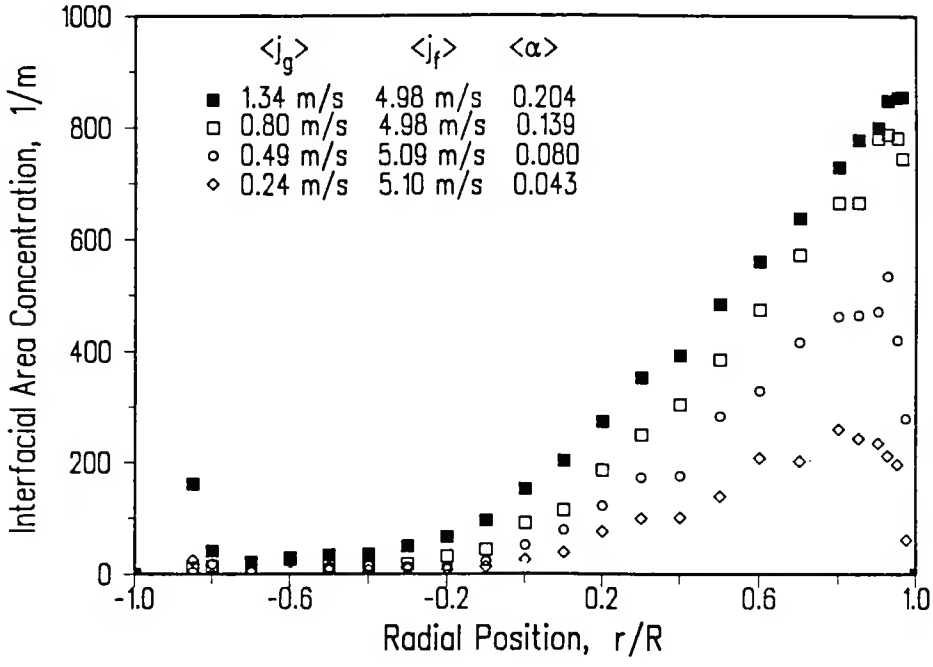

Figure 5.45 Effect of Gas Flow on Local Interfacial Area Concentration Profile at $\langle j_f \rangle \simeq 5$ m/s.

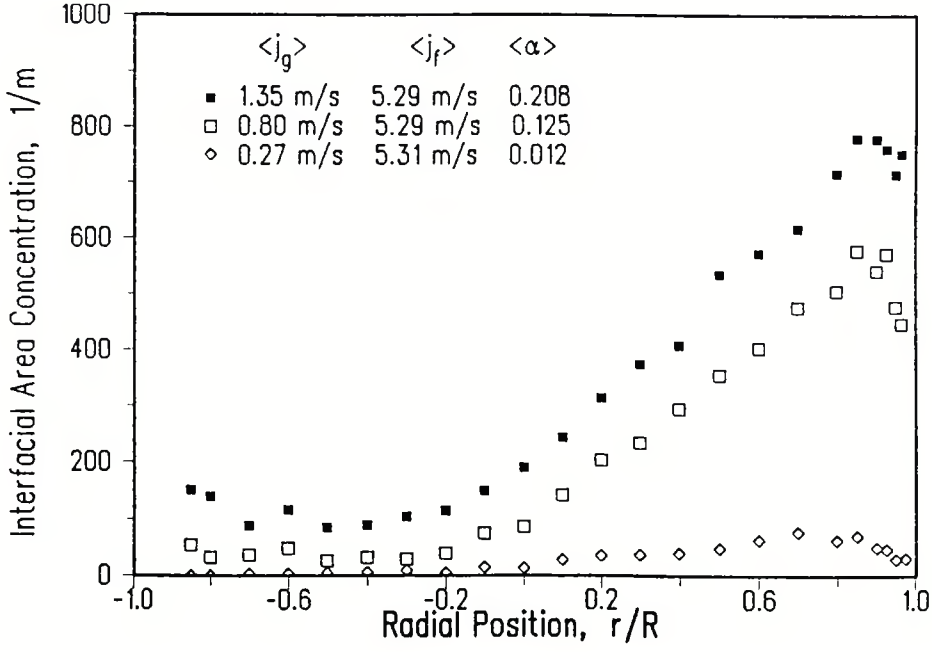

Figure 5.46 Effect of Gas Flow on Local Interfacial Area Concentration Profile at $\langle j_f \rangle \simeq 5.3$ m/s.

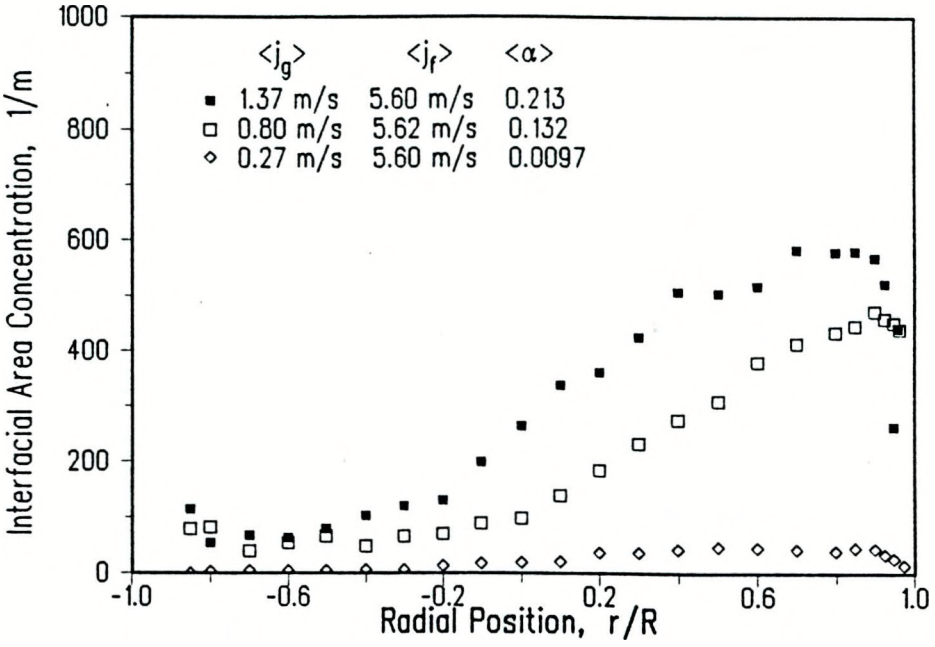

Figure 5.47 Effect of Gas Flow on Local Interfacial Area Concentration Profile at $\langle j_f \rangle \simeq 5.6$ m/s.

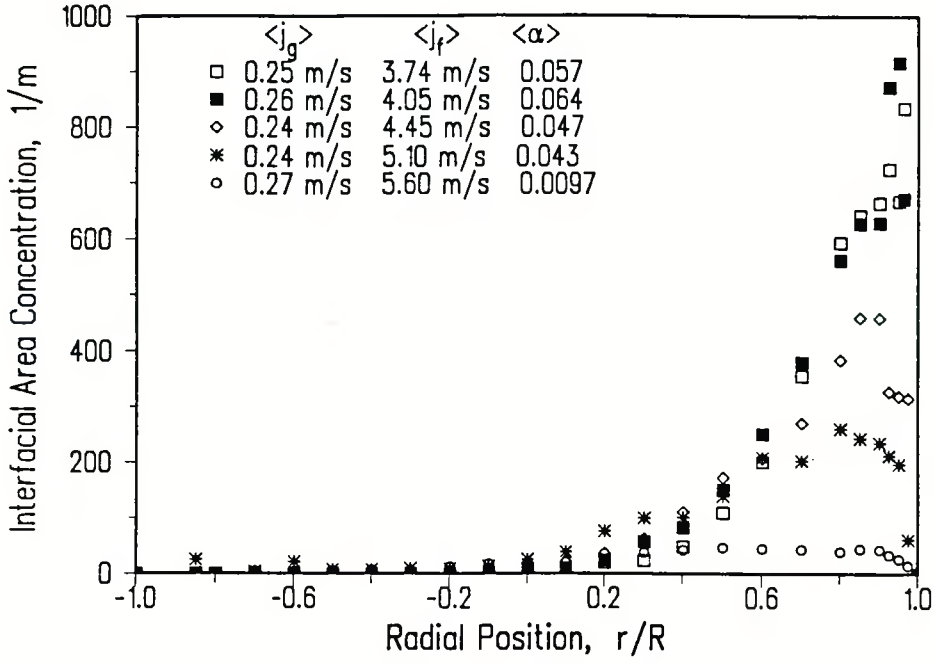

Figure 5.48 Effect of Liquid Flow on Local Interfacial Area Concentration Profile at $\langle j_g \rangle \simeq 0.25$ m/s.

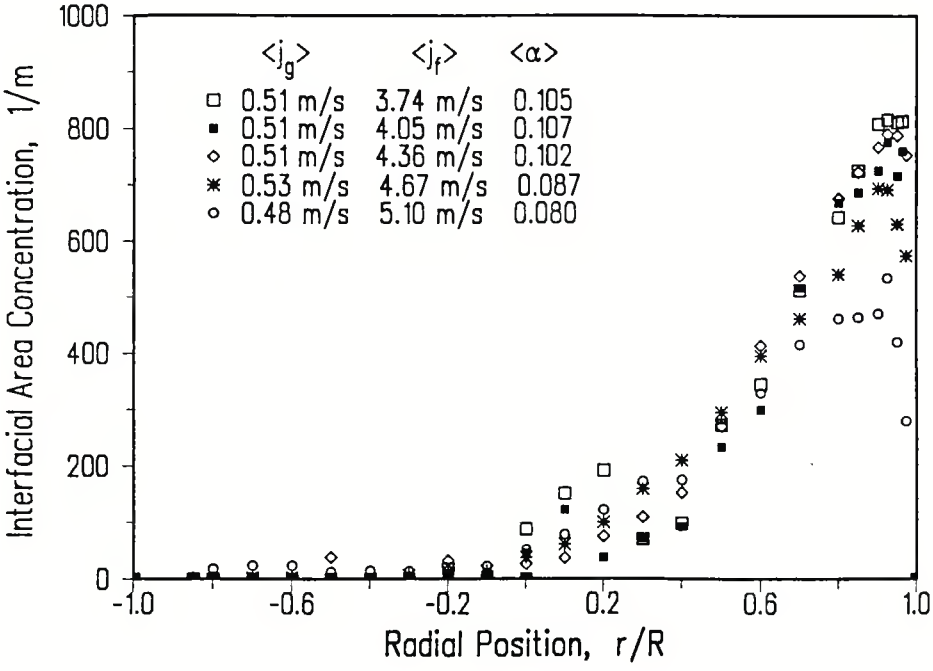

Figure 5.49 Effect of Liquid Flow on Local Interfacial Area Concentration Profile at $\langle j_g \rangle \simeq 0.5$ m/s.

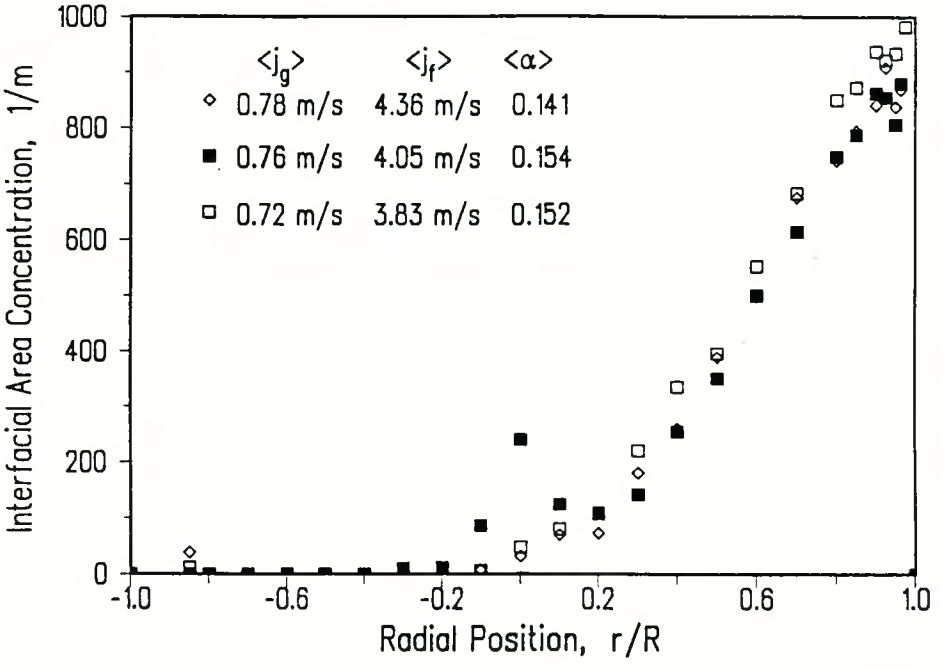

Figure 5.50 Effect of Liquid Flow on Local Interfacial Area Concentration Profile at $\langle j_g \rangle \simeq 0.76$ m/s.

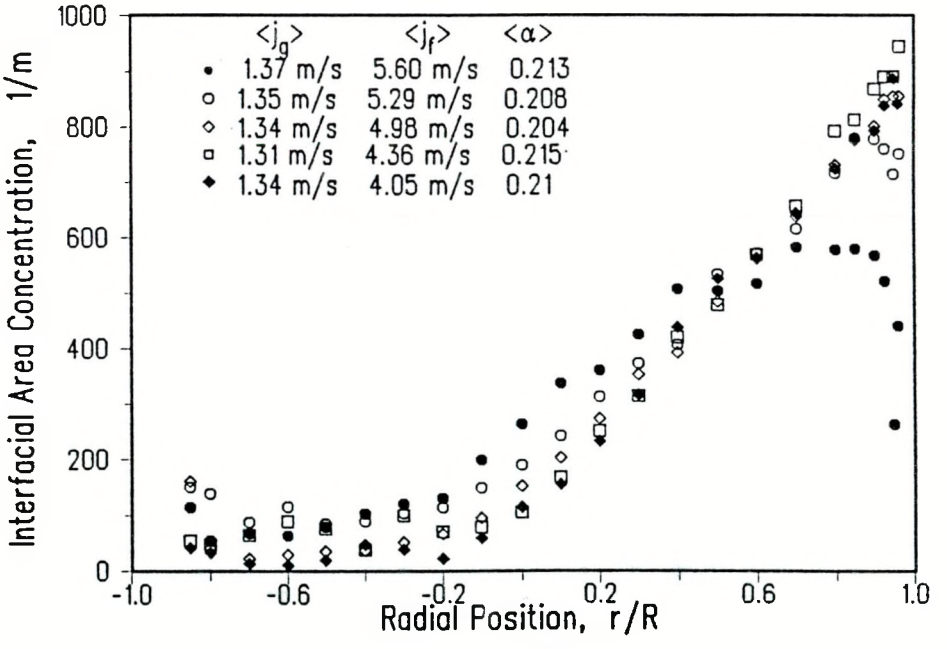

Figure 5.51 Effect of Liquid Flow on Local Interfacial Area Concentration Profile at $\langle j_g \rangle \simeq 1.3$ m/s.

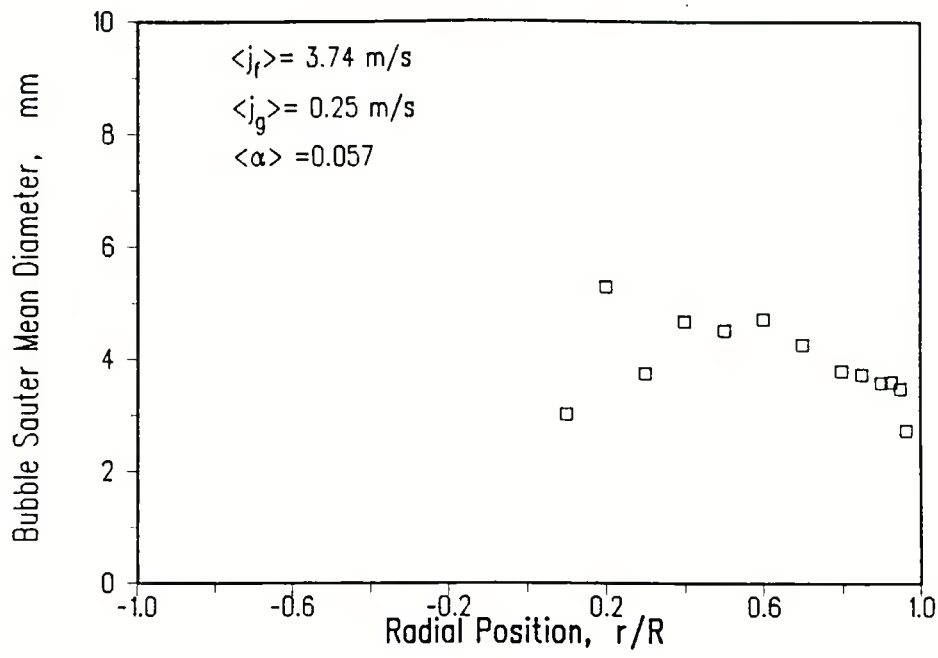

Figure 5.52 Sauter Mean Bubble Diameter at $\langle j_f \rangle$ = 3.74 m/s, $\langle j_g \rangle$ = 0.25 m/s, $\langle \alpha \rangle$ = 0.057.

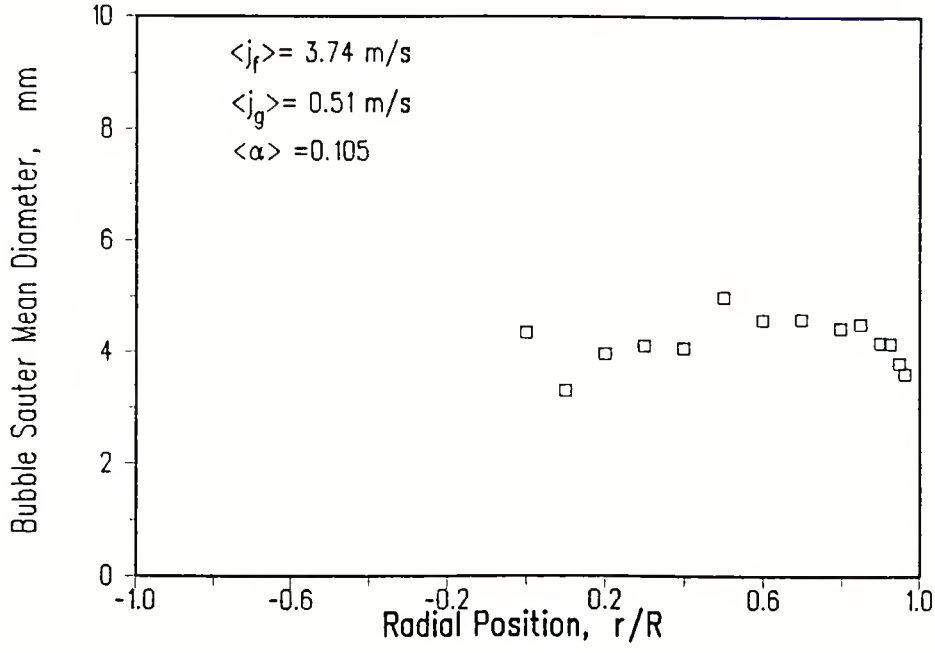

Figure 5.53 Sauter Mean Bubble Diameter at $\langle j_f \rangle$ = 3.74 m/s, $\langle j_g \rangle$ = 0.51 m/s, $\langle \alpha \rangle$ = 0.105.

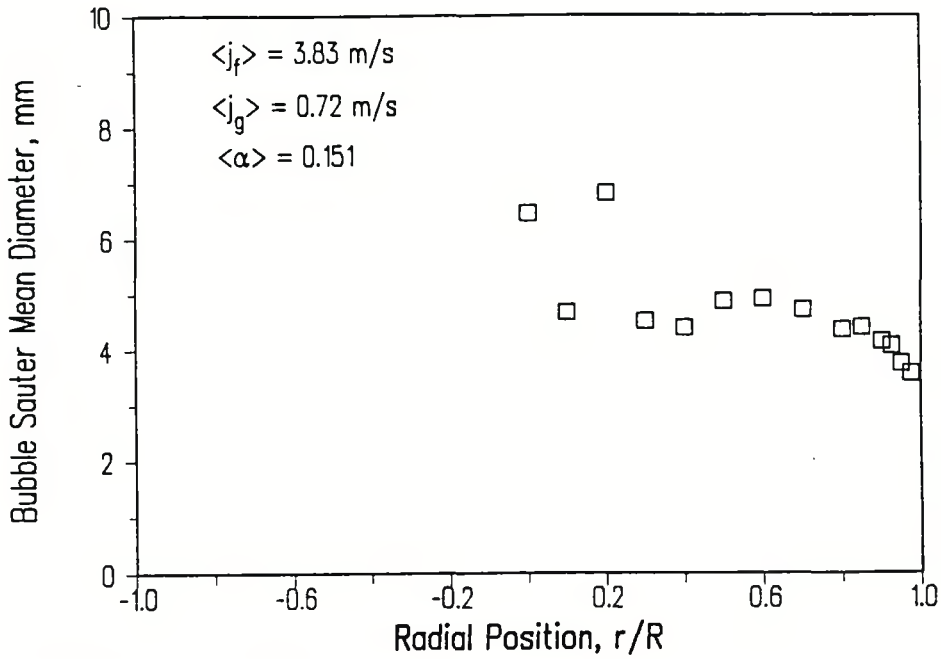

Figure 5.54 Sauter Mean Bubble Diameter at $\langle j_f \rangle$ = 3.83 m/s, $\langle j_g \rangle$ = 0.72 m/s, $\langle \alpha \rangle$ = 0.151.

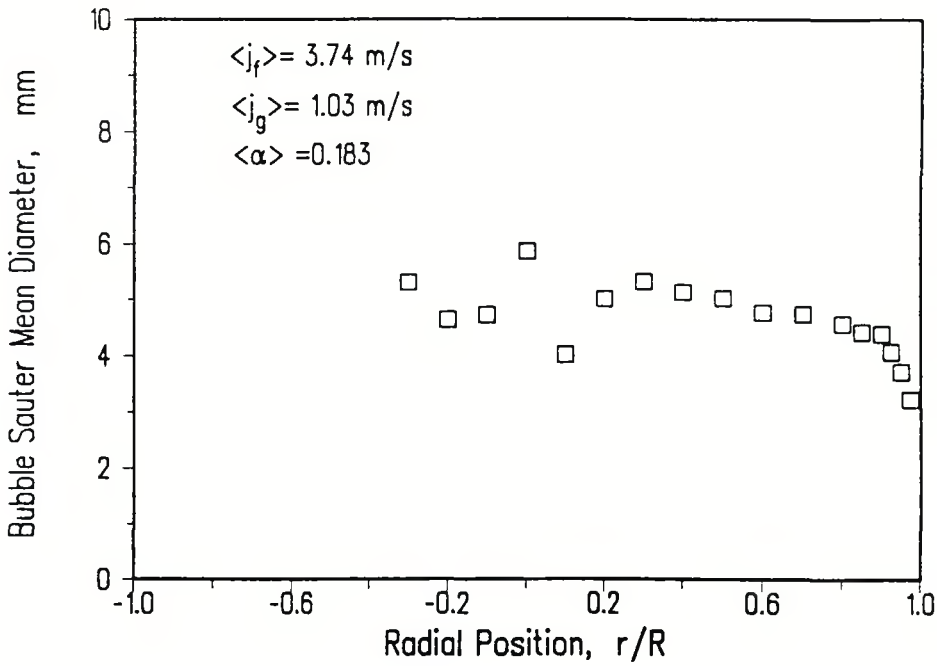

Figure 5.55 Sauter Mean Bubble Diameter at $\langle j_f \rangle$ = 3.74 m/s, $\langle j_g \rangle$ = 1.03 m/s, $\langle \alpha \rangle$ = 0.183.

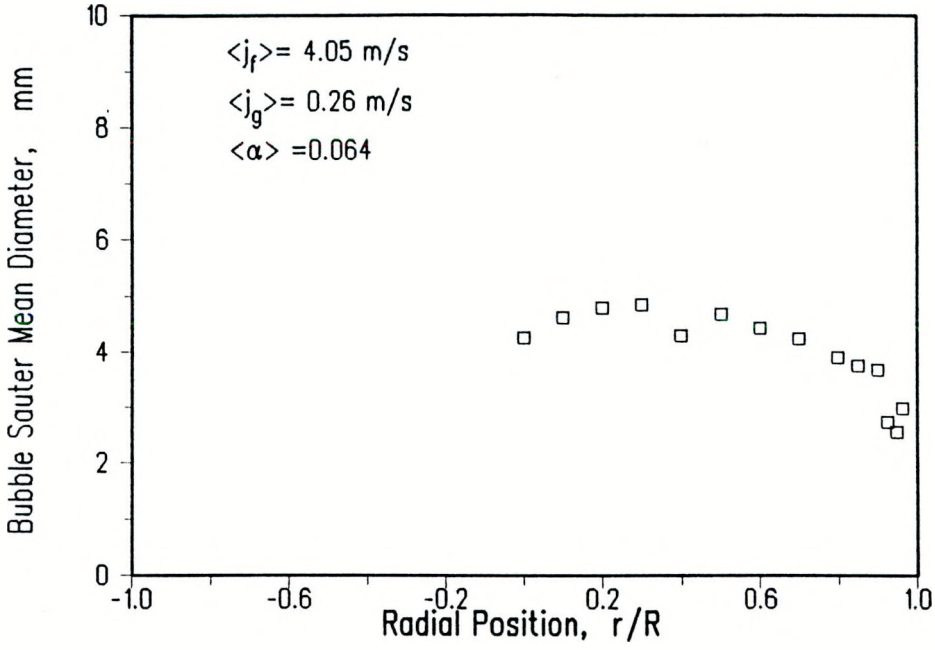

Figure 5.56 Sauter Mean Bubble Diameter at $\langle j_f \rangle$ = 4.05 m/s, $\langle j_g \rangle$ = 0.26 m/s, $\langle \alpha \rangle$ = 0.064.

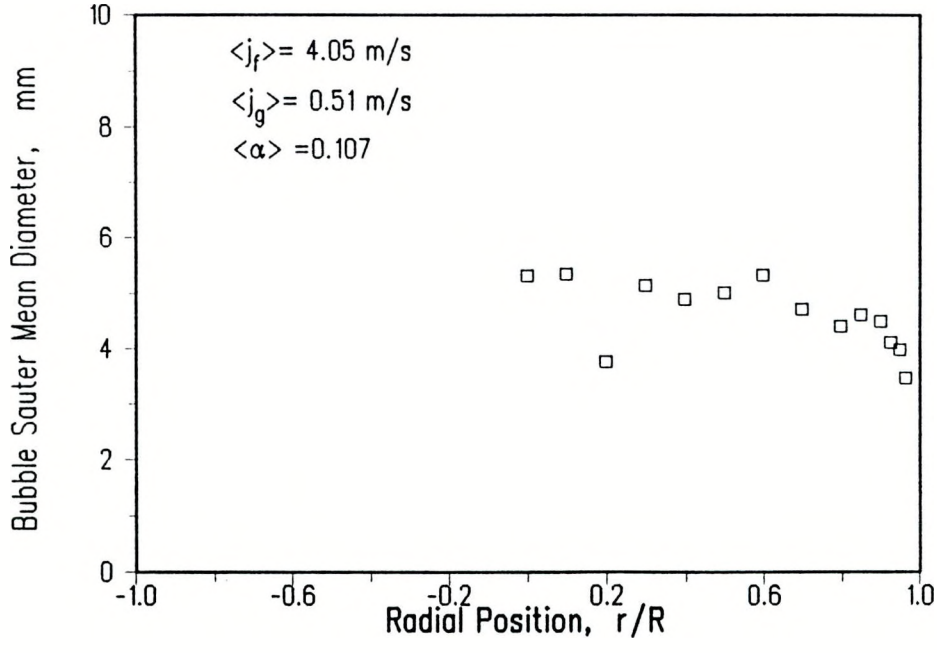

Figure 5.57 Sauter Mean Bubble Diameter at $\langle j_f \rangle$ = 4.05 m/s, $\langle j_g \rangle$ = 0.51 m/s, $\langle \alpha \rangle$ = 0.107.

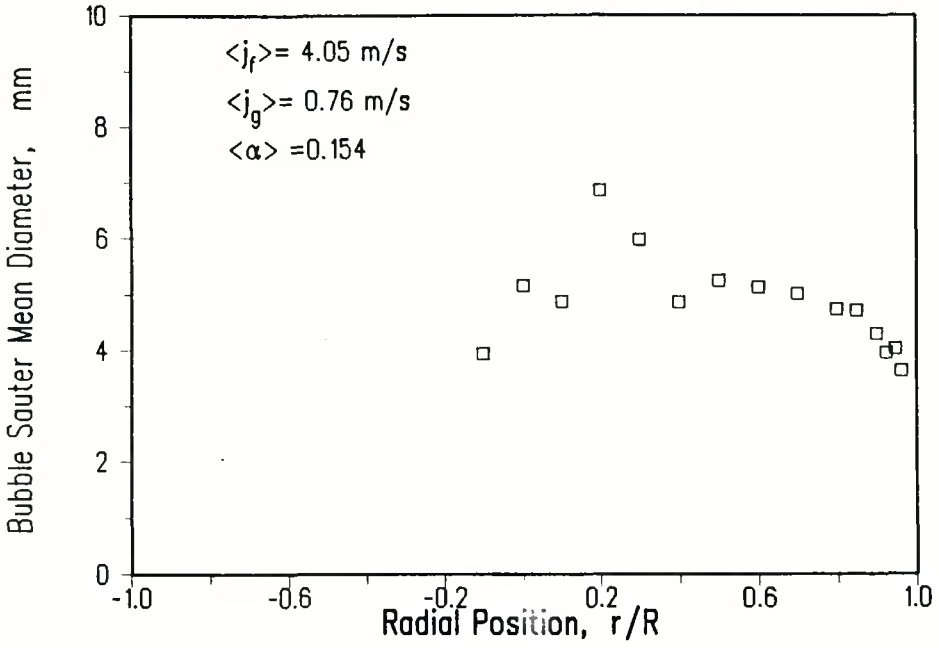

Figure 5.58 Sauter Mean Bubble Diameter at $\langle j_f \rangle$ = 4.05 m/s, $\langle j_g \rangle$ = 0.76 m/s, $\langle \alpha \rangle$ = 0.154.

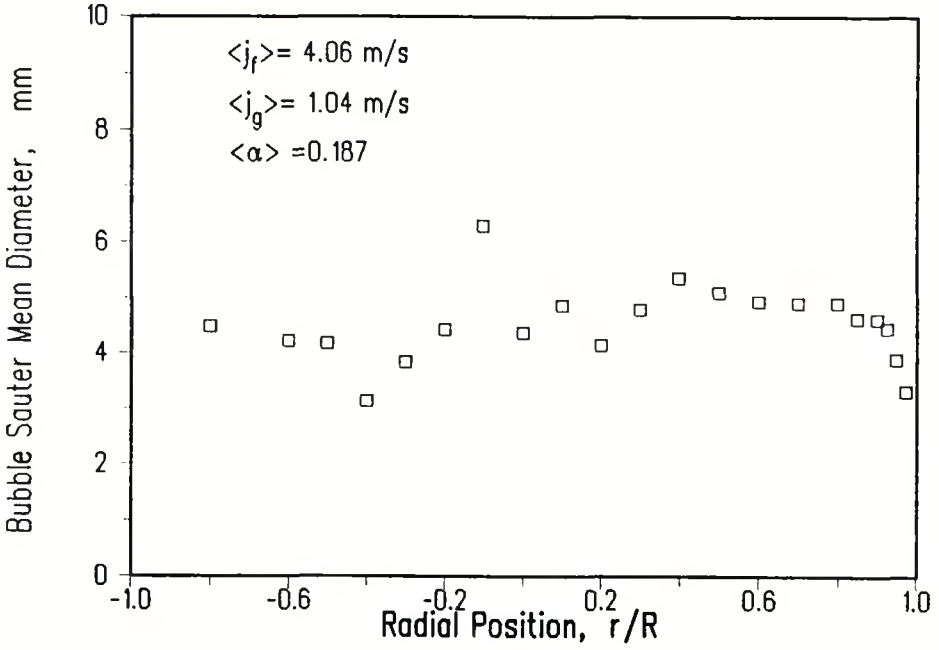

Figure 5.59 Sauter Mean Bubble Diameter at $\langle j_f \rangle$ = 4.05 m/s, $\langle j_g \rangle$ = 1.04 m/s, $\langle \alpha \rangle$ = 0.187.

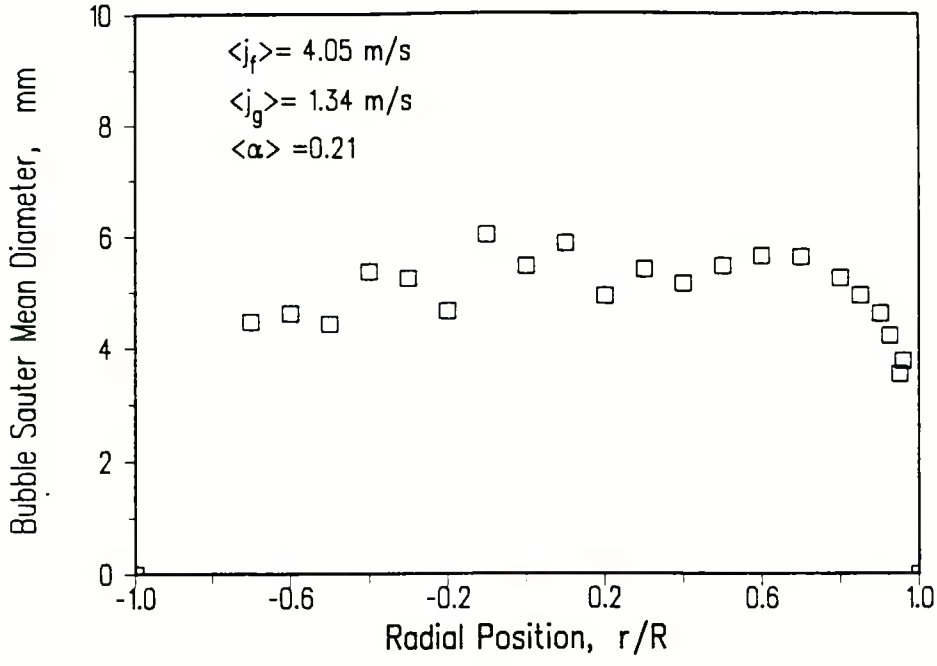

Figure 5.60 Sauter Mean Bubble Diameter at $\langle j_f \rangle$ = 4.05 m/s, $\langle j_g \rangle$ = 1.34 m/s, $\langle \alpha \rangle$ = 0.21.

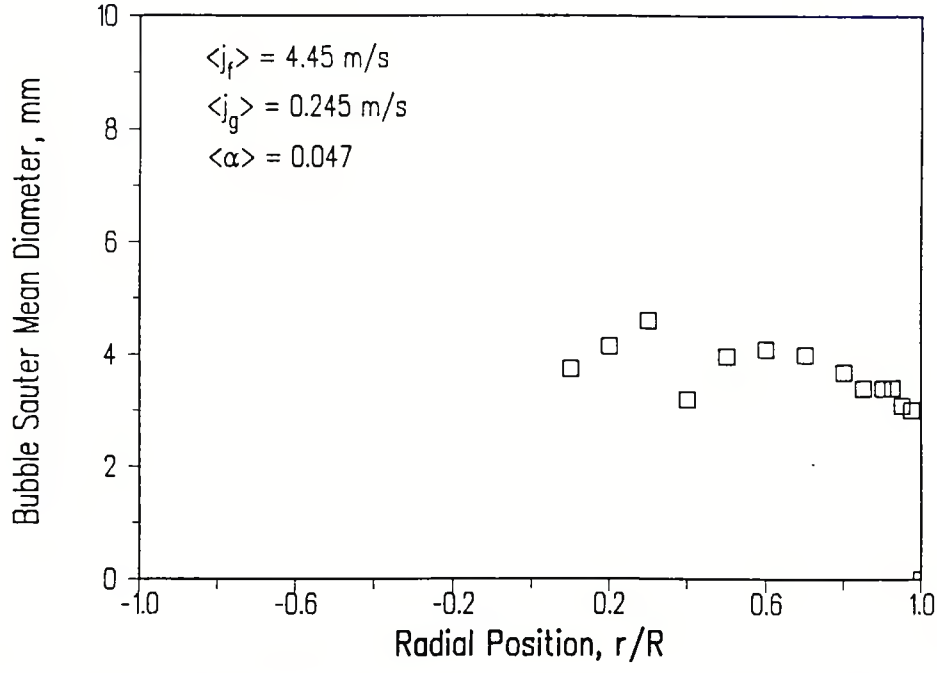

Figure 5.61 Sauter Mean Bubble Diameter at $\langle j_f \rangle$ = 4.45 m/s, $\langle j_g \rangle$ = 0.245 m/s, $\langle \alpha \rangle$ = 0.047.

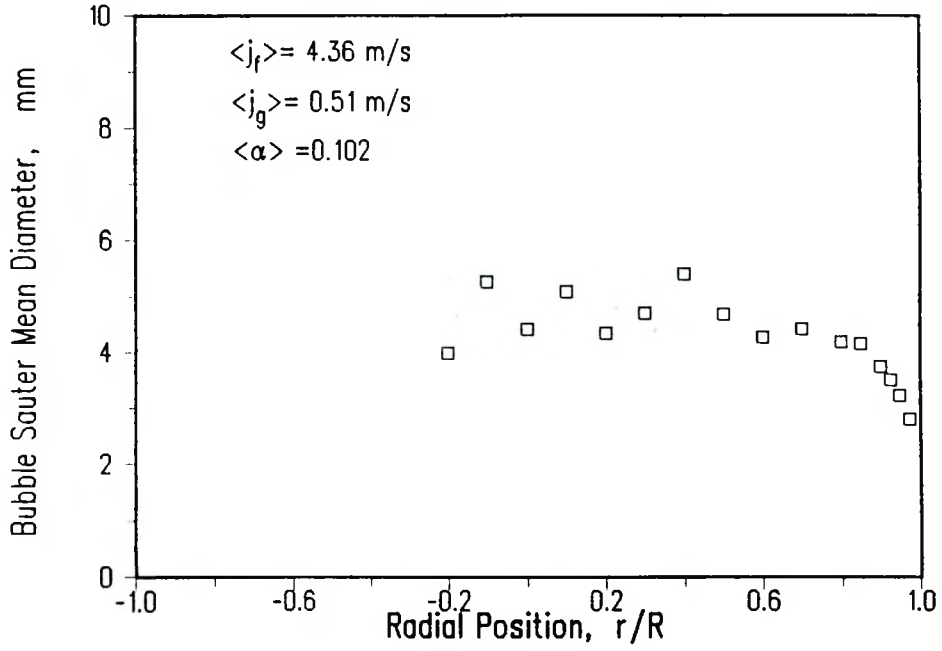

Figure 5.62 Sauter Mean Bubble Diameter at $\langle j_f \rangle$ = 4.36 m/s, $\langle j_g \rangle$ = 0.51 m/s, $\langle \alpha \rangle$ = 0.102.

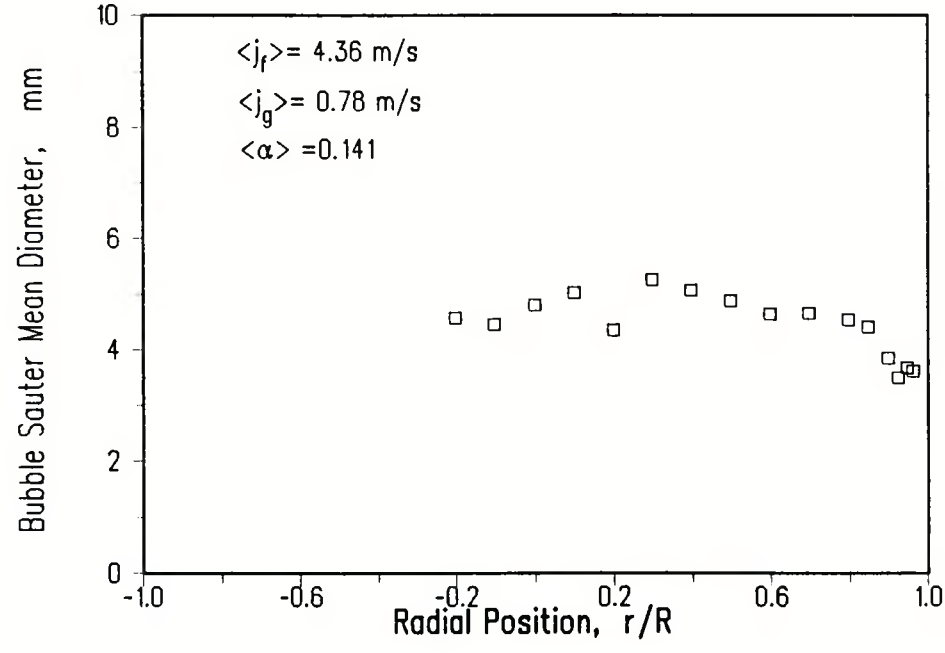

Figure 5.63 Sauter Mean Bubble Diameter at $\langle j_f \rangle$ = 4.36 m/s, $\langle j_g \rangle$ = 0.78 m/s, $\langle \alpha \rangle$ = 0.141.

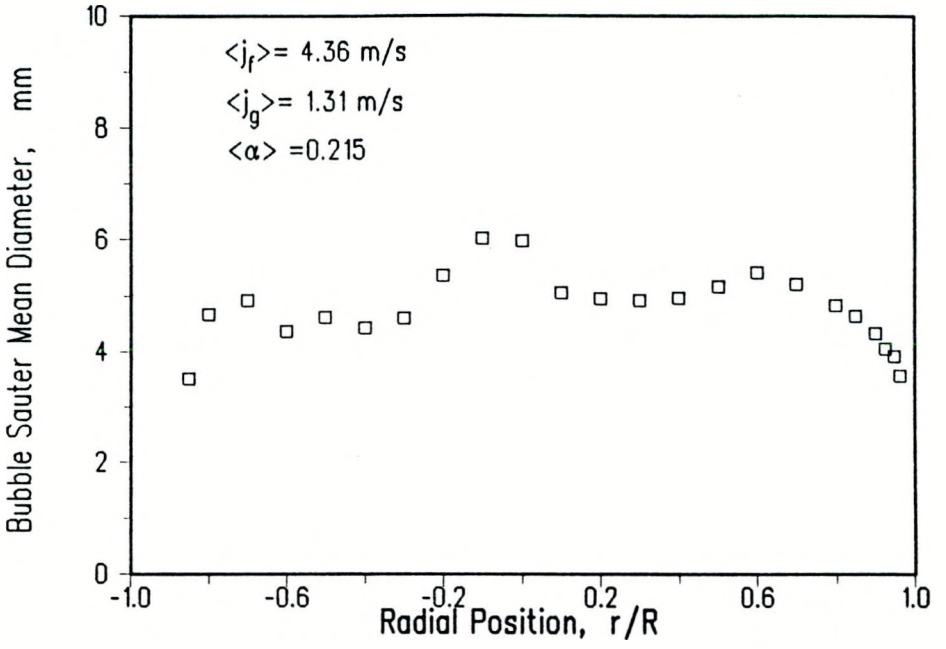

Figure 5.64 Sauter Mean Bubble Diameter at $\langle j_f \rangle$ = 4.36 m/s, $\langle j_g \rangle$ = 1.31 m/s, $\langle \alpha \rangle$ = 0.215.

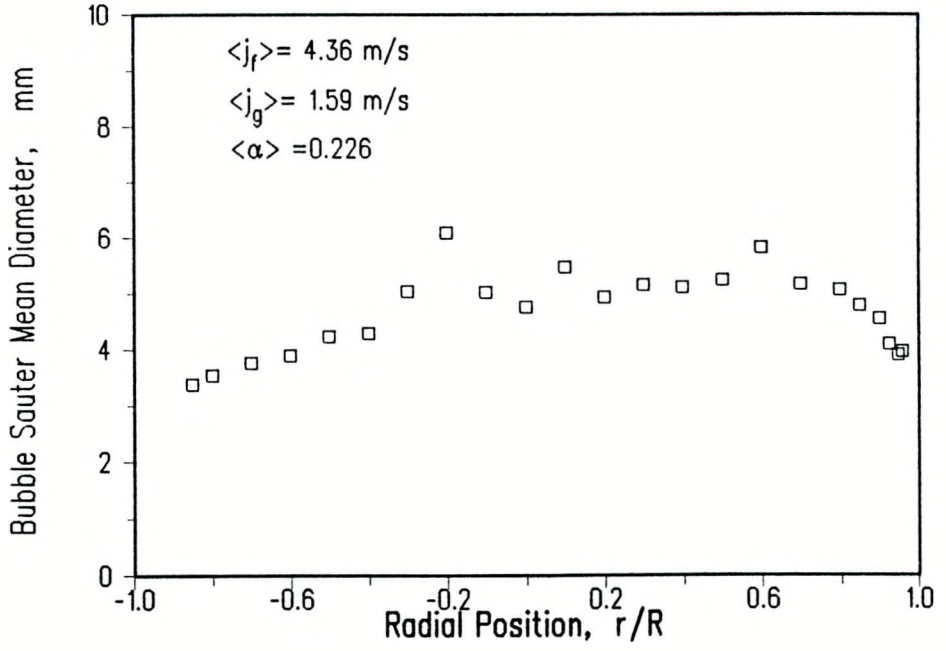

Figure 5.65 Sauter Mean Bubble Diameter at $\langle j_f \rangle$ = 4.36 m/s, $\langle j_g \rangle$ = 1.59 m/s, $\langle \alpha \rangle$ = 0.226.

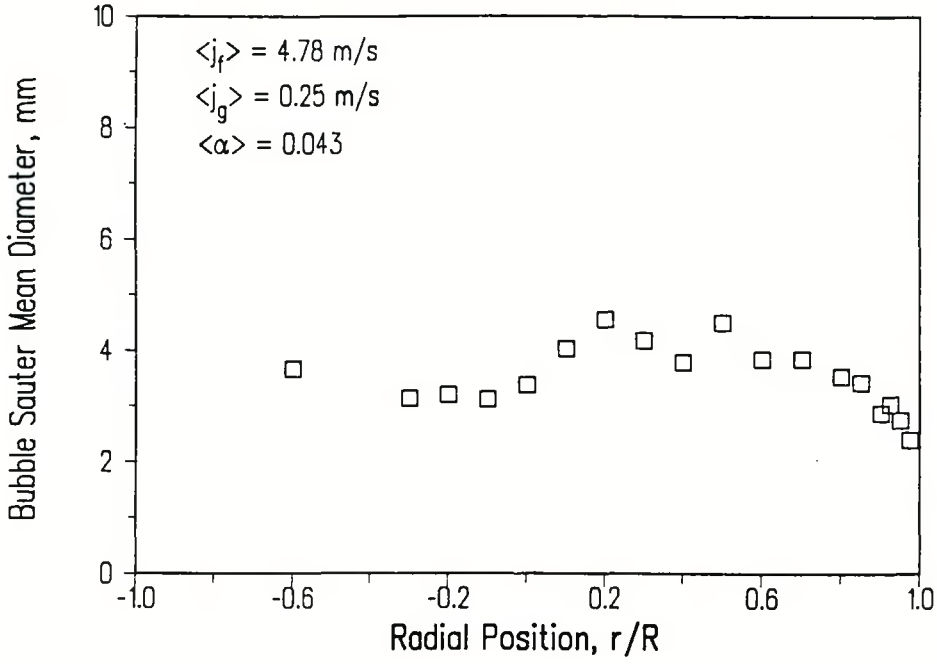

Figure 5.66 Sauter Mean Bubble Diameter at $\langle j_f \rangle$ = 4.78 m/s, $\langle j_g \rangle$ = 0.25 m/s, $\langle \alpha \rangle$ = 0.043.

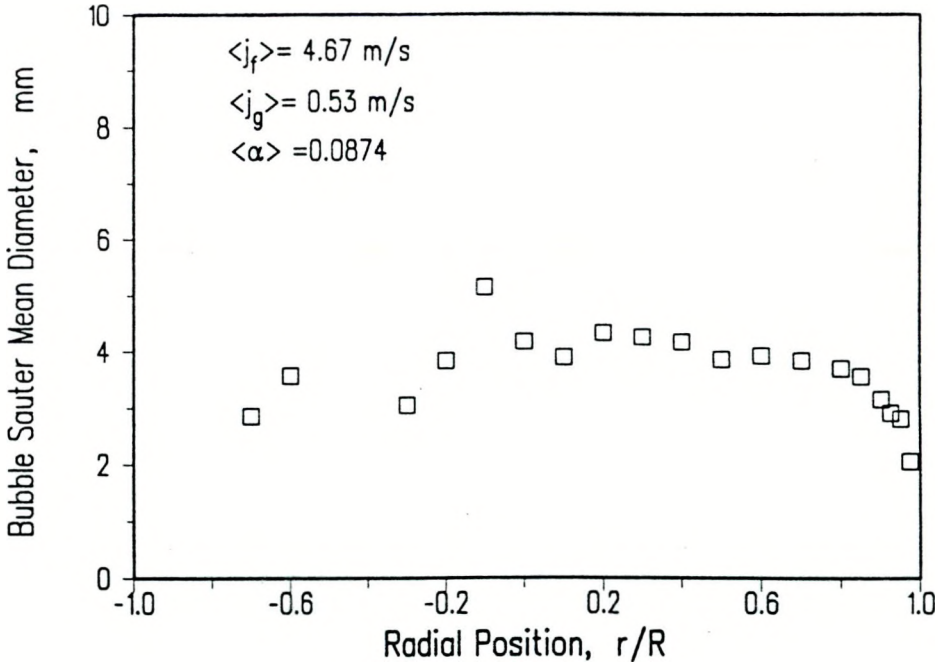

Figure 5.67 Sauter Mean Bubble Diameter at $\langle j_f \rangle$ = 4.67 m/s, $\langle j_g \rangle$ = 0.53 m/s, $\langle \alpha \rangle$ = 0.087.

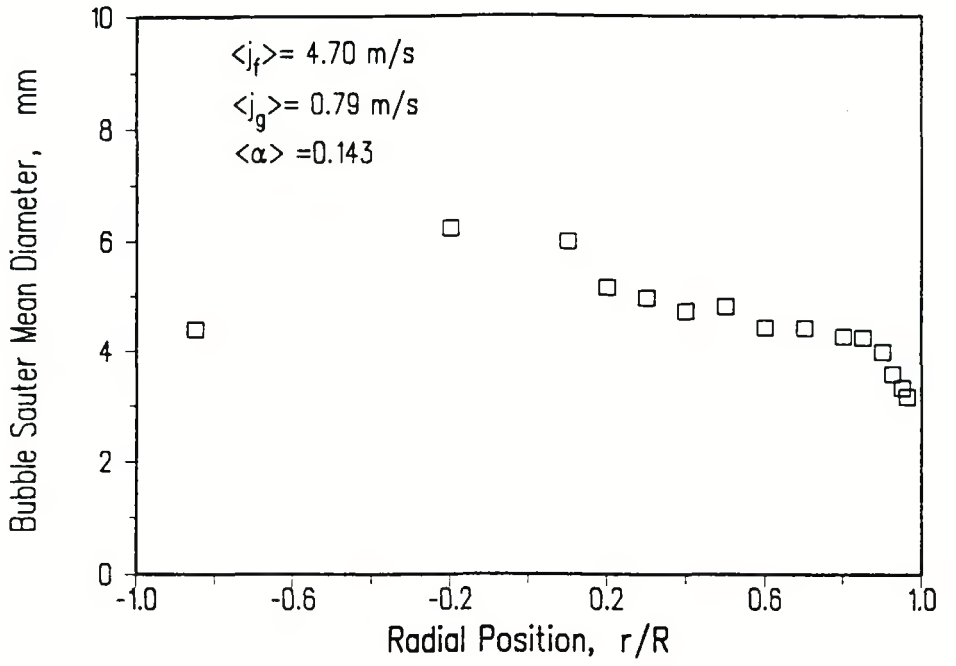

Figure 5.68 Sauter Mean Bubble Diameter at $\langle j_f \rangle$ = 4.7 m/s, $\langle j_g \rangle$ = 0.79 m/s, $\langle \alpha \rangle$ = 0.143.

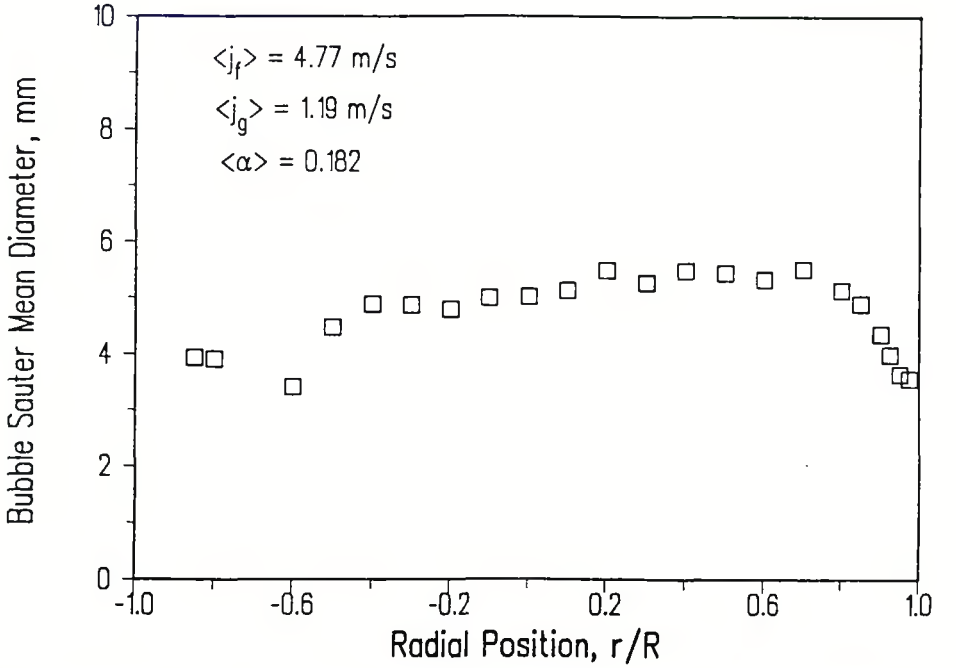

Figure 5.69 Sauter Mean Bubble Diameter at $\langle j_f \rangle$ = 4.77 m/s, $\langle j_g \rangle$ = 1.19 m/s, $\langle \alpha \rangle$ = 0.182.

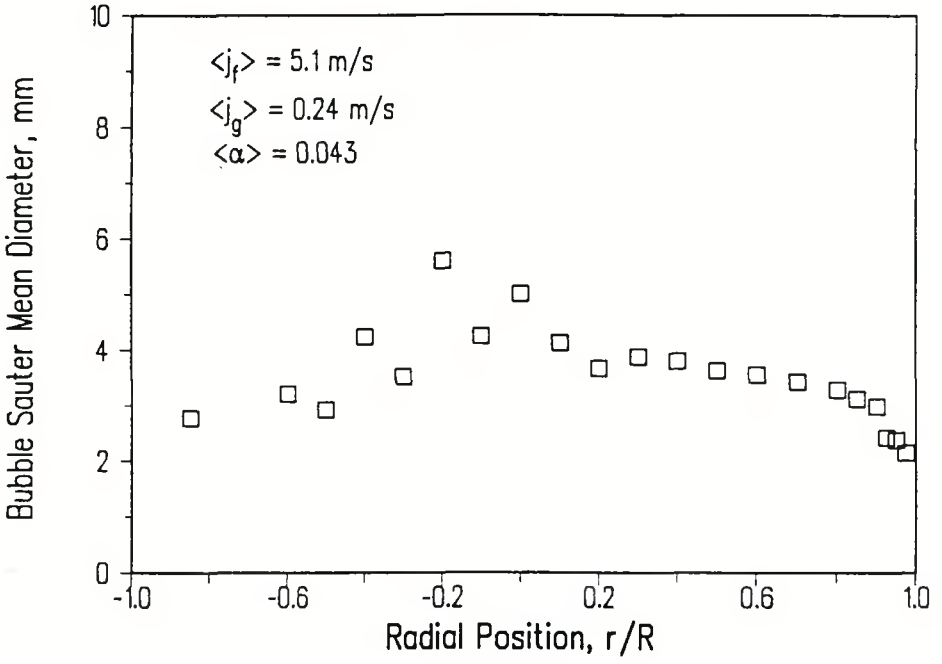

Figure 5.70 Sauter Mean Bubble Diameter at $\langle j_f \rangle$ = 5.10 m/s, $\langle j_g \rangle$ = 0.24 m/s, $\langle \alpha \rangle$ = 0.043.

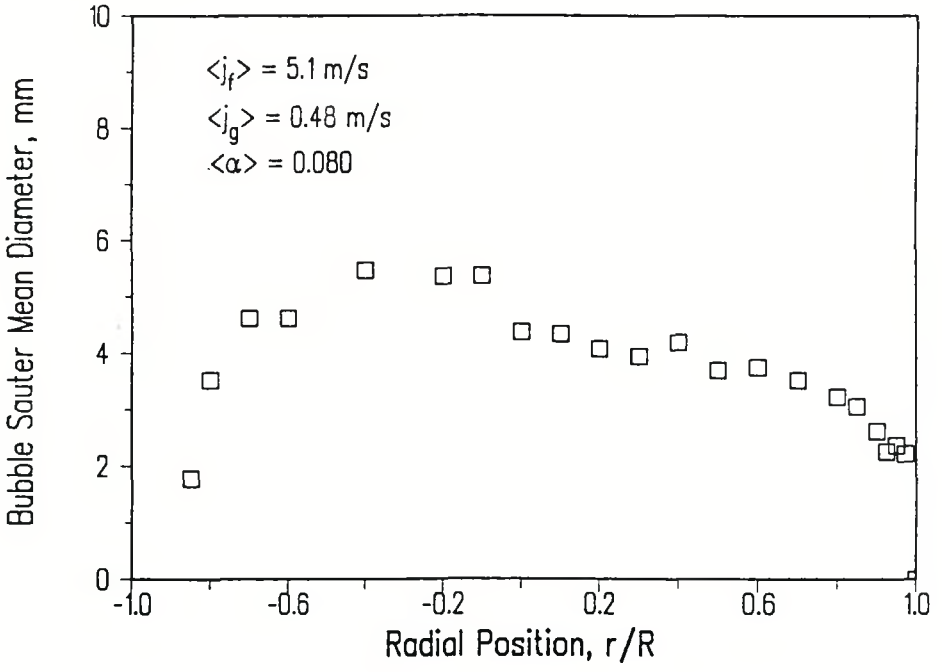

Figure 5.71 Sauter Mean Bubble Diameter at $\langle j_f \rangle$ = 5.10 m/s, $\langle j_g \rangle$ = 0.48 m/s, $\langle \alpha \rangle$ = 0.080.

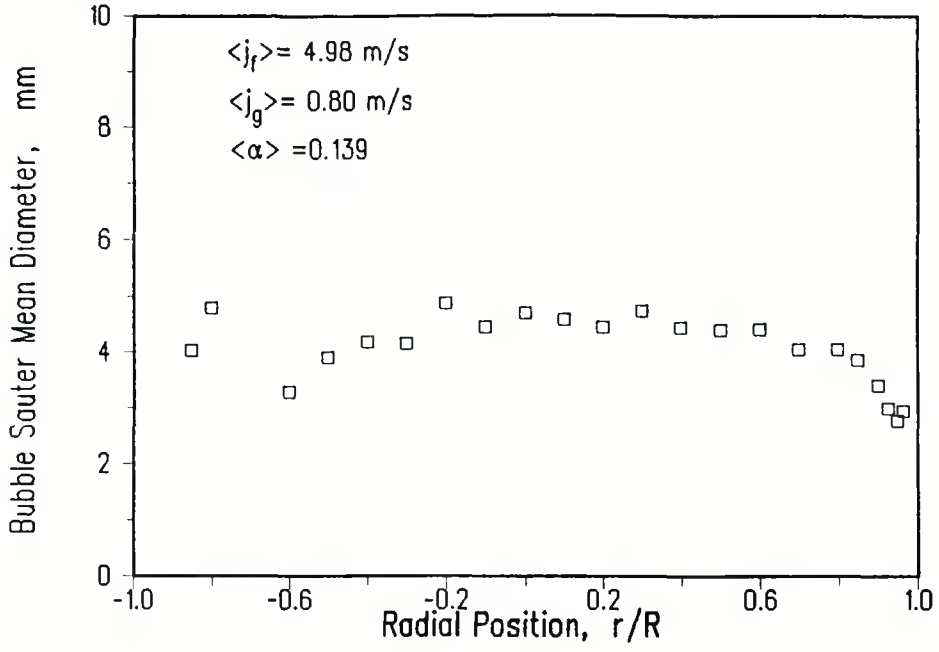

Figure 5.72 Sauter Mean Bubble Diameter at $\langle j_f \rangle$ = 4.98 m/s, $\langle j_g \rangle$ = 0.80 m/s, $\langle \alpha \rangle$ = 0.139.

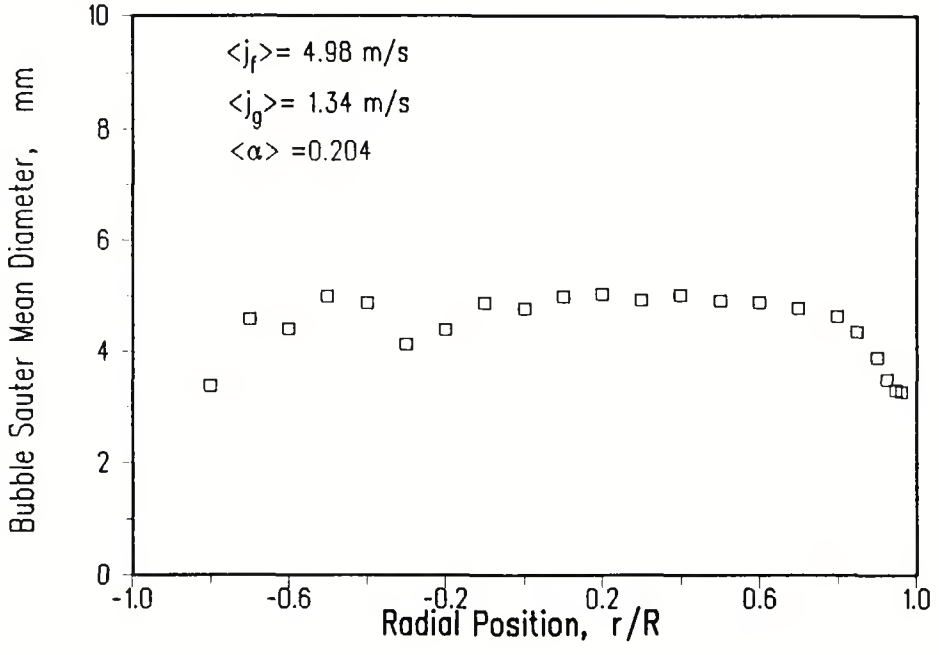

Figure 5.73 Sauter Mean Bubble Diameter at $\langle j_f \rangle$ = 4.98 m/s, $\langle j_g \rangle$ = 1.34 m/s, $\langle \alpha \rangle$ = 0.204.

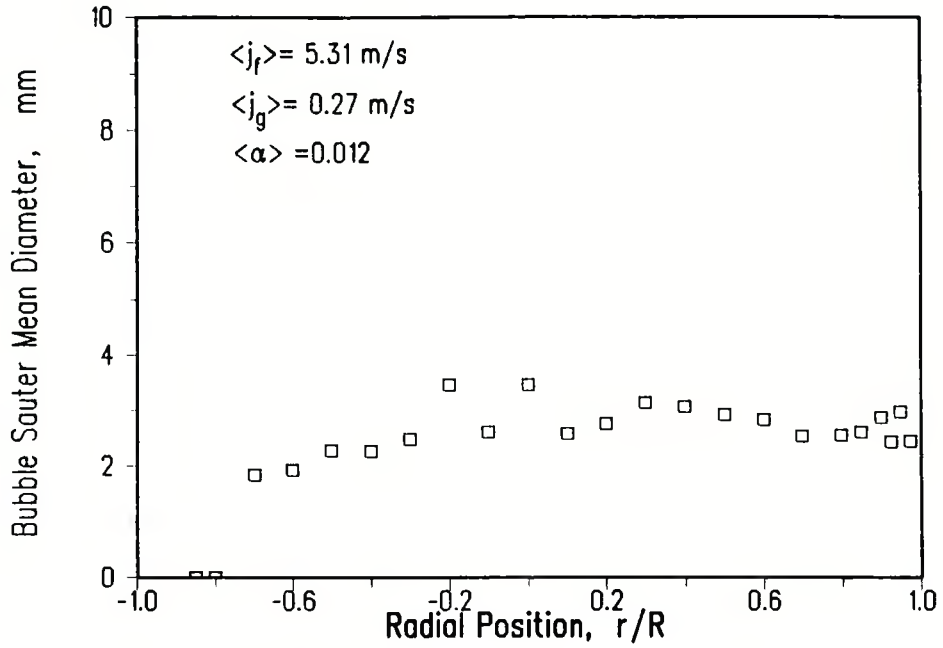

Figure 5.74 Sauter Mean Bubble Diameter at $\langle j_f \rangle$ = 5.31 m/s, $\langle j_g \rangle$ = 0.27 m/s, $\langle \alpha \rangle$ = 0.012.

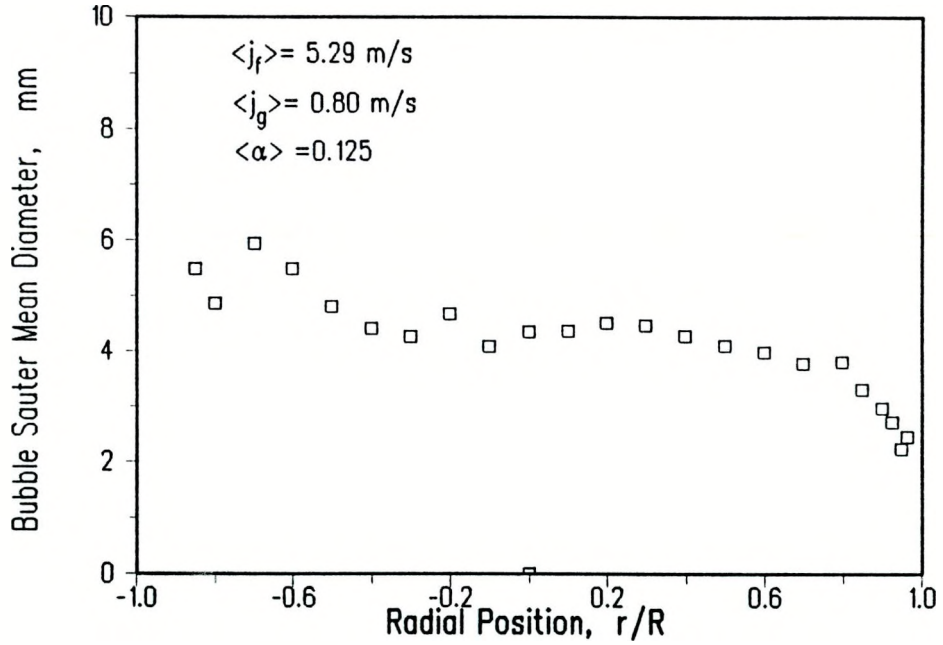

Figure 5.75 Sauter Mean Bubble Diameter at $\langle j_f \rangle$ = 5.29 m/s, $\langle j_g \rangle$ = 0.80 m/s, $\langle \alpha \rangle$ = 0.125.

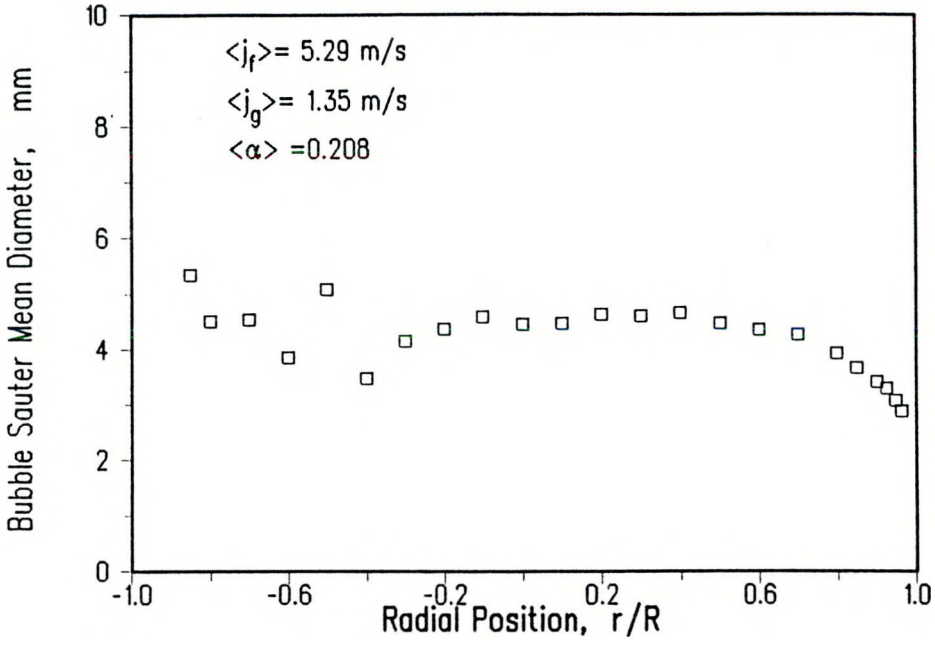

Figure 5.76 Sauter Mean Bubble Diameter at $\langle j_f \rangle$ = 5.29 m/s, $\langle j_g \rangle$ = 1.35 m/s, $\langle \alpha \rangle$ = 0.208.

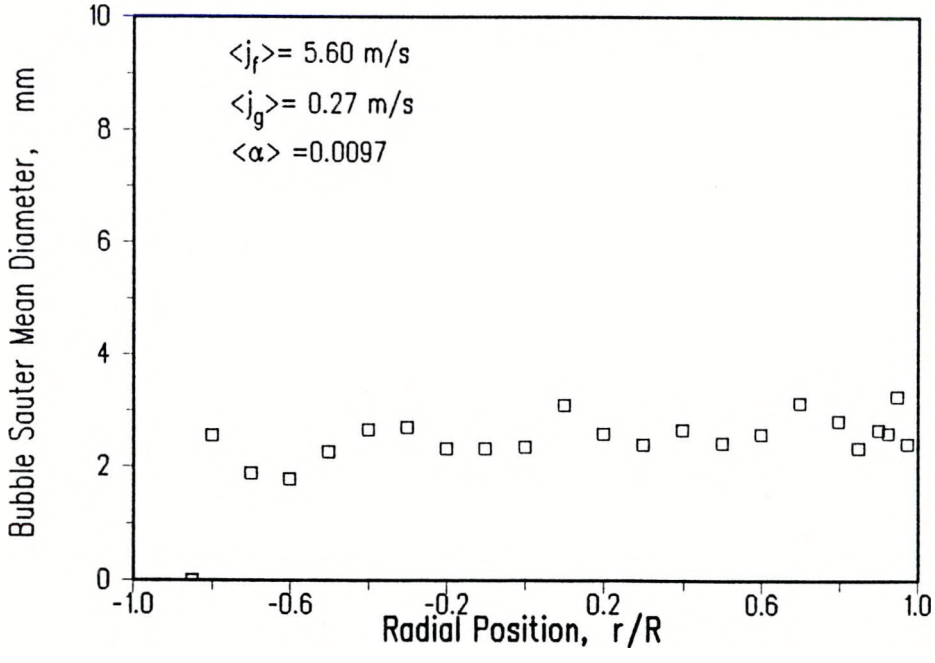

Figure 5.77 Sauter Mean Bubble Diameter at $\langle j_f \rangle$ = 5.6 m/s, $\langle j_g \rangle$ = 0.27 m/s, $\langle \alpha \rangle$ = 0.00976.

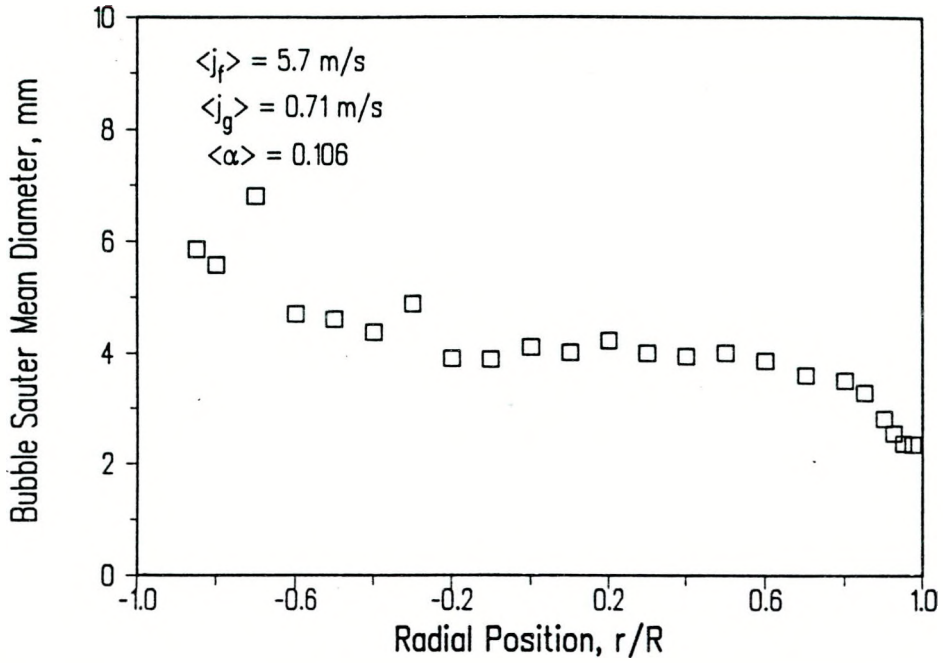

Figure 5.78 Sauter Mean Bubble Diameter at $\langle j_f \rangle$ = 5.7 m/s, $\langle j_g \rangle$ = 0.71 m/s, $\langle \alpha \rangle$ = 0.106.

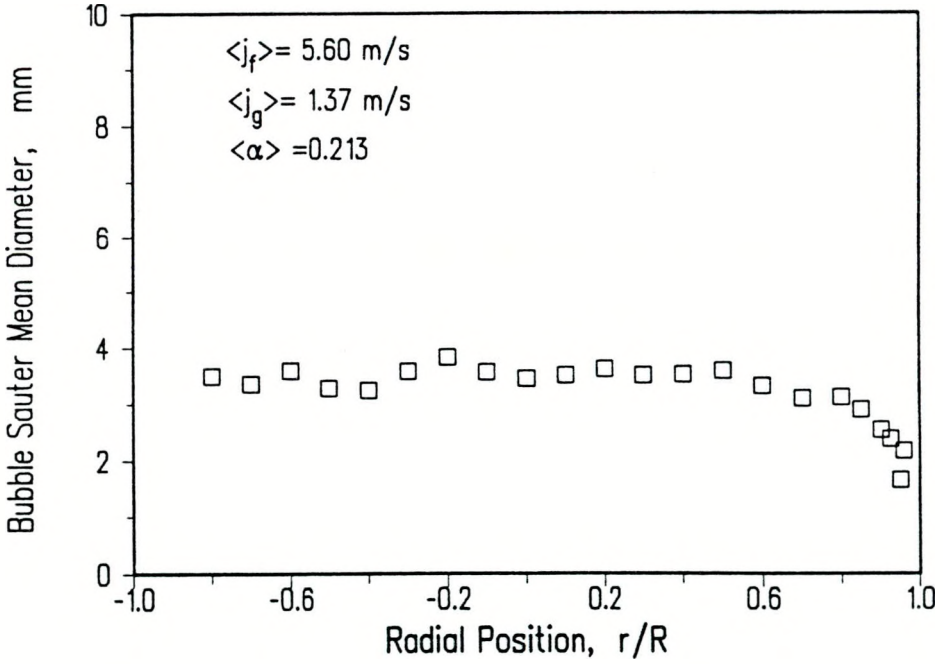

Figure 5.79 Sauter Mean Bubble Diameter at $\langle j_f \rangle$ = 5.6 m/s, $\langle j_g \rangle$ = 1.37 m/s, $\langle \alpha \rangle$ = 0.213.

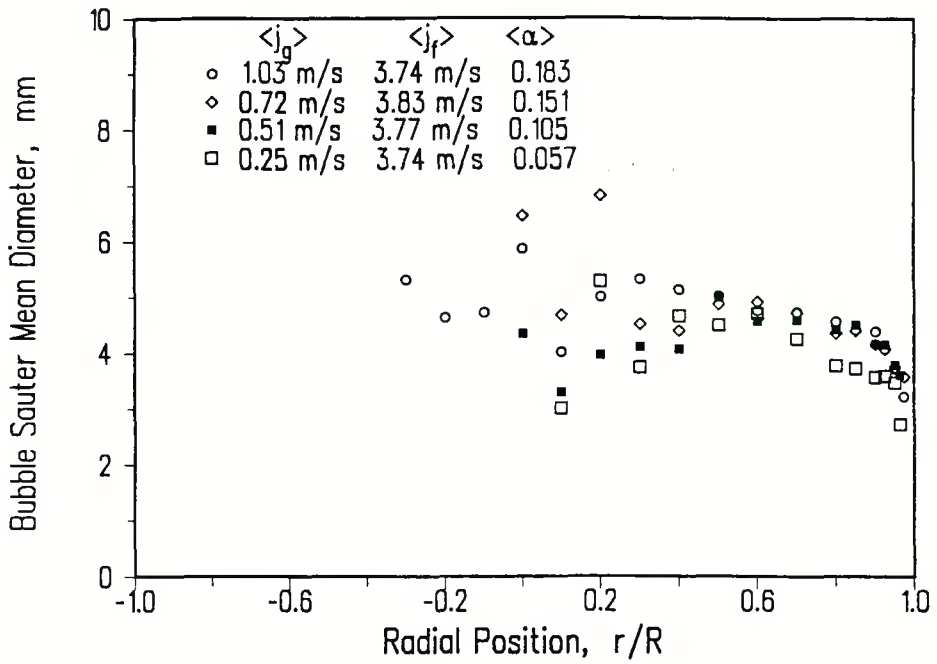

Figure 5.80 Effect of Gas Flow on Sauter Mean Bubble Diameter at $\langle j_f \rangle$ = 3.7 m/s.

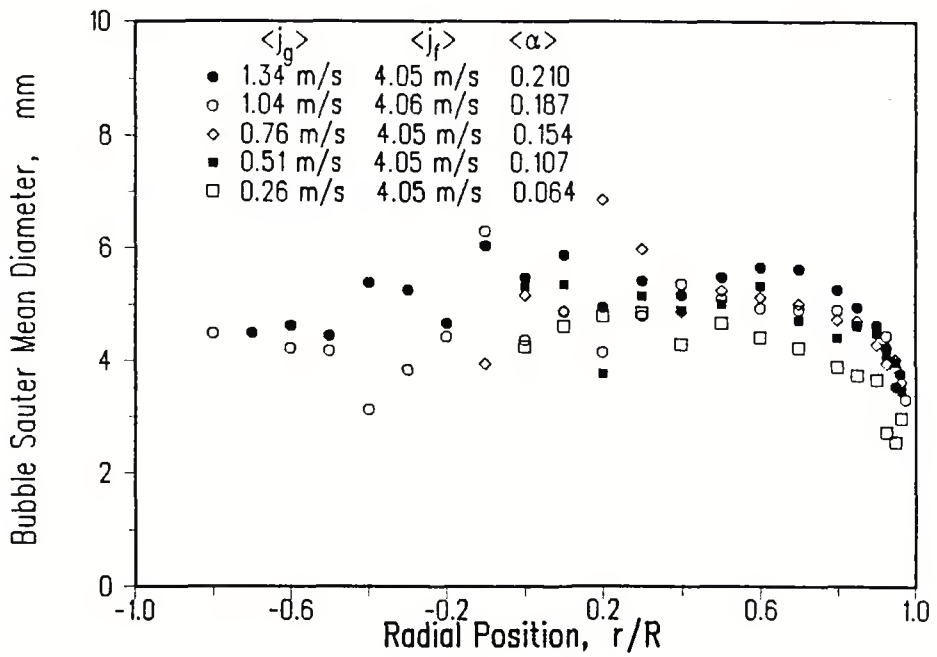

Figure 5.81 Effect of Gas Flow on Sauter Mean Bubble Diameter at $\langle j_f \rangle \simeq 4$ m/s.

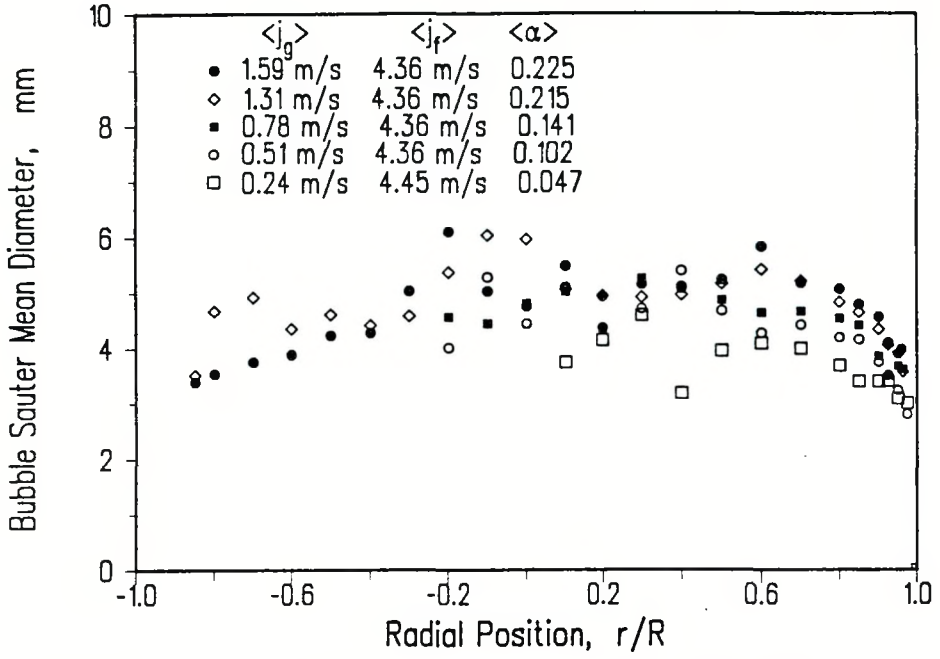

Figure 5.82 Effect of Gas Flow on Sauter Mean Bubble Diameter at $\langle j_f \rangle$ = 4.36 m/s.

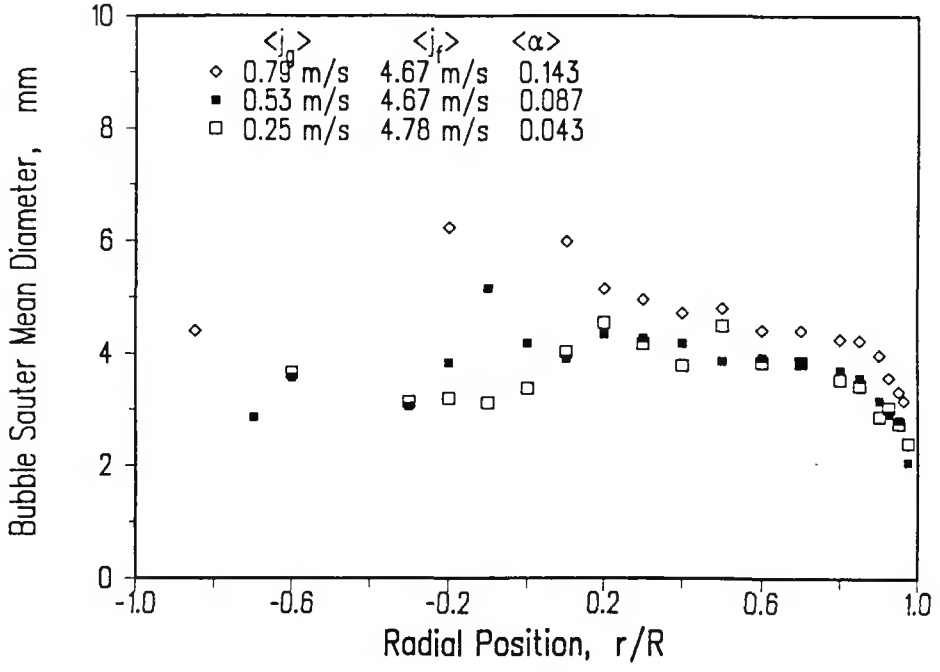

Figure 5.83 Effect of Gas Flow on Sauter Mean Bubble Diameter at $\langle j_f \rangle$ = 4.67 m/s.

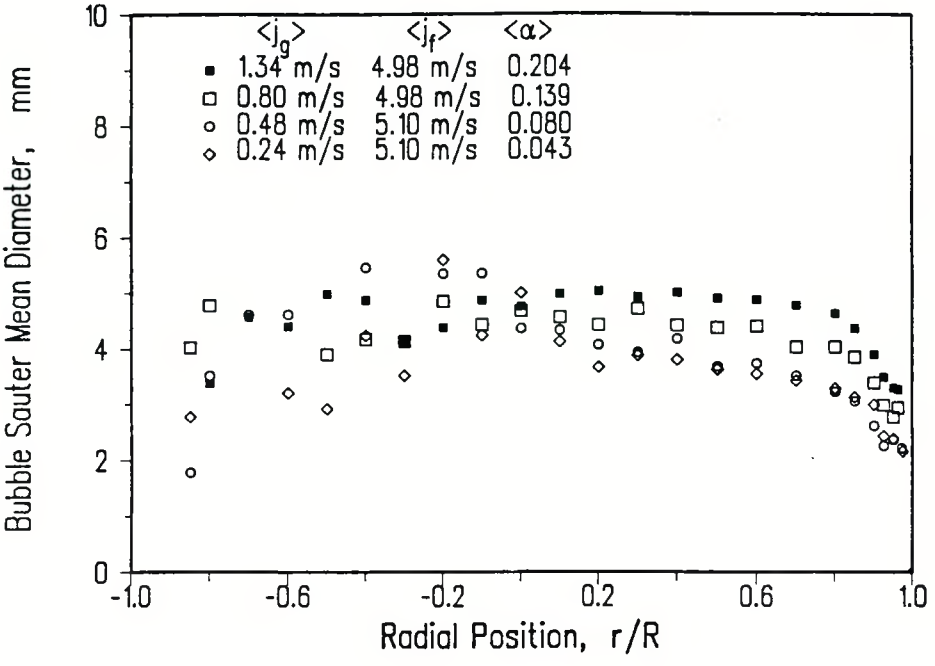

Figure 5.84 Effect of Gas Flow on Sauter Mean Bubble Diameter at $\langle j_f \rangle \simeq 5$ m/s.

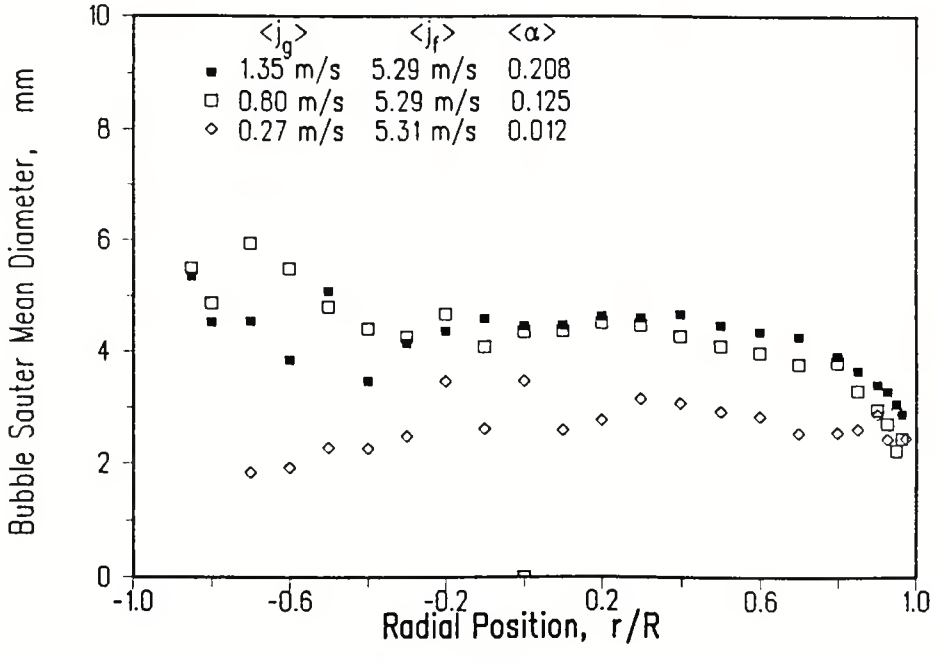

Figure 5.85 Effect of Gas Flow on Sauter Mean Bubble Diameter at $\langle j_f \rangle \simeq 5.3$ m/s.

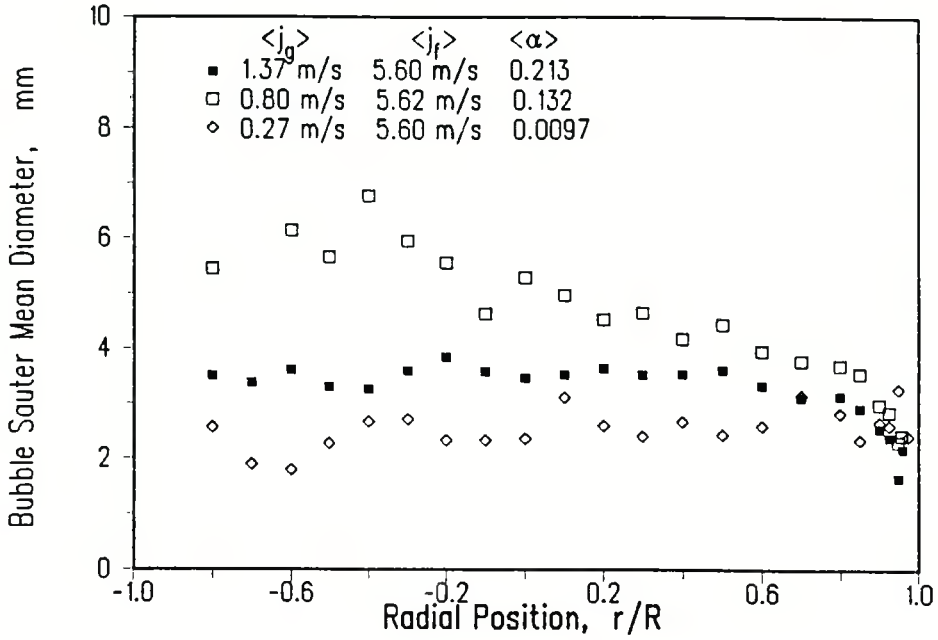

Figure 5.86 Effect of Gas Flow on Sauter Mean Bubble Diameter at $\langle j_f \rangle \simeq 5.6$ m/s.

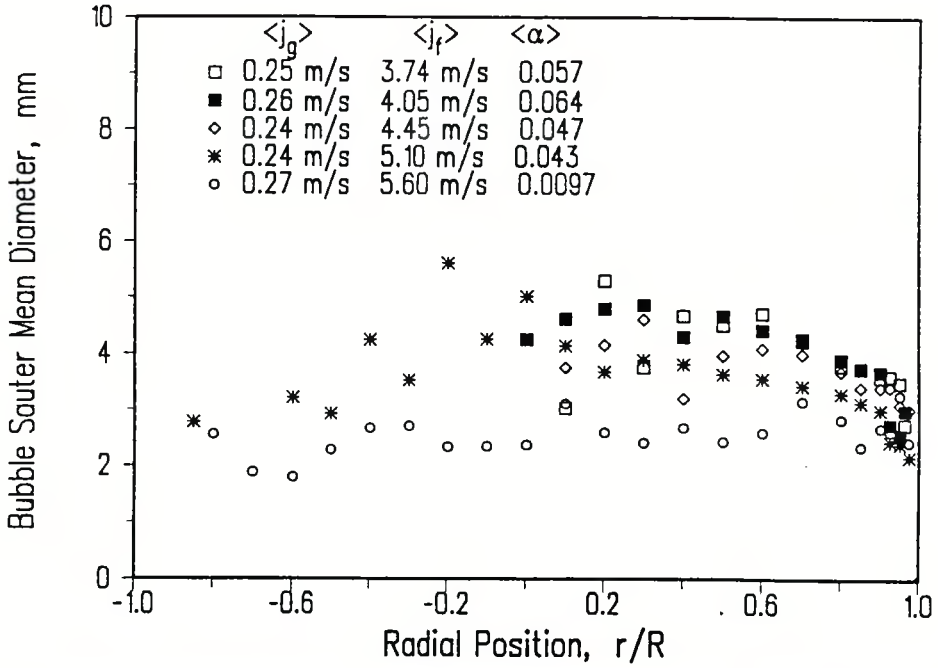

Figure 5.87 Effect of Liquid Flow on Sauter Mean Bubble Diameter at $\langle j_g \rangle \simeq 0.25$ m/s.

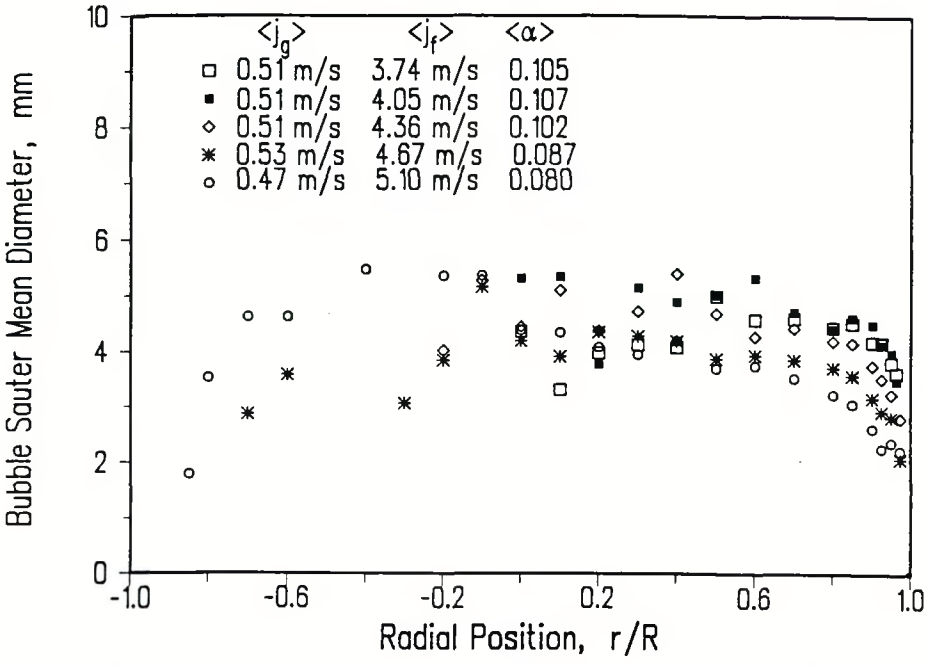

Figure 5.88 Effect of Liquid Flow on Sauter Mean Bubble Diameter at $\langle j_g \rangle \simeq 0.5$ m/s.

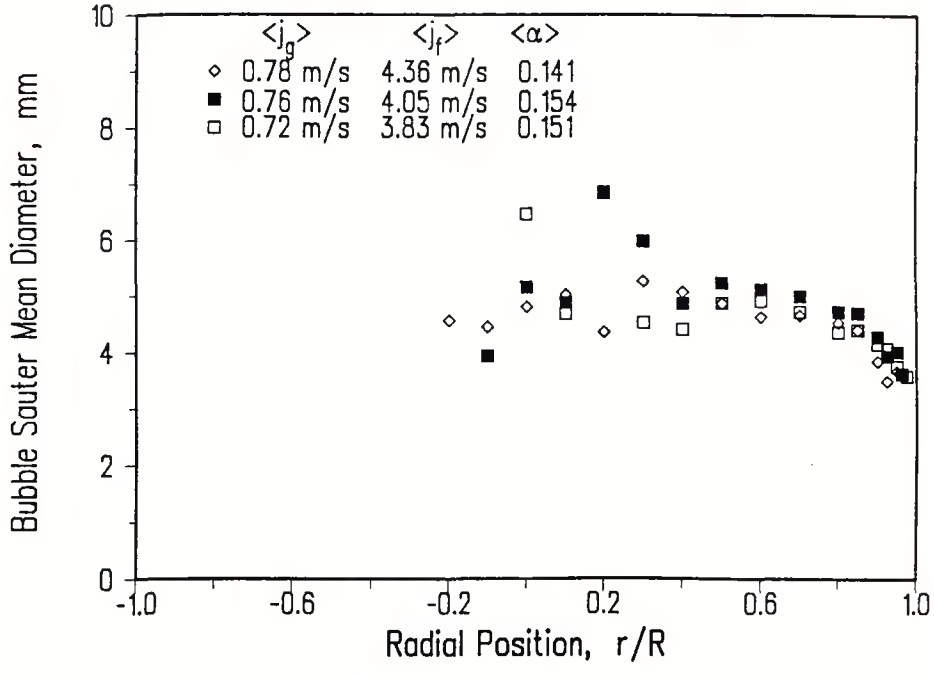

Figure 5.89 Effect of Liquid Flow on Sauter Mean Bubble Diameter at $\langle j_g \rangle \simeq 0.76$ m/s.

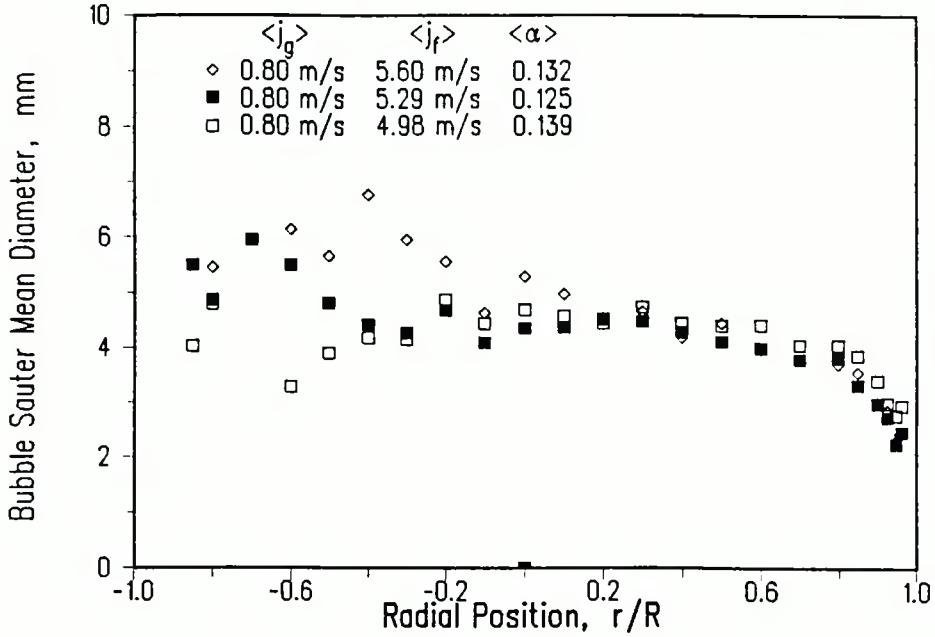

Figure 5.90 Effect of Liquid Flow on Sauter Mean Bubble Diameter at $\langle j_g \rangle$ = 0.8 m/s.

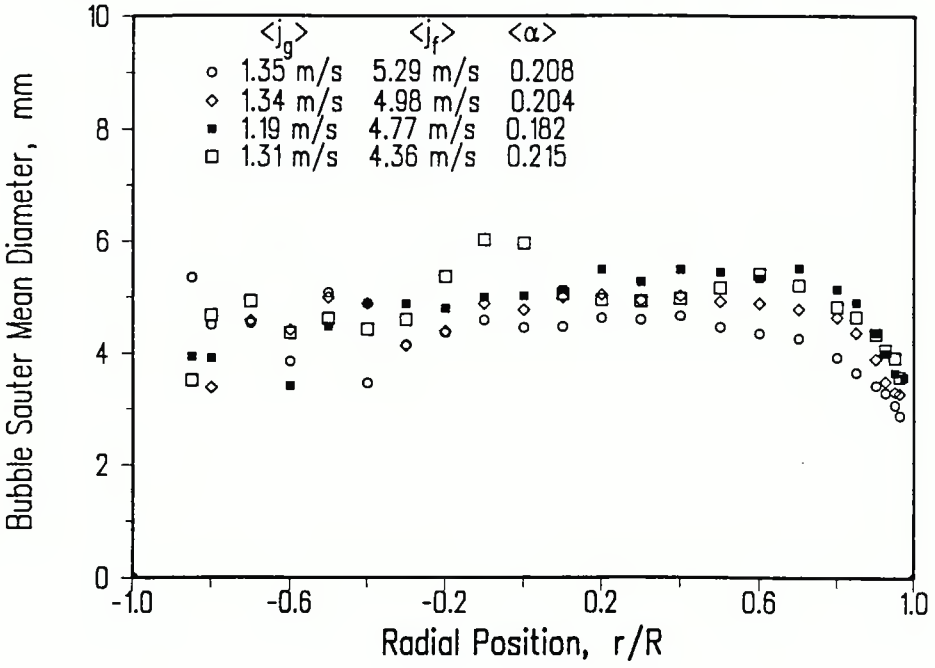

Figure 5.91 Effect of Liquid Flow on Sauter Mean Bubble Diameter at $\langle j_g \rangle \simeq$ 1.3 m/s.

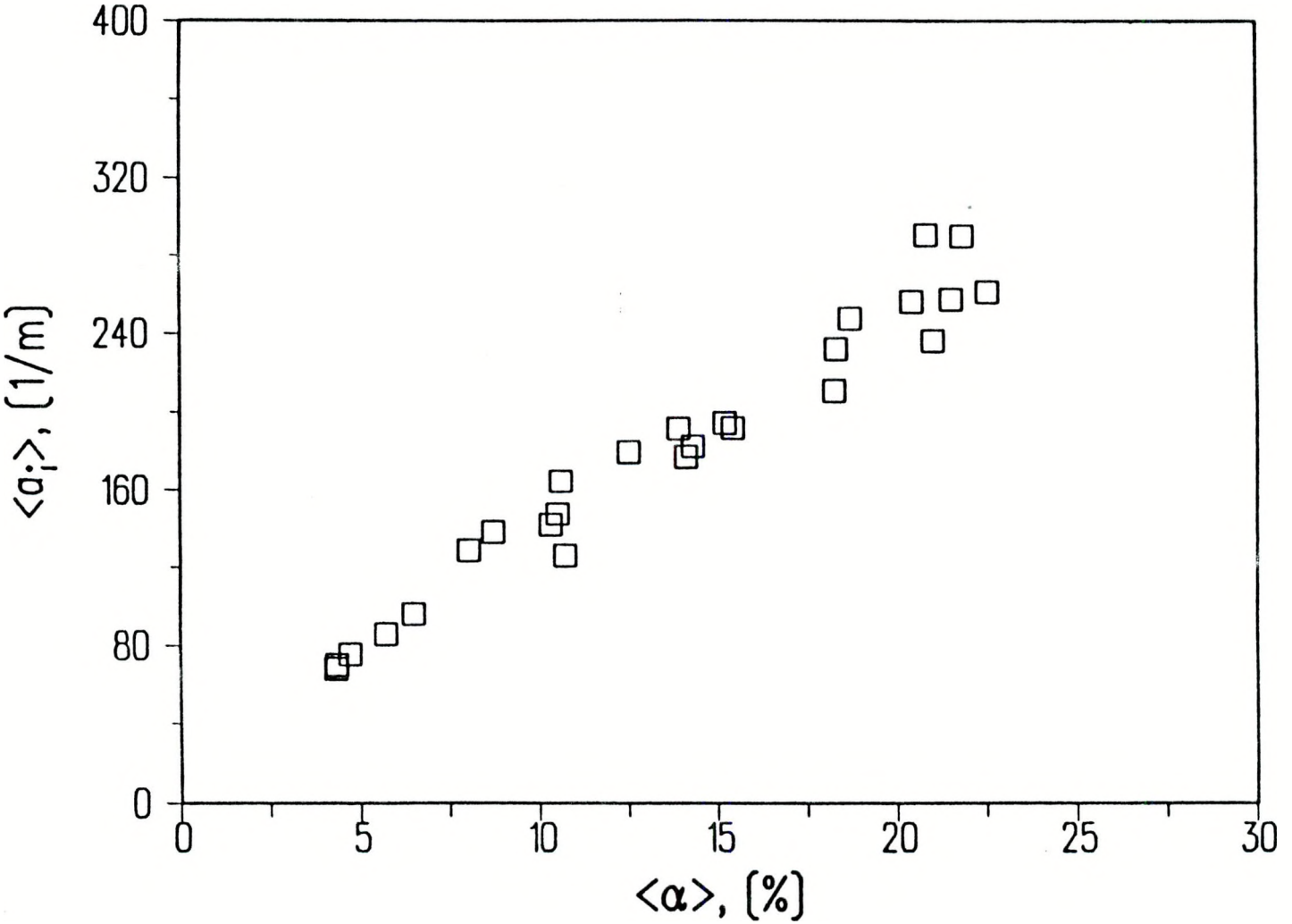

Figure 5.92 Average Interfacial Area Concentration as a Function of Void Fraction.

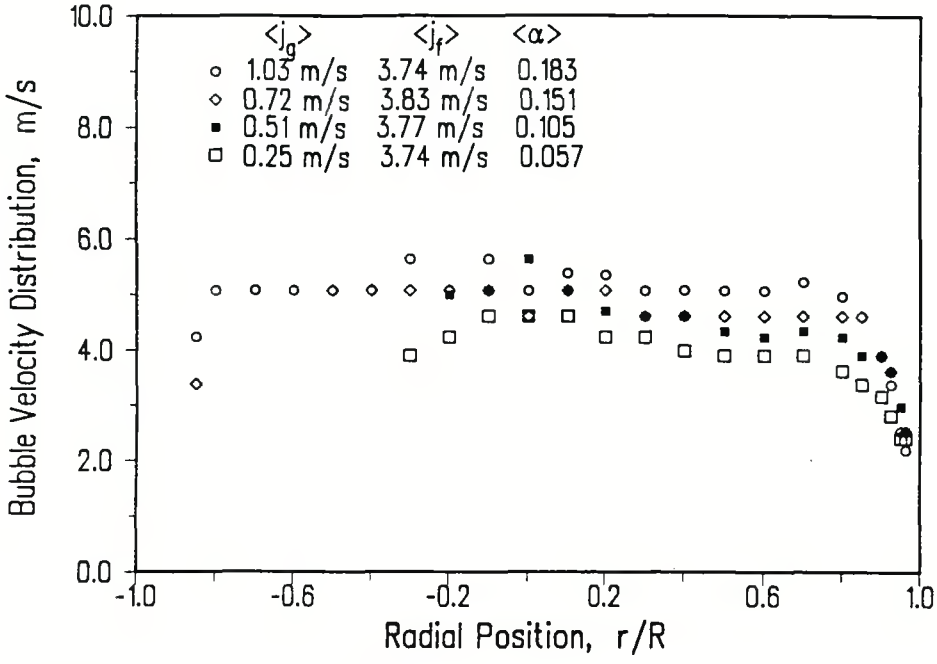

Figure 5.93 Influence of Gas Flow on Bubble Interface Velocity Distribution at $\langle j_f \rangle \simeq 3.7$ m/s.

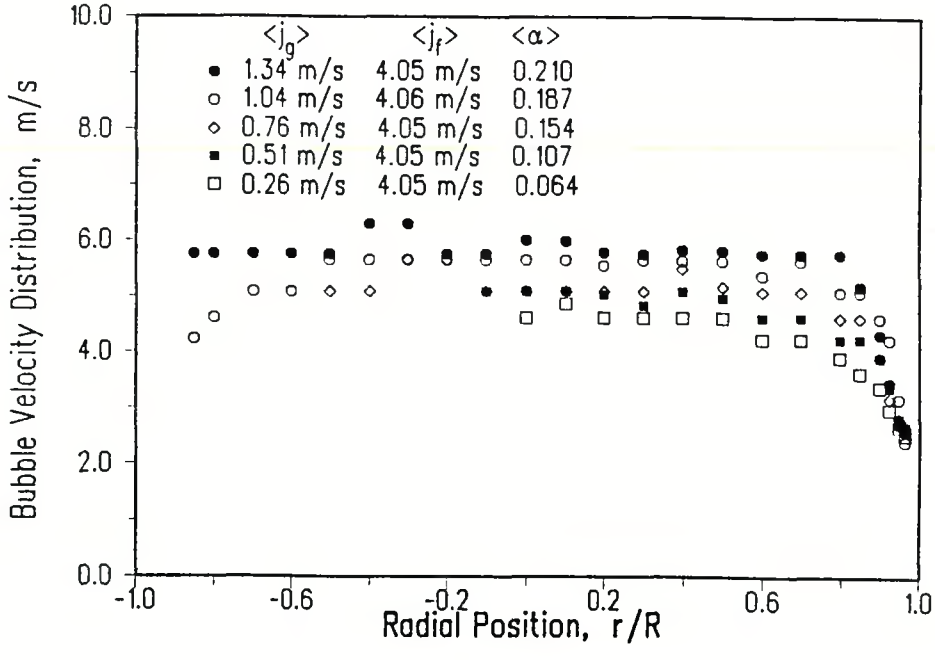

Figure 5.94 Influence of Gas Flow on Bubble Interface Velocity Distribution at $\langle j_f \rangle \simeq 4$ m/s.

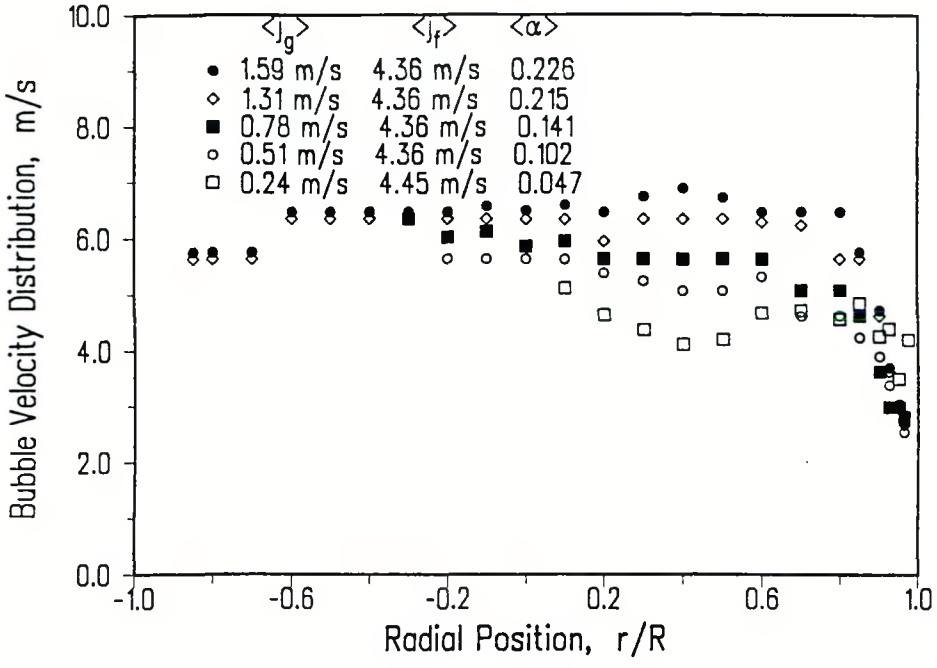

Figure 5.95 Influence of Gas Flow on Bubble Interface Velocity Distribution at $\langle j_f \rangle$ = 4.36 m/s.

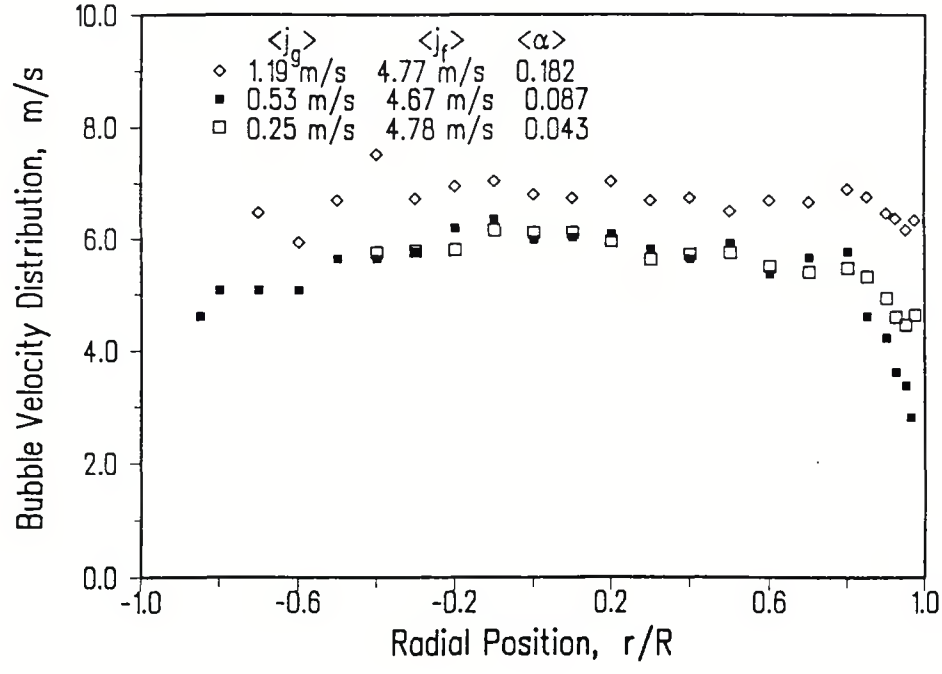

Figure 5.96 Influence of Gas Flow on Bubble Interface Velocity Distribution at $\langle j_f \rangle$ = 4.67 m/s.

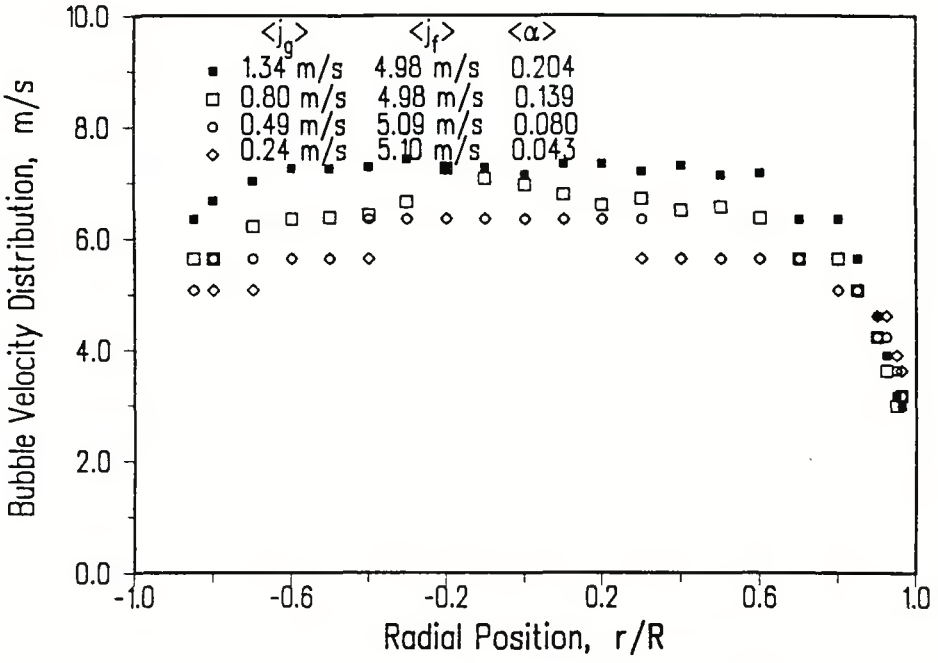

Figure 5.97 Influence of Gas Flow on Bubble Interface Velocity Distribution at $\langle j_f \rangle \simeq 5$ m/s.

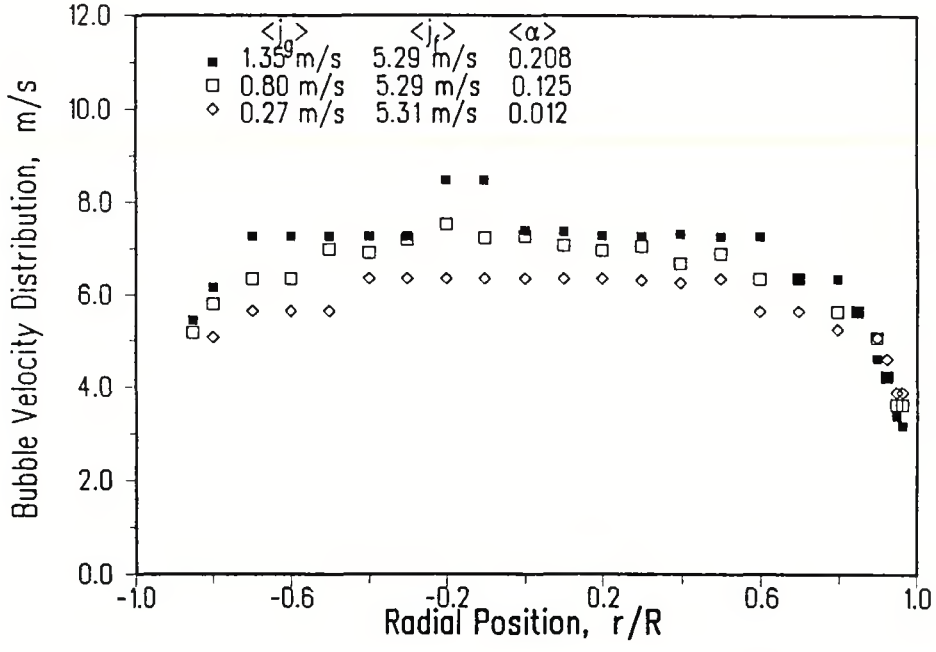

Figure 5.98 Influence of Gas Flow on Bubble Interface Velocity Distribution at $\langle j_f \rangle \simeq 5.3$ m/s.

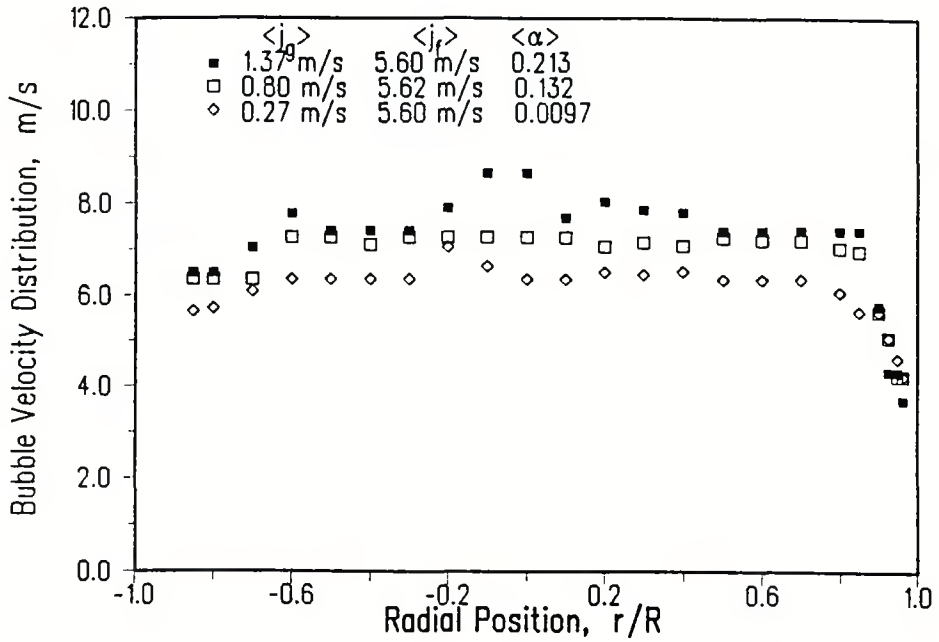

Figure 5.99 Influence of Gas Flow on Bubble Interface Velocity Distribution at $\langle j_f \rangle \simeq 5.6$ m/s.

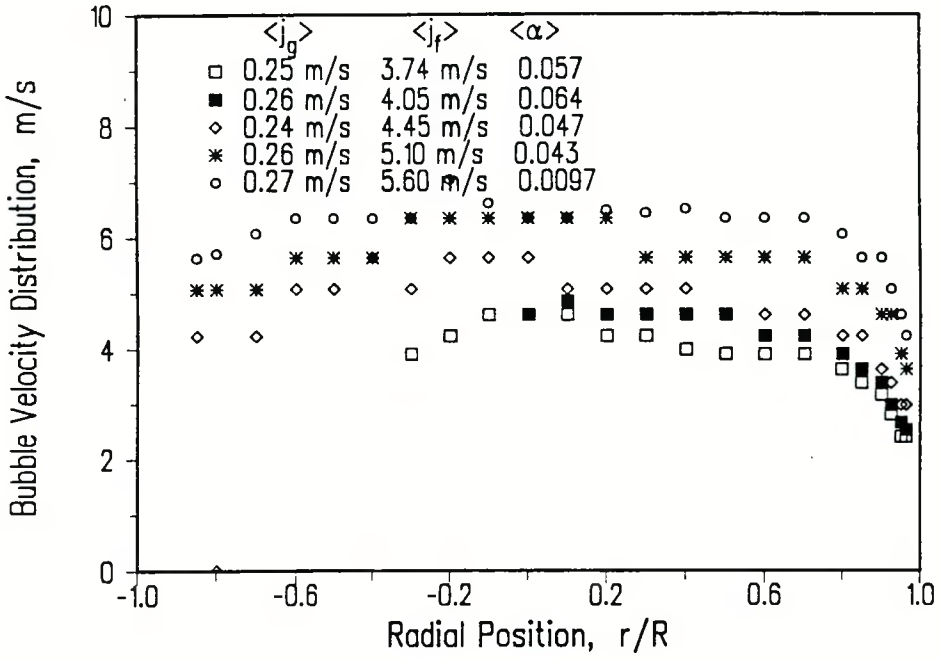

Figure 5.100 Influence of Liquid Flow on Bubble Interface Velocity at $\langle j_g \rangle \simeq 0.25$ m/s.

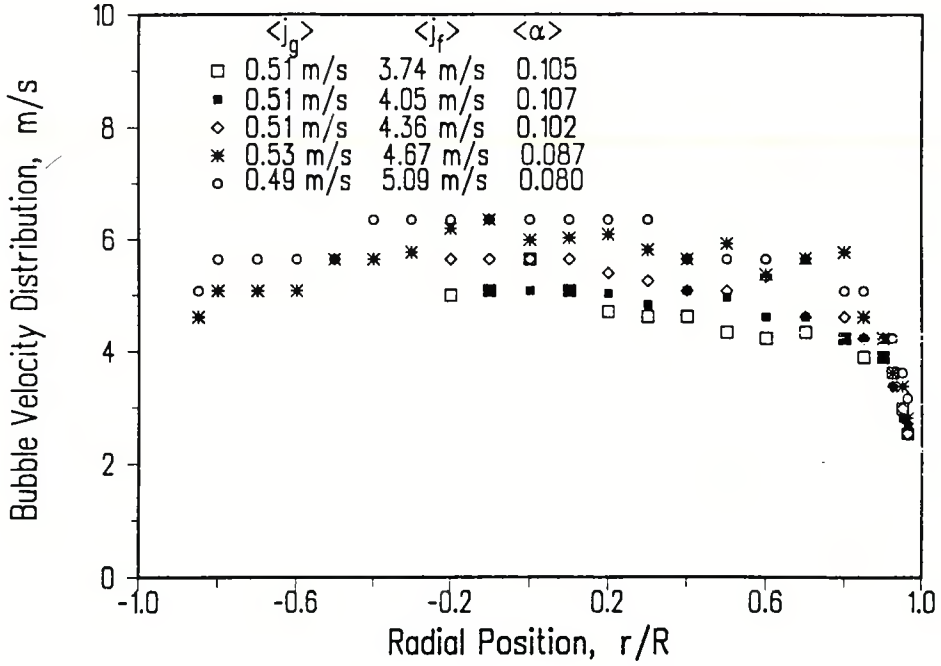

Figure 5.101 Influence of Liquid Flow on Bubble Interface Velocity at $\langle j_g \rangle \simeq 0.5$ m/s.

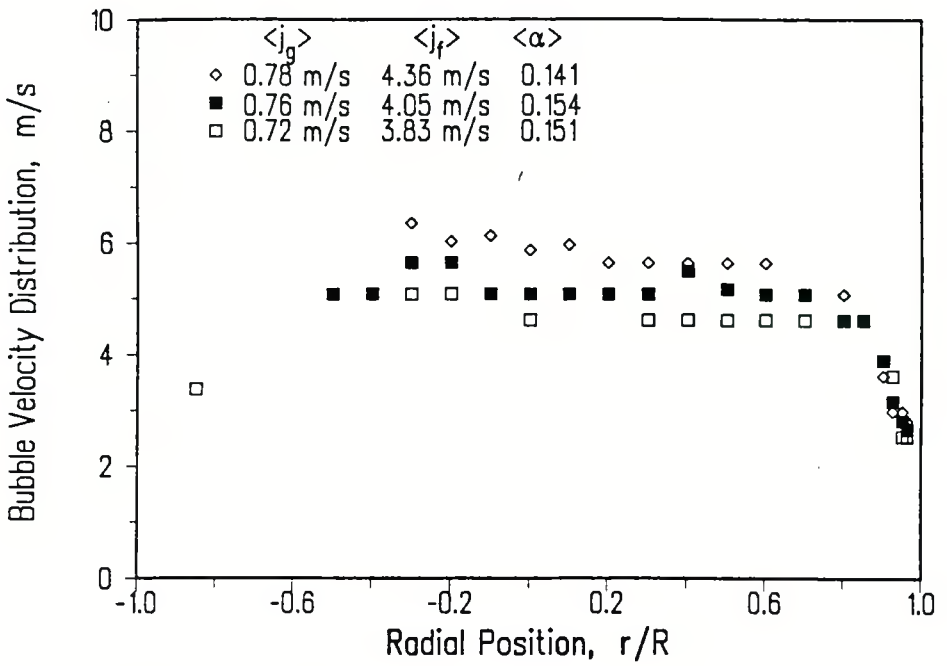

Figure 5.102 Influence of Liquid Flow on Bubble Interface Velocity at $\langle j_g \rangle \simeq 0.76$ m/s.

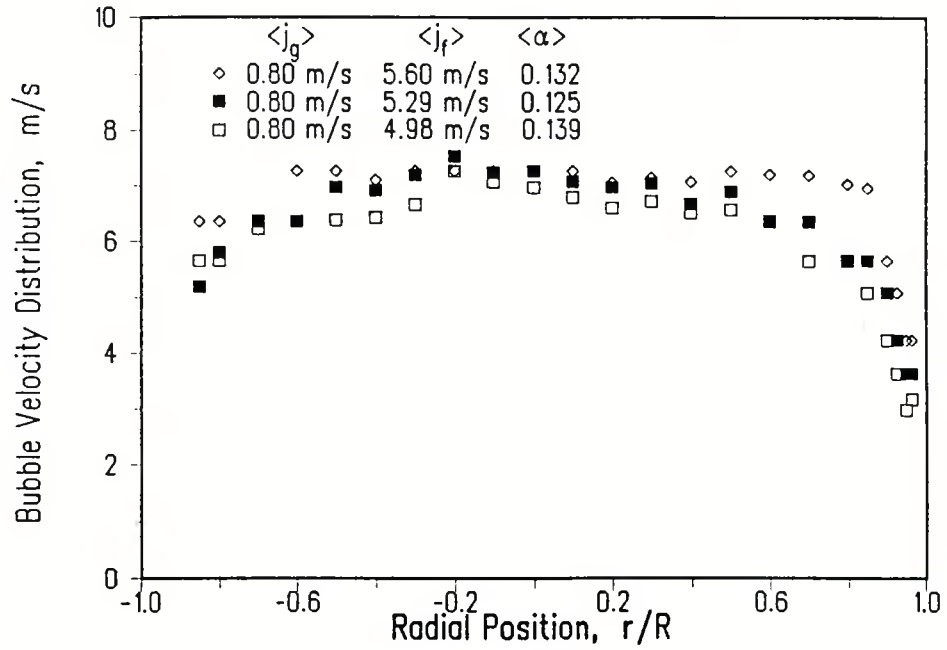

Figure 5.103 Influence of Liquid Flow on Bubble Interface Velocity at $\langle j_g \rangle = 0.8$ m/s.

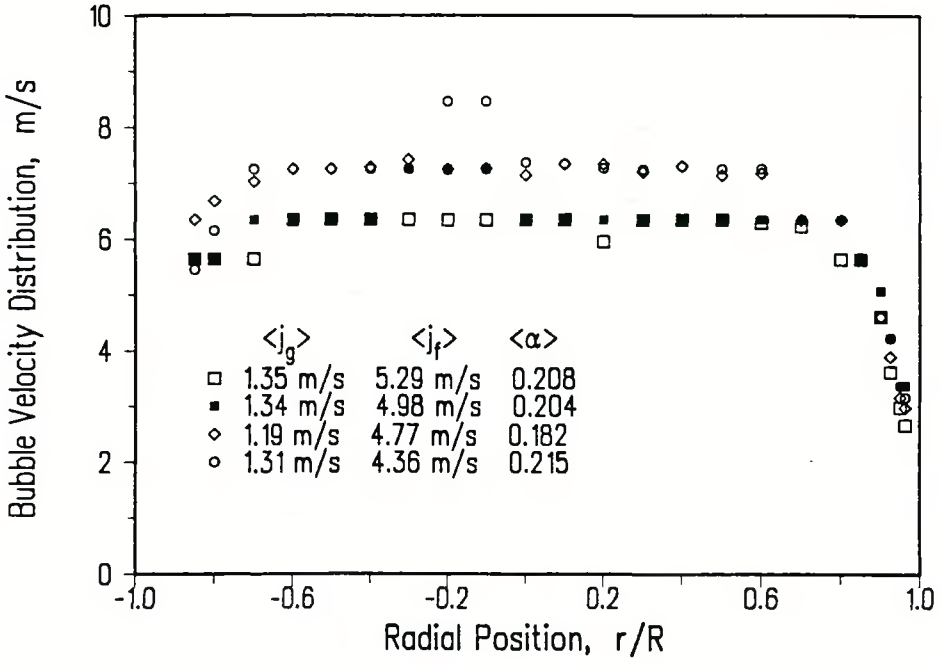

Figure 5.104 Influence of Liquid Flow on Bubble Interface Velocity at $\langle j_g \rangle \simeq 1.3$ m/s.

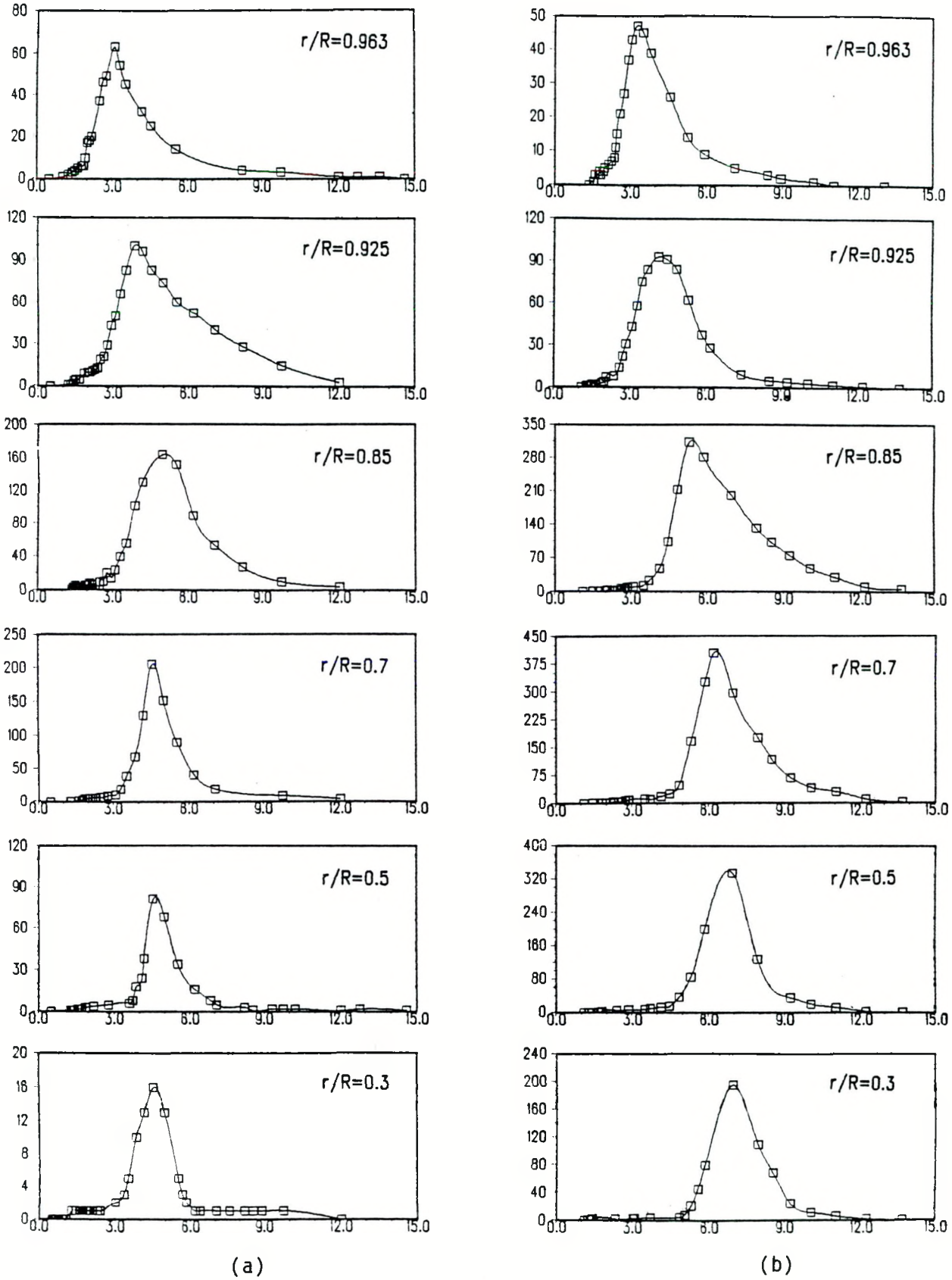

Figure 5.105 Typical Bubble Interface Velocity Spectra
a) $\langle j_f \rangle$ = 3.77 m/s, $\langle j_g \rangle$ = 0.76 m/s, $\langle \alpha \rangle$ = 0.138,
b) $\langle j_f \rangle$ = 4.96 m/s, $\langle j_g \rangle$ = 1.34 m/s, $\langle \alpha \rangle$ = 0.204.

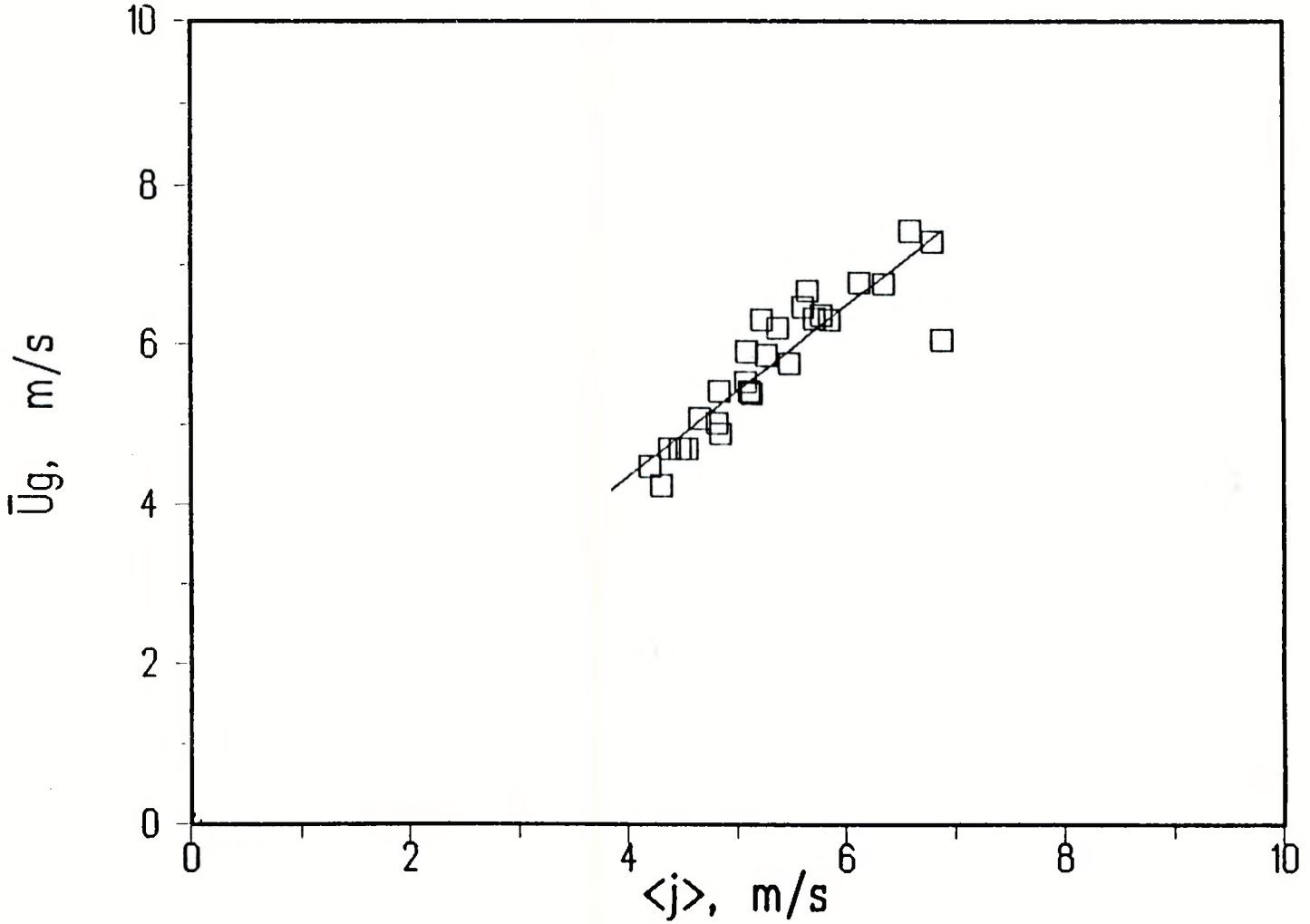

Figure 5.106 $\bar{u}_b$ - <j> Presentation.

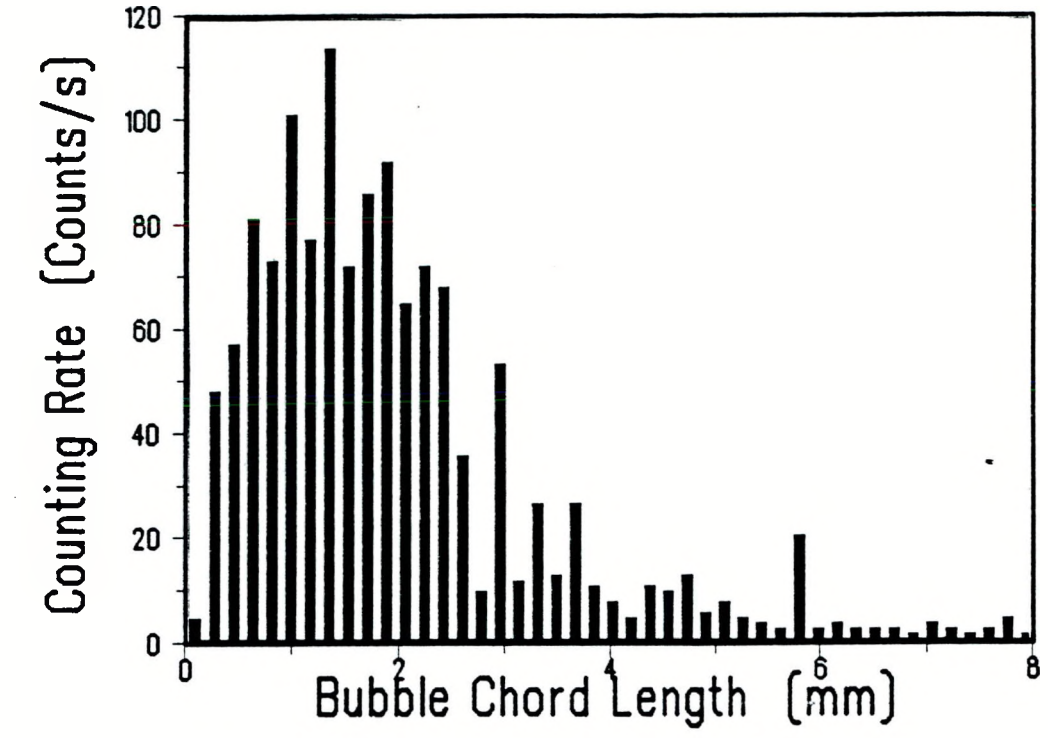

(a)

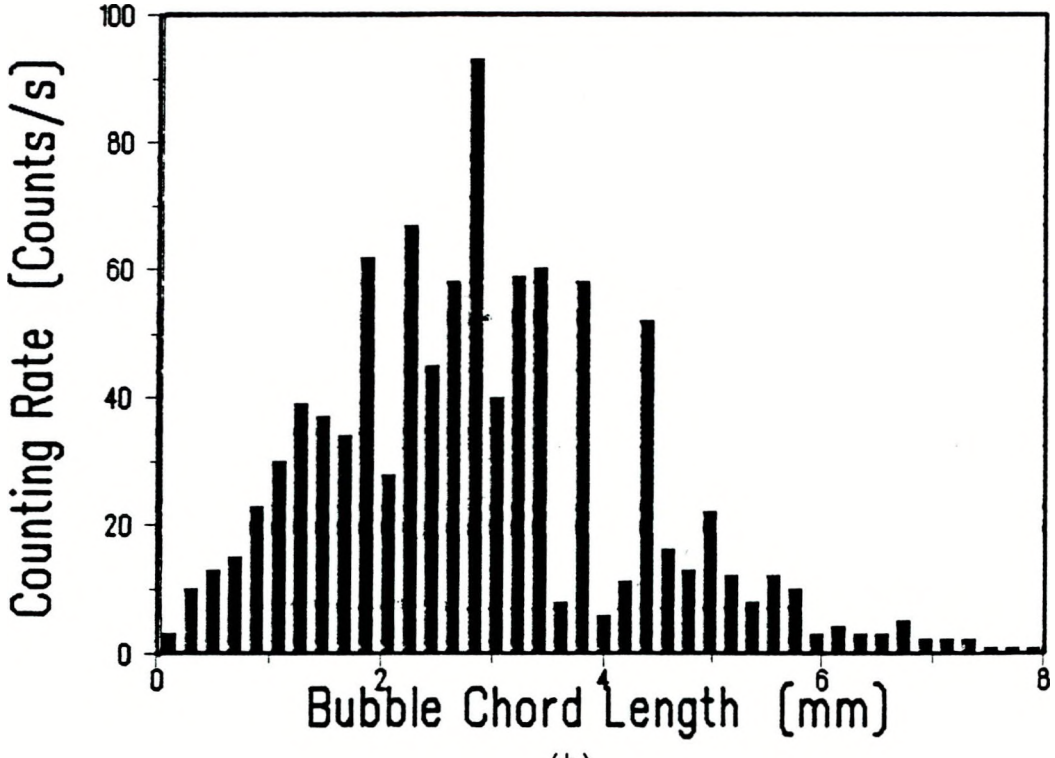

(b)

Figure 5.107 Typical Bubble Chord-Length Spectra, $\langle j_f \rangle$ = 4.96 m/s, $\langle j_g \rangle$ = 1.34 m/s, $\langle \alpha \rangle$ = 0.204; a) at r/R = 0.963, b) at r/R = a3.

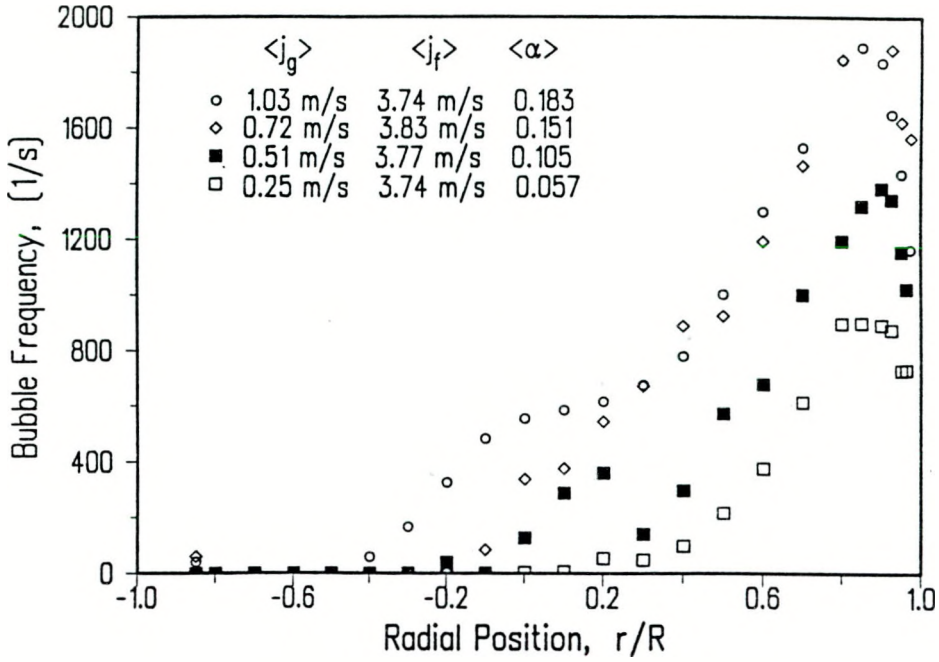

Figure 5.108 Influence of Gas Flow on Bubble Frequency at $\langle j_f \rangle \simeq 3.7$ m/s.

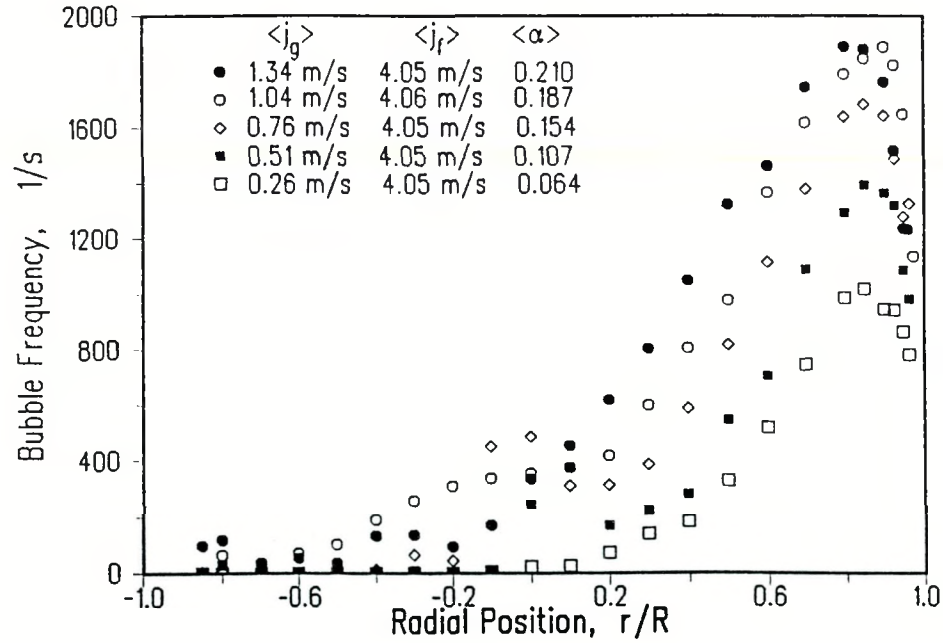

Figure 5.109 Influence of Gas Flow on Bubble Frequency at $\langle j_f \rangle \simeq 4$ m/s.

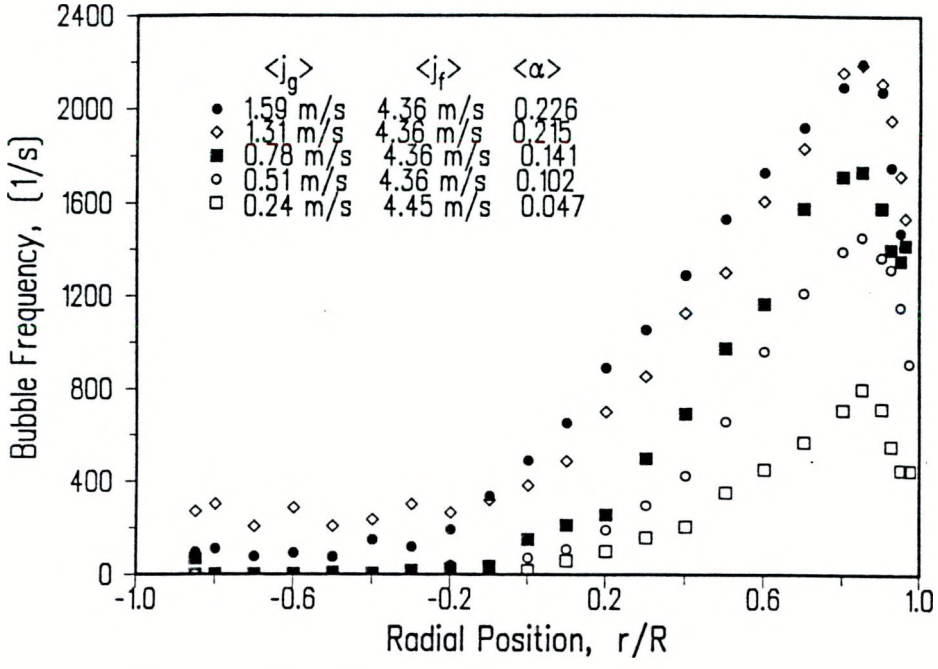

Figure 5.110 Influence of Gas Flow on Bubble Frequency at $\langle j_f \rangle$ = 4.36 m/s.

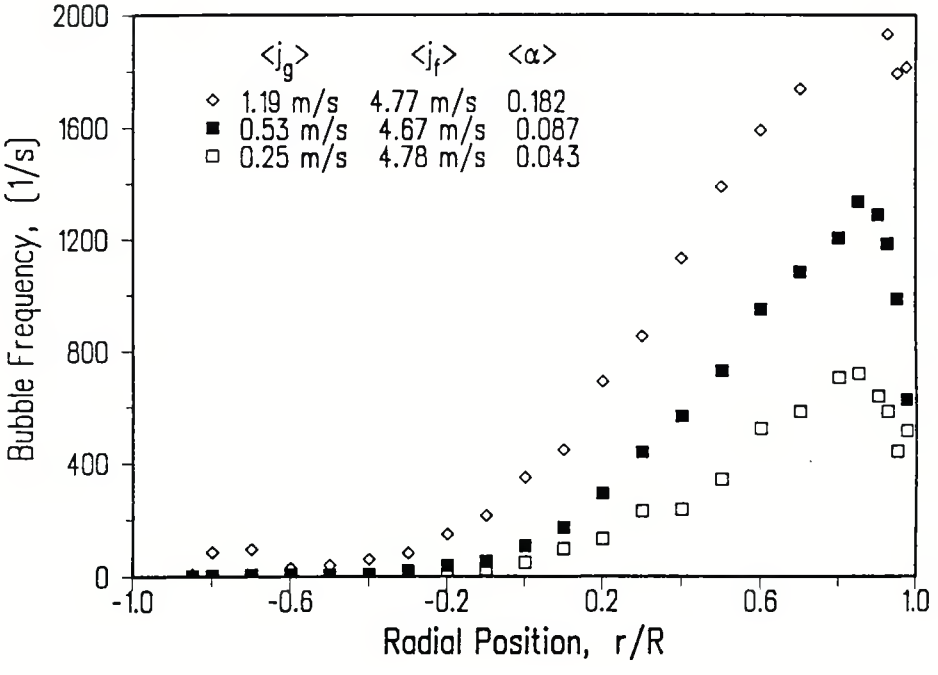

Figure 5.111 Influence of Gas Flow on Bubble Frequency at $\langle j_f \rangle$ = 4.67 m/s.

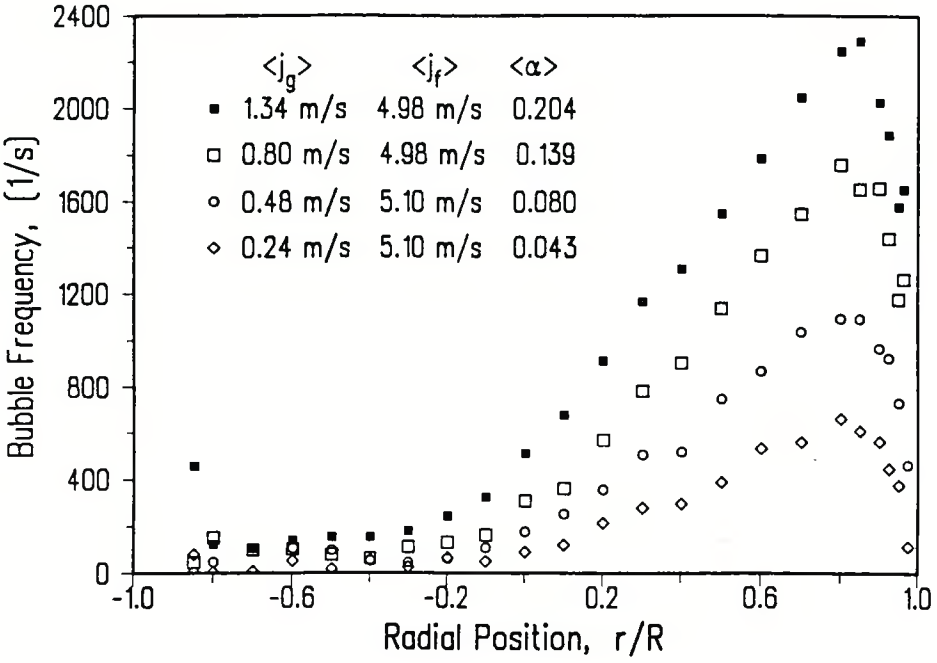

Figure 5.112 Influence of Gas Flow on Bubble Frequency at $\langle j_f \rangle \simeq 5$ m/s.

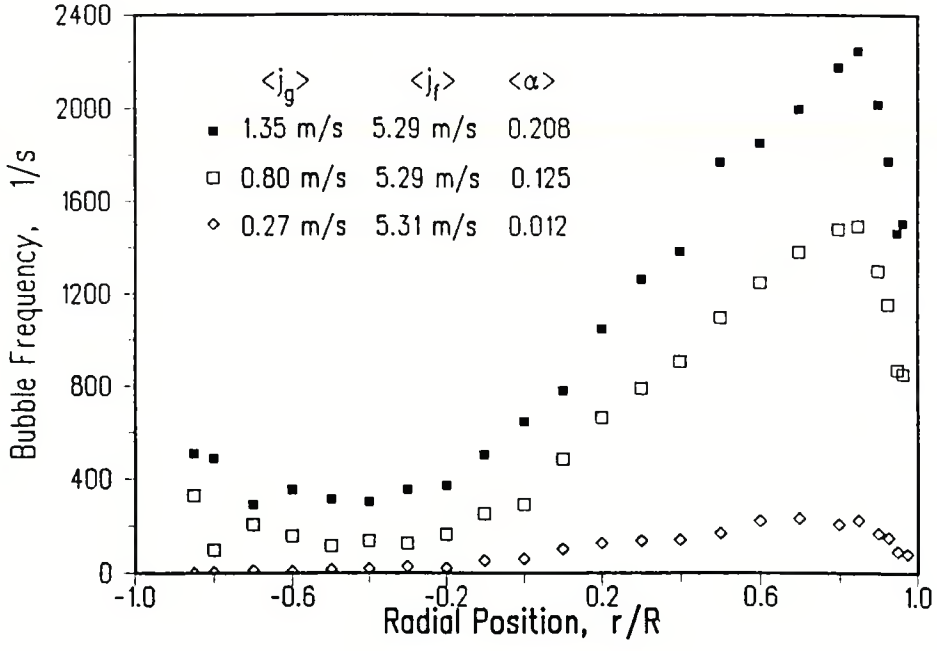

Figure 5.113 Influence of Gas Flow on Bubble Frequency at $\langle j_f \rangle \simeq 5.3$ m/s.

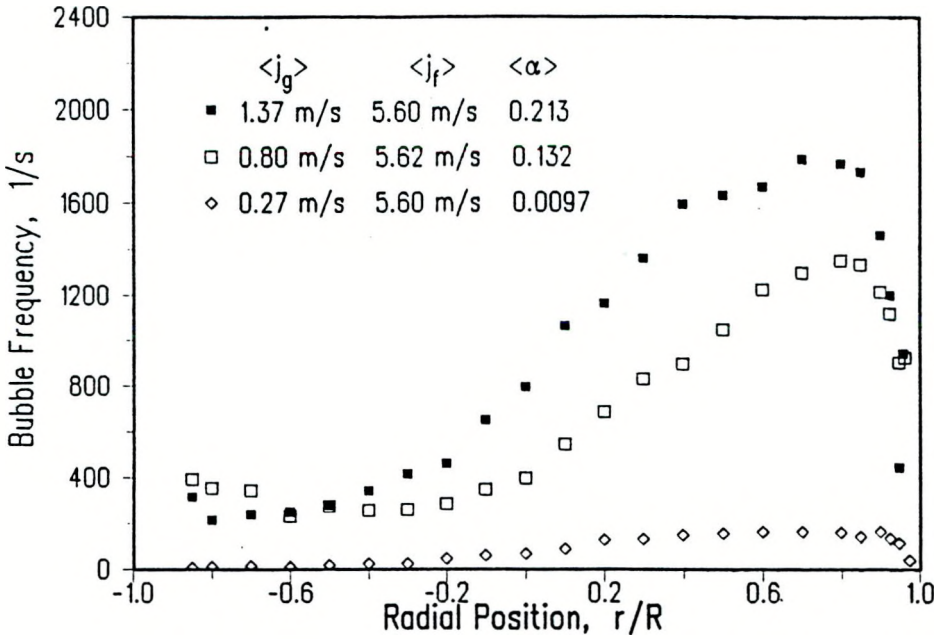

Figure 5.114 Influence of Gas Flow on Bubble Frequency at $\langle j_f \rangle \simeq 5.6$ m/s.

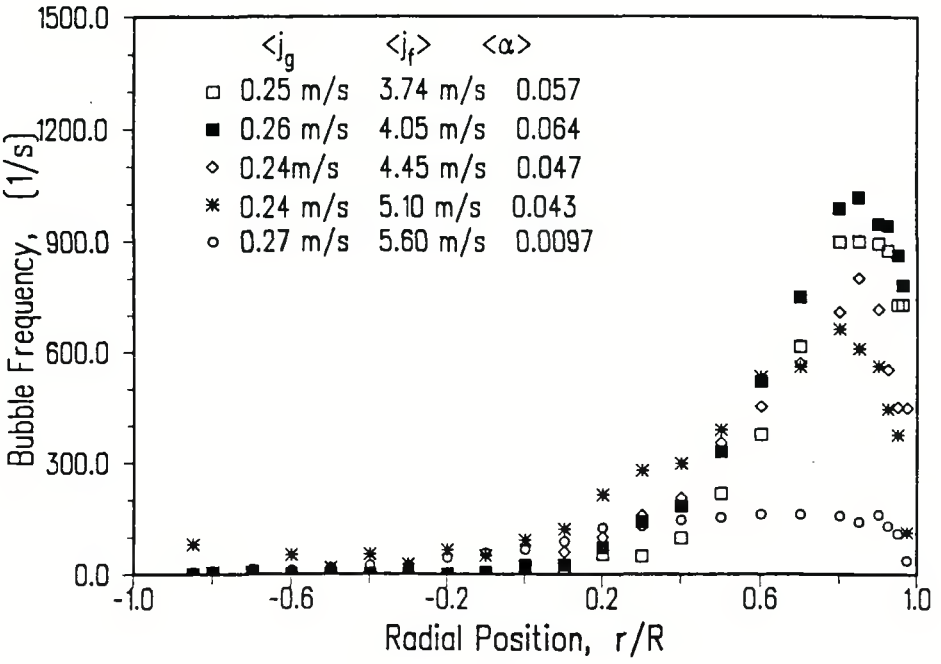

Figure 5.115 Influence of Liquid Flow on Bubble Frequency at $\langle j_g \rangle \simeq 0.26$ m/s.

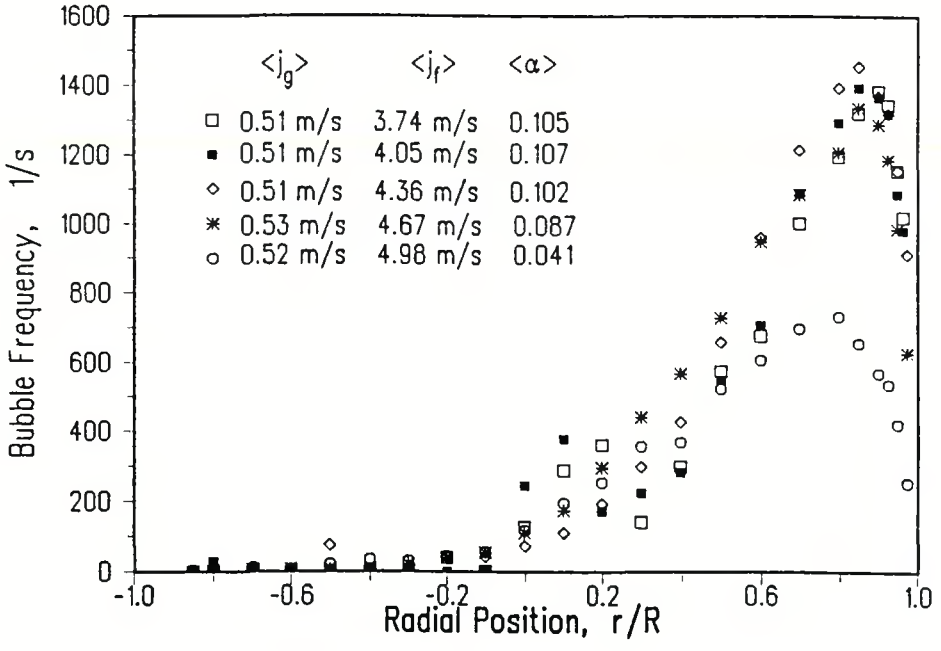

Figure 5.116 Influence of Liquid Flow on Bubble Frequency at $\langle j_g \rangle \simeq 0.5$ m/s.

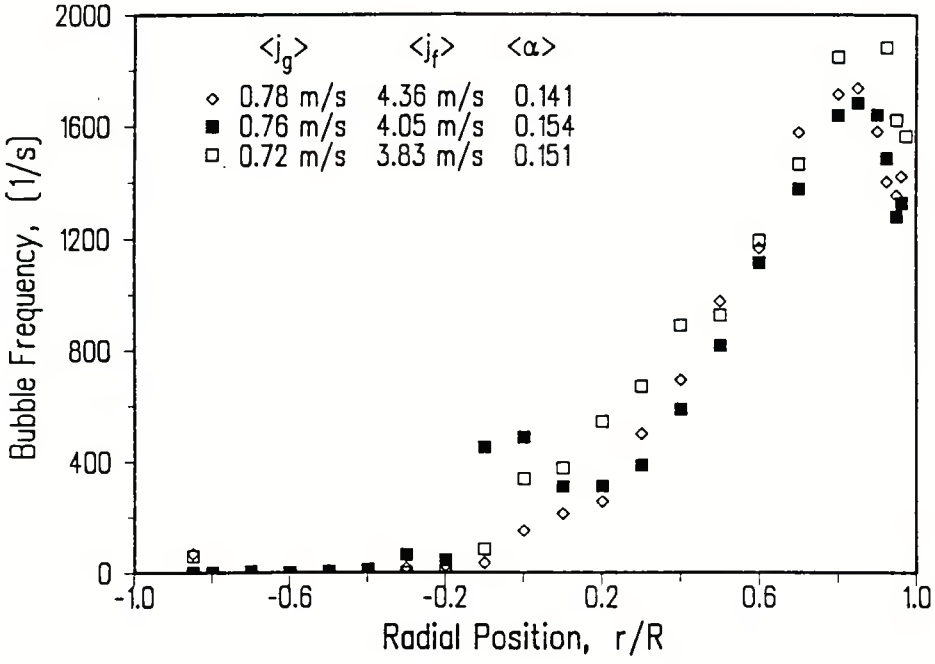

Figure 5.117 Influence of Liquid Flow on Bubble Frequency at $\langle j_g \rangle \simeq 0.76$ m/s.

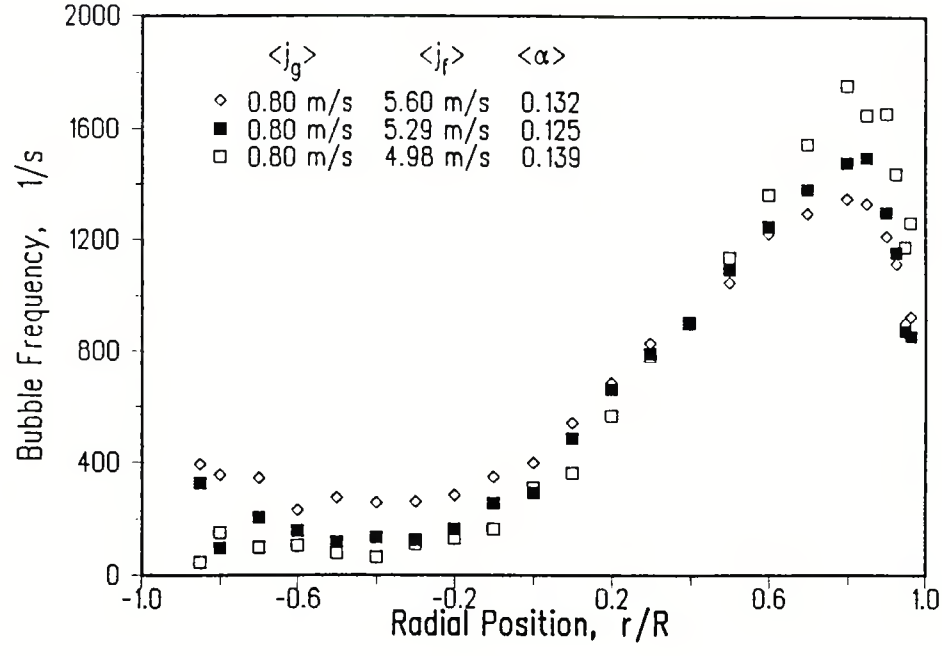

Figure 5.118 Influence of Liquid Flow on Bubble Frequency at $\langle j_g \rangle = 0.8$ m/s.

8. REFERENCES

1. Zuber, N. and Findley, J. A., "Average Volumetric Concentration in Two-Phase Flow Systems," J. Heat Trans., Vol. 87, pp. 453-468 (1965).

2. Wallis, G. B., One-Dimensional Two-Phase Flow, McGraw-Hill Publishing Co., New York, 261-263 (1969).

3. Ishii, M., "One-Dimensional Drift-Flux Model and Constitutive Equations for Relative Motion Between Phases in Various Flow Regimes," ANL-77-47 (1977).

4. Chawla, T. C. and Ishii, M., "Two-Fluid Model of Two-Phase Flow in a Pin Bundle of a Nuclear Reactor," Int. J. Heat Mass Transfer, Vol. 23, p. 991 (1980).

5. Ishii, M., Thermo-Fluid Dynamic Theory of Two-Phase Flow, Eyrolles, Paris (also Scientific and Medical Publication of France, New York, New York)(1975).

6. Vernier, P. and Delhaye, J. M., "General Two-Phase Flow Equations Applied to the Thermohydrodynamics of Boiling Nuclear Reactor," Energ. Primaire, Vol. 4, No. 1, p. 5(1968).

7. Kocamustafaogullari, G., "Thermofluid Dynamics of Separated Two-Phase Flow," Ph.D. Thesis, Georgia Institute of Technology (1971).

8. Boure', J. A., "Mathematical Modeling of Two-Phase Flows," Proc. of CSNI Specialist Meeting, Banerjee, S. and Weaver, K. R., Eds. A.E.C.L., Vol. 1, August 3-4, Toronto, 85 (1978).

9. Ishii, M. and Mishima, K., "Study of Two-Fluid Model and Interfacial Area," Argonne National Laboratory Report, ANL-80-111 (1981).

10. Chawla, T. C. and Ishii, M., "Two-Fluid Model of Two-Phase Flow in a Pin Bundle of a Nuclear Reactor," Int. J. Heat Mass Transfer, Vol. 23, p. 991 (1980).

11. Delhaye, J. M. and Achard, J. L., "On the Use of Averaging Operators in Two-Phase Flow Modeling," Thermal and Hydraulic Aspects of Nuclear Reactor Safety, Vol. 1, Light Water Reactors, Jones, D. C. and Bankoff, S. G., Eds. ASME, New York, 289 (1977).

12. Sha, W. T., Chao, B. T. and Soo, S. L., "Time Averaging of Local Volume Averaged Conservation Equations of Multiphase Flow," NUREG/CR-3434, ANL-83-49 (1983).

13. Sha, W. T., Chao, B. T., and Soo, S. L., "Time- and Volume-Averaged Conservation Equations for Multiphase Flow. Part One: System without Internal Solid Structures," NUREG/CR-3989, ANL-84-66 (1984).

14. Ishii, M. and Kocamustafaogullari, G., "Two-Phase Flow Models and Their Limitations," NATO Advanced Research Workshop on Advances in Two-Phase Flow and Heat Transfer, Spitzingsee, BRD, August 31-September 3 (1982).

15. Ishii, M., Mishima, K., Kataoka, I., and Kocamustafaogullari, G., "Two-Fluid Model and Importance of the Interfacial Area in Two-Phase Flow Analysis," Proc. 9th U.S. National Congress of Applied Mechanics, pp. 73-80, Ithaca, New York, June 21-25 (1982).

16. Veteau, J. M. and Morel, Y., "Techniques de measure des aires interfacials dans les écoulements a bulles--II la méthode chimique," CEA Report CEA-R-5092, France (1980).

17. Veteau, J. M. and Charlot, R., "Techniques de measure des aires interfacials dans les écoulements a bulles--I Comparison de la méthode d'atténuation d'un faisceau lumineux et de la méthode photographiques," CEA Report CEA-R-5075, France (1980).

18. Veteau, J. M. and Charlot, R., "Techniques de measure des aires interfacials dans les écoulements a bulles--III Comparison de la méthode d'atténuation d'un faisceau lumineux et d'une méthode locale," CEA Report CEA-R-5122, France (1981).

19. Veteau, J. M., "Contribution a l'étude des techniques de measure de l'aire interfacial dans les ecoulements a bulles," These de docteaur es sciences, Universityé Scientifique et Médicale et Institute National Polytechnique de Grenoble (1981).

20. Danckwerts, P. V., Gas-Liquid Reactions, McGraw-Hill, New York, 1970.

21. Sharma, M. M. and Danckwerts, P. V., "Chemical Methods of Measuring Interfacial Area and Mass Transfer Coefficients in Two-Fluid Systems," British Chem. Eng., Vol. 15, pp. 522-528 (1970).

22. Kasturi, G. and Stepanek, J. B., "Two-Phase Flow--III. Interfacial Area in Cocurrent Gas-Liquid Flow," Chem. Eng. Sci., Vol. 29, pp. 713-719 (1974).

23. Robinson, C. W. and Wilke, C. R., "Simultaneous Measurement of Interfacial Area and Mass Transfer Coefficients for a Well-Mixed Gas Dispersion in Aqueous Electrolyte Solutions," AIChE J., Vol. 20, pp. 285-294 (1974).

24. Sridharan, K. and Sharma, M. M., "New Systems and Methods for the Measurement of Effective Interfacial Area and Mass Transfer Coefficients in Gas-Liquid Contactors," Chem. Eng. Sci., Vol. 31, pp. 767-774 (1976).

25. Landau, J., Boyle, J. Gomaa, H. G., and Al Tawell, A. M., "Comparison of Methods for Measuring Interfacial Areas in Gas-Liquid Dispersions," Canadian J. of Chem. Eng., Vol. 55, pp. 13-18 (1977).

26. Shilimkan, R. V. and Stepanek, J. B., "Interfacial Area in Cocurrent Gas-Liquid Upward Flow in Tubes of Various Size," Chem. Eng. Sci., Vol. 32, pp. 149-154 (1977).

27. Shilimkan, R. V. and Stepanek, J. B., "Mass Transfer in Cocurrent Gas-Liquid Flow: Gas Side Mass Transfer Coefficients in Upflow, Interfacial Areas and Mass Transfer Coefficient in Gas and Liquid in Downflow," Chem. Eng. Sci., Vol. 33, pp. 1675-1680 (1978).

28. Sridhar, T. and Potter, O. E., "Interfacial Area Measurements in Gas-Liquid Agitated Vessels, Comparison of Techniques," Chem Eng. Sci., Vol. 33, pp. 1347-1353 (1978).

29. Watson, A. P., Cormack, D. E., and Charles, M. E., "A Preliminary Study of Interfacial Areas in Vertical Cocurrent Two-Phase Upflow," Canadian J. of Chem. Eng., Vol. 57, pp. 16-23 (1979).

30. Dhanuka, V. R. and Stepanek, J. B., "Simultaneous Measurement of Interfacial Area and Mass Transfer Coefficient in Three-Phase Fluidized Beds," AIChe J., Vol. 26, pp. 1029-1038 (1980).

31. Farritor, R. E. and Hughmark, G. A., "Interfacial Area and Mass Transfer with Gas-Liquid Systems in Turbine-Agitated Vessels," Chem. Eng. Com., Vol. 4, pp. 143-147 (1980).

32. Hassan, I. T. M. and Robinson, C. W., "Mass-Transfer-Effective Bubble Coalescence Frequency and Specific Interfacial Area in a Mechanically Agitated Gas-Liquid Contractor," Chem. Eng. Sci., Vol. 35, pp. 1277-1289 (1980).

33. Vavruska, J. S. and Perona, J. J., "Measurements of Interfacial Areas in Cocurrent Gas-Liquid Downward Flow," Canadian J. of Chem. Eng., Vol. 58, pp. 141-144 (1980).

34. Schumpe, A. and Deckwer, W.-D., "Comparison of the Photographic and the Sulfite Oxidation Method for Interfacial Area Determination in Bubble Columns," Chem. Eng. Com., pp. 313-324 (1982).

35. Schumpe, A. and Deckwer, W. D., "Analysis of Chemical Methods for Determination of Interfacial Areas in Gas-in-Liquid Dispersions with Non-Uniform Bubble Sizes," Chem. Eng. Sci., Vol. 35, pp. 2221-2233 (1980).

36. Kulkarmi, A., Shah, Y., and Schumpe, A., "Hydrodynamics and Mass Transfer in Downflow Bubble Column," Chem. Eng. Com., Vol. 24, pp. 307-337 (1983).

37. Capuder, E. and Koloini, T., "Gas Hold-up and Interfacial Area in Aerated Suspensions of Small Particles," Chem. Eng. Res. & Design, Vol. 62, pp. 255-260 (1984).

38. Nagy, E., Borlai, O., Laurent, E., and Charpentier, J.-C., "Determination of the Gas-Liquid Interfacial Area of a Perforated Plate Operating with Cross Flow," Intl. Chem. Eng., Vol. 26, pp. 637-646 (1986).

39. Schumpe, A. and Deckwer, W.-D., "Analysis of Chemical Methods for Determination of Interfacial Areas in Gas-in-Liquid Dispersions with Non-uniform Bubble Sizes," Chem. Eng. Sci., Vol. 35, pp. 2221-2233 (1980).

40. Shilimkan, R. V., "Mass Transfer in Co-Current Gas-Liquid Vertical Flows," Ph.D. Thesis, University of Salford (1975).

41. Tomida, T. Yuse, F., and Okezaki, "Effective Interfacial Area and Liquid-Side Mass Transfer Coefficient in the Upward Two-Phase Flow of Gas-Liquid Mixture," Chem. Eng. J., Vol. 16, pp. 81-88 (1978).

42. Benerjee, S., Scott, D. S., and Rhodes, E., "Studies on Cocurrent Gas-Liquid Flow in Helically Coiled Tubes," Can. J. Chem. Eng., Vol. 48, pp. 542-551 (1970).

43. Wales, C. E., "Physical and Chemical Absorption in Two-Phase Annular and Dispersed Horizontal Flow," AIChE J., Vol. 12, pp. 1166-1171 (1966).

44. Shah, A. K. and Sharma, M. M., "Mass Transfer in Gas Liquid Pipeline Contractors," Can. J. Chem. Eng., Vol. 53, pp. 572-574 (1975).

45. Gregory, G. A. and Scott, D. S., "Physical and Chemical Mass Transfer in Horizontal Cocurrent Gas-Liquid Slug Flow," Int. Symp. on Research in Gas-Liquid Flow, Waterloo, Canada, Sept. 19, 2, F3.1-F3.44 (1968).

46. Kulic, E. and Rhodes, E., "Chemical Mass Transfer in Co-Current Gas-Liquid Slug Flow in Helical Coils," Can. J. Chem. Eng., Vol. 52, pp. 114-116 (1974).

47. Radhkerishen, V. R. and Mitra, A. K., "Pressure Drop, Holdup and Interfacial Area in Vertical Two-Phase Flow of Multi-Jet Ejector Induced Dispersions," Can J. Chem. Eng., Vol. 62, pp. 170-178 (1984).

48. DeJesus, J. M. and Kawaji, M., "Measurement of Interfacial Area and Void Fraction in Upward, Cocurrent Gas-Liquid Flow," pp. 137-145 (1989).

49. Akita, K. and Yoshida, F., "Bubble Size, Interfacial Area, and Liquid-Phase Mass Transfer Coefficient in Bubble Columns," Ind and Eng. Chem. Process Design and Development, Vol. 13, pp. 84-91 (1974).

50. Jeng, J. J. Jer, R. M., and Yang, Y. M., "Surface Effects and Mass Transfer in Bubble Column," Ind. and Eng. Chem., Process Design and Development, Vol. 25, pp. 974-978 (1986).

51. Yang, N. S., Shen, Z.-Q., Chem, B. H., and McMillian, A. F., "Pressure Drop, Gas Holdup, and Interfacial Area for Gas-Liquid Contact in Karr Columns," Ind. and Eng. Chem., Process Design and Development, Vol. 25, pp. 660-664 (1986).

52. Burgess, J. M. and Calderbank, P. H., "The Measurement of Bubble Parameters in Two-Phase Dispersions, I--The Development of an Improved Probe Technique," Chem. Eng. Sci., Vol. 30, pp. 743-750 (1975).

53. Kawecki, W., Reith, T., Van Heuven, J. W., and Beck, W., "Bubble Size Distribution in the Impeller of a Stirred Vessel," Chem. Eng. Sci., Vol. 22, pp. 1519-1523 (1967).

54. Reith, T. and Beck, W. J., Proc. 4th European Symp. Chem. Rect. Engng., pp. 191-197, Brussels, Belgium (1968).

55. Weiss, S. and Ziegel, G., Chem. Technik, Vol. 24, pp. 15-26 (1972).

56. Gunn, D. J. and Al-Doori, H. H., "The Measurement of Bubble Flows in Fluidized Beds by Electrical Probe," Int. J. Multiphase Flow, Vol. 11, pp. 535-551 (1985).

57. Vermeulen, T., Williams, G. M., and Langlois, G. E., "Interfacial Area in Liquid-Liquid and Gas-Liquid Contractors," AIChE J., Vol. , pp. (1955).

58. Calderbank, P. H., "Physical Rate Processes in Industrial Fermentation, Part I: The Interfacial Area in Gas-Liquid Contacting with Mechanical Agitation," Trans. of the Inst. of Chem. Engineers, Vol. 36, pp. 443-463 (1958).

59. McLaughlin, C. M. and Rushton, J. H., "Interfacial Areas of Liquid-Liquid Dispersions from Light Transmission Measurements," AIChE J., Vol. 19, pp. 813-822 (1973).

60. Curl, R. L., "Note on Light Transmission Through a Polydisperse Dispersion," AIChE J., Vol. 20, pp. 184-190 (1974).

61. Ohba, K. and Itoh, T., "Light Attenuation Technique for Void Fraction Measurement in Two-Phase Bubbly Flow, Part I. Theory," Technology Reports of the Osaka University, Vol. 28, 1448, pp. 487-494 (1978).

62. Ohba, K. and Itoh, T., "Light Attenuation Technique for Void Fraction Measurement in Two-Phase Bubbly Flow, Part II. Experimental," Technology Reports of the Osaka University, Vol. 28, 1449, pp. 495-506 (1978).

63. Ohba, K., Itoh, T., and Yuhera, T., "Light Attenuation Technique for Void Fraction Measurement in Two-Phase Bubbly Flow, Part III. Effect of Some Parameters on Accuracy of Measurement," Technology Reports of the Osaka University, Vol. 28, 1450, pp. 507-516 (1978).

64. Stravs, A. A. and von Stockar, U., "Measurement of Interfacial Areas in Gas-Liquid Dispersions by Ultrasonic Pulse Transmission," Chem. Eng. Sci., Vol. 40, pp. 1169-1175 (1985).

65. Marston, P. L., Langley, D. S., and Kingsbury, D. L., "Light Scattering by Bubbles in Liquids: Mie Theory, Physical-Optics Approximation, and Experiments," appl. Sci. Res. Vol. 38, pp. 373-383 (1982).

66. McLaughlin, C. M. and Rushton, J. H., "Interfacial Areas of Liquid-Liquid Dispersions from Light Transmission Measurements," AIChE J., Vol. 19, pp. 813-822 (1973).

67. Jones, S. W., Ambland, A., and Favreau, C., "Interaction of an Ultrasonic Wave with a Bubbly Mixture," Experiments in Fluids, Vol. 4, pp. 341-349 (1986).

68. Delhaye, J. M., "Recent Advances in Two-Phase Flow Instrumentation," in Heat Transfer, Tien, C. L., Canly, V. P., and Ferrel, J. K., Eds., Vol. 1, pp. 215-226, Hemisphere Publ. Corp. (1986).

69. Bensler, H. P. Delhaye, J. M., and Farreau, C., "Measurement of Interfacial Area in Bubbly Flows by Means of an Ultrasonic Technique," Proc. ANS, 1987 National Heat Transfer Conference, pp. 240-246.

70. Nishi, R., "The Scattering and Absorption of Sound Waves by a Gas Bubble in a Viscous Liquid," Acustica, Vol. 33, pp. 65-74 (1975).

71. Neal, L. G., and Bankoff, S. G., "A High Resolution Resistivity Probe for Determination of Local Void Properties in Gas-Liquid Flow," AIChE J., Vol. 9, pp. 490-494 (1963).

72. Park, W. H., Kang, W. K., Capes, C. E., and Osberg, G. L., "The Properties of Bubbles in Fluidized Beds of Conducting Particles as Measured by an Electroresistivity Probe," Chem. Eng. Sci., Vol. 24, pp. 851-865 (1969).

73. Rigby, G. R., van Blockland, G. P., Park, W. H., and Capes, C. E., "Properties of Bubbles in Three Phase Fluidized Beds as Measured by an Electroresistivity Probe," Chem. Eng. Sci., Vol. 25, pp. 1729-1741 (1970).

74. Hoffer, M. S., and Resnick, W., "A Modified Electroresistivity Probe Technique for Steady-and Unsteady-State Measurements in Fine Dispersions-I., Hardware and Practical Operating Aspects," Chem. Eng. Sci., Vol. 30, pp. 473-480 (1975).

75. Serizawa, A., Kataoka, I., and Michiyoshi, I., "Turbulence Structure of Air-Water Bubbly Flow-I. Measuring Techniques," Int. J. of Multiphase Flow, Vol. 2, pp. 221-233 (1975).

76. Herringe, R. A., and Davis, M. R., "Structural Development of Gas-Liquid Mixture Flows," J. of Fluid Mechanics, Vol. 73, pp. 97-123 (1976).

77. Kataoka, I., Ishii, M., and Serizawa, A., "Interfacial Area in Two-Phase Flow; Formulation and Measurement," Proc. 23rd Natl. Heat Trans. Conf. ASME, Denver (1985).

78. Hilgert, W. and Hofmann, H., "Characterization of Gas Phase Flow in Bubble Columns at Low Superficial Gas Velocities with the Aid of Ultrasonic Doppler Techniques," Ger. Chem. Eng. Vol. 9, pp. 180-190 (1986).

79. Wang, S. K., "Three-Dimensional Turbulence Structure Measurements in Air/Water Two-Phase Flow," Ph.D. Thesis, Rensselaer Polytechnic Institute, Troy, New York (1985).

80. Liu, T., Tay-Jian, "Experimental Investigation of Turbulence Structure in Two-Phase Bubbly Flow," Ph.D. Thesis, Northwestern University, Evanston, Illinois (1989).

81. Wang, S. K., Lee, S. J., Jones, O. C., Jr., and Lahey, R. T. Jr., "Three-Dimensional Turbulence Structure and Phase Distribution Measurements in Bubbly Two-Phase Flow," Int. J. Multiphase Flow, Vol. 13, pp. 327-340 (1987).

82. Michiyoshi, I., and Serizawa, A., "Turbulence in Two-Phase Bubbly Flow," Nucl. Eng. and Design, Vol. 95, pp. 253-267 (1986).

83. Matsui, G., "Characteristic Structure of Upward Bubble Flow Under the Same Flow Rate Conditions," Proc. of Japan -- U.S. Seminar on the Two-Phase Flow Dynamics, July 1988.

84. Van der Welle, R., "Void Fraction, Bubble Velocity and Bubble Size in Two-Phase Flow," Int. J. Multiphase Flow, Vol. 11, pp. 317-345 (1985).

85. Beattie, D. R. H., "Two-Phase Flow Structure and Mixing Length Theory," Nucl. Eng. and Design, Vol. 2, pp. 46-64 (1972).